REPORT DOCUMENTATION PAGE	Form Approved OMB No. 0704-0188

1. AGENCY USE ONLY *(Leave blank)*	2. REPORT DATE	3. REPORT TYPE AND DATES COVERED
	28.Oct.98	THESIS

4. TITLE AND SUBTITLE
AN EXPERIMENTAL STUDY OF SURGE CONTROL IN THE ALLIED SIGNAL LTS-101 HELICOPTER TURBOSHAFT ENGINE

5. FUNDING NUMBERS

6. AUTHOR(S)
2D LT NELSON ERIC B

7. PERFORMING ORGANIZATION NAME(S) AND ADDRESS(ES)
MASSACHUSETTS INSTITUTE OF TECHNOLOGY

8. PERFORMING ORGANIZATION REPORT NUMBER

9. SPONSORING/MONITORING AGENCY NAME(S) AND ADDRESS(ES)
THE DEPARTMENT OF THE AIR FORCE
AFIT/CIA, BLDG 125
2950 P STREET
WPAFB OH 45433

10. SPONSORING/MONITORING AGENCY REPORT NUMBER
98-119

11. SUPPLEMENTARY NOTES

12a. DISTRIBUTION AVAILABILITY STATEMENT
Unlimited distribution
In Accordance With AFI 35-205/AFIT Sup 1

12b. DISTRIBUTION CODE

13. ABSTRACT *(Maximum 200 words)*

14. SUBJECT TERMS	15. NUMBER OF PAGES
	16. PRICE CODE

17. SECURITY CLASSIFICATION OF REPORT	18. SECURITY CLASSIFICATION OF THIS PAGE	19. SECURITY CLASSIFICATION OF ABSTRACT	20. LIMITATION OF ABSTRACT

An Experimental Study of Surge Control in the Allied Signal LTS-101 Helicopter Turboshaft Engine

by

Lt. Eric Benjamin Nelson
United States Air Force

B.S., Mechanical Engineering (1996)
United States Air Force Academy
Colorado Springs, Colorado

Submitted to the Department of Aeronautics and Astronautics
in Partial Fulfillment of the Requirements for the Degree of

Master of Science in Aeronautics and Astronautics

at

Massachusetts Institute of Technology
June 1998

Signature of Author 
Department of Aeronautics and Astronautics
23 May 1998

Certified by 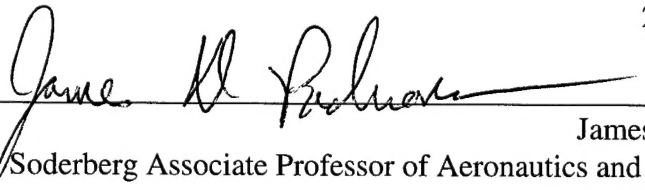
James D. Paduano
C.R. Soderberg Associate Professor of Aeronautics and Astronautics
Thesis Supervisor

Accepted by _____
Associate Professor Jaime Peraire
Chairman, Department Graduate Committee

An Experimental Study of Surge Control in the Allied Signal LTS-101 Helicopter Turboshaft Engine

by

Lt. Eric Benjamin Nelson
United States Air Force

Submitted to the Department of Aeronautics and Astronautics on 23 May 1998
in Partial Fulfillment of the Requirements for the Degree of
Master of Science in Aeronautics and Astronautics

Abstract

Surge dynamics and surge control techniques are experimentally examined on an Allied Signal LTS-101 helicopter engine. Diffuser throat injection is used for actuation. A mean level of 95 psig air injection modifies the system dynamics. Steady state injection creates a relatively large, surge-free region of near zero characteristic slope at the speedline peak, which is conducive for control.

Low frequency unsteadiness is observed prior to surge for the open loop baseline case. With mean air injection, the system has a 27 Hz surge mode, and a series of higher frequency acoustic resonances, the first of which occurs at 68 Hz. These modes are one dimensional, with no rotating stall development.

Surge is stabilized in the LTS-101 using active feedback control. The control strategy is to sense upstream static pressure patterns at multiple axial locations and feed back the measured signals to a high speed valve in the air injection flow path. At 95% N1 corrected, an H-infinity compensator achieves a 0.98% reduction in stalling mass flow. This equates to 10.7% increase in the overall operating range of the engine.

The H-infinity compensator achieves range extension by damping the surge mode. The scheme successfully avoids excitation of the acoustic resonances. Less complex feedback schemes are unable to achieve compressor stalling mass flow reduction. This research effort incorporates a rigorous, systematic robust control redesign process.

A linear, acoustic model is derived for the transfer function relation between the high speed valve command and the static pressure signal at the inlet. The model predicts a surge mode at 27 Hz and various acoustic frequencies. Based on this model, the 68 Hz mode is attributed to acoustic resonances in the system, which includes the LTS-101 and inlet ducting.

Thesis Supervisor: James D. Paduano
C. R. Soderberg Associate Professor of Aeronautics and Astronautics

Thesis Supervisor Alan H. Epstein
R. C. MacLaurin Professor of Aeronautics and Astronautics

Acknowledgments

There are numerous people whom I wish to thank for their contribution and continual support throughout this project.

Professor Jim Paduano. He is personally responsible for many of the ideas that I pursued in this research effort. He is an excellent advisor, pushing me in the right direction from the start of my MIT Masters program. He was always responsive to various aspects of my project.

Professor Alan Epstein. He is a continual source of technical advise. I want to thank him for trusting me with the half million dollar project, even after I broke the load cell. He also provided "the big picture" throughout my GTL days.

The next group of people contributed many hours, enabling me to understand the test facility. Fouzi Al-Essa and Jinwoo Bae. Not only are they good friends, but I thank them for the technical foundation. They each dedicated hours to my project. Thanks to Brian Corn and Laurence Didierjean. I realize that I wasn't "up to speed" while you were here, but I appreciate the patience when I was "getting my feet wet" in this project.

A number of laboratory technicians contributed time to my project. Thanks for the insight and inspiration. They include James Letendre, Bill Ames, Viktor Dubrowski, Mariano Hellwig, Tom Ryan, Mike Peete, and Alan Chandler. A special thanks to Jimmy and Bill for the numerous hours they operated the LTS-101 with me.

I would like to thank several staff members for their assistance during my time here at MIT: Holly Anderson, Diana Park, Lori Martinez, and Elizabeth Zotos.

The next group of individuals contributed many hours to explaining theoretical concepts to me. Harald Weigl was always available for a question or two. I especially appreciate the interest he showed in my research, even after graduating and going to California. The compensators worked!!! ..... John Chi, Luc Ferchette, Zolti Spakovzky, thanks for all the assistance in understanding various controls concepts. And John, thanks for helping me with the controller hardware. In addition, I want to thank to all members of the smart engines group at MIT.

Next, a number of individuals contributed to my understanding of various concepts along the way. Ammar Al-Nahwi, for the hours we spent talking about various theoretical concepts (modeling, the compressor map, and of course, how the USA is going to take the World Cup in 1998). Sonia Ensenat, I appreciate the help in 16.357; there is no way I would have survived the course without her. Thanks for the tips on Volleyball too; only winning one championship isn't that bad. Ken Gordon, thanks for the advice on homework, tips for the seminar, and your humorous points along the way.

A number of individuals contributed to my general well being while attending MIT. J.B, I want to thank him for "scooping me up" when I needed a roommate. He is one of the best roommates that I've had. Thanks for reading parts of this thesis and best of luck down in Florida. Jake, my Chicago buddy, thanks for the mental support while I was stressing with this thesis. Thanks for the intellectual conversations, the clubbing, and work outs. To the two Brians, I've enjoyed playing sports at MIT. Good luck in Denver Teeple. Take the Basketball championship next year Schueler.

I'd like to thank the members of my family for the continual support throughout my educational experience. I appreciate the thoughts and experiences that we've shared. Dan, a special thanks for the advice throughout my life. Let the soccer story live on!!!! I'd also like to thank my Church friends at Antioch and Park Street for the prayers and thoughts. To God, my source of strength and perseverance, thanks for your continual guidance throughout my life.

Finally, to Amy Reijonen, my new wife (in about a month), I really appreciate the emotional support throughout our long distance relationship. I did this for you.....

This project was funded by the Air Force Office of Scientific Research (AFOSR), grant number F49620-95-1-0409. I would like to thank the Air Force Institute of Technology (AFIT) program manager, Captain Rick Sutter, for his services. A special thanks to Industrial Devices Inc. for the linear motion controller and actuator and technical support.

Table of Contents

List of Figures

Chapter 1

Chapter 2

Chapter 3

Chapter 4

Chapter 5

Chapter 6

Appendix B

Appendix E

Appendix G

Appendix H

List of Tables

Chapter 2

Chapter 3

Chapter 4

Chapter 5

Appendix A

Appendix C

Appendix E

Nomenclature

Chapter 1

a_p - Speed of sound within the plenum
B - Compressor stability parameter
L_{CD} - Length of compressor or pump ducting
U - Blade speed at mean radius of axial compressor
U_T - Reference velocity; axial inducer tip speed
V_p - Volume of the plenum
ω_H - Helmholtz resonator frequency

Chapter 2

CCW - Counter clock wise

$\dot{m}_{corr}$ - Corrected mass flow. A derived quantity for the LTS-101, and is used to quantify engine performance. --- *Also used in Chapter 5 and Appendix A*

$\dot{m}_{des}$ - The design massflow for the LTS-101 --- *Also used in Chapter 5*

$\dot{m}_{fuel}$ - Fuel massflow rate

$\dot{m}_{inj}$ - Massflow rate for air injection

N1 - Gas producer turbine shaft speed --- *Also used in Chapter 7 and Appendix A*

$N1_{corr}$ - Gas producer turbine shaft speed, corrected for ambient temperature --- *Also used in Chapters 3,5, and 6*

$P_{ambient}$ - Measured atmospheric pressure --- *Also used in Chapter 3*

P_{oil} - Oil Pressure for LTS-101

P_1 - Inlet static pressure --- *Also used in Chapters 3 and 5 and Appendix A*

P_3 - Compressor exit static pressure --- *Also used in Appendix A*

P_5 - Gas producer turbine entrance static pressure --- *Also used in Appendix A*

RSS - Root Sum Squares Method (See reference [22])

TDC - Top dead center; used as a reference for Kulite pressure tap location

T_{EGT} - A measured temperature of the exit gas at the nozzle

$T_{exhaust}$ - Temperature of the exhaust air in the duct, measured immediately downstream of the exhaust cooling nozzles.

T_{inlet} - Inlet temperature, measured at the inlet duct entrance.

$T_{nozzlemetal}$ - Surface temperature of the outside nozzle

T_{oil} - Oil temperature of LTS-101

T_{shroud} - Temperature immediately inside the engine shroud

T_{T4} - Total temperature of the combustor --- *Also used in Appendix A*

η_c - *Compressor efficiency*

π *(or* π_c) - Pressure Ratio. A nondimensional ratio between the compressor exit pressure and ambient pressure. Used to quantify engine performance. --- *Also used in Appendix A*

Chapter 3

Defined in Chapter 2: $N1_{corr}$, $P_{ambient}$, P_1

A, B, C, D - Standard state space representation of system. May contain subscripts associated with plant, compensator, or augmented plant matrix. --- *Also used in Chapter 4 and Appendices D, E, and F.*

$a_k(t)$ - Spatial Fourier coefficient

DFFT - Discrete fast Fourier transform.

FFT - Fast Fourier Transform

FORSE - Frequency dependent Observability dependent Range Space Extension. the software package used for transfer function identification --- *Also used in Chapter 5*

$f_{resolution}$ - The frequency resolution for power spectral density plots

f_s (or $f_{sampling}$) - Sampling frequency of the high speed data acquisition computer

G(jω) (or P(s)) - Engine dynamics, including the LTS-101, high speed valve dynamics, computer delay, and digital filters. --- *Also used in Chapter 4 and Appendices E and F*

G_{mn} - Complex transfer functions, where m is the designated input number and n is the designated output number.

G_p - The transfer function representing the power spectral density of the given input and output signals

I (or j) - Imaginary component of a complex number --- *Also used in Chapters 4 and 6 and Appendix H*

k - Constant (i.e. 1, 2, 3, 4, etc.)

MIMO - Multiple input multiple output, referring to the number of input actuators and number of output sensors

MISO - Multiple input single output. (See MIMO above) --- *Also in Chapter 4*

N - Process noise associated with the output signal in forced response testing

nfft - Number of data points on which a fast Fourier transform is calculated.

n - Indicates the harmonic order (i.e. zeroth, first, etc.) --- *Also in Chapter 5*

n(jω) - Process noise

P(s) - (See G(jω) above)

PSD - Power spectral density. The units are $\frac{psia^2}{Hz}$ for this thesis --- *Also used in Chapter 5 and Appendices B and G.*

P_{feed} - Static Pressure of the injector into the LTS-101 --- *Also used in Chapter 6*

Q - Volume flow rate of injected air

S - Signal of sinusoid for forced response testing

s - Equals jω --- *Also used in Chapter 4 and Appendices E and H*

SIMO - Single input multiple output (See MIMO above) --- *Also used in Chapter 6*

SISO - Single input single output (See MIMO above) --- *Also used in Chapter 4*
$S(j\omega)$ - True output signal from engine dynamics
$S_{uu}(j\omega)$ - Power spectral density of input u
$S_{uy}(j\omega)$ - Cross spectral density between input u and output y
t - Time, in seconds --- *Also used in Appendices D and H*
$U(j\omega)$ (or U(s)) - High speed valve command input
u_n - input of general system
x - state of system --- *Also used in Chapter 4 and Appendices D and E*
y (or $y(j\omega)$) - vector of measured plant outputs. the Kulite pressure measurements in this experiment that are used for feedback(or with subscript designation) --- Also used in *Chapter 4 and Appendices D and E*
Δf - Frequency resolution for waterfall plots
$\delta P(\theta,t)$ - Pressure perturbations with respect to circumferential location and time
θ - circumferential location of the pressure sensor from top dead center of the engine annulus
ω - frequency, measured in Hz --- *Also found in Chapter 4 and 6 and Appendix H*

Chapter 4

Defined in Chapter 3: A, B, C, D, j, MISO, s, SISO, P(s), y (or $y(j\omega)$), x, and ω

C(s) - Complimentary sensitivity transfer function between measured plant output signal and reference input signal --- *Also used in Appendix E*
CF - Correction factor for Pade approximation
CT - Continuous time domain
D(s) - Pure time delay transfer function approximated by the pure time delay
DT - Discrete time domain, as implemented by the control computer
e(s) - Error signal --- *Also used in Appendix E*
K(s) - Robust compensator dynamics --- *Also used in Appendix E*
MSV - Maximum singular value
R(s) - Actuator transfer function between control command signal and reference input signal --- *Also used in Appendix D*
r(s) - reference input signal --- *Also used in Appendix D*
S(s) - Sensitivity transfer function between reference input and error signal --- *Also used in Appendix E*
u(s) - Control command signal from --- *Also used in Appendices D and E*
w(s) - Unknown disturbances --- *Also used in Appendices D and E*
W_1 - Weighting in mixed sensitivity H-infinity design that shapes the sensitivity transfer function, S(s) --- *Also in Appendix E*
W_{11}, ΔE, W_{12}, $w_1(s)$, and $z_1(s)$ - Associated with eigenvalue perturbation circles to stabilize particular frequencies of interest.
W_2 - Weighting in mixed sensitivity H-infinity design that shapes the actuator transfer function, R(s) --- *Also in Appendix E*

W_3 - Weighting in mixed sensitivity H-infinity design that shapes the complimentary sensitivity transfer function, C(s) --- *Also in Appendix E*

z(s) - Error signals deviant from typical plant output --- *Also used in Appendices D and E*

$\Delta(s)$ - Unknown perturbation dynamics that include plant model variation, unmodeled dynamics, and unknown disturbances --- *Also used in Appendix E*

$\|\Delta(s)\|_\infty$ - Infinity norm for MIMO system. equivalent to maximum value of Bode magnitude for a SISO system

σ - Eigenvalue real part (growth rate)

τ - Time delay parameter for pure time delay

Chapter 5

Defined in Chapter 2: $\dot{m}_{corr}$, $\dot{m}_{des}$, $N1_{corr}$, and $P_{ambient}$, P_1, and P_3

Defined in Chapter 3: FORSE, n, PSD

Chapter 6

Defined in Chapter 2: $N1_{corr}$,

Defined in Chapter 3: i, P_{feed}, s, SIMO, and ω

A - Area of component --- *Used in Appendix H*

a - Speed of sound --- *Also used in Appendix H*

a, b, c, d, e, f - Symbolic representation for matrix terms multiplied by Matlab (may include subscripts)

a_s - Area ratio between the desired duct and some reference duct (where s is some associated subscript (either r, s, y, 0, or 1)) --- *Also used in Appendix H*

L_{inj} - Length of injector duct in model

L (or L_{ref}) - Reference length for nondimensionalizing --- *Also used in Appendix H*

$\dot{m}$ - Dimensional massflow

P - Dimensional pressure --- *Also used in Appendix H*

u - Velocity through the component --- Also *used in Appendix H*

U_{ref} - Reference velocity, usually selected as the speed of sound through the inlet duct --- Also *used in Appendix H*

V_{comm} - Voltage signal from the high speed valve --- *Also used in Appendix A*

ϕ - Nondimensional axial flow (A subscript of inj or s refers to the injected axial flow, while a number subscript refers to a station number designation). --- *Also used in Appendix H*

ρ - Density --- *Also used in Appendix H*

ψ - Nondimensional pressure (Subscript of "inlet" refers to inlet static pressure, while a number subscript refers to a station designation). --- *Also used in Appendix H*

Chapter 7

Defined in Chapter 2: N1

Appendix A

Defined in Chapter 2: $\dot{m}_{corr}$, N1, P_1, P_3, P_5, T_{T4}, *and* π *(or* π_c)

EGT - Exhaust gas temperature
T_{T3} - Total compressor exit temperature
T_{45} - Temperature associated with Allison engine en route to the turbine

Appendix B

Defined in Chapter 3: PSD

Appendix C

x - intermediate variable

Appendix D

Defined in Chapter 3: A, B, C, D, x(s), and y(s)
Defined in Chapter 4: u(s), w(s), and z(s)

F_∞ - Defined as $-B_2^T X_\infty$ in H-infinity compensator design

L_∞ - Defined as $-(Y_\infty^{-1} - X_\infty)^{-1} C_2^T$ in H-infinity compensator design, where

$L_\infty(\hat{y}(t) - y(t))$ is the observer term that corrects for error between estimated output and measured output

$\hat{w}_{worst}$ - a worst case disturbance to counter the H-infinity compensator

Appendix E

Defined in Chapter 3: A, B, C, D, P(s), x(s), and y(s)
Defined in Chapter 4: C(s), e(s), K(s), R(s), S(s), s, u(s), w(s), W_1, W_2, W_3, z(s), and Δ(s)

J - Used to simplify expressions by representing $\left[I + D_p D_c\right]^{-1}$

I - Identity matrix --- *Also used in Appendix F*

Appendix F

Defined in Chapter 3: A, B, C, D, P(s)
Defined in Appendix E: I

Appendix G

Defined in Chapter 3: PSD

Appendix H

Defined in Chapter 3: i, s, t, and ω
Defined in Chapter 6: A, a, a_s, L, P, u, U_{ref}, ϕ, ρ, and ψ

m_c - nondimensional slope of compressor characteristic
m_T - nondimensional slope of throttle characteristic
$V_{injector}$ - Injection velocity

Chapter 1

Introduction

1.1 Motivation

Surge is a violent, one dimensional oscillatory flow instability inherent to turbomachinery operating at high pressure ratios and low mass flows relative to design conditions. Cycles of flow reversal occur during this event, rendering the engine unusable for productive thrust output, causing engine degradation and possible damage. Because engine surge can have catastrophic consequences, compressors are designed to operate at larger mass flows for a given design pressure ratio. This surge margin ensures that a surge event will not occur; however, the engine's thermodynamic efficiency and thrust output are compromised as a result (Figure 1.1).

The term "Active control" encompasses a number of potential methods to prevent the onset of surge while operating at a lower air massflow for a given compressor pressure ratio. If successful techniques are developed that extend the stable operating range, engine manufacturers can safely design engines to run at operating points closer to the open loop unstable region. This enables the engine performance to increase without the threat of surge.

1.2 Background Surge Work

In 1955, Emmons [1] investigated the oscillatory behavior of centrifugal compressors. He proposed a Helmholtz acoustic resonator model, which explains the behavior of a duct attached to a plenum, as a framework for modeling surge. In 1976, Greitzer [2,3] developed a

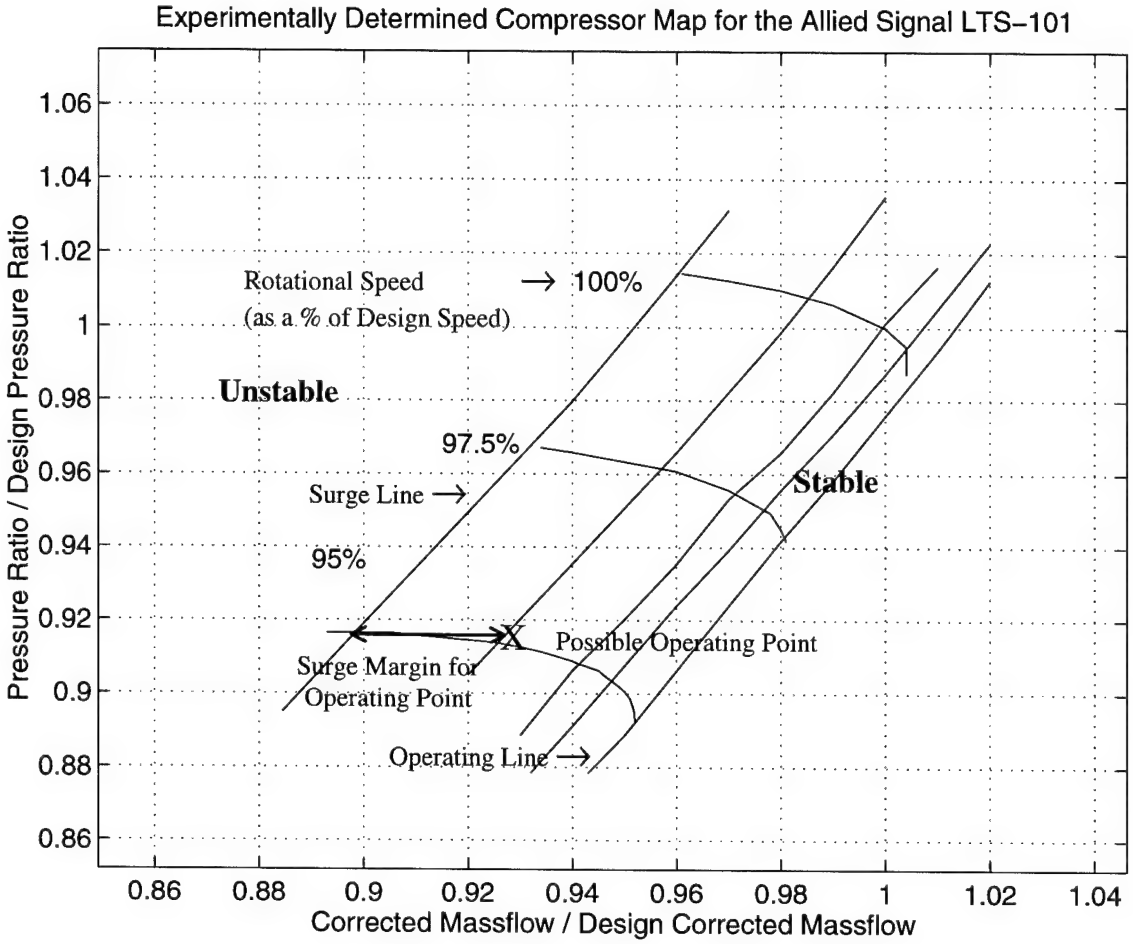

Figure 1.1 LTS-101 Inlet Compressor Map with Definitions

nonlinear model that captured the surge cycle behavior observed in compression systems. To categorize system behavior, he introduced a nondimensional parameter that measures the ratio of a system's compliance (plenum compressibility) to inertia (mass of fluid within compressor ducting).

$$B = \frac{U_T}{2 * a_p} * \sqrt{\frac{V_p}{L_{cd} * A_c}} = \frac{U_T}{2 * \omega_H * L_{CD}} \qquad (1.1)$$

where a_p is the speed of sound within the plenum, U_T is the compressor rotor tip speed, and V_p, A_c, and L_{cd} are geometric parameters (See definitions on page 21). Greitzer discussed dynamic versus static compression system instabilities. The typical limiting dynamic instability requires a very small positive slope in a constant speed compressor characteristic. As a result, the surge line is almost always near the line connecting the peaks of the speed lines.

In 1989, Epstein et al. [4] suggested feedback control as a means to suppress oscillations that develop into surge. He suggested that one could employ active control techniques to stabilize the precursors that lead to surge. If the surge line is thus moved to lower massflows with control techniques, engine manufacturers can move the operating point to higher efficiency regions without the risk of surge. These theoretical ideas triggered experimental efforts to extend the surge line via active control.

1.3 Previous Surge Control Work

Many experimental efforts are documented that have the goal of extending the compressor speedline. In 1960, Bodine [5] reported a 16% flow range extension on a two stage centrifugal compressor with 1.7 lb/sec design mass flow rate. He used an acoustic absorber to extend the flow range. Amann et al. (1975) [6] worked with a centrifugal compressor of an automotive turbine engine with a ~4 lb/s design mass flow rate and 3.7 design pressure ratio. They demonstrated a reduced surge flow rate by adding a chamber to the casing. In 1988, Fink [7] investigated surge dynamics on a small centrifugal turbocharger test rig. Huang [8], Pinsley (1991) [9], Gysling [10], and Simon [11] demonstrated feedback surge control on lab scale turbocharger rigs. Various actuation schemes were used: a

movable plenum wall, a plenum exit bleed valve, and a valve close coupled to the compressor. Meanwhile, in 1990 and 1993 Williams et al. [12,13] demonstrated a 2.6% decrease in corrected mass flow on a 60 hp auxiliary power unit with a compression ratio of 3:1 by injecting 100 psig compressed air into the combustor.

Two simultaneous engine control efforts persist at the Gas Turbine Laboratory, Massachusetts Institute of Technology. In 1994, Borror [14] began experiments on an the Allied Signal LTS-101, reporting that it has abrupt surge behavior with no precursor. He also reported a 0.7% total pressure loss across the diffuser at an operating point near surge due to injection of at, at 1.3% of nominal engine massflow, into the diffuser passages. Corn [15] showed that this mean air injection changes the compressor characteristic resulting in mild surge precursors. His work constitutes the first detailed system identification effort of an engine; he obtained transfer functions between diffuser throat air injection with a high speed valve and static pressure at various locations. Corn then implemented several compensators in an effort to control the engine. Successful speedline extension was not achieved. In [16,17], Diderjean developed two versions of nonlinear sliding mode control for the LTS-101. However, these designs were not implemented before engine problems stopped experimentation.

Meanwhile, on an Allison 250-C30, Al-Essa [18] investigated presurge behavior and measured forced response behavior. Throttling orifices were inserted between the compressor and combustor to move the steady state operating line toward the surge line. The compressor was then throttled into surge using water injection downstream of the throttling orifices. System identification by forced response tests, as well as feedback control, were achieved using one dimensional high pressure air injection through inducer bleed slots near the impeller

face. Bae [19] then attempted several compensation schemes. Successful corrected massflow range extension was not achieved.

The primary focus for this experimental effort is H-infinity compensator design. Using this approach, Weigl [20] demonstrated successful control of rotating stall on a NASA Lewis, single stage compressor. This compressor has a total pressure ratio per stage of ~1.9:1, with ~20 kg/s mass flow rate, and a rotor rotational frequency of 286.5 Hz. Eight Kulite static pressure transducers and twelve actuators were used to obtain 11% and 3.5% reduction in stalling mass flow for relative Mach numbers of 1.0 and 1.5 respectively. To achieve these results, Weigl used a two by two multiple input multiple output system identification and subsequent multivariable controller design using H-infinity methods.

1.4 Motivation and Technical Objectives.

The overall goal of this research effort is to establish an engineering framework to design and implement compensation schemes that extend an engine's operating range. This task is accomplished by adopting a linear framework and systematically characterizing the engine at various operating points. Next, a systematic method is used to design a compensator that produces optimal performance of the closed loop system. Finally, the compensator is converted to discrete form and is implemented using a control computer and high speed injection system.

While the ultimate goal is to operate the LTS-101 at lower mass flow levels with compensation, two specific aspects of the problem are categorized as discussed below: the engineering perspective and the theoretical perspective.

1.4.1. Engineering Perspective

Since previous control system design efforts were conducted in a rather ad hoc manner, an experimental outline for successful control has not been documented for control on full scale engines. Such documentation should include more than the means of control, such as the high speed valve, its control, and source of actuation. One must understand the theoretical framework for compensator design, a means of converting that compensator to an implementable form, and a rigorous method to redesign the compensators based on previous experiments.

In addition, obtaining good experimental results depends on much more than just having the right compensator design. There is a need to evaluate the engine loading techniques and minimum requirements for approaching the surge line. Real time system monitoring is often critical in an effort to achieve good results. Finally, external conditions play a large role in experimental performance.

1.4.2 Theoretical Perspective

A model is required that explains the occurrence of various modes within the engine system. Various lumped parameter models have been proposed to explain the existence of the surge mode of the engine system. Yet, the acoustic resonances are largely explained away as local disturbances and remain unmodelled. There is a need to develop models with acoustic properties that reasonably predict the eigenmodes. This model should also attempt to explain why the engine appears to enter surge in different ways.

1.4.3 Objectives

Based on these needs, the objectives for this thesis are as follows:

1. Assess the need for engine and instrumentation modifications for this series of Allied Signal engine runs. Implement any necessary modifications.

2. Identify any engine behavior that is different from that found in previous experiments. In addition to identifying the changes, one should offer an explanation for shifts in operating line, speed line, and surge line.

3. Use open loop forced response testing to generate a linear, multivariable input-output model of the engine.

4. Apply the H-infinity design process to generate a compensator that will successfully stabilize the closed loop engine beyond the open loop surge line.

5. Obtain a statistical analysis of improvement with compensation.

6. Offer an effective method of compensator redesign within the H-infinity theoretical framework.

7. Use acoustic modeling techniques to explain the engine's linearized modes.

8. Report on shortcomings of the model. Propose possible explanations as to why the closed loop engine surge behavior differs from open loop surge behavior.

1.5 Thesis Organization

1. Chapter one introduces concepts, previous research, and current motivations and objectives.

2. Chapter two describes the Allied Signal LTS-101 engine and test facility, instrumentation, actuation scheme, and control law implementation equipment. Since much of the experimental setup is covered by predecessor experiments, the emphasis is placed on the rebuild, modifications, and instrumentation additions for these runs. Finally, the experimental setup and shut-down procedures are discussed, as well as data reduction techniques.

3. Open loop features of the LTS-101 engine are addressed in the third chapter. This includes the effects of mean air injection, surge precursors, and system identification.

4. The fourth chapter covers the theoretical basis and design procedure for H-infinity control. Since much of the theory is well established, this study emphasizes design specifics.

5. The closed loop engine runs are discussed in the fifth chapter. The H-infinity control schemes reduce the surge mode precursors, allowing for a ~1% reduction in corrected mass flow.

6. The sixth chapter explains the modeling efforts for the LTS-101. This model uses acoustic theory that couples pressure and massflow to generate modes at correct frequencies.

7. The final chapter summarizes this research effort.

Chapter 2

Experimental Facility and Test Procedures

2.1 Engine and Test Facility

The Gas Turbine Laboratory at Massachusetts Institute of Technology has two engines to study surge control. Prior to this research, active control efforts focused on the Allison 250-C30P, 600 HP class helicopter engine in 1997-98. On the other hand, the experiments described in this thesis use the Allied Signal (formerly Textron / Lycoming) LTS-101-600A-2 600 horse power class helicopter engine. The LTS-101 is used in the Aerospatiale HH-65 Dauphin, the Eurocopter BK117, and the Bell 222B and 222UT helicopters. The engine peak pressure ratio is about 8 to 1 and the design mass flow is about 5 lb/s. The air enters through a converging inlet duct, and flows through a compressor with a single axial and centrifugal stage (Figure 2.1). The air then moves through a vaned diffuser and annular combustor. The engine normally contains a single stage gas generator turbine and a single stage power turbine with output shaft. In the experimental setup, the power turbine and shaft are removed [14,15] (Figure 2.2). Accessories and compressor stages are driven by the gas producer turbine. The air then exits a variable area nozzle.

Two hardware differences exist on the experimental test rig when compared to its counterpart in commercial use. First, the diffuser throat area is slightly enlarged. This modification ensures that the centrifugal stage limits the stable operating range of the engine. Second, the turbine nozzle guide vane area is reduced. This engine modification increases the pressure ratio achieved for a given massflow. As a result, the no load operating line is closer

to the surge line, as is detailed in chapter 3.1. The primary benefit is to reduce the turbine inlet temperatures while operating the engine near surge.

The test rig is mounted on a steel frame inside a large reinforced concrete test cell

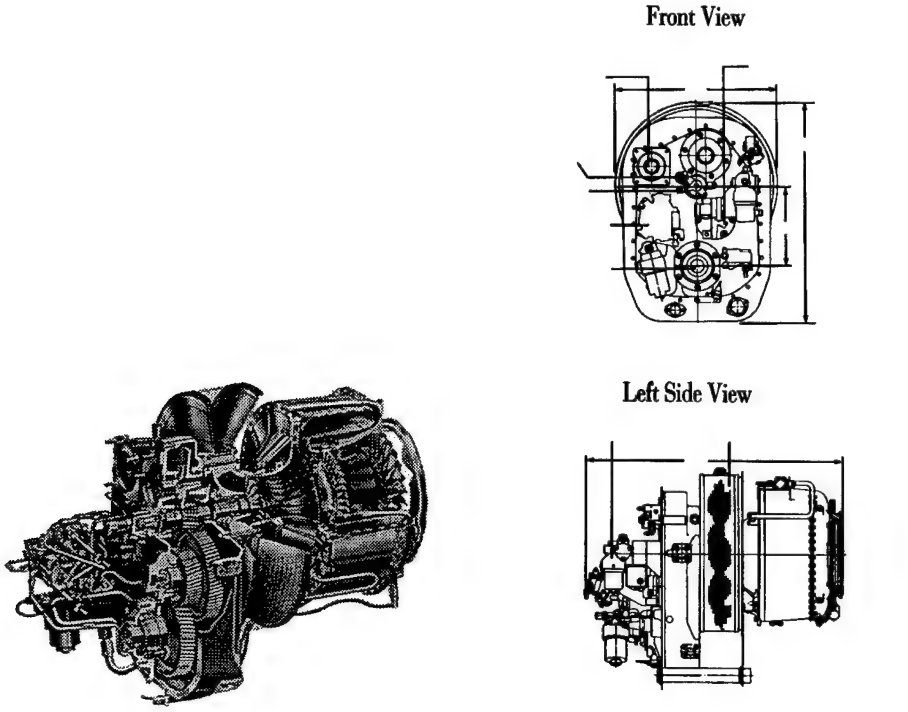

Figure 2.1 Schematic of the LTS-101 Helicopter Engine

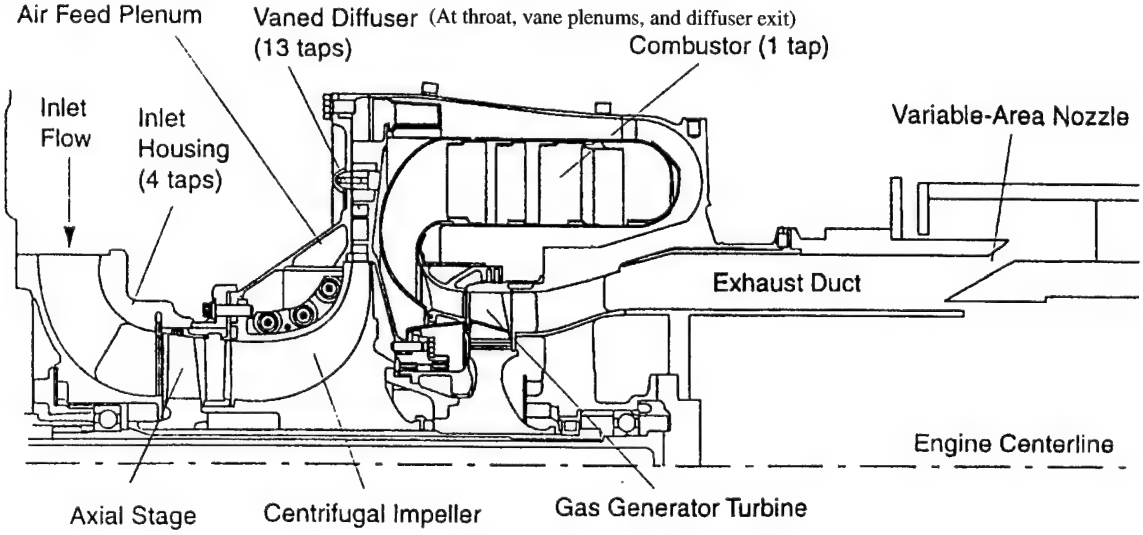

Figure 2.2 Test Stand Schematic

(Figure 2.3). Details of the experimental setup are found in [21] and recapped in [15]. A Dell 433DE computer operates all engine and test stand functions, via the software package Genesis, from outside the test cell. Video cameras allow the operators to monitor the engine throughout the engine run. A front camera view emphasizes the throttle position, which is controlled by a BEI Motion Systems Co. stepper motor and Parker Co. encoder. The stepper motor is used to control the throttle, which controls the gas producer turbine rotational speed (N1). The throttle is used to maintain the design corrected operating speed ($N1_{corr}$) of 95%. A side view camera displays the linear actuator position, which is described later in this chapter.

The experimental rig is equipped with a variable area exit nozzle to control the mass flow. The nozzle design consists of two concentric nozzle sections. The outer radius nozzle section is attached to the engine, closing towards the inner nozzle and stationary exhaust

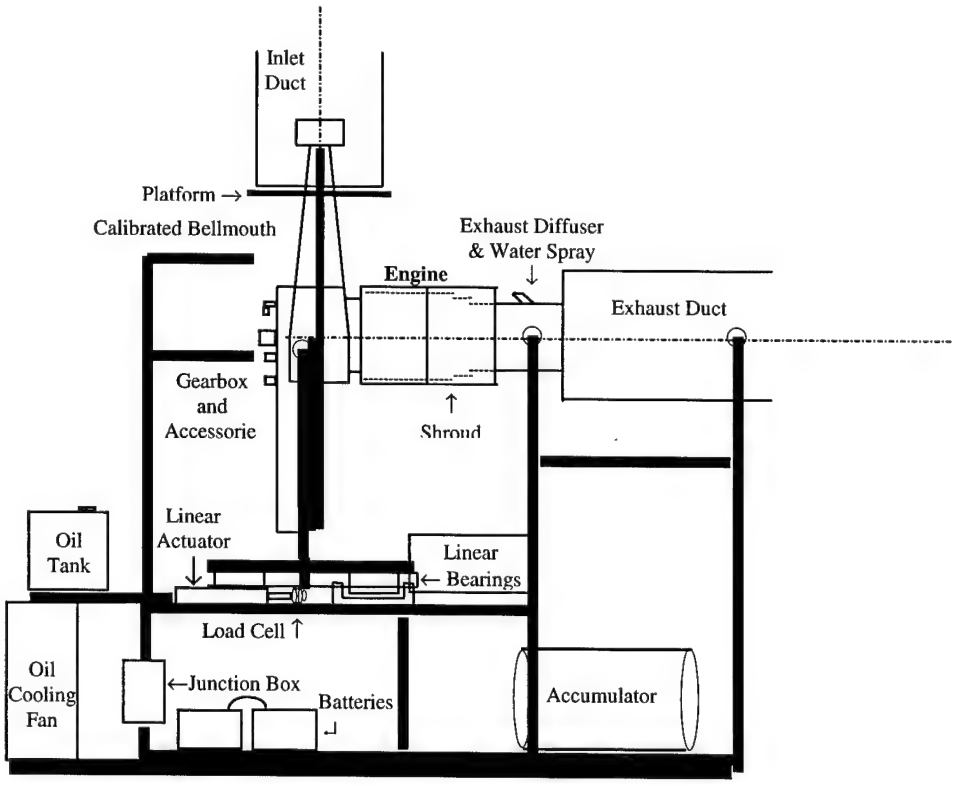

Figure 2.3 LTS-101 Helicopter Test Rig and Instrumentation. (Note: Wires, hoses and other connections between components are not pictured.)

diffuser. The LTS-101 is located on a steel mount supported by linear bearings (Figure 2.3). The bearings allow movement in the engine's axial direction only, and the exhaust area decreases as the engine is pushed towards the stationary exhaust diffuser. Thus, the air massflow is reduced.

Inlet ducting provides the engine with outside air from the laboratory roof. This limits thermal inlet distortion effects from the radiated engine heat. An additional step is taken for the experiments reported here. To reduce inlet distortion, fiberglass insulation surrounds the entire inlet ducting. Another inlet ducting modification incorporates a removable inlet ducting segment for the LTS-101. This provides two breaks in the ducting circulation paths shared between the engines. The new ducting insert keeps Allison 250-C30P surges from depositing engine exhaust debris in the LTS-101 inlet. The Allison engine already has a removable inlet section. Finally, while running the LTS-101, a rubber skirting provides an interface between the removable inlet ducting segment and a flat wood platform mounted at the bellmouth entrance.

Exhaust ducting channels hot air and emissions out of the test cell. The ducting contains acoustic absorbers and extends to a 40 foot tower on the laboratory's roof for attenuation of acoustic energy. Because the experimental test rig does not have a power turbine, high exit temperatures are generated, especially while the engine is under load. The exhaust ducting is cooled by water injection when the temperature exceeds a threshold level. Air is cooled most effectively by spraying a stream that is fine enough to evaporate completely in the exhaust. Previous exhaust nozzles sprayed excess water. In addition, a large portion of the cooling stream hit the duct wall and pooled inside the exhaust duct. By reducing both the quantity of water flow and the jet angle, new cooling nozzles eliminate the

water atomization problem while maintaining efficient exhaust cooling. Table 2.1 summarizes the modification.

A significant test stand modification involves the replacement of the linear motion controller and actuator. The previous system incorporated a weight and pulley system to assist an undersized actuator in reducing the nozzle area. Following an engine run, the actuator could not retract to return the test sled to the home position. An Industrial Devices' replacement system was installed that has adequate force to easily overcome the engine's thrust output when closing the nozzle area. Minor test frame modifications and oil tank placement accommodate the larger actuator. Another benefit of the new actuator is greater precision for linear movement. One can see the reduction in transient overshoot of the measured engine thrust output (Figure 2.4). In addition, the new actuator removes a cumbersome homing procedure required by the old actuator. Table 2.2 summarizes the performance features of the modification. Table 2.3 summarizes the hardware modifications prior to the engine runs.

2.2 Instrumentation and Data Acquisition

There are two types of data collected during the research effort. First, steady state

	Former Veejet spray nozzle	New Veejet spray nozzle
Spray Angle at City water pressure	114°	68°
Flow Capacity per jet	~1.2 gal. per minute	0.61 gal. per minute
Width of jet stream	0.078 inches	0.057 inches
Total Spray capacity	9.6 gal. per minute	4.88 gal per minute

Table 2.1 Exhaust Nozzle Cooling Modification Summary

performance measurements are taken on a Dell 433DE computer. This machine provides steady state engine performance data recording, engine operation control, and diagnostic parameter monitoring. Bell [21], Borror [14], and Corn [15] developed the associated real time process control software using Genesis, by Iconics Inc. The data is logged at a sampling rate of 2 Hz, unless otherwise stated (Table 2.4). Steady state data is used to determine the compressor operating point on the compressor map, which is displayed as the corrected mass flow versus compressor pressure ratio (Table 2.5). Error estimates are determined using the

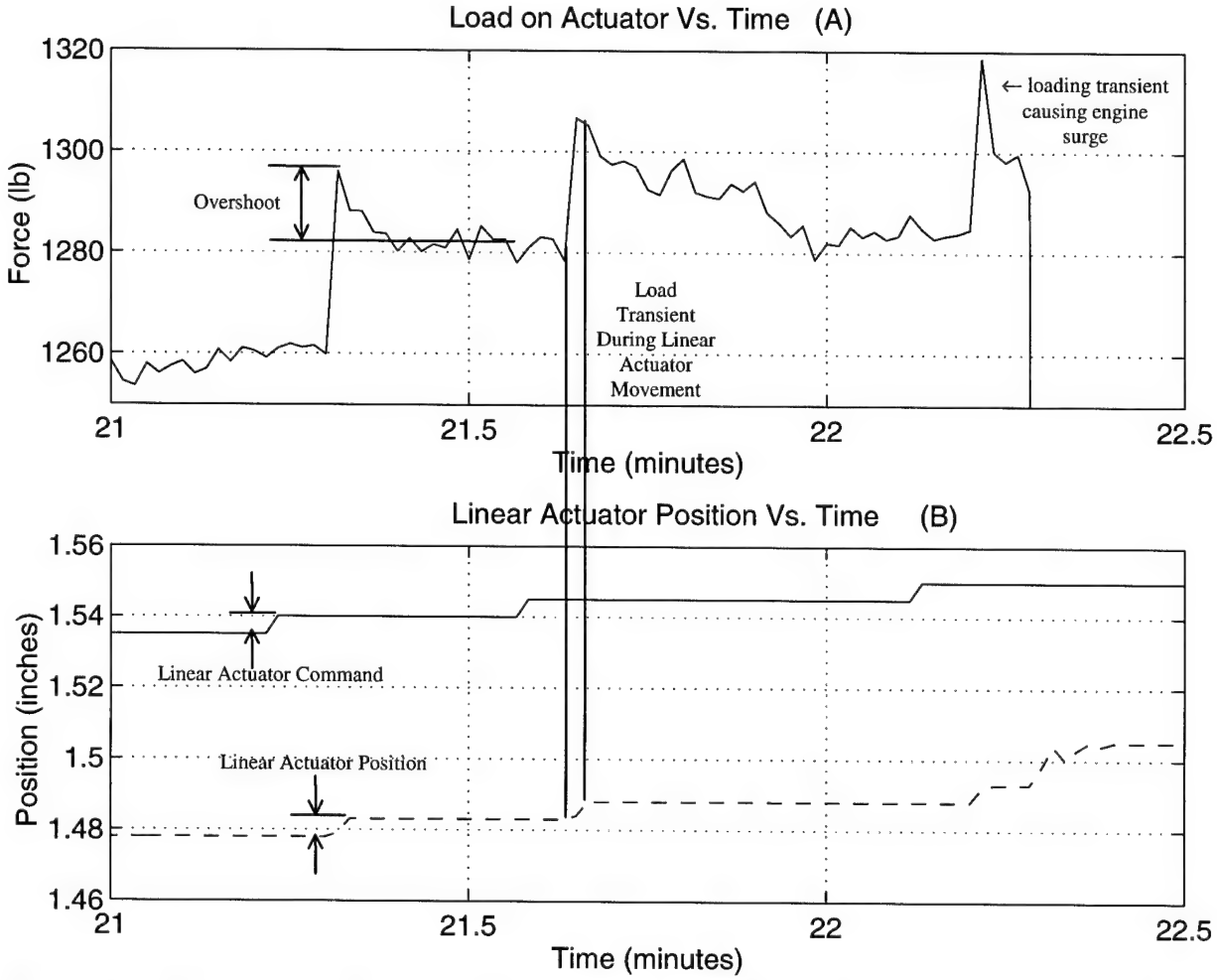

Figure 2.4A, B Loading Transient Caused by the H3581A Linear Actuator Used for Engine Runs prior to July 1997. Nozzle position values are relative.
- Nozzle Command - - Nozzle Position
Note that the loading transient appears to induce the surge.

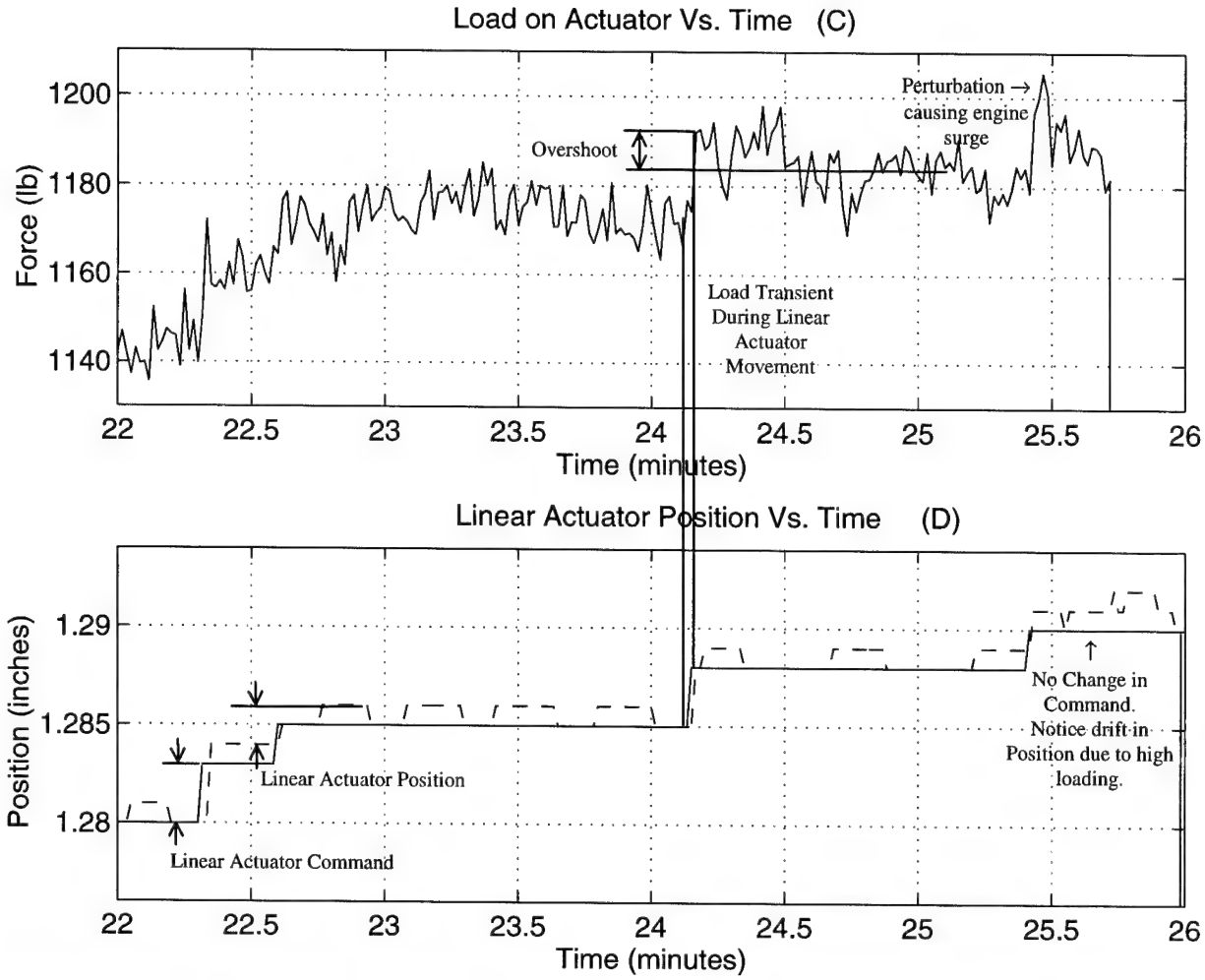

Figure 2.4C, D Loading Transient Caused by the New TB32-1004B Linear Actuator Used for Current Experiments. Nozzle position values are corrected to actual linear motion controller placement. - Nozzle Command - -Nozzle Position The surge is induced by aerodynamic perturbation.

Root Sum Squares (RSS) method and are expressed in terms of percentage of full scale.[18,22].

The second major type of data is high frequency pressure measurements. The Allied Signal LTS-101 engine was modified to include nineteen static pressure taps at five axial locations (Table 2.6). The current tap configuration, which is also summarized in [15], is as follows. Four of the taps are located just prior to the axial compression stage. Six taps are

found at the diffuser throat immediately down stream of the impeller. The LTS-101 incorporates a vaned diffuser as shown in Figure 2.5. Each passage in this diffuser has a slot that connects it to a small cavity, referred to as the vane plenum, inside the adjacent diffuser vane [14]. Three taps are placed in vane plenums; these taps provide the best unsteady static pressure measurements, as will be discussed shortly. Four taps exist at the diffuser exit. Finally, there is a single combustor tap. Figure 2.2 shows the pressure tap axial locations, while Figure 2.5 shows the circumferential tap locations within the diffuser of the centrifugal compressor stage.

A Dell 425E computer acquires the high speed dynamic data. Because the computer has a 4 kHz sampling rate, the Nyquist criterion is satisfied for frequencies well above the low pass filter cutoff frequency of 1020 Hz. Data is recorded for thirteen pressure taps, the high

	Former Actuator H3581A	**New Actuator TB32-1004B**
Linear Motion Controller	H3951	B8961
Supplier	Industrial Devices Corporation	Industrial Devices Corporation
Thrust Output	~900 lbf	2400 lbf
Additional Effective Thrust output with Pulley system	300 lbf	Not necessary
Movement precision with Genesis computer interface	.05 inches per movement (Limited by Linear Motion Controller)	.002 inches per movement (Limited by Genesis software)
Computer Language	Precursor to "Ideal" language (Genesis uses a control loop, written in C language, to communicate with the LMC: no keypad for direct interface)	"Ideal" Language (communicates with Genesis and permits direct interface with keypad)

Table 2.2 Linear Motion Controller and Actuator Modification Summary

New Modification	Former Hardware	Reason for Modification
Rebuild LTS-101 and Assembly	LTS-101	Unknown foreign object damage bent 4 rotor blades and 3 stator blades in axial stage.
Linear Motion Controller B8961 Actuator TB32-1004B	Linear Motion Controller H3581 Actuator H3951	Former actuator produced insufficient thrust output to close nozzle.
Fuel flow correction. A new flow meter was installed. The Signet 2507 Mini Flow Sensor	No accurate fuel flow meter measurement.	New fuel flow meter required calibration.
2000 lb In Line Transducer Amplifier Produced by Sensotec	1000 lb In Line Transducer Amplifier. Produced by Sensotec	Replacement of broken load cell.
Nozzle Exit Cooling: Replaced the cooling nozzles: Spraying Systems Company VeeJet 68° spray angle 4.88 gal/min	Nozzles: Spraying Systems Company VeeJet 114° 9.6 gal/min	The former nozzles did not atomize sufficiently. Water pooled in exhaust duct and leaked to floor.
Hazardous Location Sealles Drum Pump 100/60. Company: Lutz Explosion Proof. 13 GPM Flow Rate 25 Feet Head	Fill Pump FA-100A Oriental Koshin 13 GPM Flow Rate 23 Feet Head	The former pump is not designed for JP-4 transfer. In addition, the availability of two electric pumps replaces cumbersome fuel transfer with a hand pump.
Fuel Storage Unit for Drum in use.	None existent	Safety precaution.
Inlet Ducting Removable Section	Continuous Inlet Ducting	Provides ability to remove LTS-101 inlet ducting for Allison engine runs.
Stand Modification and Oil Tank Adjustment	N/A	Accommodates new 2400 lbf actuator.
Accumulator	Not used.	Permits accurate air mass flow rate readings (Detailed in Chapter 2.3)

Table 2.3 Summary of Hardware Modifications.

Reading	To Calculate	Transducer	Measurement Location	Uncertainty at 95% $N_{1\,corr}$
P_1	$\dot{m}_{corr}$	Setra, model 239	bellmouth	± 0.59% of reading
P_3	π	Setra, model 204D	aft of centrifugal compressor	± 0.37% of reading
P_5	Diagnostic	Setra, model 204D	aft of nozzle	± 0.37% of reading
$P_{ambient}$	$\dot{m}_{corr}$, π	Setra, model 370	upstream duct	±0.1% of reading
P_{oil}	Diagnostic	Omega PX 603	oil tank	±0.57% of reading
T_{inlet}	$N1_{corr}$	Type K Thermo Couple	inlet duct entrance	±2.1°C
T_{oil}	Diagnostic	Type K Thermo Couple	oil tank	±2.1°C
$\dot{m}_{fuel}$	Tt4	Signet 3-2507-3s	fuel line, just prior to engine	±0.57% of reading
N1	$N1_{corr}$	N1 tachometer, updated every two seconds	on gearbox/ accessories	±0.15% of reading
$T_{exhaust}$	Diagnostic	Type K Thermo Couple	exit duct air stream	±2.1°C
$T_{nozzle\ metal}$	Diagnostic	Type K Thermo Couple	nozzle temperature	±2.1°C
T_{EGT}	Diagnostic	Type K Thermo Couple	aft of Nozzle	±2.1°C
Throttle Position	Diagnostic	BEI Motion Systems Industrial Encoder	on gearbox/ accessories	±0.5% of full scale
Vibrometer	Diagnostic	Type 4-128 Velocity Vibration Transducer	right side of combustor housing	±4.0333% of full scale
Load on Actuator	Diagnostic	Sensotec Model 41 2000 lb Load Cell	under moving part of frame	±0.1% of full scale
Water Valve Potentiometer	Diagnostic	Worcestor Series 74 Ball Valve Potentiometer	under exhaust duct on frame	±2.222% of full scale
Flow Fence Potentiometer	Diagnostic	Position Transmitter Potentiometer (KFFI)	bottom of combustor housing	N/A
Nozzle Position	Diagnostic	B8961 Linear Motion Controller	under moving part of frame	± 0.0005 inches check on
Injected air mass flow	air injection	McCrometer V cone flowmeter	upstream of high stream valve	±0.5% of reading
T_{shroud}	Diagnostic	Type K Thermo Couple	on the shroud	±2.1°C

Table 2.4 Engine Steady State Measurements

speed Moog valve command and position, and the forcing function (if used). For instantaneous monitoring, a variety of the taps were evaluated. The vane plenum taps provide the most responsive tap location for detecting surge precursors. While the engine approaches the surge line, these taps show large power spectral density growth of the critical 28 Hz surge mode and the 68 Hz first acoustic mode. The experimental crew monitors a single vane plenum Kulite tap using either the HP63365 spectrum analyzer or HP89410A vector signal analyzer, depending on availability during the run. Table 2.7 summarizes the high speed data acquisition system.

2.3 Actuation System for Active Control

2.3.1 System Configuration

Based on a maximum attainable positive compressor slope criteria, McNulty [23] concluded that the diffuser throat is the best actuation location for active surge control in the LTS-101. Using 95 psig, oil free air, the actuation scheme forces the aerodynamics of the compressor (Figure 2.6). A Sullair industrial air compressor and dryer generate the high pressure air. En route to the engine, the air is filtered and flows through an adjustable pressure regulator. The next section addresses the flow rate measurement system.

The flow passes through a manually operated, pneumatically actuated ball valve, the primary on/off control for the injection system. If there is a power interruption or mechanical problem, the engine operator manually closes the valve. This valve serves as a safety precaution. The air then flows to a McCrometer V-cone differential pressure flowmeter, an accumulator, and on to the high frequency response valve (designated "Moog 1" in Berndt [23]), which is explained more in Section 2.3.3.

The valve output enters an annular feed plenum that is within the impeller cover of the engine. Twenty four angled slots around this annulus connect the feed plenum to pressure losses within the system were associated with this connection [14,15]. The slots were

	Uncertainty Estimate at 95% $N1_{corr}$
$\dot{m}_{corr}$	±0.16% of m_{design} (using bellmouth calibration)
π	±0.37% of full scale reading
$N1_{corr}$	±0.645% of full scale reading
T_{T4}	± 0.92 % of full scale reading
Compressor Efficiency	± 0.96% of full scale reading

Table 2.5 Uncertainty Estimates for Derived Quantities

Tap ID	Axial Station	Used in these runs	Angle CCW from TDC front view (in °)	Transducer Used (Kulite Model)
I01005G	Inlet	Yes	50	XCS-062-5D
I02005G	"	Yes	170	XCS-062-5D
I03005G	"	Yes	210	XCS-062-5D
I04005G	"	Yes	340	XCS-062-5D
T05050G	Diffuser Throat	Yes	50	XCQ-062-50G
T13050G	"	Yes	130	XCQ-062-50G
T17050G	"	No	170	None
T21050G	"	Yes	210	XCQ-062-50G
T28050G	"	No	280	None
T35050G	"	No	350	None
V13250A	Vane Plenum	Yes	130	XCQ-062-250G
V21250A	"	Yes	210	XCQ-062-250G
V27250A	"	No	270	None
V35250A	"	No	350	None
E05250A	Diffuser Exit	Yes	50	XCQ-062-250G
E18250A	"	Yes	180	XCQ-062-250G
E31250A	"	No	310	None
COM250A	Combustor	Yes	170	XCQ-062-250G

Table 2.6 Pressure Tap Location and Naming Convention

therefore enlarged to approximately seven times their original area. After entering the vane openings directly over the vane plenum chambers (Figure 2.5). In previous experiments, large plenums, air injects perpendicular to the primary gas path through slots in the vane walls.

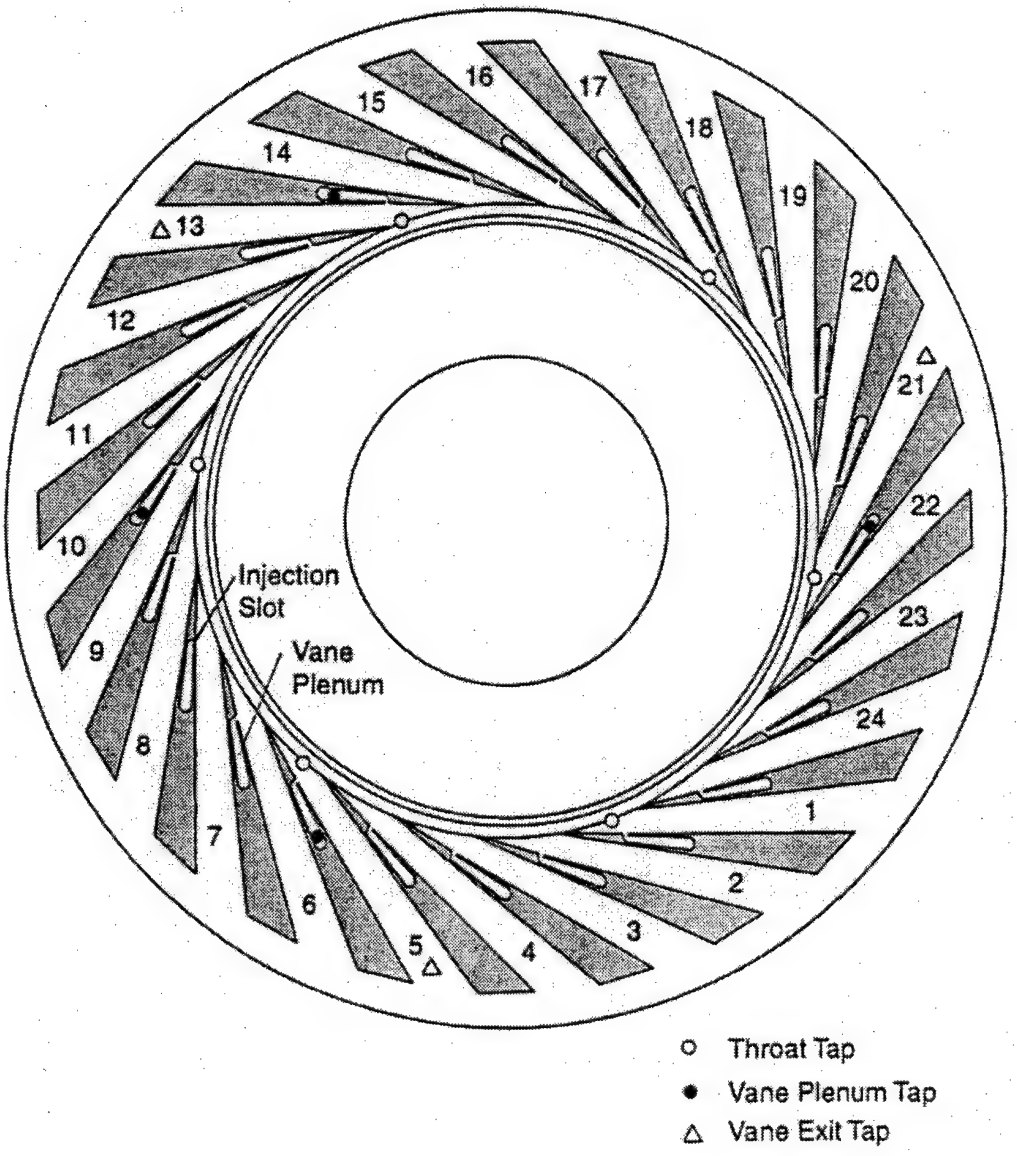

Figure 2.5 Circumferential Tap Locations within Diffuser [15].

Computer	Dell 425E
DAQ Cards	2 X 8 Channel 12 bit Adtek AD830 A/D card 4 kHz sampling
Anti-aliasing Filters	Onsite Instruments, TF-16-04 Cauer, 16 Channel, 8 Pole Roll off: 75 dB/octave Cut off Frequency: 1020 Hz
Amplifiers	Pacific Model 8650
Tap Monitoring	HP 63365 Spectrum Analyzer
Tap Monitoring	HP 89410A Vector Signal Analyzer
Pressure transducers	See Table 2.6

Table 2.7 Data Acquisition System

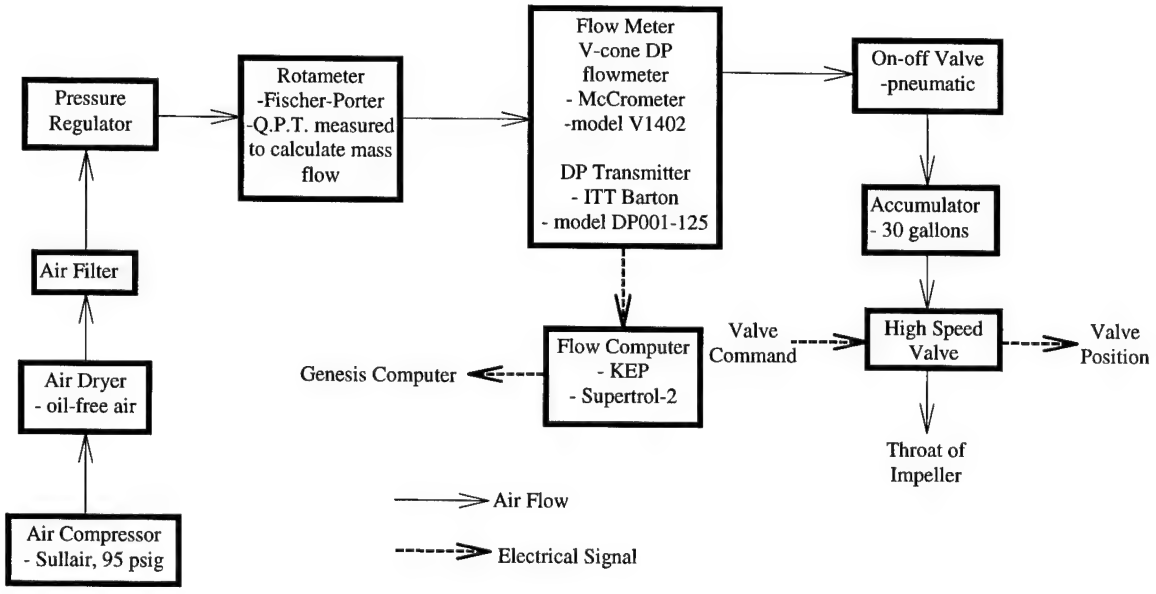

Figure 2.6 Actuation System Schematic

2.3.2 Injected Airflow Rate Measurement

Previous flow rate measurements on the LTS-101 were taken using a Fisher Porter rotameter. This volume flow rate meter used inlet pressure and temperature to calculate the mass flow rate of the injected air. However, Bae [19] enhanced this method on the Allison

engine to obtain a more accurate mass flow measurement.

Previously, the flowmeter linked directly to the high speed valve. When the high speed valve oscillated due to feedback during closed loop engine operation, or due to applied sinusoidal inputs during transfer function acquisition, the resulting unsteady flow rates effected flowmeter performance. The flowmeter requires steady flow rates, and consequently overestimates the massflow by more than 10% for a sinusoidal input at 100 Hz sine wave. The problem increases at higher frequencies. Bae's addition of a 30 gallon air tank between the high speed valve and the flowmeter effectively damps the pressure fluctuations upstream of the high speed valve. The 30 gallon tank, referred to as an accumulator, resolved the overestimation problem. The LTS-101 experiments incorporate this improved measuring technique.

2.3.3 High Speed Valve

The high speed valve was designed by Berndt [23]. Moog Inc. supplies the actuator (Figure 2.7) and corresponding control electronics unit, referred to as the V command box. The Moog 1 valve is actually composed of two major components, a linear servo motor and a valve. The valve modulates the injected air mass flow rate with a bandwidth of 330 Hz for these experiments. The mean injection flow rate is ~3.75% of the engine design flow ($\dot{m}_{des}$). The first set of experiments (detailed in Chapter 3.1) characterize the valve.

2.4 Control Law Implementation Equipment

A digital computer is used to implement control laws. When compared to an analogue approach, digital implementation provides flexibility for design modifications. Simon,

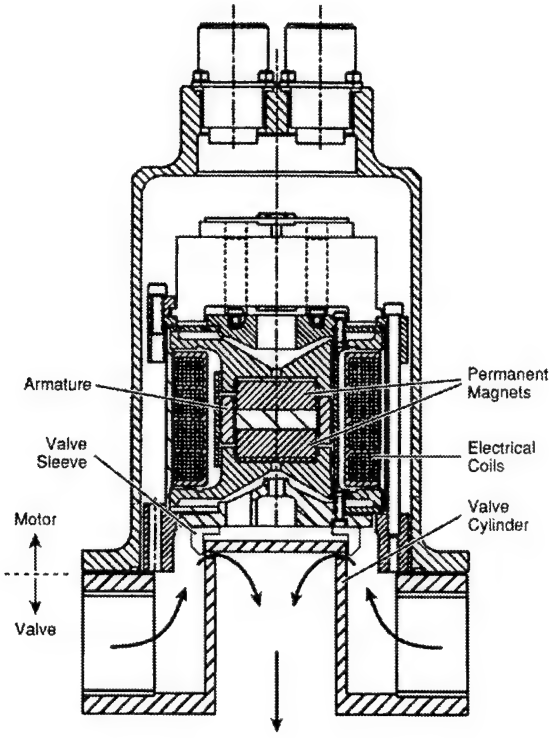

Figure (2.7) Schematic of High Speed Air Injection Valve [23]

Van Schalkwyk, and Didierjean [24] wrote control law programs in Fortran, to which the author adds various control subroutines.

A Dell 450/T computer implements the control laws. Two cards are installed to perform controller functions. A Data Translations DT2801 12-bit A/D card converts inputs to digital counts. The computer samples at a 13700 Hz total throughput rate, which is split into the number of channels needed. Since five to seven channels are used in most experiments, the sampling rate is 2740 Hz to 1957 Hz respectively. If seven channels are used, this is close to the Nyquist frequency requirement with the anti-aliasing filter set at 1020 Hz. However, because of the 330 Hz actuator bandwidth, the possible aliasing near the Nyquist frequency

(~1000 Hz) does not cause a problem.

A certain degree of compensator complexity is required to successfully extend the surge line. However, as the number of computer calculations increase, the computational delay may overwhelm the sampling rate. If extra time is required to complete the calculation, the control engineer can increase the number of channels in the DMA process to slow the sampling rate. But as the control computer delay increases, the performance of the discretized control law tends to degrade (as will be discussed in Chapter 4.3). Because the compensator size is limited by the control computer, this trade off defines the best compensator design.

After the computer calculates the control output value, the signal is converted from digital to analog by a Burr Brown PCI-20093 W-1 12-bit card. A Pacific Scientific 8650 amplifier card amplifies the D/A output to the level required by the valve servo system. The valve command from this card and the actual position are recorded by the high speed data acquisition computer. A Tektronix TDS 524A oscilloscope monitors valve command and position in real time to assure that the high speed valve is responding correctly. Figure 2.8 summarizes the closed loop system.

2.5 Experimental Procedures

Engine runs require three people. The test engineer is responsible for the run, including the setup, calibration, engine operation, and shutdown. The engine operator controls and monitors the steady state behavior of the engine. The final member of the team is responsible for high speed data acquisition and safety aspects.

Prior to the run, the test engineer performs general start-up procedures. In order to avoid error, engine runs require the completion of a check list, which is included in Appendix

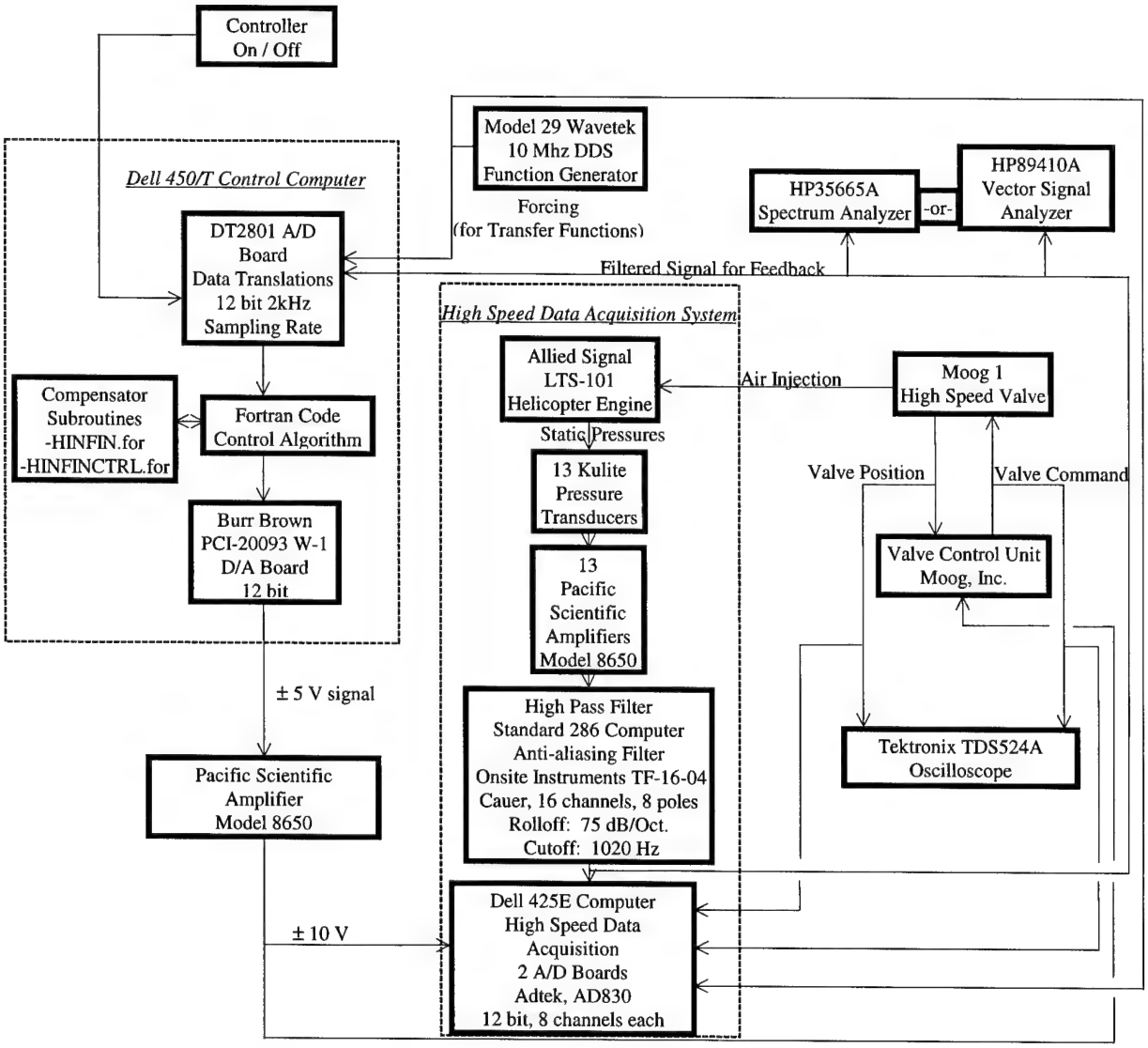

Figure 2.8 Closed Loop System Schematic

A. The pre-start checklist includes a calibration sequence for both the steady state instrumentation and the high frequency response pressure transducers. Upon checklist completion, personnel vacate the test cell. The engine is started and idled for three minutes at ~ 50% $N1_{corr}$. The engine is then throttled to 95% $N1_{corr}$ and maintains this speed for the run duration.

At this point, air injection is initiated at the desired feed pressure, 95 psig. The high

speed valve is pre-positioned at the mean injection level. The variable area nozzle exit is then closed with linear motion controller movements. Testing begins once the desired operating point is established. The general test objectives for this research effort fall into three classes. First, after steady engine performance is verified with several runs, speed lines with mean air injection are measured. These speed lines are referred to as open loop speed lines.

Next, engine system identification is performed by commanding air injection at particular sinusoidal frequencies. These frequencies are generated with a Wavetek model 29 10mhz DDS Function Generator. Based on performance results of predecessors [15, 18, 19], 32 discrete forcing frequencies are used. The high speed data acquisition computer records 15 second data sets. To best capture the characteristics of the system modes, the transfer functions are obtained as close to the surge line as possible. If conducted too close to the surge line, forcing may trigger surge.

The final test type is feedback stabilization. The thrust output on the load cell and the corrected mass flow are specifically monitored to estimate how close the engine is to the surge line. Monitoring of the spectral content of the vane plenum pressure is highly emphasized during these tests. Using the HP63365 Spectrum Analyzer or the HP 89410A Vector Signal Analyzer, sudden growth of the surge mode (~27.8 Hz) indicates surge precursors. The surge mode is the primary focus for engine monitoring during open loop engine operation. Closed loop engine operation requires monitoring of the surge mode, low frequency modes, and various acoustic resonances (primarily the 68 Hz) that could trigger surge. Simultaneously, the high speed data acquisition system captures the unsteady pressure characteristics for post run analysis.

Chapter 3

Open Loop Engine Behavior

3.1 Introduction

This chapter's purpose is to quantify the open loop behavior of the LTS-101 for the mean air injection case. The base line performance described here is used for comparison with the closed loop engine runs. First, the high speed valve is characterized. Next, steady state performance is measured for the repaired engine. Third, open loop surge precursors are analyzed in the time and frequency domain using filtered time traces, waterfall plots, and PSD plots. Then, forced response tests are used to estimate single-input multiple-output transfer functions between the valve command and various static pressure transducer signals. Finally, the plant model from experimental results is discussed.

3.2 High Speed Valve Characterization

The first step in engine testing is to verify the high speed valve performance. At a typical 95% corrected engine speed operating point, the input voltage signal to the valve, referred to as valve command, is bound by a ±10 volt range. The injected mass flow has a 2.195% leakage flow, and a maximum injected flow of ~5.45%, as a percentage of the design mass flow (Figure 3.1A). In Figure 3.1B, "valve position" refers to the voltage reading of the position transducer on the servo. As one can see, valve command and valve position maintain an approximately linear relationship between ±7.5 volts. Beyond this voltage

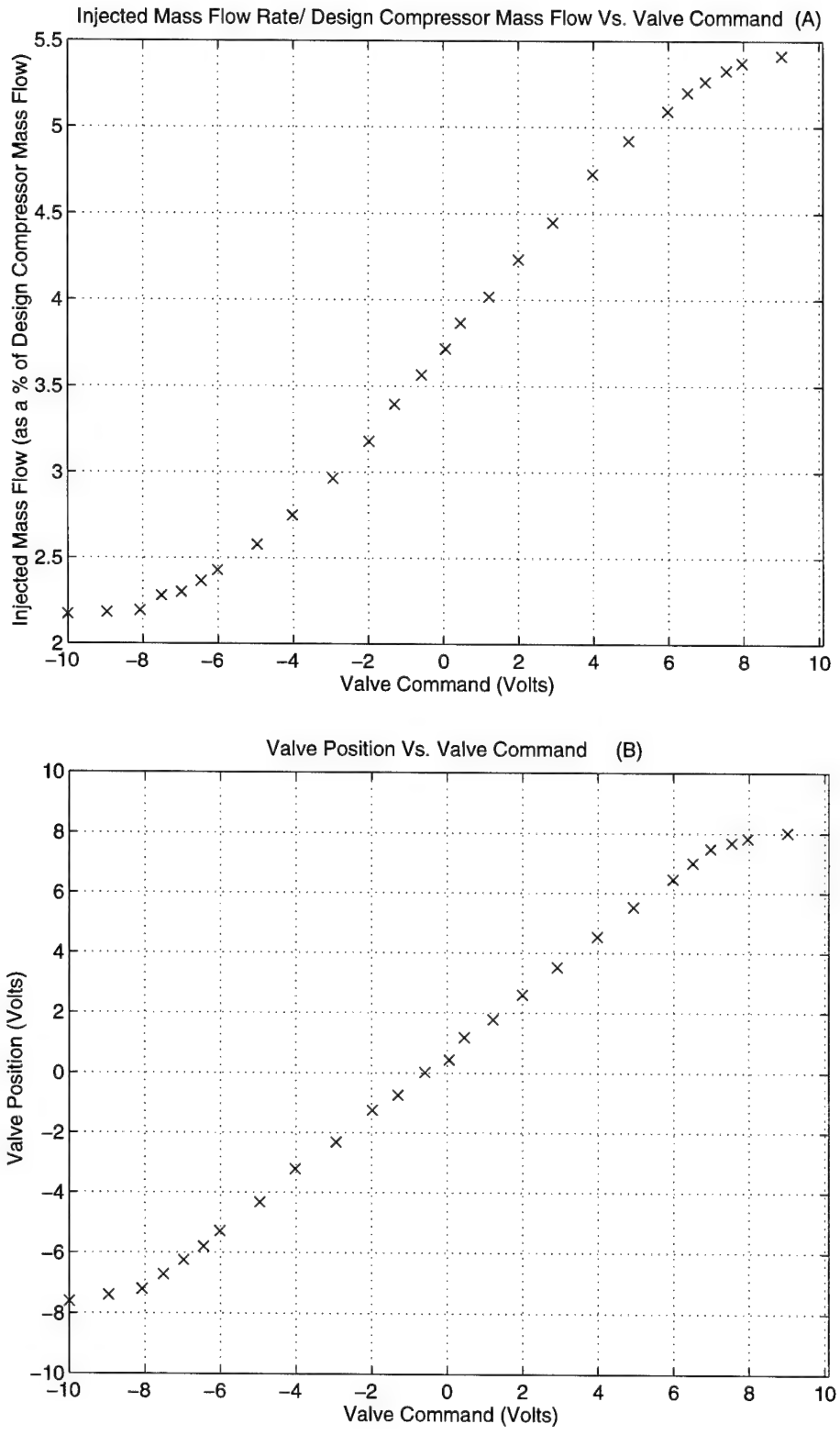

Figure 3.1. Steady State Valve Characterization

range, there is little change in the actual slider position.

Figure 3.2 shows the frequency response between valve position and valve command, for a ±1 volt sinusoidal commands. Data is obtained while operating the engine at 95% prior to closing the exit variable area nozzle from the "home position". The important information for compensator design is that the actuator bandwidth is approximately 330 Hz.

3.3 Steady State Injection Response

3.3.1 Engine Runs in 1996

To remain consistent with predecessors [23] and with linear control methods, all

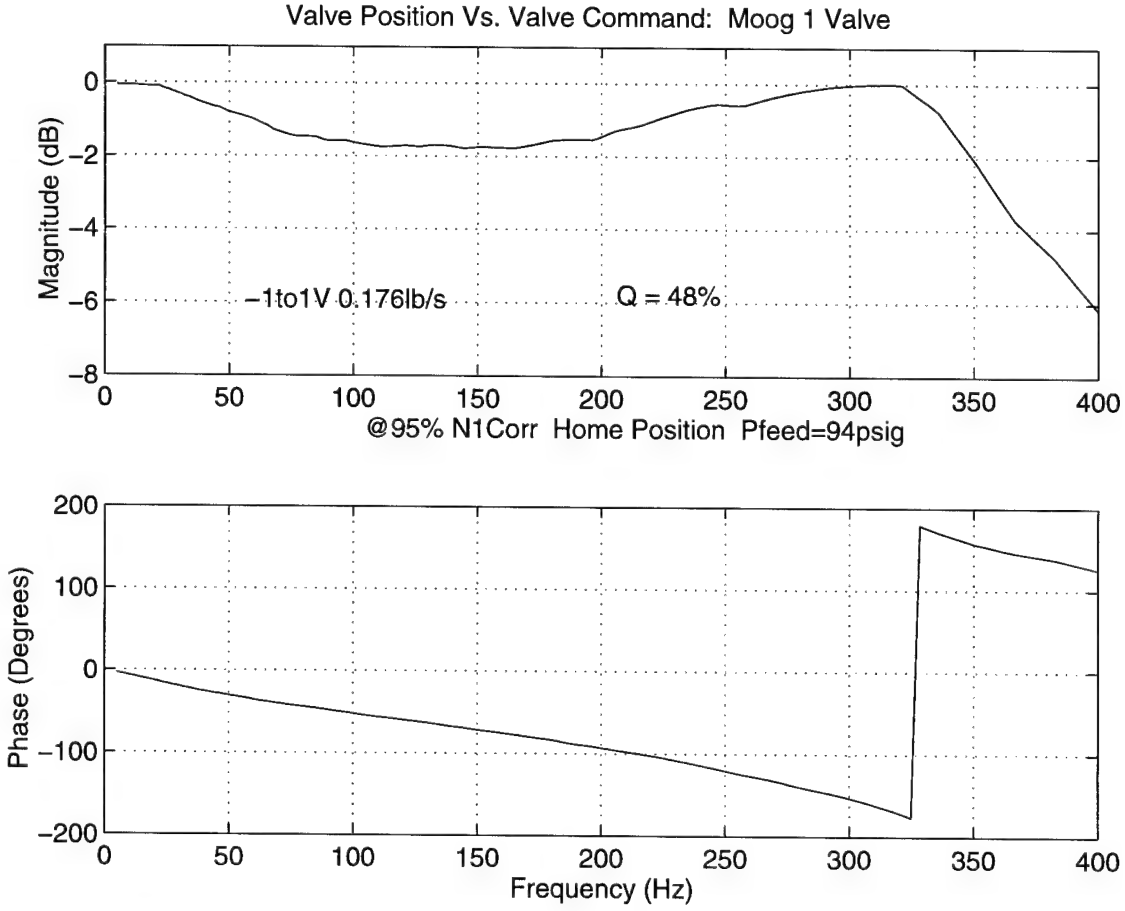

Figure 3.2 High Speed Valve Transfer Function

control tests are performed with mean air injection. This allows unsteady valve commands that are both positive (opening) and negative (closing). Therefore, the "base line" is the performance with steady mean air injection. Brian Corn [15] performed a number of tests to quantify and explain the compressor characteristics with mean air injection; specifically, he measured the operating line and speed line. These are briefly described here for the previous installation of the engine. Section 3.3.2 then gives results for the current, rebuilt engine.

An operating line is a series of points on the pressure ratio versus corrected mass flow map with constant nozzle area and varying engine speed. In these tests, the variable area nozzle remains open at the "home position" and is throttled in speed from idle (~.3 times the design corrected mass flow) to 95% N1 corrected speed. Figure 3.3 shows that the operating lines remains unchanged for the given compressor with and without mean air injection.

Another test to characterize air injection is a speed line, which is a series of engine operating points with constant corrected speed, while closing the variable area nozzle. These experiments focus on the 95% N1 corrected speed line. Corn comments on the important features of mean air injection versus the no injection case (Figure 3.4). The baseline characteristic's stable region slopes negatively, and flattens to a peak over a short range of corrected mass flow. On the other hand, the mean injection characteristic contains a large zero sloped region. This region appears to change surge inception to a more gradual process involving evolution of a dynamic instability, as described in Section 3.3. Corn also notes that the mean air injection actually stabilizes the compressor to lower corrected mass flows.

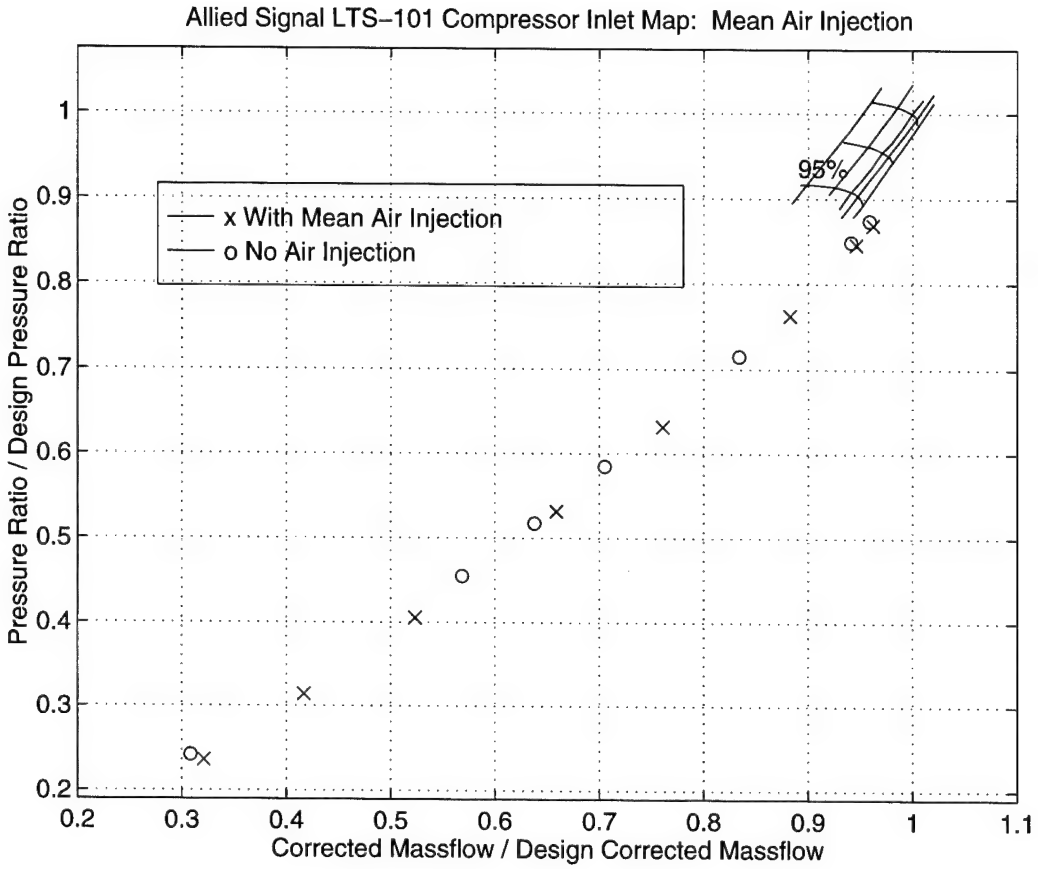

Figure 3.3 Operating Lines of LTS-101 Engine Runs in 1996 [26].

3.3.2 Recent Experimental Work

In this section, the rebuilt engine performance is presented. Figure 3.5 shows the operating line with and without mean air injection. The corrected mass flow decreases across the entire operating line for both the mean air injection and no injection case. A difference in the variable area nozzle position is a primary contributor to the operating line shift. Corn observed ~1.52 inches of linear actuator extension from his designated "home position" to the position of typical open loop surge [28]. The current linear actuator extension from the "home position" to the position of typical open loop surge is between 1.28 and 1.29 inches, depending on weather conditions. Therefore, current engine runs maintain a smaller nozzle

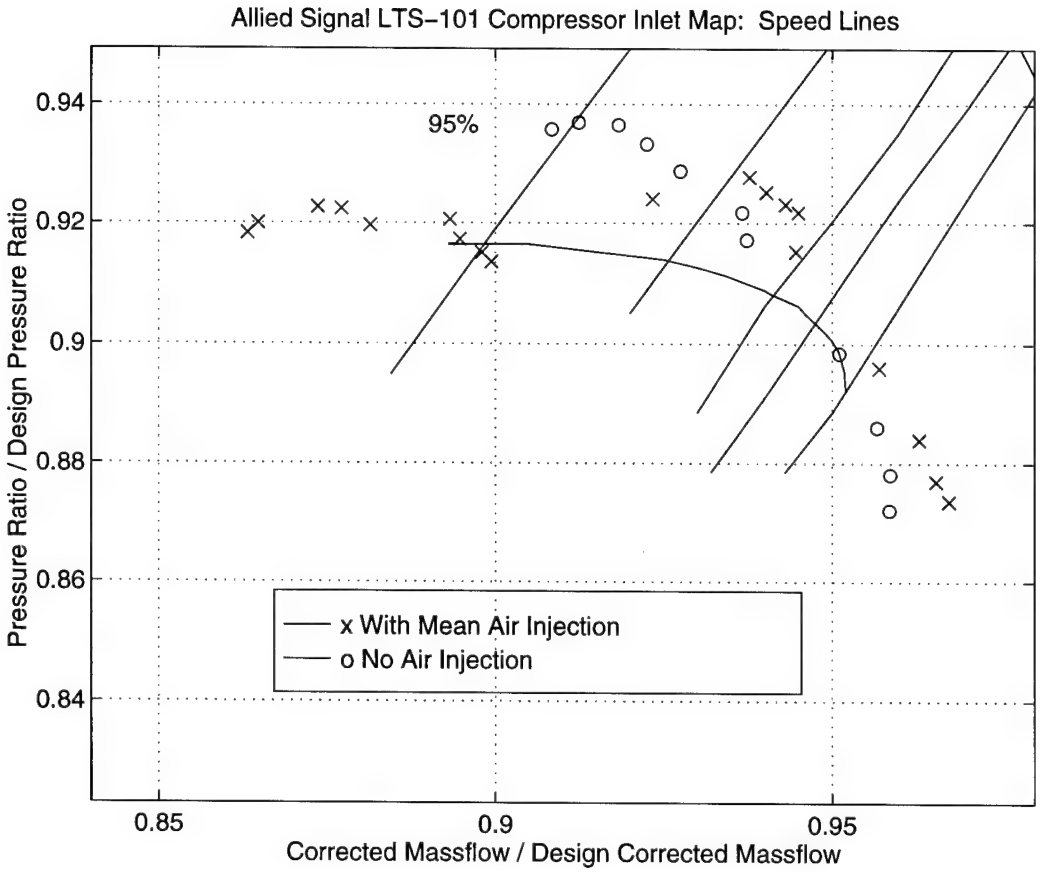

Figure 3.4 Speed Lines of LTS-101 Engine Runs in 1996 [27].

exit area at the home position, thus permitting less massflow at a given pressure rise. Engine performance changes may also contribute slightly to operating line changes.

Figure 3.6 shows the speed line for the current engine installation. Comparing with Figure 3.4, one can note a decrease in obtainable massflow prior to surge. The mean pressure ratio also decreases slightly along the new speedline. The P1 and $P_{ambient}$ transducer outputs check against previous runs, and the bellmouth parameters are unaltered. The engine repair involved several stator blades of the axial stage, as well as rotor replacement. Thus, one can conclude that these changes are responsible for the pressure ratio decrease. Because the surge line moves to lower massflows with pressure rise, one would expect a decrease in

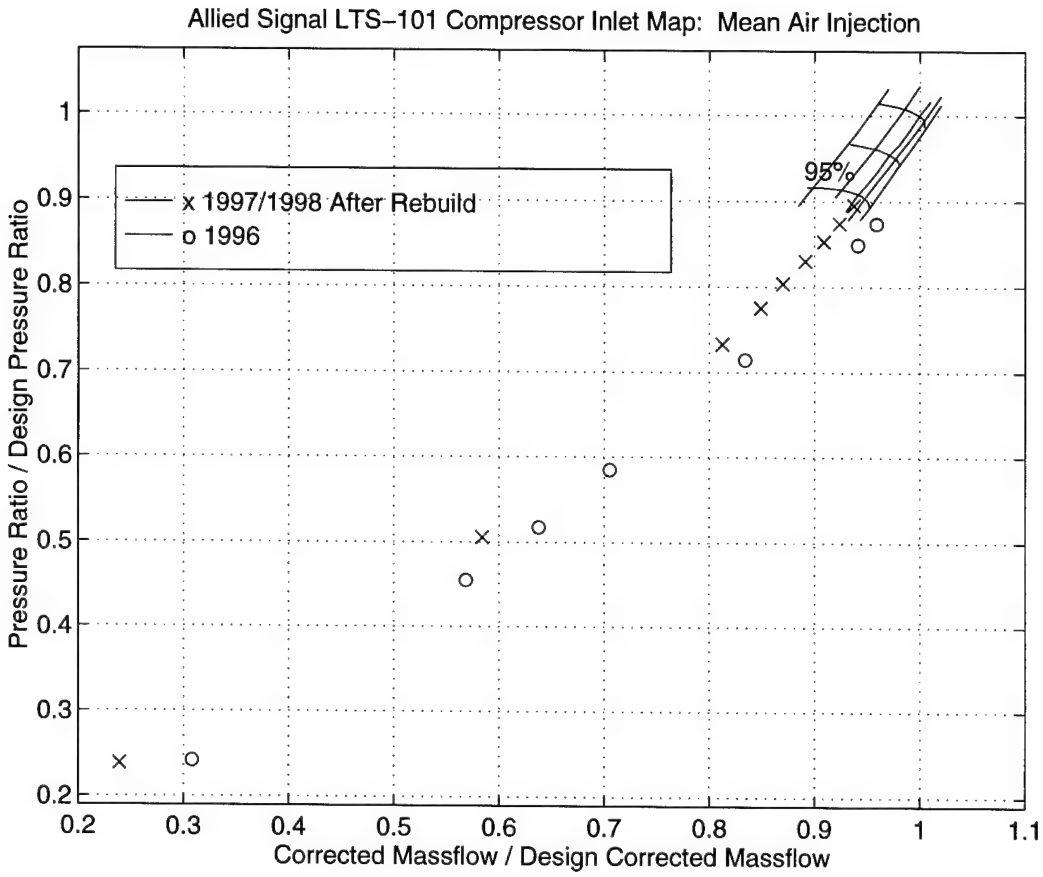

Figure 3.5 New Operating Line for LTS-101: With Mean Air Injection

corrected massflow prior to surge due to the pressure ratio decrease. However, a larger contributor to the lower massflow at surge is the reduction of the transients associated with decreasing the nozzle area with the new linear actuator (see Chapter 2.1 and Figure 2.4). The transients in operating point effect the corrected massflow as well as the measured force output of the engine (Figure 3.7). When comparing the rebuilt engine and its predecessor, one can not eliminate a possible change in the linearized engine eigenvalues. Therefore, it is important for compensator development to recharacterize the engine.

3.3.3 Deviation from the Mean Operating Point

As indicated in Chapter 2, there are errors associated with the measurements used to

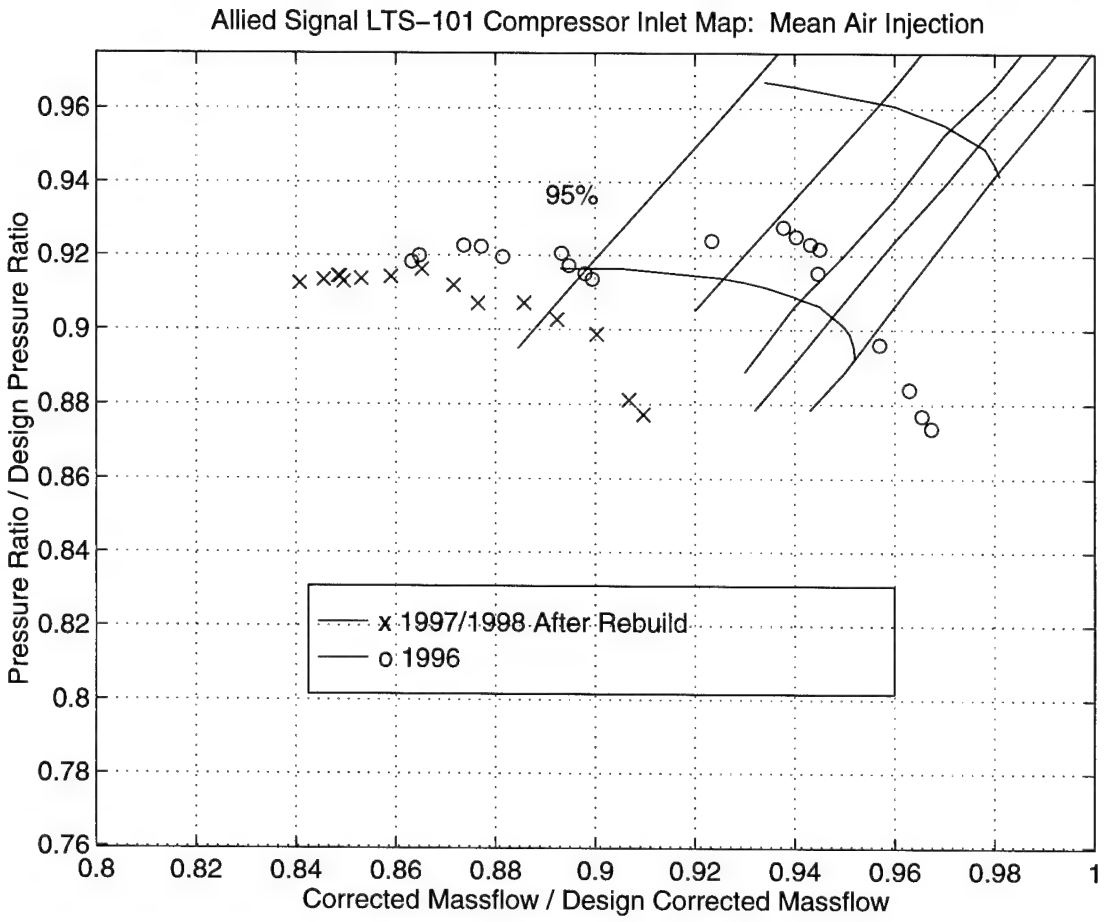

Figure 3.6 New Speed Line for LTS-101: With Mean Air Injection

generate the compressor map. These errors are actually quite small compared to the unsteadiness of the operating point (Table 3.1). Figure 3.8 shows the operating point with standard deviations due to unsteadiness. These operating point variations are quantified for characterization of closed loop performance in Chapter 5.

An important point to note is that the engine often surges because of a sudden change in operating point. It is unclear how these sudden changes occur. One possibility is that mechanical triggers may produce the surge event. Consider Figure 3.9, which shows how a

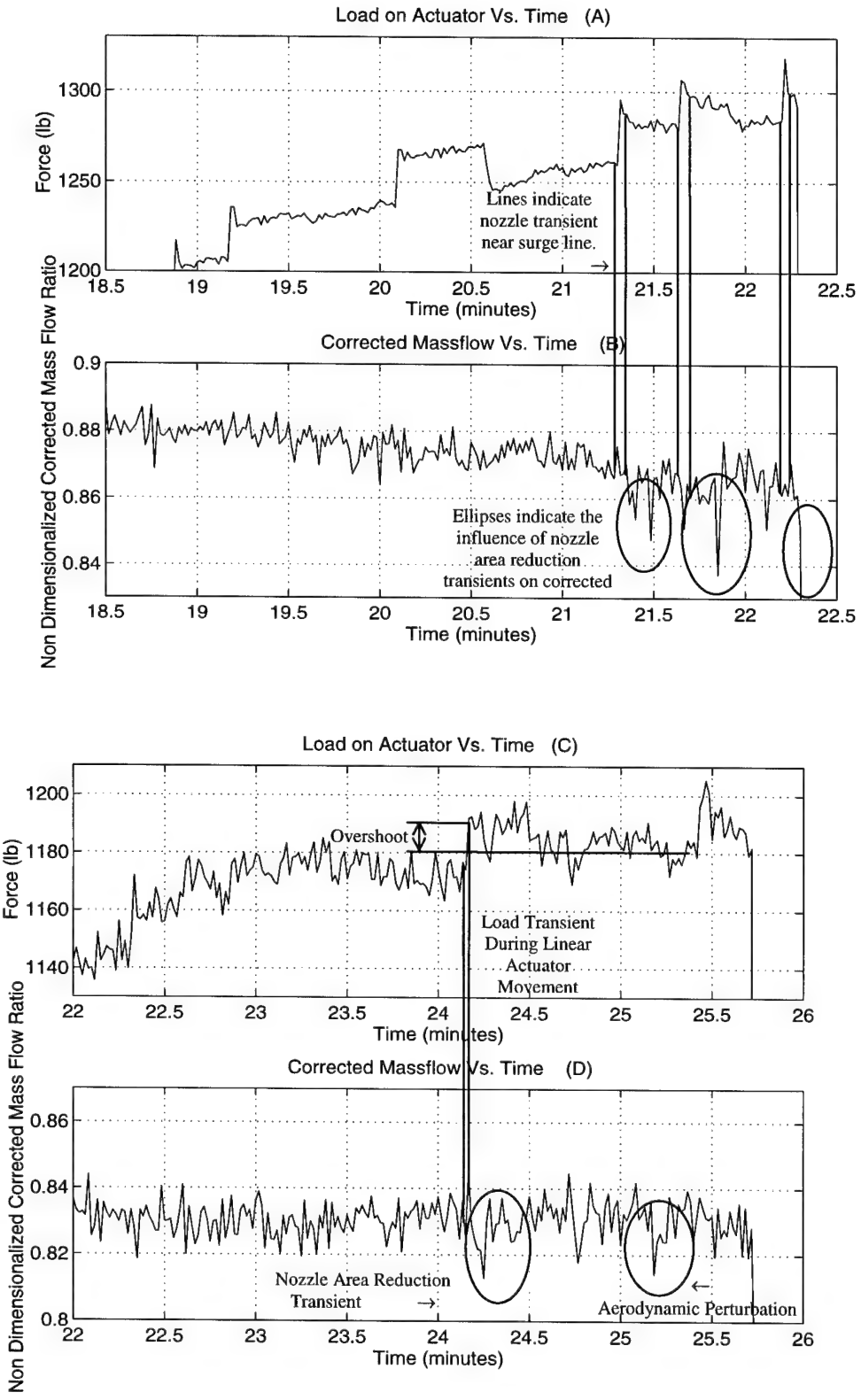

Figure 3.7 Corrected Massflow Transients with Linear Actuator Movement A, B Correspond to Engine Runs Prior to 1996. C, D Correspond to Current Runs.

Source of Variation from Mean Operating Point	% Variation of Corrected Mass Flow	% Variation of Pressure Ratio
Measurement Error in Instrumentation	±0.1601 % of mass flow immediately prior to surge	±0.37% of pressure ratio immediately prior to surge
Unsteadiness of the Operating Point	± 1.199 % of mass flow immediately prior to surge	±0.50865 of pressure ration immediately prior to surge

Table 3.1 Sources of Deviation from the Mean Operating Point. These values correspond to representative open loop surge data.
Note: The measurement errors are derived from the instrument error using the Root Sum Squared method. The unsteadiness estimates assume a normal distribution and 95% confidence level.

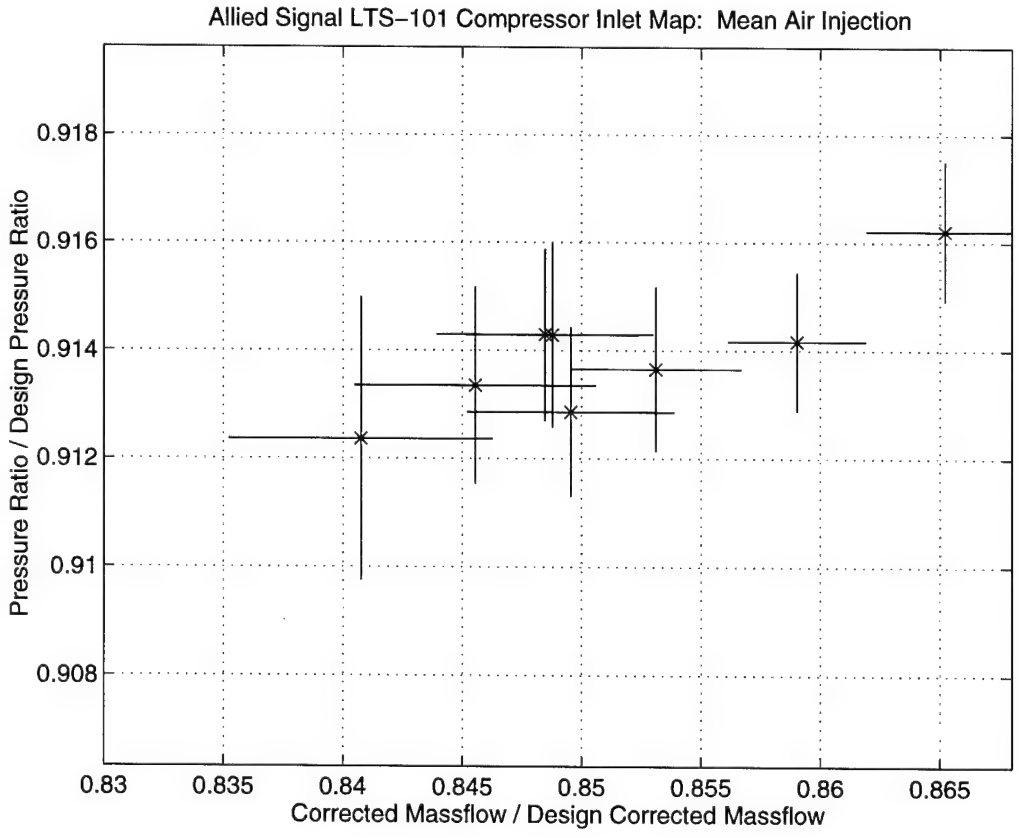

Figure 3.8 Variation in Corrected Massflow and Pressure Ratio While Maintaining a Steady Operating Point

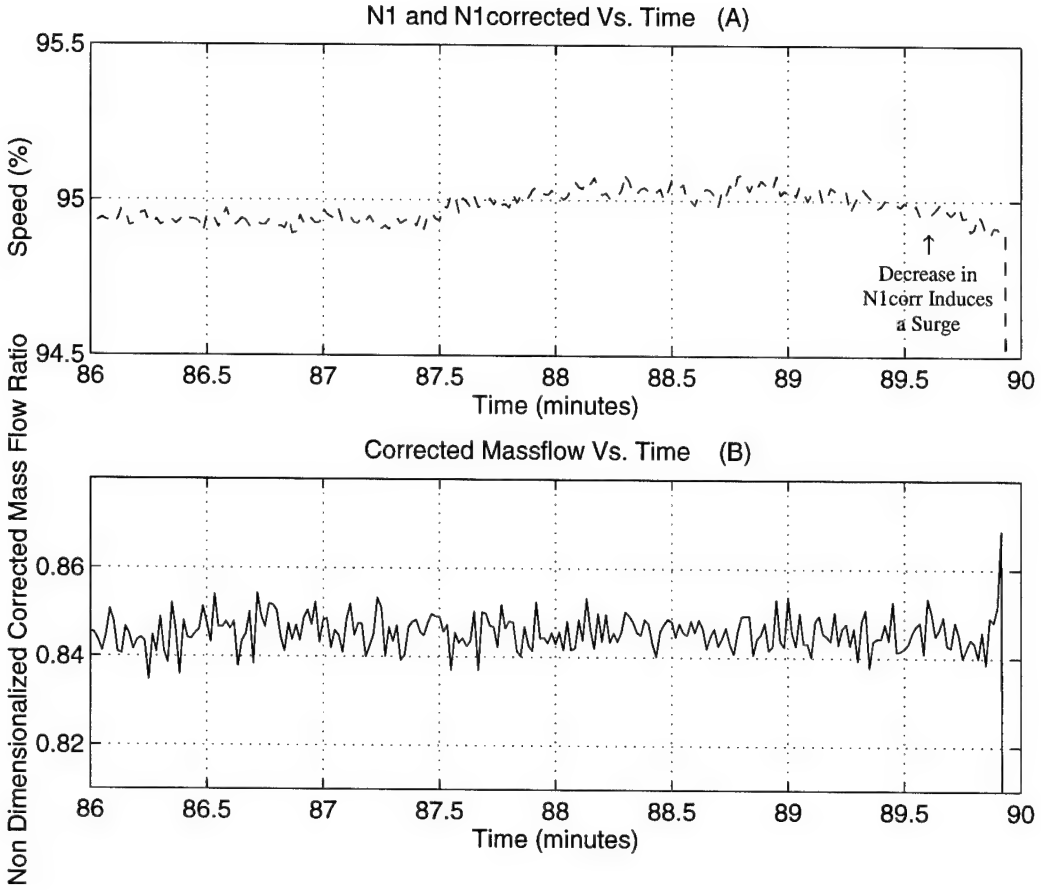

Figure 3.9 Operating Variation: Drift in N1 Corrected Induces Surge.

decrease in $N1_{corr}$, while all remaining parameters are constant, triggers a surge.

In other cases, mechanical changes, such as a sudden change in $N1_{corr}$, do not precede the surge event. Figure 3.10 demonstrates a case in which $N1_{corr}$ remains constant while an instability drives the engine to surge. Likewise, the linear actuator position remains constant for this case. One possible explanation from literature reviewed suggests surge inception is triggered by a breakdown or separation of air flow within the vane passages [29]. An inlet air perturbation may trigger this vane separation. In the air injection case, Corn noted that air injection may enhance surge stability by adding momentum to the region which is normally

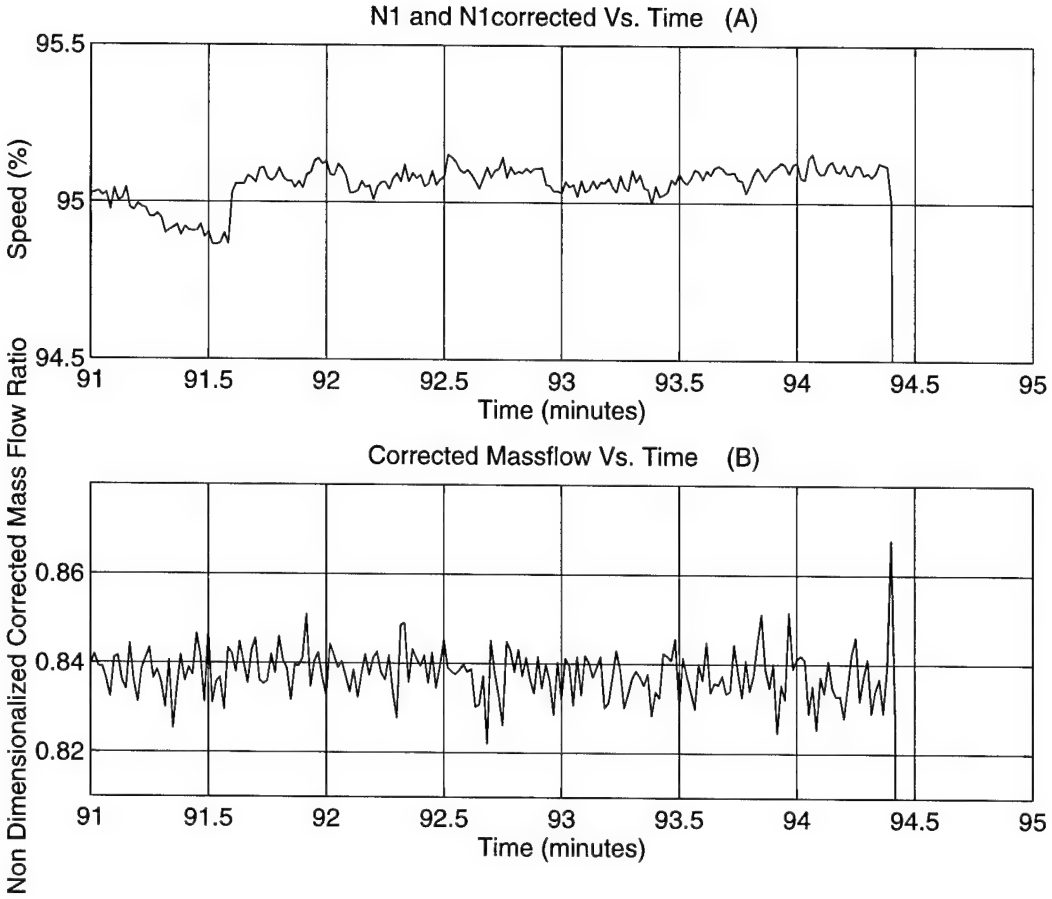

Figure 3.10 Aerodynamic Perturbations Causes Surge: Corrected Massflow with Time. $N1_{corr}$, Nozzle Area is Constant.

affected by inlet separation. However, air injection fluctuations typically varied by ±2.63% of the injected air flow rate. While operating near surge, these variations represent a loss of momentum while operating near surge, which could trigger surge.

3.4 Presurge Behavior at 95% $N1_{corr}$

High speed data is collected at various operating points during an engine run. If a surge event is captured during one of these high speed data sets, the unsteady characteristics

of the surge precursors are analyzed. One can consider the data in both the time and frequency domains. Note that the mean air injection cases will serve as the baseline. One can evaluate the effectiveness of a given control scheme using the described analysis tools and comparing the closed loop results to the baseline cases.

Specifically, this section considers the static pressure time traces for the various Kulite transducers. Digitally filtered time signals contain valuable phase information that can assist in determining the origin of resonances. Next, waterfall plots reveal frequency perturbation information with respect to time. Finally, power spectral density plots reveal modal information at particular frequencies. This information is useful to predict the onset of surge. All data used in these analysis techniques are obtained while the engine maintains its operating point. Specifically, the engine's $N1_{corr}$ and nozzle exit area are maintained constant for at least 15 seconds prior to the 15 second data set, and are constant during data acquisition.

3.4.1 Time Domain Presurge Behavior

In this section, presurge pressure traces are plotted in the time domain for the mean air injection (baseline) engine runs. Throughout the duration of these experiments, the two vane plenum and four inlet taps are emphasized. The vane plenums (refer to Figure 2.5) respond noticeably to sudden changes in critical modes. Time domain inlet and vane plenum pressure traces are plotted two seconds prior to surge (Figure 3.11). The purpose of this plot is to explain the plotting procedures used throughout this thesis. The vertical axis indicates the circumferential locations of the pressure taps in degrees. The DC component of the pressure measurement is removed, while the AC component is plotted at its circumferential

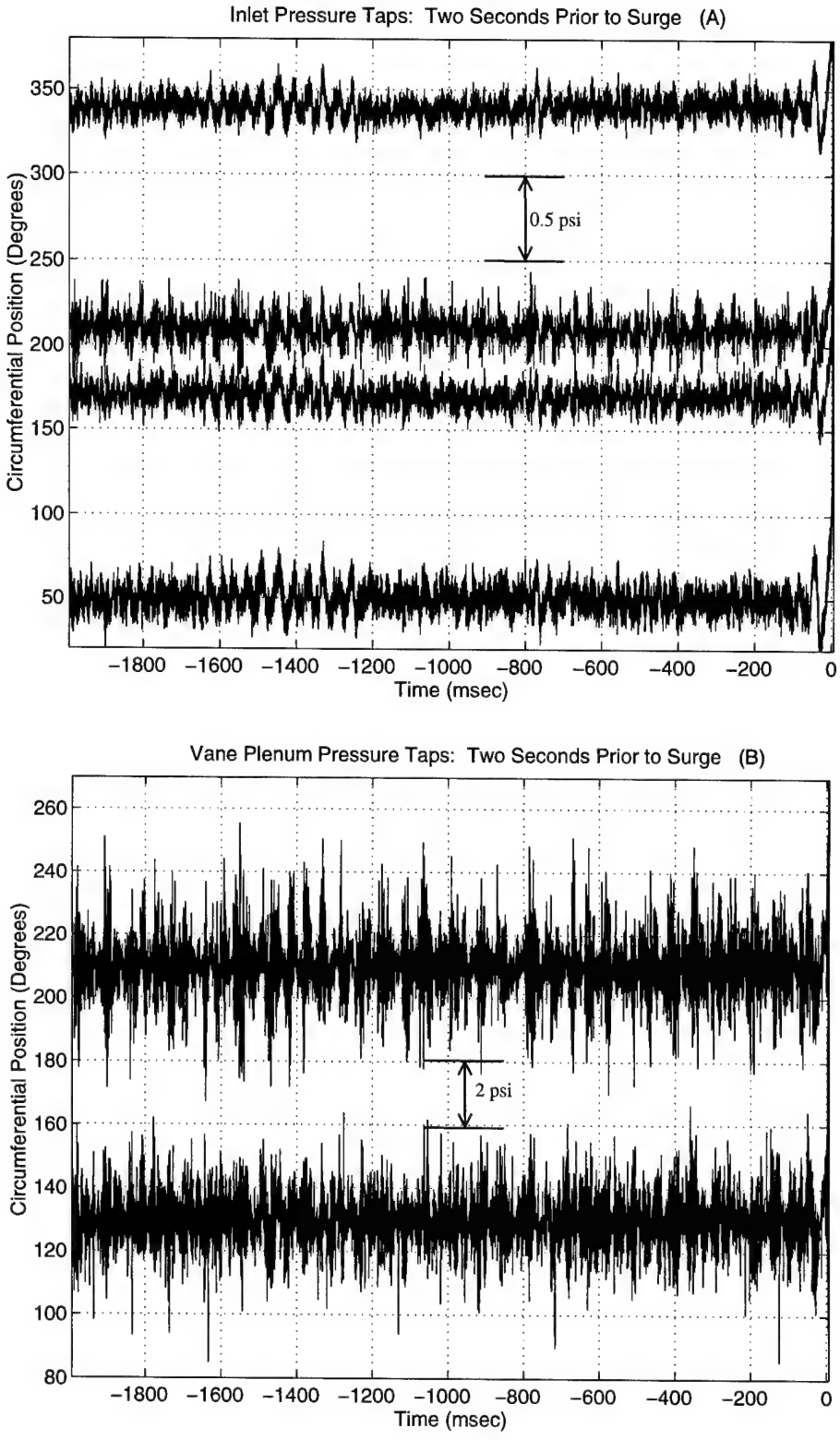

Figure 3.11 Open Loop Presurge Characteristics: Unfiltered Pressure Signals.

location. The pressure values are scaled to enlarge the features of the plots. Inlet pressure perturbations are scaled by 100, while vane plenum perturbations are scaled by a factor of 10. The scale bar is used to indicate the absolute size of a psi unit of measure.

At this point, digital Butterworth filters process the data in order to display the frequencies of interest [30]. A low pass filter (Figure 3.12A) is used to highlight the ~28 Hz surge mode (Figure 3.13A, C), while a band pass filter (Figure 3.12B) removes all but the first acoustic resonance at ~65 Hz (Figure 3.13B, D). Figure 3.14 gives the filtered presurge data for a single inlet and vane plenum tap. Note that the time traces do not tend to indicate a clear growth as surge is approached. Instead, oscillations of the critical frequencies tend to grow and decay in a random fashion, reflecting the random nature of the perturbations in the aerodynamical or mechanical domain. Both the 28 and 65 Hz modes oscillate in this way prior to surge.

The prevalent modes reveal important information about the engine. The 28 Hz oscillations of the inlet and vane plenum are ~180 degrees out of phase with the combustor and diffuser exit tap (Figure 3.15). This indicates that the surge mode is created by a separation between the vane plenum and the diffuser exit. As Bae concluded for the Allison [19] engine, the pressure at the diffuser exit of the compressor will drop, and decelerate the flow downstream of the compressor. The 28 Hz mode is one dimensional, and oscillates at the natural frequency of the compression system. Surge initiation is at the same frequency as these precursors. The pressure initially rises at the inlet and vane plenum at surge initiation, and decreases at the diffuser exit and combustor.

We next consider the 65 Hz mode. As shown in 3.15, the phase of the inlet and vane plenum taps are the same as the diffuser exit and combustor taps. Similarly to the Allison

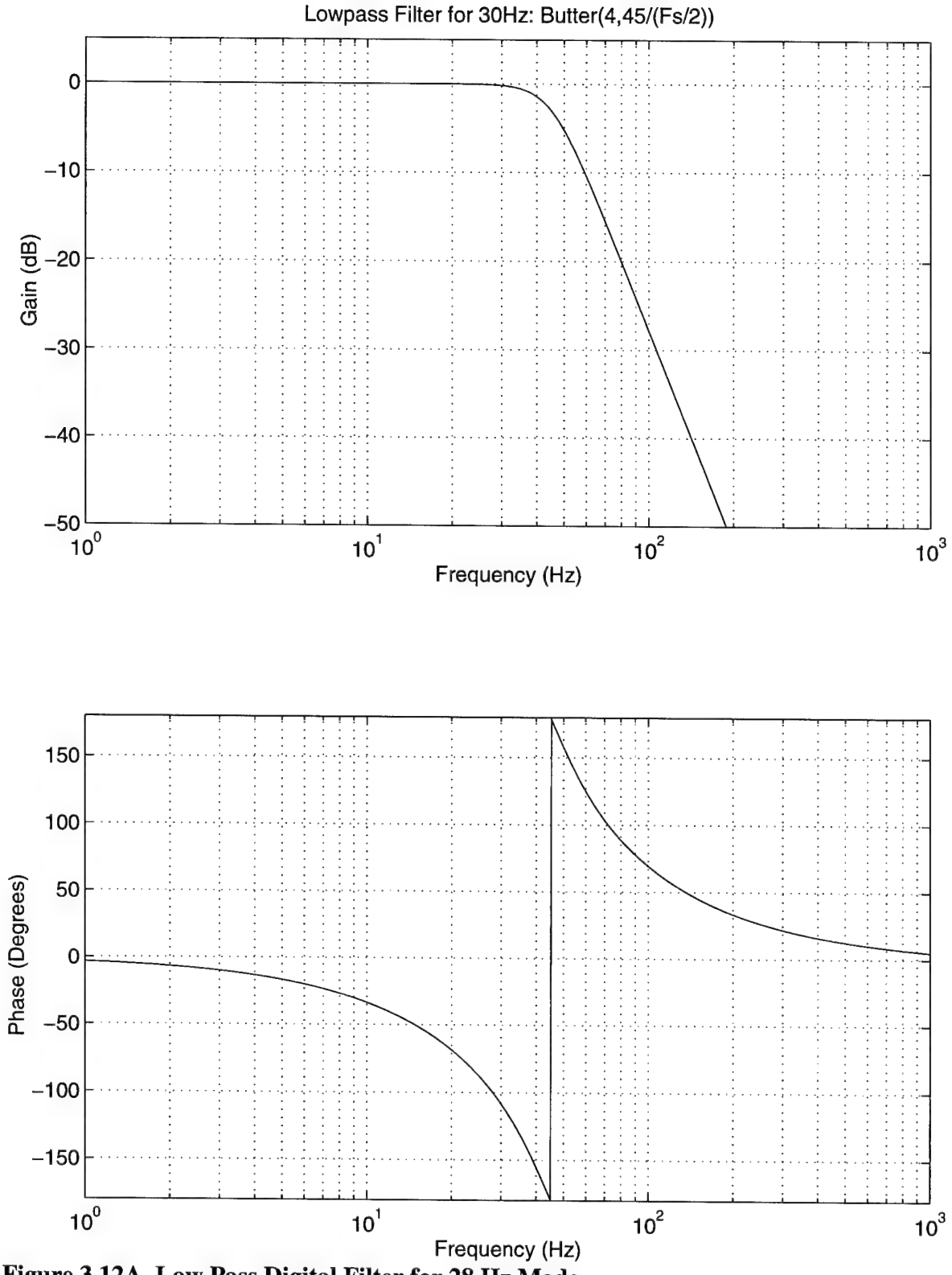

Figure 3.12A Low Pass Digital Filter for 28 Hz Mode.

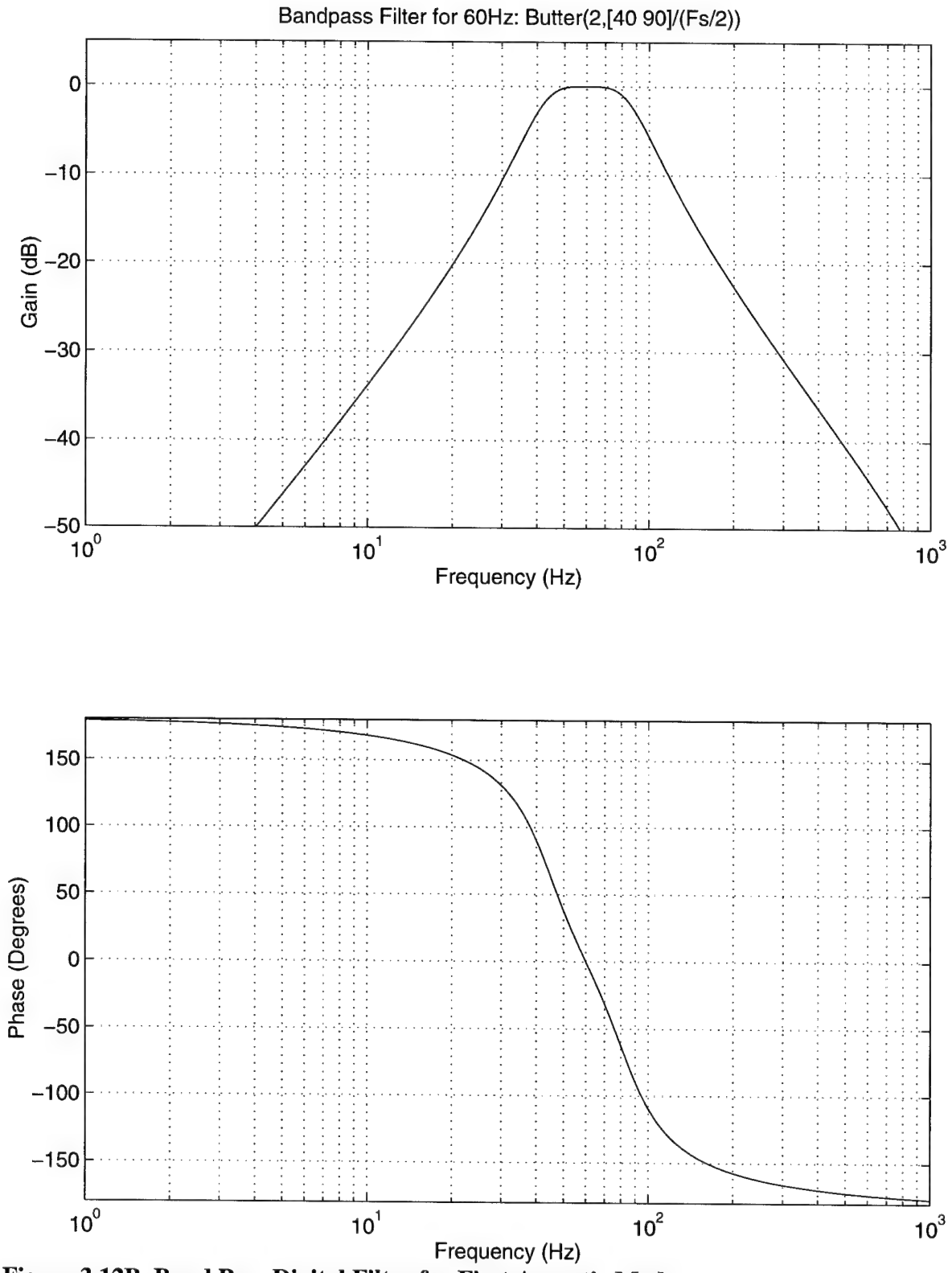

Figure 3.12B Band Pass Digital Filter for First Acoustic Mode.

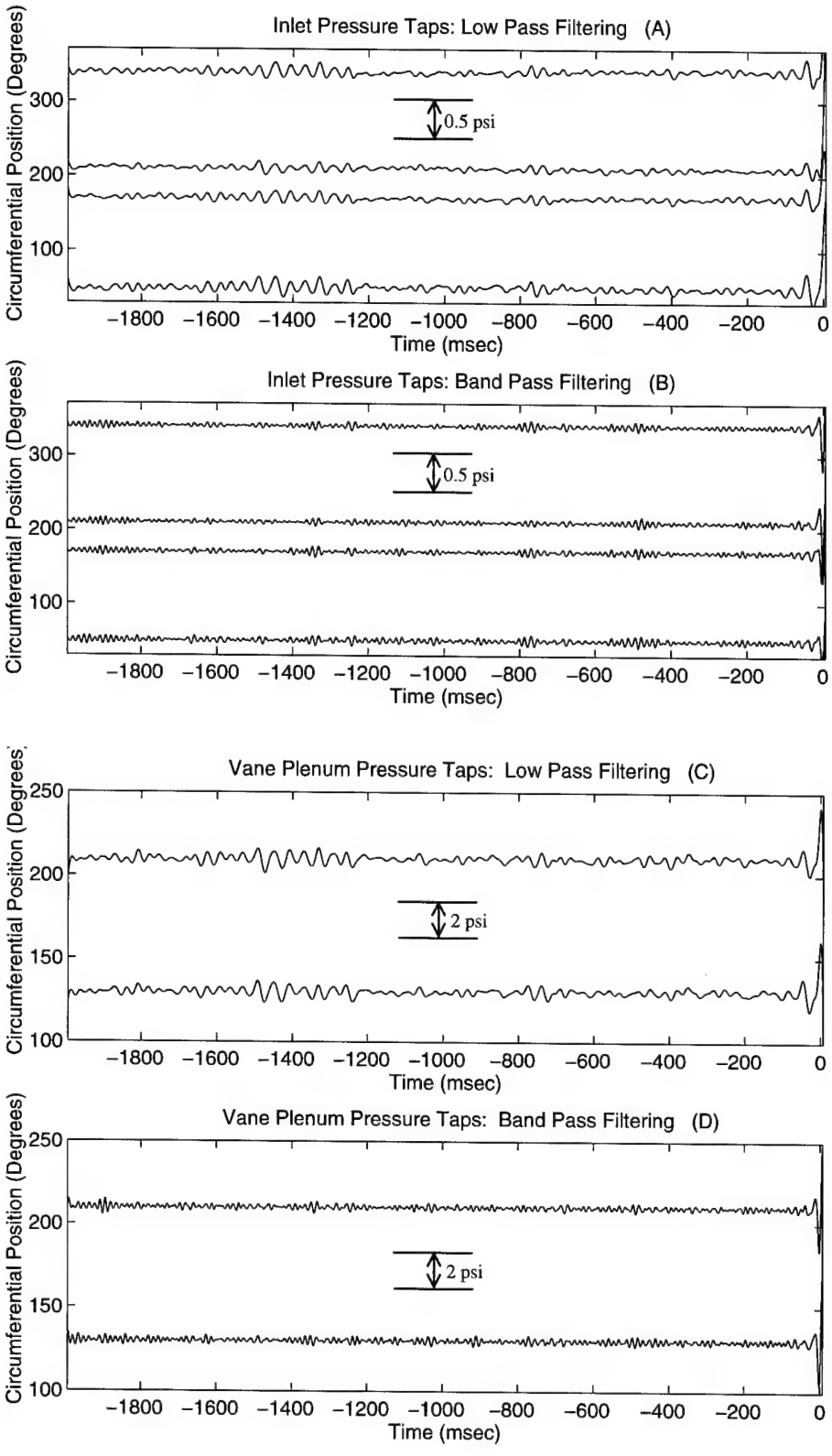

Figure 3.13 Open Loop Presurge Characteristics: Filtered Time Signals

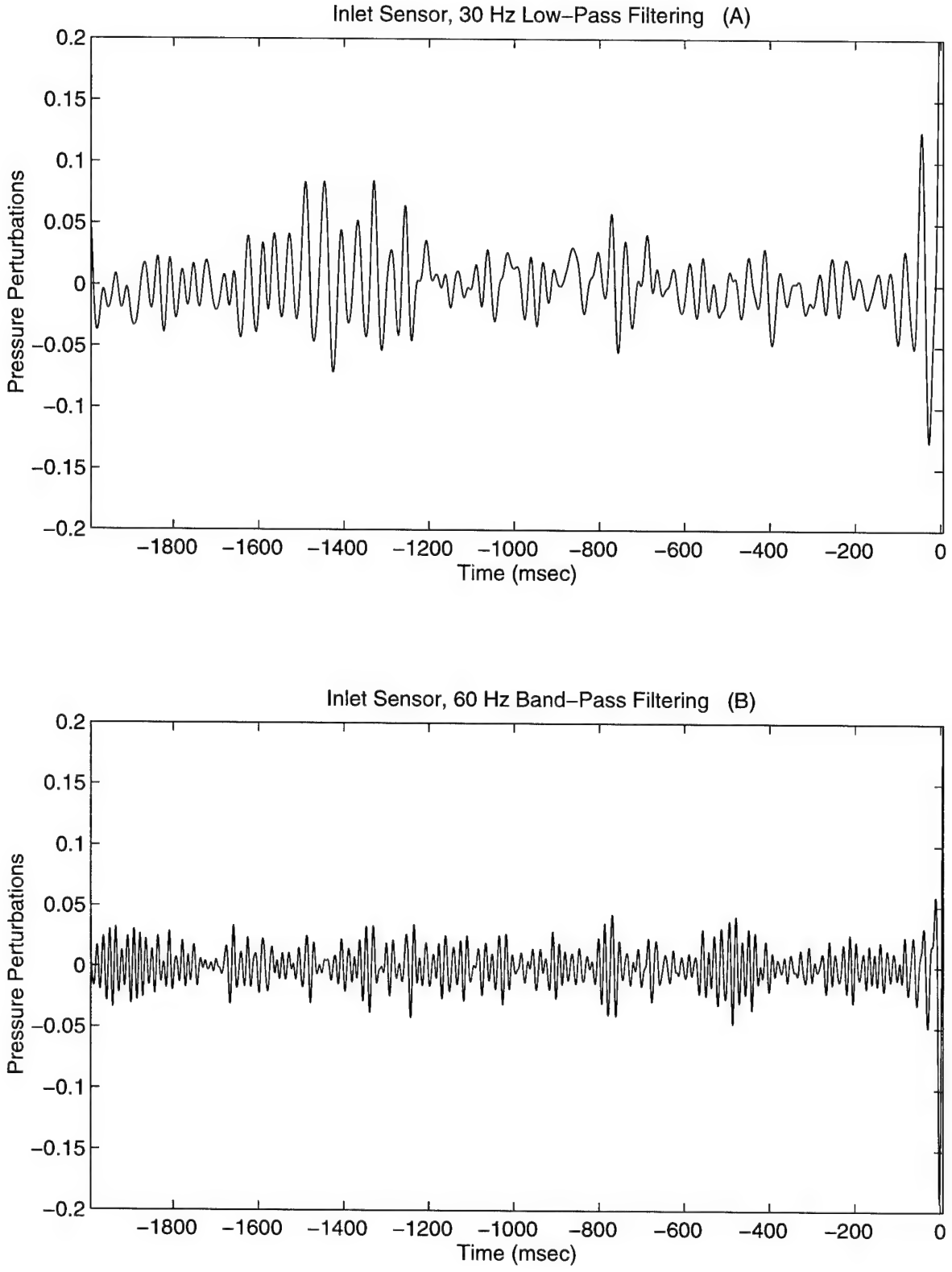

Figure 3.14A, B Open Loop Pre Surge Characteristic: A Single Filtered Inlet Pressure Signal

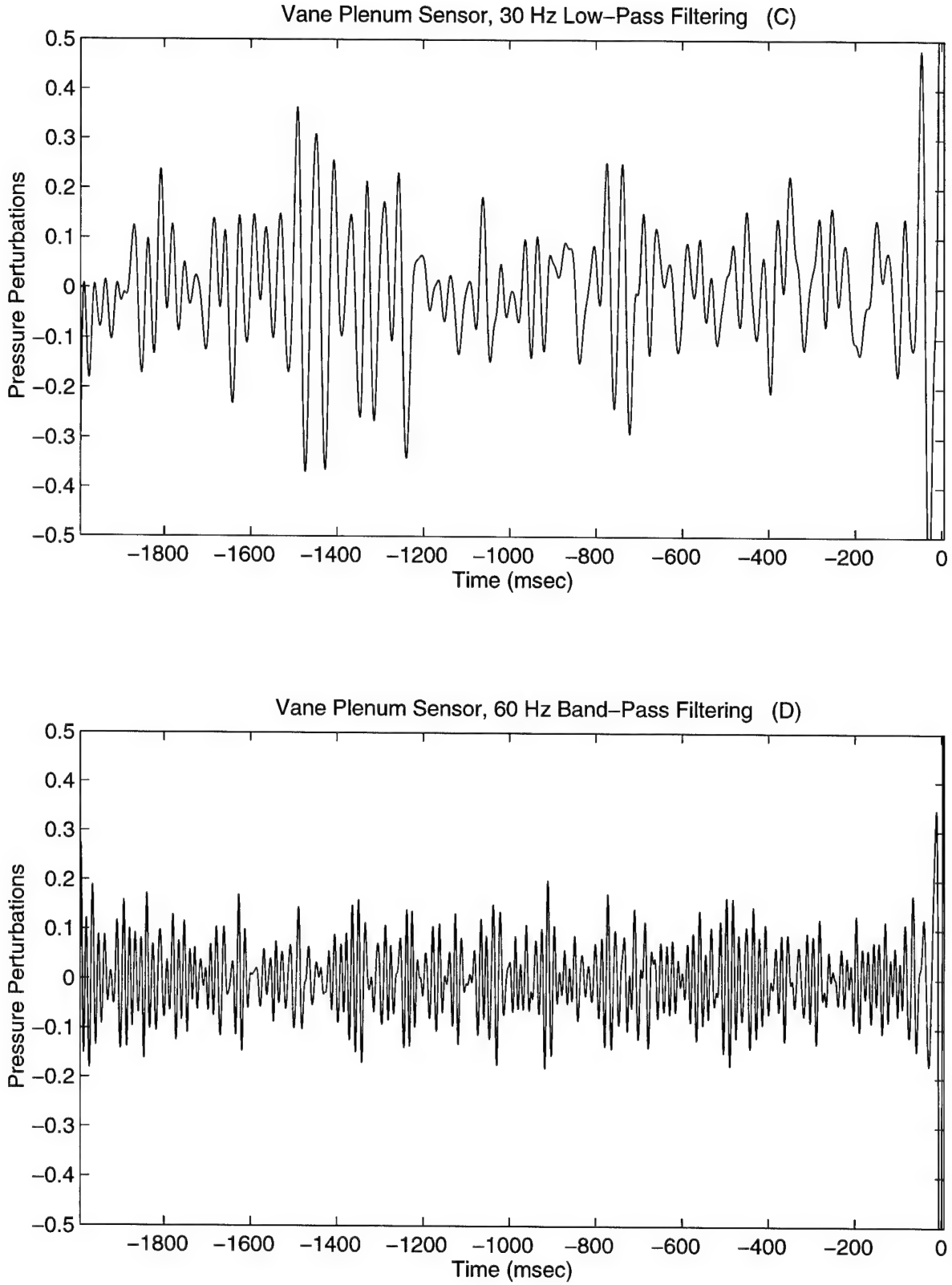

Figure 3.14C, D Open Loop Pre Surge Characteristic: A Single Filtered Vane Plenum Pressure Signal

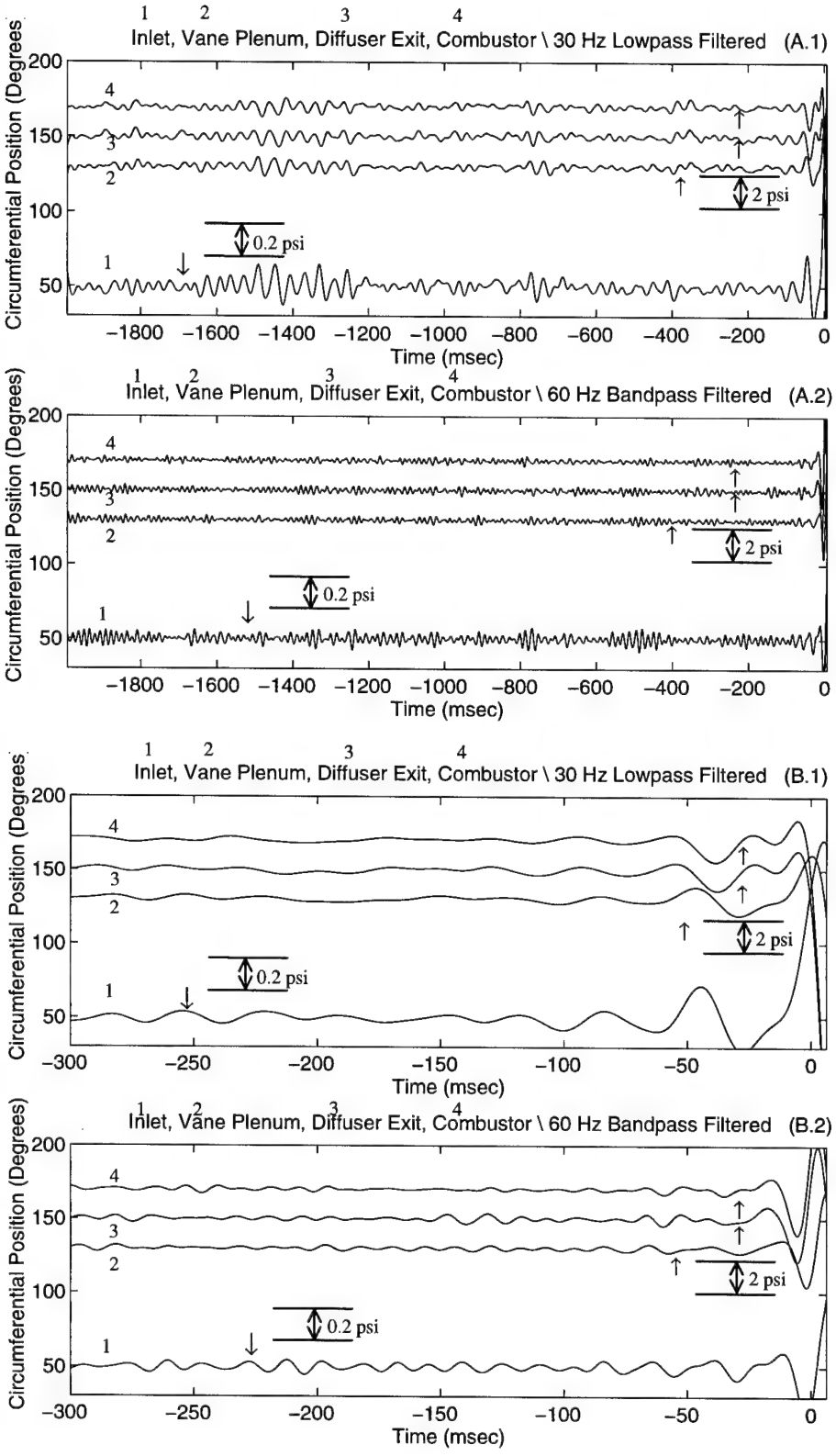

Figure 3.15A, B All Filtered Pressure Taps: Open Loop Prior to Surge

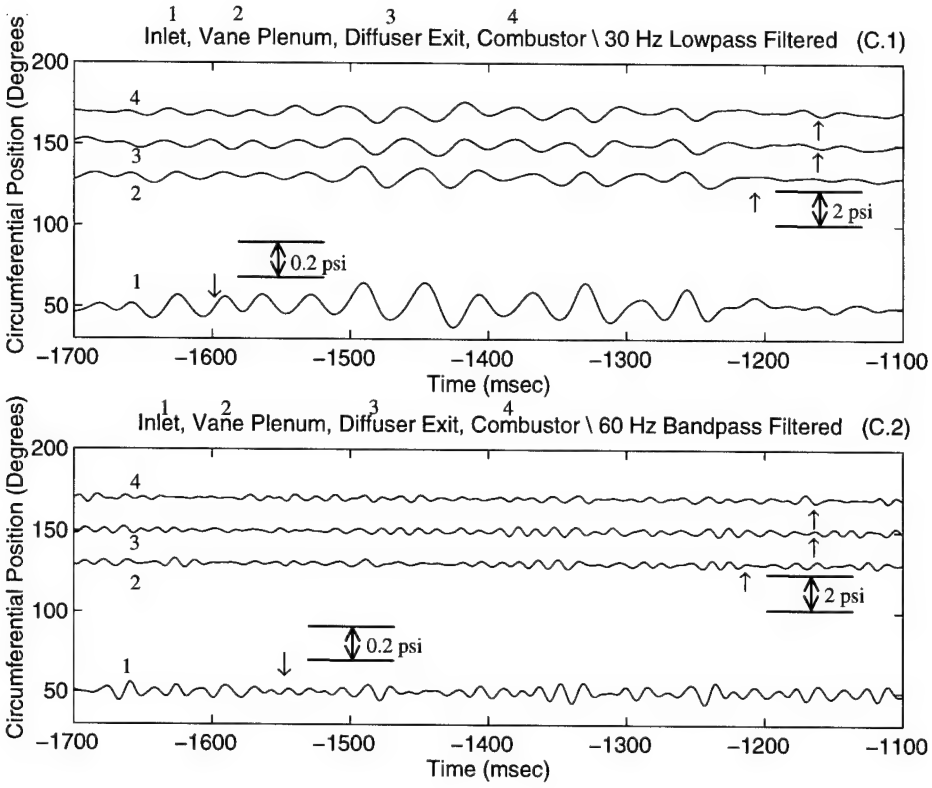

Figure 3.15C All Filtered Pressure Taps: Open Loop Prior to Surge.

250 engine [19], the in phase signals indicate that the 65 Hz mode is not related to the Helmholtz resonance. The 65 Hz mode appears throughout the system and does not appear to be locally generated. This suggests that the 65 Hz mode is acoustic in nature, resulting from acoustic resonance of the engine ducting. The combustor signal leads the diffuser exit, vane plenum, and inlet taps (in that order) indicating that the acoustic resonance originates from the combustor region. In the mean air injection cases, the acoustic resonances (65 Hz and higher frequencies) do not seem to trigger the surge mode. However, feedback controllers may inadvertently excite these resonances, and thus trigger a surge event.

3.4.2 Waterfall Plots

Waterfall plots show the frequency content of a given signal for a series of time

increments. Frequency (ω) in Hz, time in milliseconds, and power spectral density magnitude (PSD) are plotted on the x, y, and z axes, respectively. A number of parameters are selected to best display the various water fall plots. The data reduction requires a window size parameter, which determines the number of time domain data points over which to perform the PSD. 2048 data points, representing 0.512 seconds, are selected for the window size. This window is shifted in increments of 128 data point to time march the waterfall plot calculations.

Nfft represents the number of data points on which a fast Fourier transform are calculated. These data points determine the frequency resolution for the x-axis of the waterfall plot.

$$\Delta f = \frac{f_s}{nfft} = \frac{4000Hz}{2048} = 1.953Hz \qquad (3.1)$$

Note that in general, nfft is not equal to the window size, and averaging is performed. In this case, averaging is not performed.

Four inlet static pressure taps are used to examine the existence of first modal rotating perturbations. Bae details the calculation of spatial Fourier coefficients [19]. To highlight this material, the pressure perturbations (δP) are expressed as follows:

$$\delta P(\theta,t) = Re[\sum_{k=0}^{\infty} a_k(t) \cdot e^{ik\theta}] \qquad 3.2$$

where θ represents the circumferential location of the particular pressure sensor. $a_k(t)$ is the spatial Fourier coefficient of the perturbation. A pseudoinverse is used the calculate $a_k(t)$.

$$\begin{bmatrix} a_1(t) \\ a_2(t) \\ a_3(t) \\ a_4(t) \end{bmatrix} = \begin{bmatrix} e^{i\theta_1} & e^{2i\theta_1} & e^{3i\theta_1} & e^{4i\theta_1} \\ e^{i\theta_2} & e^{2i\theta_2} & e^{3i\theta_2} & e^{4i\theta_2} \\ e^{i\theta_3} & e^{2i\theta_3} & e^{3i\theta_3} & e^{4i\theta_3} \\ e^{i\theta_4} & e^{2i\theta_4} & e^{3i\theta_4} & e^{4i\theta_4} \end{bmatrix}^{pinv} \begin{bmatrix} \delta P(\theta_1,t) \\ \delta P(\theta_2,t) \\ \delta P(\theta_3,t) \\ \delta P(\theta_4,t) \end{bmatrix} \quad (3.3)$$

The spatial Fourier coefficients are complex for the first harmonic. They contain both magnitude and phase information for the given harmonic. The sign of ω determines the direction of rotation of the harmonic waves. The PSD of negative frequency is subtracted from the PSD of positive frequency, resulting in the PSD of the traveling wave at the frequency ω. Negative values indicate negative traveling waves.

Figure 3.16 displays the waterfall plots for the inlet pressure zeroth and first harmonics. Only the zeroth mode is displayed for the vane plenum taps, since the two sensors at this location can not satisfy the Nyquist minimum for a first mode plot. Both sensors indicate a sudden growth in the 28 Hz mode prior to surge. The first acoustic resonance appears around 65 to 70 Hz in the zeroth harmonic. The inlet first harmonic shows a slight peak at the surge frequency; however, the amplitude is small compared to the peak in the zeroth harmonic. All resonances greater than 70 Hz are very small in amplitude compared to the 30 and 65 Hz modes.

3.4.3 Power Spectral Density Plots

Perhaps the best analysis tool during the engine run and post analysis is the power spectral density (PSD). These plots give information about the condition of the engine. The

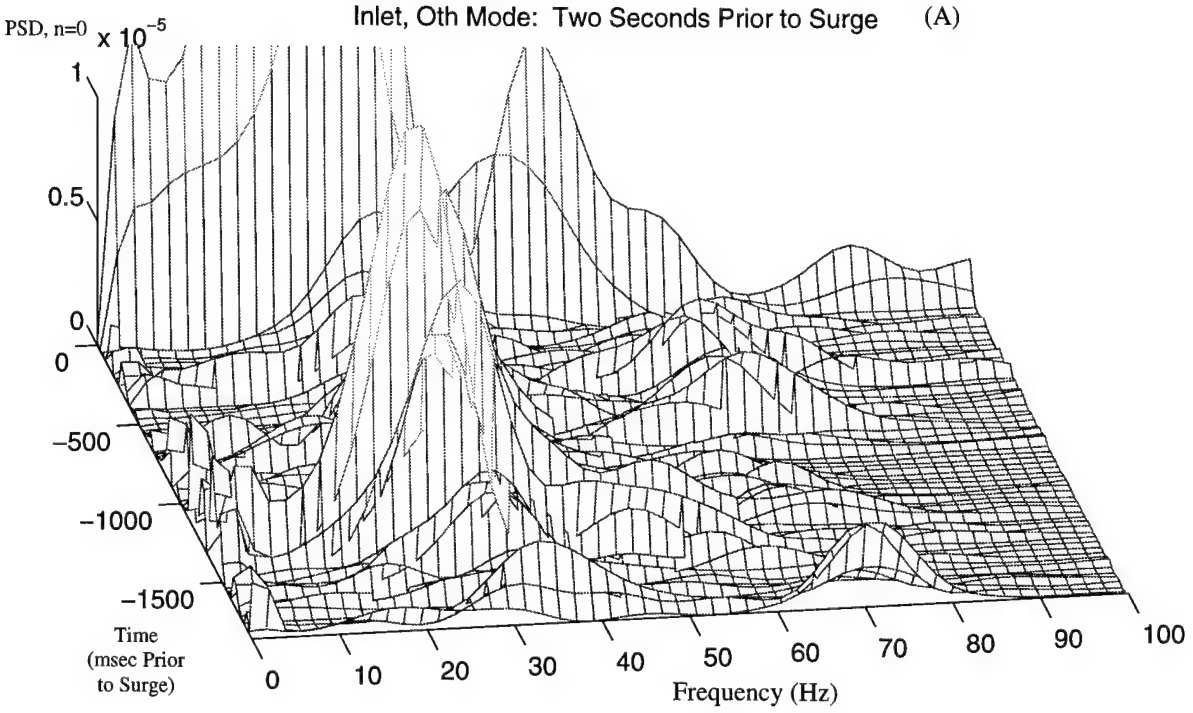

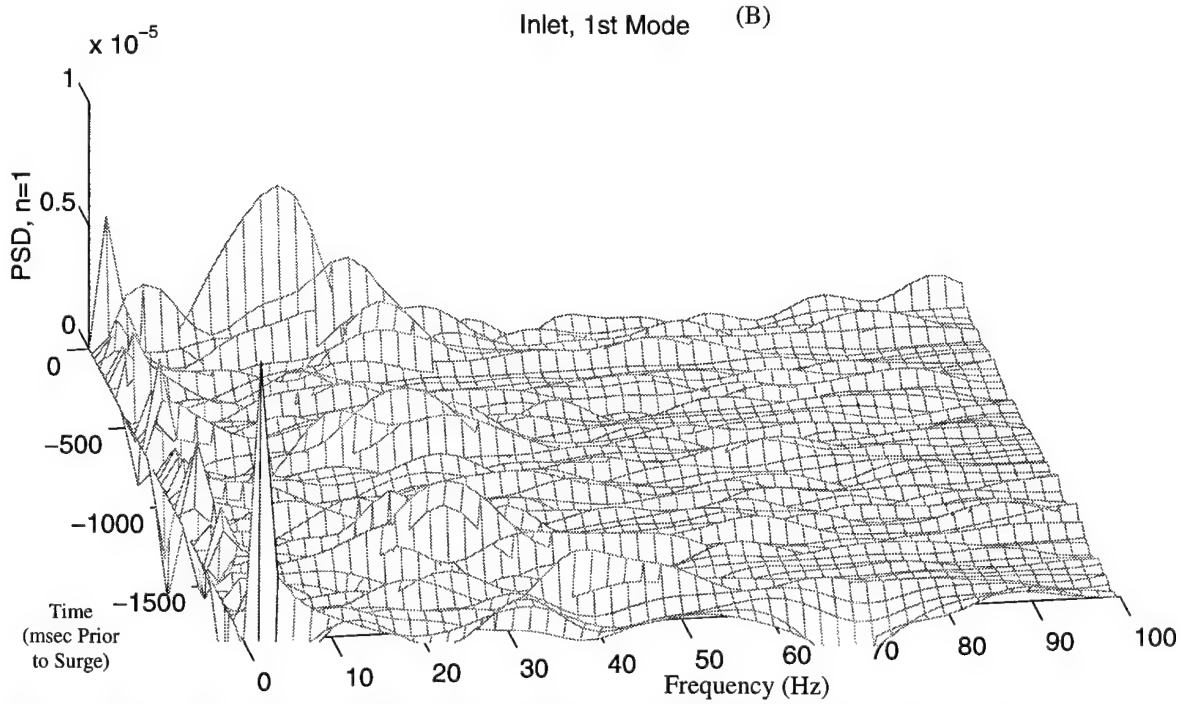

Figure 3.16A, B Open Loop Pre-Surge Water Fall Plot: Inlet Pressure Taps

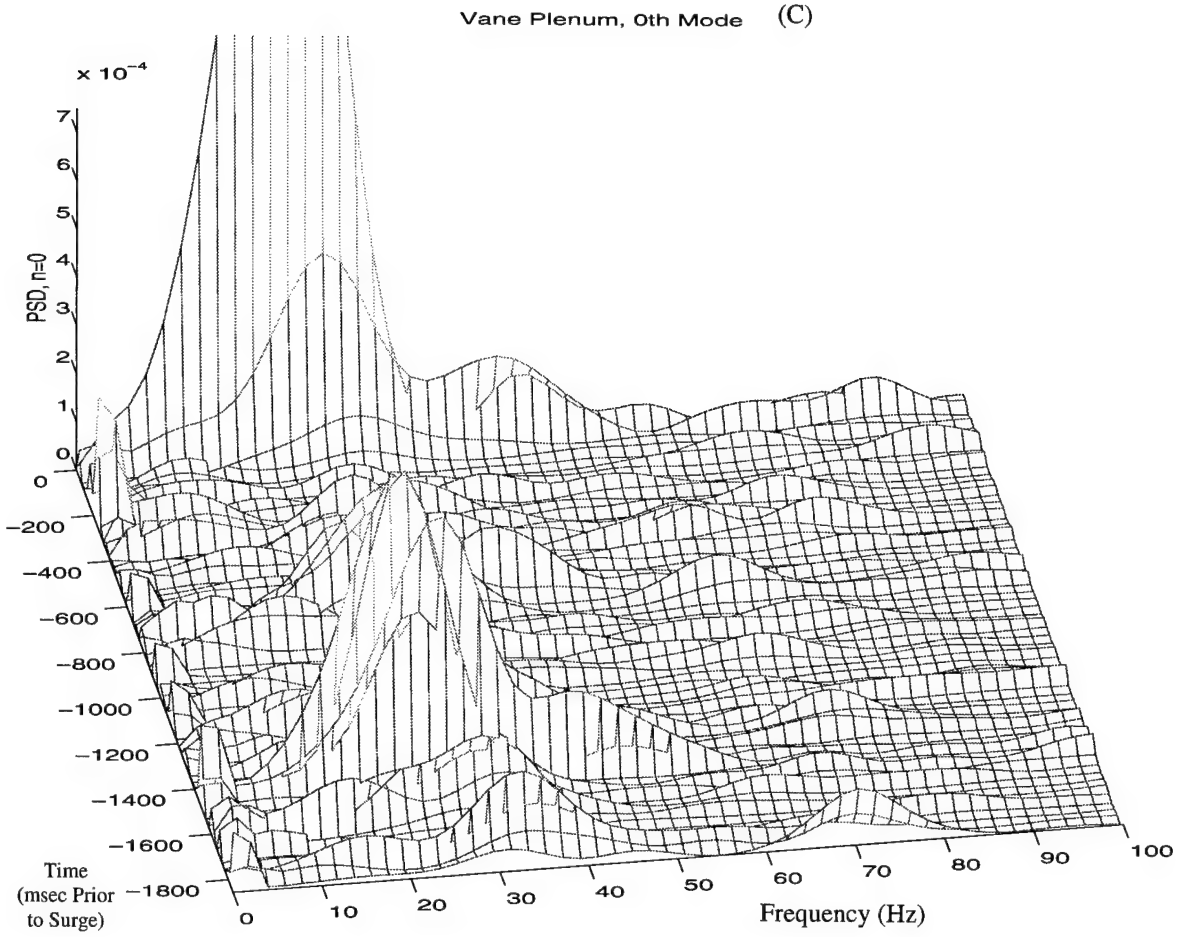

Figure 3.16C Open Loop Pre-Surge Water Fall Plot: Vane Plenum Pressure Taps

existence of modal information at particular frequencies can indicate the imminence of a surge event. The HP63365 Spectrum Analyzer or the HP81630A Vector Signal Analyzer provide continuously updated PSD estimates. In particular, the vane plenum tap is sensitive to resonance of the surge mode, as well as acoustic resonances, both of which always precede the surge event in the mean injection case.

Predecessors have published detailed descriptions of the LTS-101 PSDs. Borror [14] examines the LTS-101 baseline surge behavior without mean air injection and concluded the following:

1) No linearly growing disturbances preceded the surge event.

2) Frequency content below 100 Hz at the throat, combustor, and inlet tap locations increases simultaneously around 250 ms prior to surge.

3) Based on measurements at the throat, rotating stall is not present in the vaned diffuser.

Corn [15] provides a detailed study of the unsteady pressure tap spectral content for mean air injection. There are two key differences in the data acquisition and analysis between predecessors and experiments described here. First, because predecessors thought that the engine rotor frequency at 760 Hz would corrupt compensation, experimental data was previously filtered at 600 Hz with an analog, eight pole Caur (elliptic), anti aliasing filter. The current experiments set this low pass filter's cutoff frequency to 1020 Hz. High order frequencies actually have little effect on the closed loop compensator output, since the high speed Moog valve has a bandwidth of 330 Hz. The current approach is to record all frequency data that could possibly influence the engine performance, rather than ignore it. The information is used in the single input multiple output system identification code (FORSE [31]) to place higher acoustic resonances (see discussion in chapter 3.5).

Second, old analysis techniques eliminated data at 60 Hz . The digitally applied notch had spill-over effects which reduce the amplitude of the nearby acoustic resonance at 68 Hz. Although electrical noise is noticeable on PSD plots and oscilloscope readings for values of exit nozzle area that are unchoked (i.e. high massflow) its effects are negligible in the PSD averaged plots after the nozzle chokes and the modal resonances begin to appear. Therefore, the analysis used here maintains all information.

The power spectral density (PSD) of the zeroth mode in Figure 3.17 and 3.18 shows the distribution of signal power with frequency. Therefore, the units of the PSD are

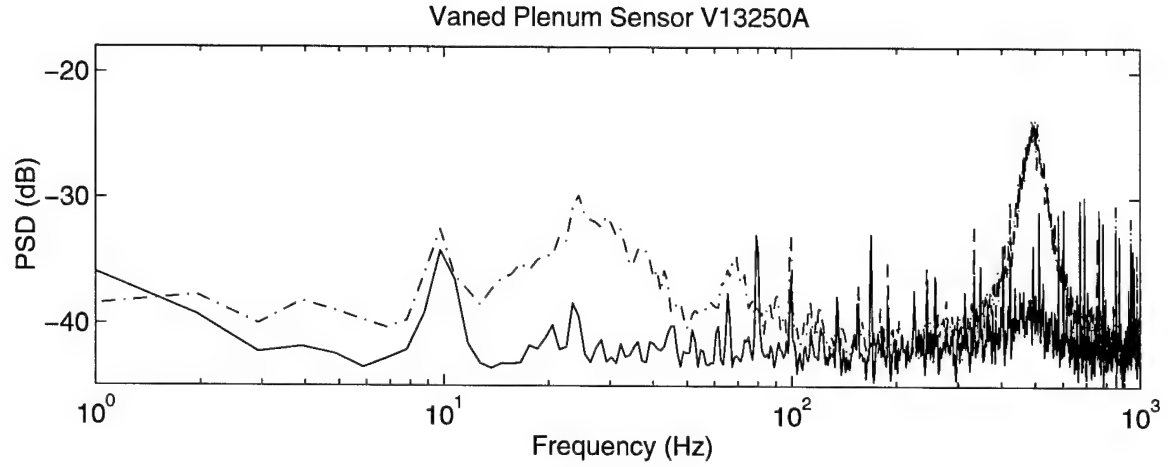

Figure 3.17 Power Spectral Density:
Dark Line -- Prior to Choked Exit Nozzle: Linear Actuator Position is 1.15"
Dash Pot Line -- Intermediate Loading Condition: Linear Actuator Position is 1.275"

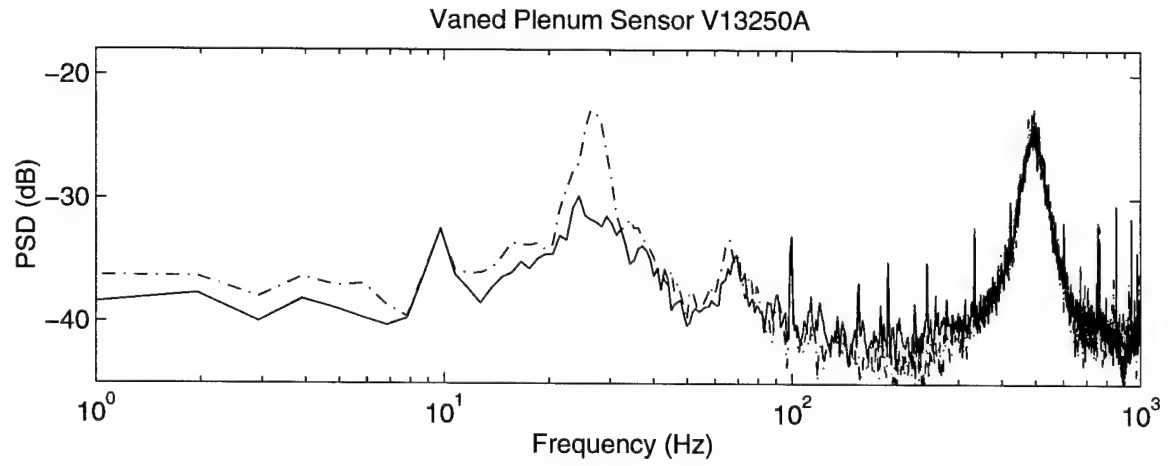

Figure 3.18 Power Spectral Density:
Dark Line -- Intermediate Loading Condition: Linear Actuator Position is 1.275"
Dash Pot Line -- Operating Prior to Surge: Linear Actuator Position is 1.288"

$\frac{psia\text{^}2}{Hz}$. The PSD is determined via the Matlab function called "spectrum.m" [30]. This routine uses the discrete fast Fourier transform with Hanning windows of 4096 points, which yields the following frequency resolution:

$$f_{resolution} = \frac{f_{sampling}}{\#of \quad DFFT \quad points} = \frac{4000Hz}{4096} = 0.977Hz \qquad (3.4)$$

Thus, frequency resolution is ~1 Hz for these calculations. A window overlap region of 2048 provides smoothing for the spectral plots.

Figures 3.17 and 3.18 display the PSD plots for the vane plenum sensors, the most responsive at the critical modes. A representative PSD plot for every sensor is included in Appendix B. The pressure taps in this appendix are as follows: one vane plenum tap, four averaged inlet taps, one combustor, one diffuser exit, and three averaged throat taps. Recall from Chapter 2.1 that linear actuator position refers to the operator input measured from the designated "home position". As the linear actuator position increases, the exit nozzle area decreases, which decreases the corrected massflow through the engine. The plots for 1.15" linear actuator position show the spectral content prior to when the nozzle chokes. The plots for 1.275" linear actuator position ("intermediate loading condition") show the spectral content prior to noticeable surge precursors. At 1.288" linear actuator position ("operating prior to surge"), the engine is operating as close to surge as possible for this engine run. The PSD plots show a large growth of the 28 and 68 Hz peaks.

The experimental data is summarized in Table 3.2. The primary difference between these results and previous accounts is that the new instrumentation permits much smoother exit area reduction near surge. As a result, the surges spontaneously result from aerodynamic or mechanical perturbations rather than caused by external disturbances to the flow. Thus, these experiments better capture the dynamics near surge. The primary difference between this observed data and the previous data is the occurrence of the 10 Hz

	Frequency Peaks	(in Hz)
Tap Location	Growing Peaks	Invariant
Axial Inlet 4 Averaged taps	28, 68	10,130,250,325, 600,800
Diffuser Throat 3 Averaged taps	28	
Vane Plenum 2 taps (same trend)	28, 66	10, 500
Diffuser Exit 2 taps (same trend)	28	10,400
Combustor 1 tap	28,68	10

Table 3.2 Observed Peaks for Current Mean Injection Cases.

peak. Although this peak is invariant during each engine run, the magnitude of the peak increased after each surge event, as is discussed in Chapter 5.5. No peak was evident at ~50 Hz for these current tests, as was previously reported.

3.5 Forced Response Testing at 95% $N1_{corr}$

The purpose of forced response testing is to obtain transfer functions of the engine dynamics. The high speed valve command provides the input, while the outputs are the most reliable pressure signals among the several possible axial locations. The measured "engine dynamics" include the filtered pressure responses from the selected Kulite pressure transducers, the valve characteristic, the tap characteristic, and the anti-aliasing filter dynamics (described in Chapter 3.3.3). The measured transfer functions of these elements are used to perform a linearized model of the system, as described in Section 3.6.

System identification is similar to that performed in [15]. However, there are several reasons that new transfer functions were desired for control law development. First,

as was pointed out in section 3.2, the operating line and speed line have shifted with the engine rebuild. Thus one can not assume that the previous identification correctly portrays the features of the current test rig.

Second, previous control laws for both the Lycoming and Allison engine focus strictly on a single sensor location for controller input. These compensators were single-input single-output, based on an averaged measurement at the inlet pressure taps. The new research approach incorporates several taps at different compressor locations.

Third, the methodology for obtaining good transfer functions using system identification is well established for the helicopter engine testing. Al-Essa[18], Bae[19], and Corn [15] found that forcing at fixed frequencies yielded good transfer functions with good coherence measurements. They eliminated a sine wave frequency sweep option, since the engine data was corrupted by high levels of background noise. Therefore, repeating this procedure is relatively straight forward.

Finally, the transfer functions are obtained by post processing a given set of 15 second data sets containing discrete forcing frequencies. FORSE code system identification improves as more detail is added to the measured transfer functions. For instance, more data points are required in the regions of the assumed pole locations, including the surge and first acoustic modes. In addition, transfer function data at higher frequencies is desired. Previous experiments for the LTS-101 only obtained transfer function data up to ~280 Hz. The new transfer functions extend to 680 Hz.

Several engine runs in this research effort focus on obtaining good transfer functions. See Appendix C for details on the discrete forcing frequencies that are used. The objective is to obtain a data set that is as close to the surge point as possible, while

maintaining reasonable coherence levels (near unity). Figure 3.19 shows the transfer functions obtained at various operating points for one of the inlet taps. The level of damping decreases at particular frequency locations as the transfer function is obtained closer to the surge line. The compressor inlet operating map shows the operating locations where these transfer functions are obtained (Figure 3.20). The transfer function magnitude increases as the corrected massflow decreases. A typical speedline is also plotted on the compressor map to show how close to the surge line the transfer functions are obtained.

To estimate the transfer function, Matlab's "spectrum.m" was first used to obtain the magnitude and phase for the complete data sets. Spectrum.m calculates the power spectral density and cross spectral density for the given input and output signals. The transfer function (G_p) is defined as:

$$Gp(\omega) = \frac{S_{uy}(\omega)}{S_{uu}(\omega)} \qquad (3.6)$$

S_{uy} is the cross spectral density between the input u and output y, while S_{uu} is the power spectral density of input u. Valve command (voltage) is the input while the selected pressure tap (psia) is the output. This method produced poor coherence for the transfer functions beyond ~100 Hz, independent of the pressure tap used.

Figure 3.21 provides a block diagram of the forced response testing. The coherence for the signal to noise ratio is expressed:

$$\frac{S}{N} = \frac{rms(s)}{rms(n)} \qquad (3.7)$$

As S/N approaches infinity, the coherence tends towards 1. As S/N approaches zero, the

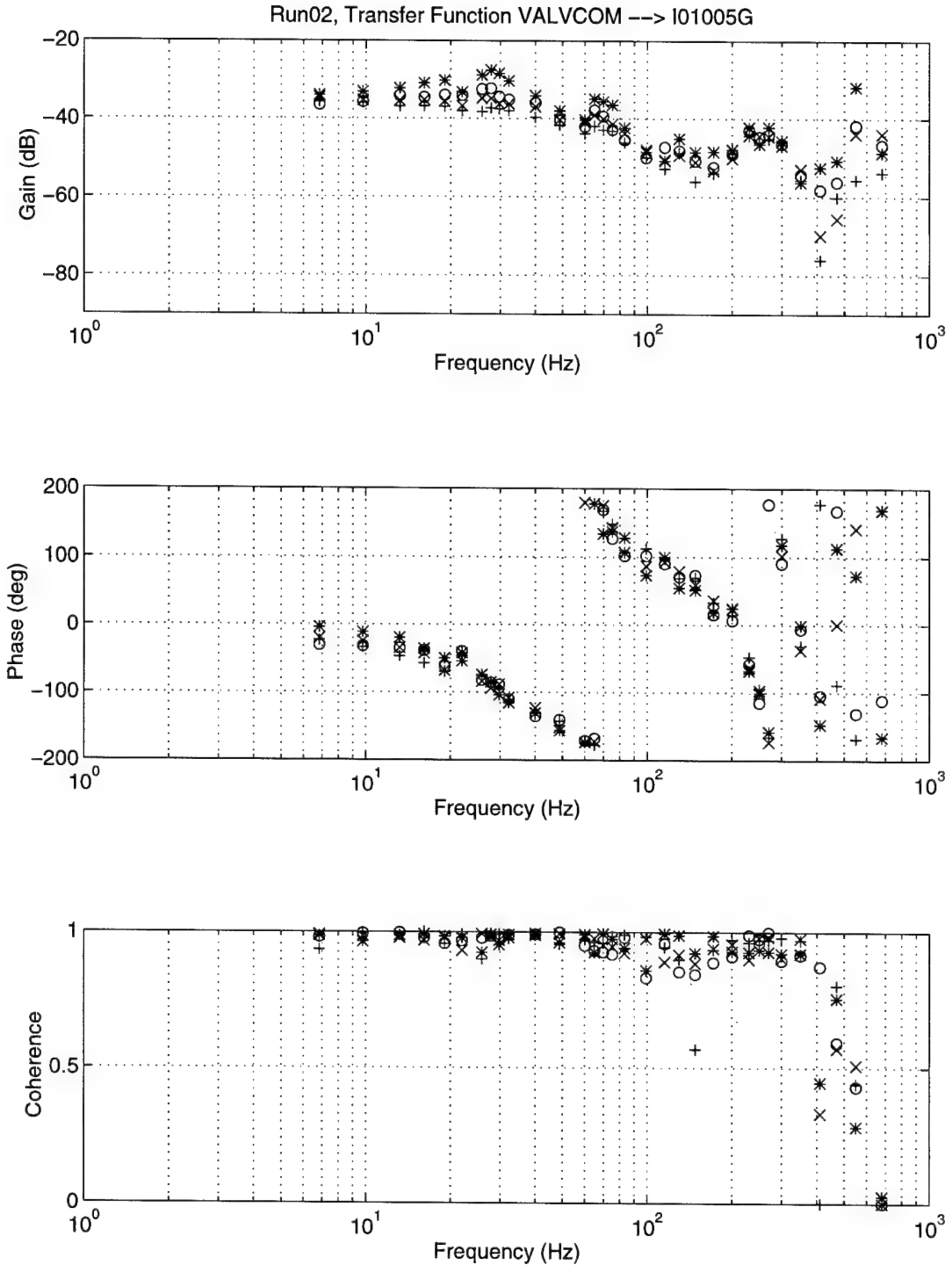

Figure 3.19 Transfer Function Data:
+ -- @ 975 lbf (on the load cell)
X -- @ 1069 lbf
O -- @ 1095 lbf
*** -- @ 1130 lbf**

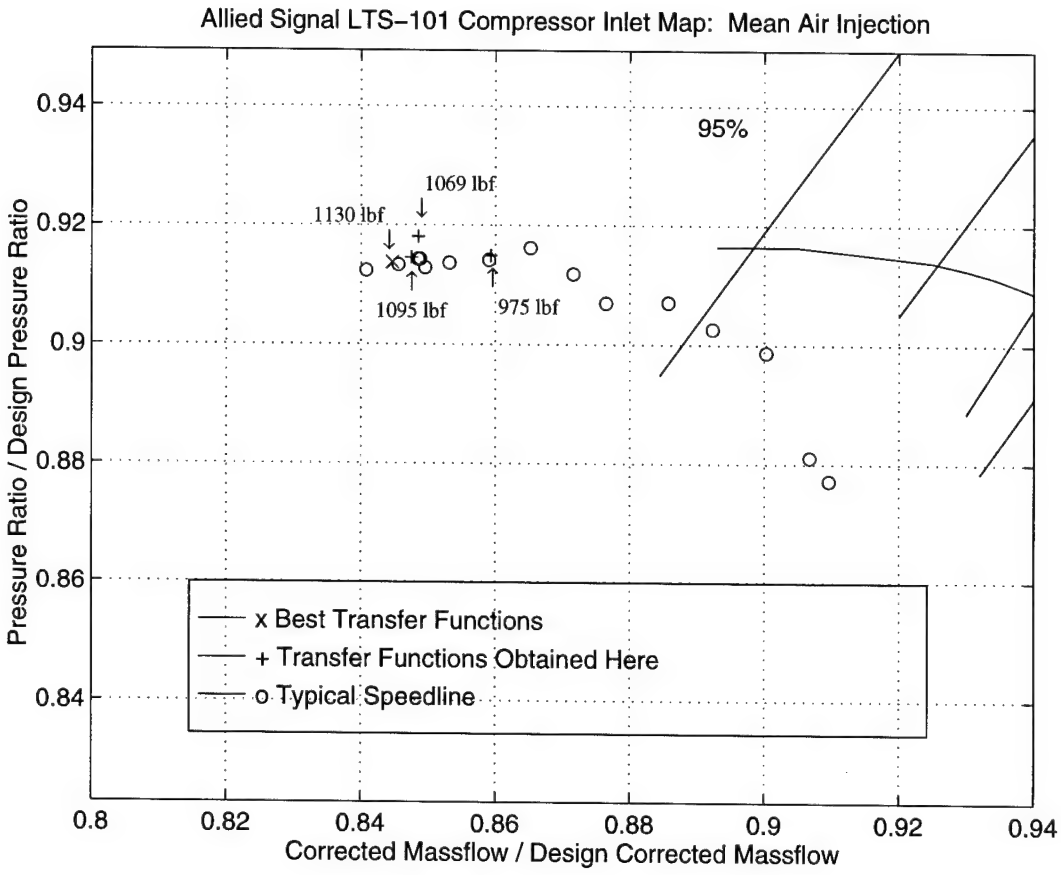

Figure 3.20 Operating Points Where Transfer Functions are Obtained

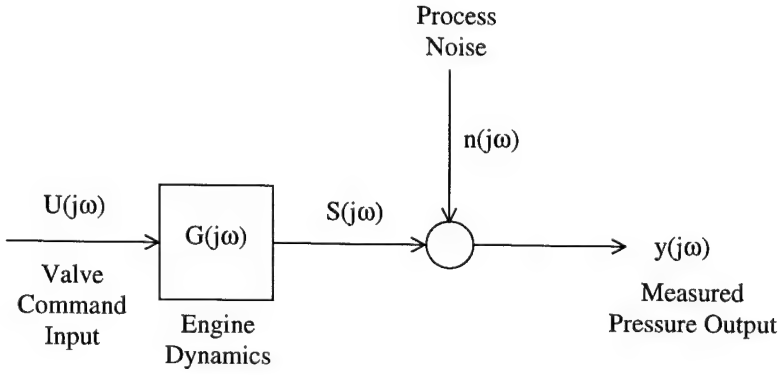

Figure 3.21 Block Diagram of Signal to Noise Ratio: Coherence for Forced Response Testing

coherence tends towards 0.

Improved coherence is obtained using a correlation analysis method described by Ljung [32]. This method attempts to fit the primary forcing frequency in the data set with a sine and cosine wave at the particular assigned frequency. The results are cumulated and averaged to obtain the desired transfer function (including magnitude, phase, and coherence). The correlation method tends to minimize the effects of particularly poor coherence regions within the entire data set. Both spectrum.m and the correlation method produce similar transfer functions within the desired frequency range; however, the correlation analysis transfer function fit yields a much improved coherence.

Attempts were made to produce transfer function data sets at operating points closer to the surge line; however, surge resulted. Large forcing amplitudes, even at frequencies viewed as non-critical, sometimes triggered surge. Figure 3.22 demonstrates a case where the engine surged with a 7 Hz nominal forcing frequency input of ±1 Vpp. One could attempt to decrease the forcing amplitude; however, this approach increases the risk that engine noise will overwhelm the signal and yield a low coherence. A number of sensor transfer function combinations were used to generate system identification data and final compensator designs. The most successful compensator results use a combination of two inlet sensors, designated I01 and I04, and one throat sensor (T05) (Figure 3.23).

3.6 SIMO System Identification

Three major goals drove the system identification process for the LTS-101. First, all previous compensation attempts used a single pressure tap location as input to the controller. Resonances at one pressure tap location may not exist at another. In [15], all

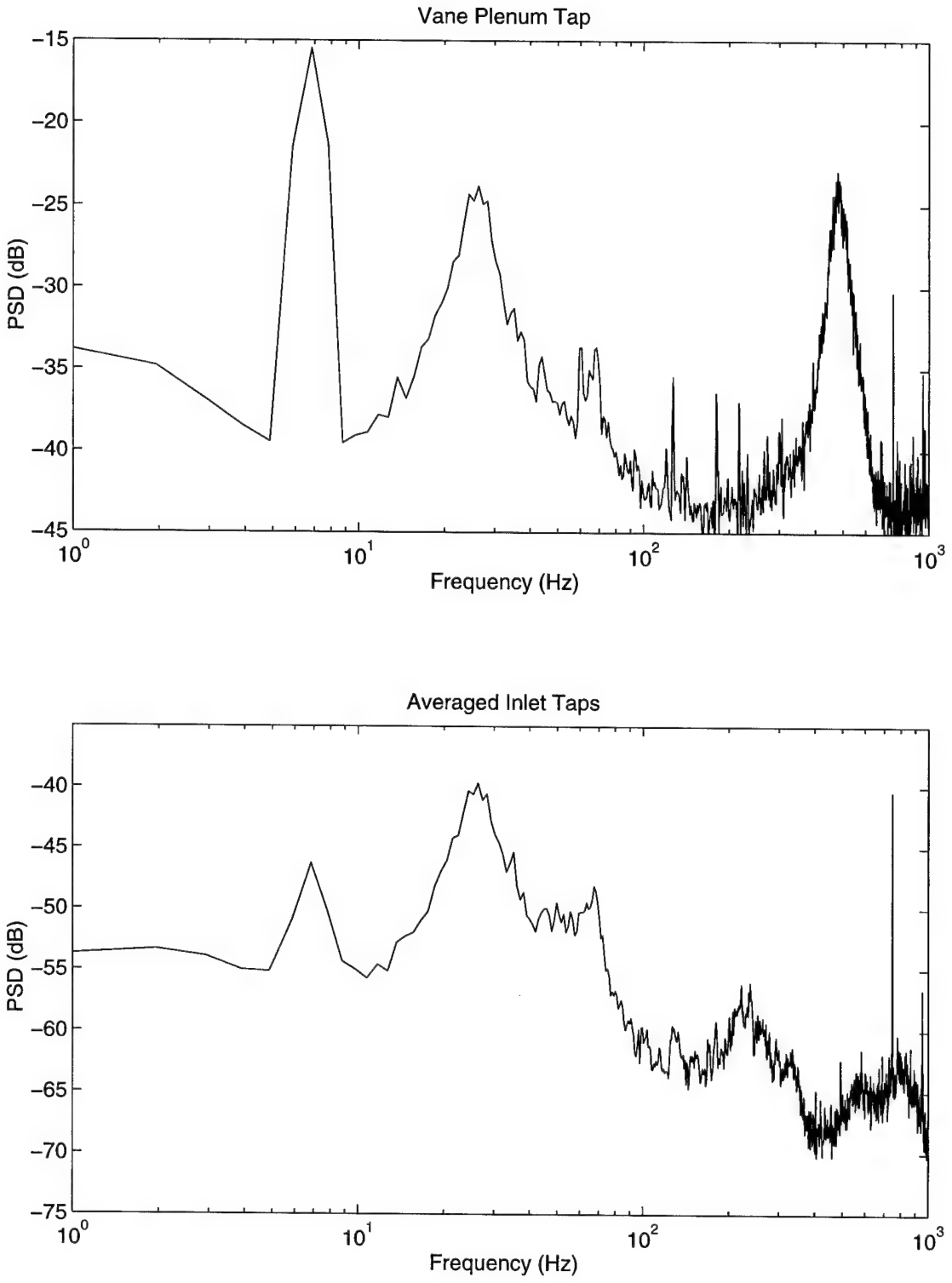

Figure 3.22 Forcing at ±1 Vpp at an Operating Point too Close to the Surge Line. This is the Time Segment Just Prior to Surge.

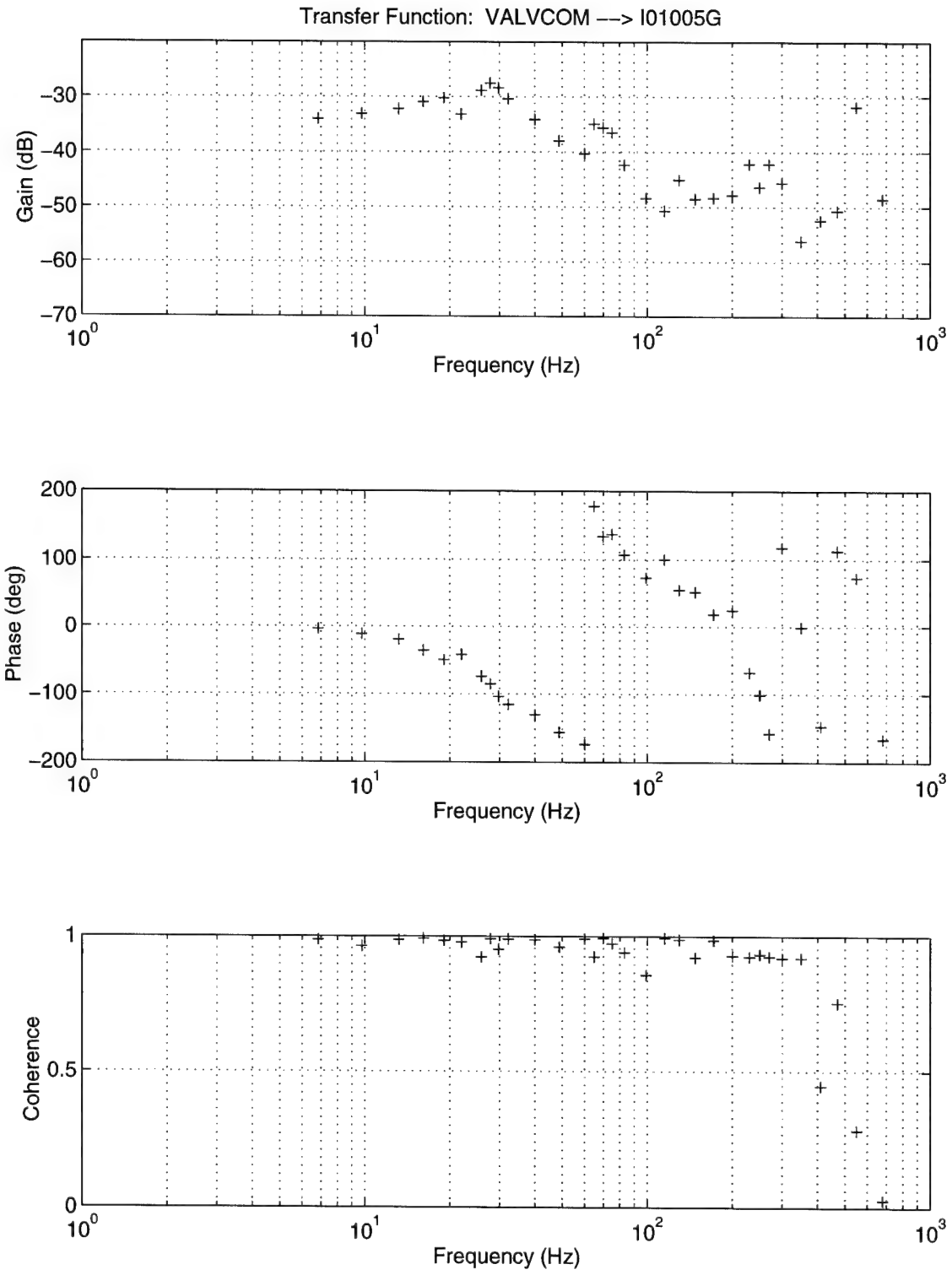

Figure 3.23A Best Transfer Functions (Used to Design Best Compensators.) Valve Command to First Inlet Tap.

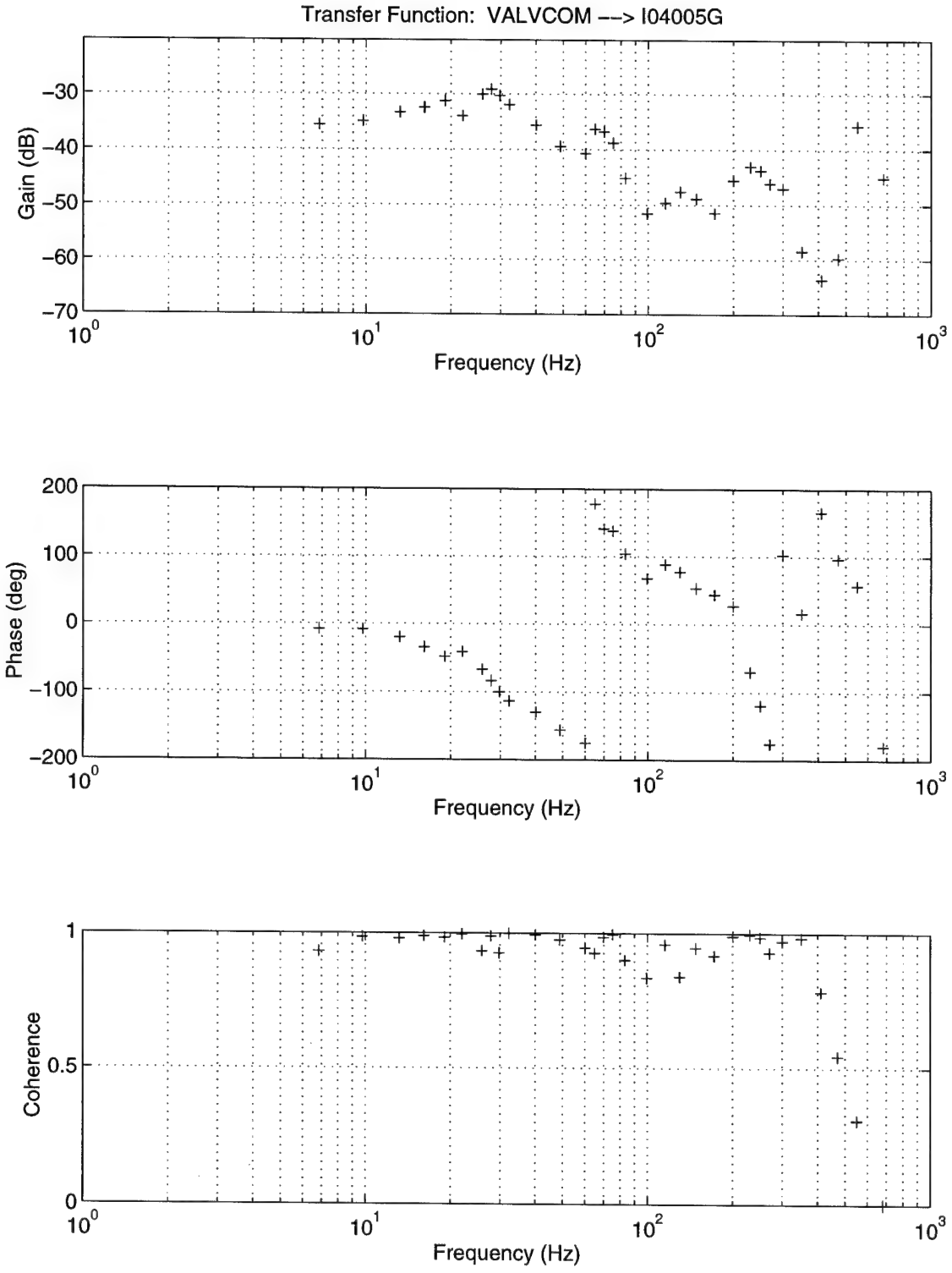

Figure 3.23B Best Transfer Functions: Valve Command to Second Inlet Tap

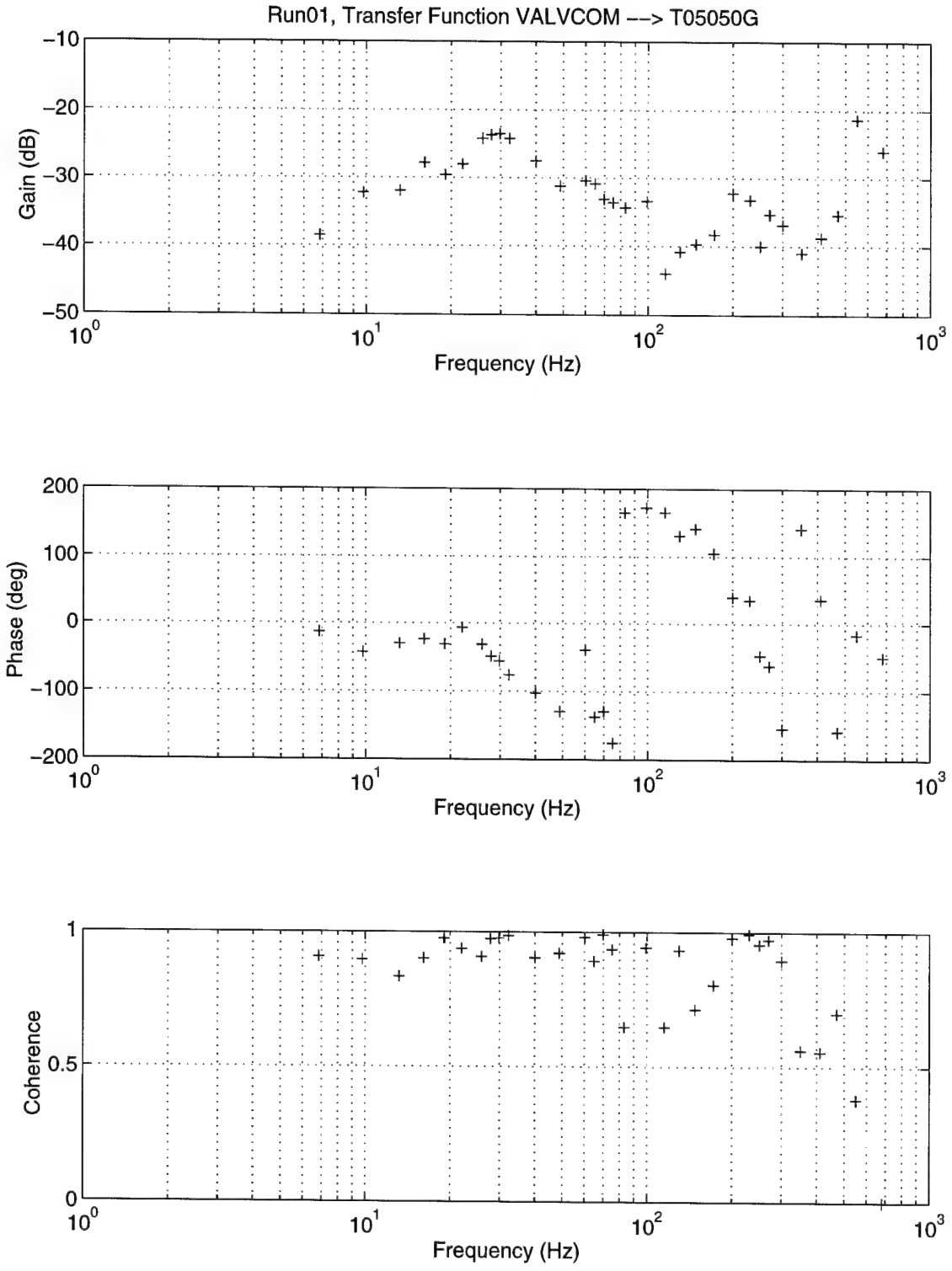

Figure 3.23C Best Transfer Functions: Valve Command to Throat Tap

of the LTS-101 information was gathered from the inlet taps, a single circumferential slice preceding the axial compressor stage. The current identification goal is to include as much information as possible into the model used for controller design. Therefore, system identification is performed using numerous combinations of taps, ranging from the inlet to combustor.

Second, all previous system identification attempts [15, 18, 19] are acquired using Matlab's invfreqs.m with a single transfer function. The plant is generated using a rather ad hoc method of specifying a number of poles and zeros to match the measured data. The best fit is then determined by the lowest order system which generated an acceptable fit of magnitude and phase. The current system identification approach utilizes a method that quantifies the search for the best transfer function fit. Cost function minimization provides a quantitative means of showing how well the pole and zero placement fit the supplied transfer functions.

Finally, previous transfer function fits took a considerable amount of manual effort to produce, and provided little flexibility to redesign based on the results of experiments. In order to test multiple combinations of pressure tap outputs in an efficient manner, a method to quickly produce optimized transfer function fits is necessary. This method requires flexibility to generate fits with particular designed constraints, such as the size of the final plant size, and the elimination of any identified transfer function points that create unreasonable fits.

FORSE (Frequency dependent Observability Range Space Extension) for transfer function identification, designed by Robert Jacques [31] in 1994, provides the means to accomplish all of these objectives. This multiple input multiple output (MIMO) code is

flexible to accommodate any input/output combination. The user can manipulate inputs in a timely manner, and quantitatively optimize the desired plant to a state size that is workable for the compensation scheme. FORSE also provides a number of other excellent features in the plant optimization process. The user can prohibit particular pole placement locations if desired. He or she could also assign particular pole placement locations which may actually produce superior cost function optimization compared to the code's spontaneous transfer function fit. FORSE updates the user about the stability of the particular system at hand, and can eliminate unstable poles from the design.

To use the FORSE routine, the user needs to represent the MIMO system in a complex transfer function form.

$$\begin{bmatrix} y_1 \\ y_2 \\ \cdot \\ y_n \end{bmatrix} = \begin{bmatrix} G_{11} & G_{12} & \cdot & G_{1n} \\ G_{21} & G_{22} & & \\ \cdot & & \cdot & \\ G_{n1} & & & G_{nn} \end{bmatrix} \cdot \begin{bmatrix} u_1 \\ u_2 \\ \mathrm{M} \\ u_n \end{bmatrix} \qquad (3.7)$$

FORSE requires each complex transfer function value at each particular forced frequency (Table 3.3). After the FORSE manipulations, the code outputs a state space plant representing the dynamics which best fit the observed data. These outputs are in the following standard form:

$$\dot{\underline{x}} = A\,\underline{x} + B\,\underline{u} \qquad (3.8)$$

$$\underline{y} = C\,\underline{x} + D\,\underline{u} \qquad (3.9)$$

Numerous models to fit the experimental transfer functions were considered, using

ω_1	$G_{11}(j\omega_1)$	$G_{12}(j\omega_1)$	...	$G_{1n}(j\omega_1)$	$G_{21}(j\omega_1)$	...	$G_{2n}(j\omega_1)$	$G_{nn}(j\omega_1)$
ω_2	$G_{11}(j\omega_2)$	$G_{12}(j\omega_2)$	...	$G_{1n}(j\omega_2)$	$G_{21}(j\omega_2)$	...	$G_{2n}(j\omega_2)$	$G_{nn}(j\omega_2)$
:	:	:		:	:		:	:
ω_n	$G_{11}(j\omega_n)$	$G_{12}(j\omega_n)$	...	$G_{1n}(j\omega_n)$	$G_{21}(j\omega_n)$	...	$G_{2n}(j\omega_n)$	$G_{nn}(j\omega_n)$

Table 3.3 FORSE Inputs

various combinations of sensors. The set that produces the most successful compensators used two inlet taps (designated I01 and I04) and one throat tap (designated T05) (Figure 3.24). This particular set excludes the forcing frequency sets at 550 and 680 Hz. FORSE attempted to place a nearly unstable pole at this higher frequency location prior to exclusion of this frequency range. Based on engine operating experience, the design should not

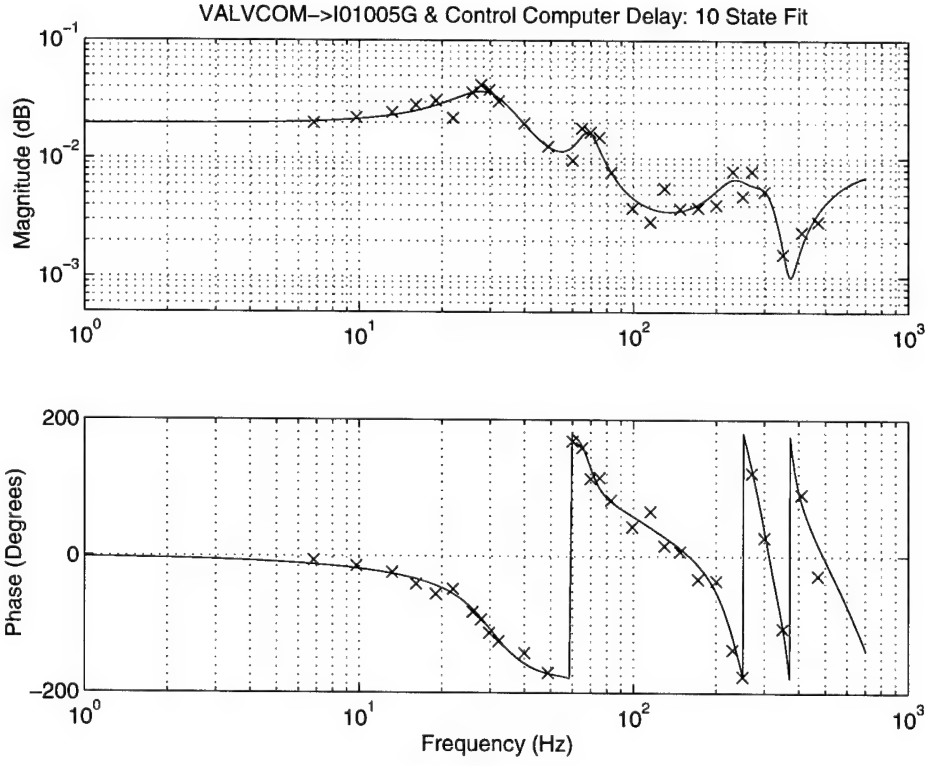

Figure 3.24A SIMO Transfer Function Fit for Best Compensator Designs.

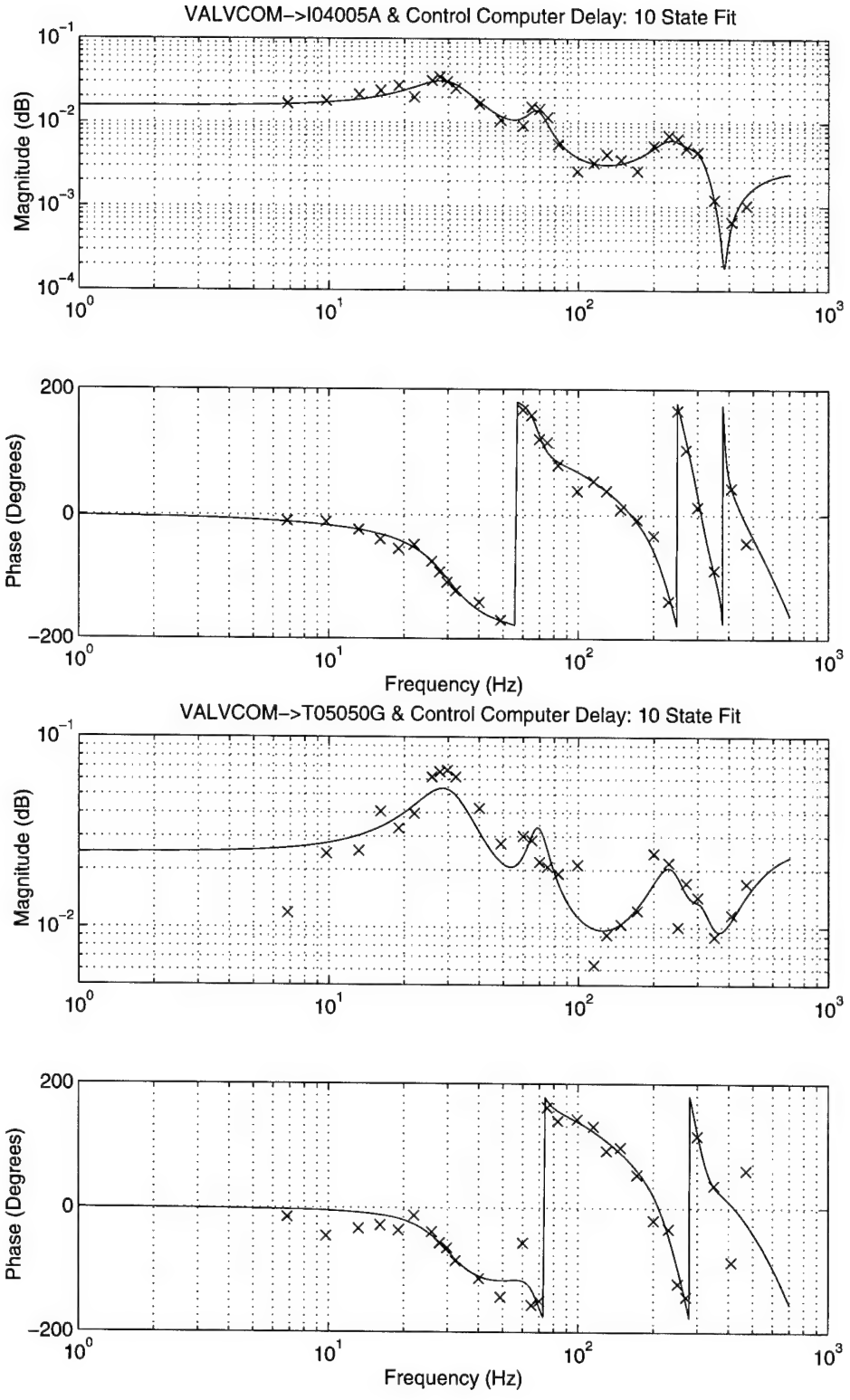

Figure 3.24B, C SIMO Transfer Function Fit for Best Compensator Designs.

emphasize a higher frequency mode, which decreases the compensator's effect on the surge and low acoustic resonances. In addition, the author did not allow FORSE to place a pole at a lower frequency than the observed surge mode. Figure 3.25 displays the eigenvalues the best FORSE fit; the most effective compensator is designed using this system . Notice that the 28 Hz mode has been moved to the neutral axis. This is because the compensator is designed using this assumption, to force the controller to have the ability to make the plant closed loop stable, even after it has become unstable.

A competing identified model is also included (Figure 3.26). The reader may notice that it includes the same pressure taps as the fit used in the "best" identified model (designated I01, I04, and T05). FORSE typically places a pole at 21 Hz as well as at the surge frequency (Figure 3.27). More explanation focuses on this plant in Section 5.5. The

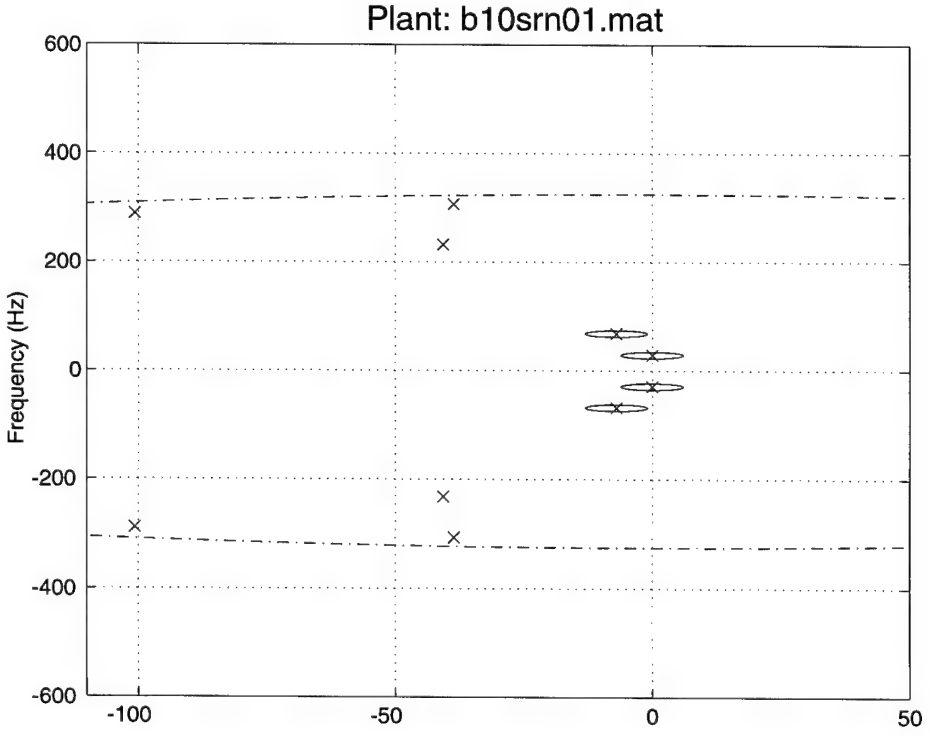

Figure 3.25 Plant Model, Based on FORSE Fit. Used in Best Compensator Designs

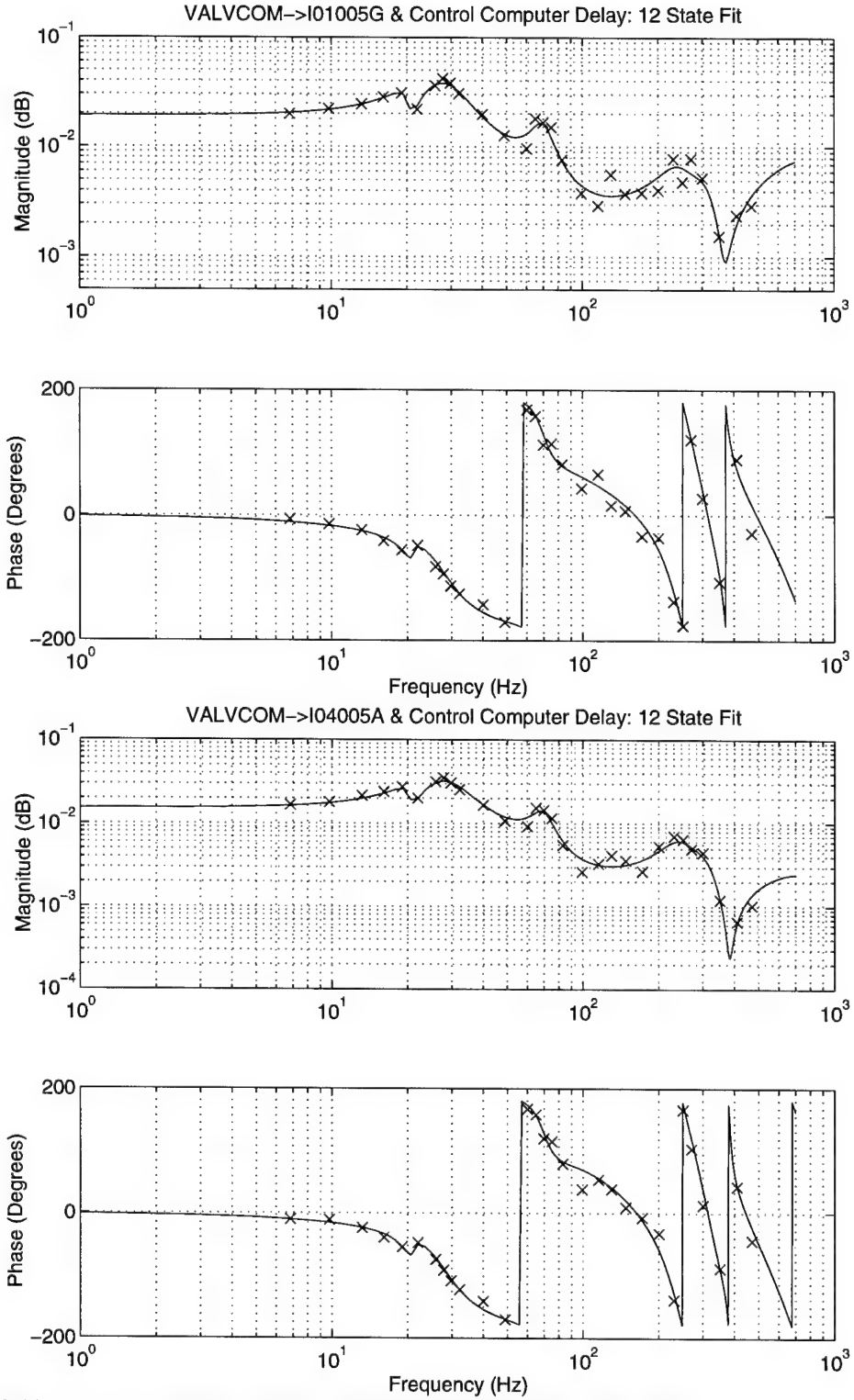

Figure 3.26A, B Competing Design, SIMO Transfer Function Fit

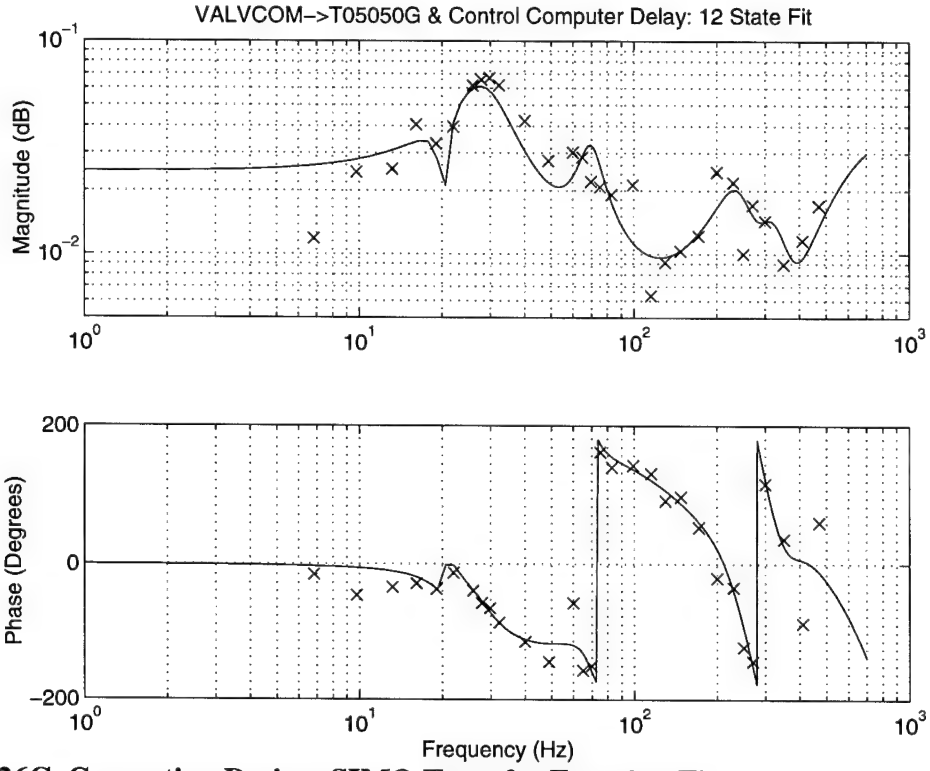

Figure 3.26C Competing Design, SIMO Transfer Function Fit

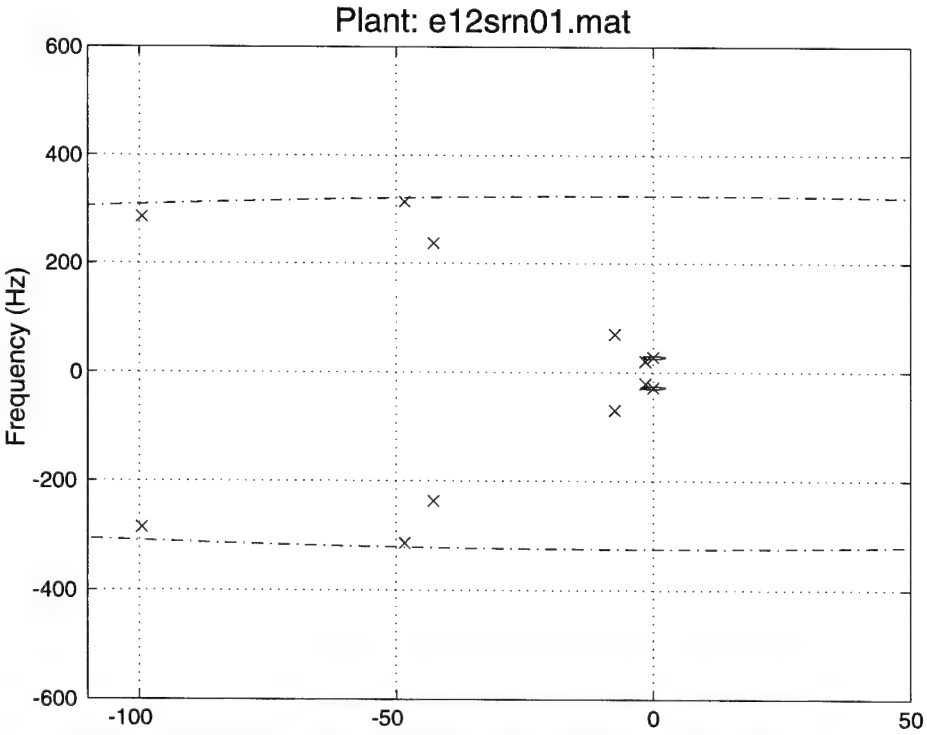

Figure 3.27A Competing Design Plant Model (See details in next title.)

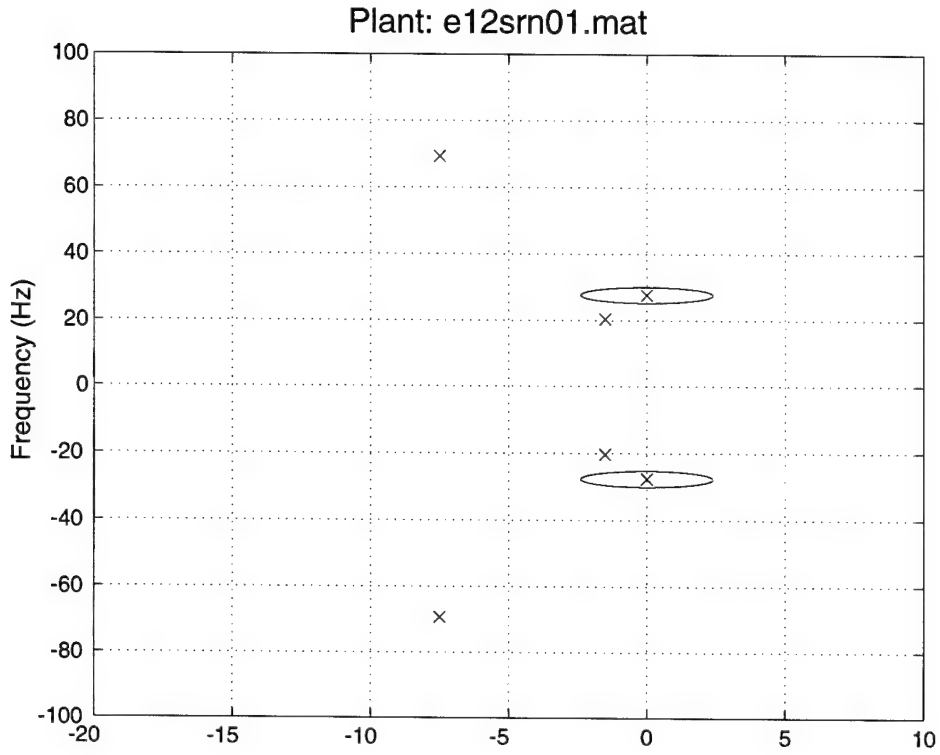

Figure 3.27B Close Up on Critical Modes. Competing Design Plant Model, Based on FORSE Fit. This model actually achieves a lower cost function than the "best model". However, compensators using this plant were not sufficiently tested.

cost function actually indicates improved results with this particular identified model. However, compensators that utilize this model were not tested sufficiently to either continue testing with them or to eliminate them as unsuccessful controllers.

Chapter 4

Robust Dynamic Compressor Compensator Design

4.1 Introduction

To stabilize surge in engines using feedback control, a compensator, or transfer function between measured signals and commanded valve motion, is required. Because of the poorly known dynamics, with closely spaced eigenvalues and non minimum phase zeros, the design of such compensators is a difficult task. This chapter presents the H-infinity approach used in this research effort. A motivation is presented, followed by an overview of the H-infinity procedure. Next, the eigenvalue perturbation H-infinity design is discussed. Finally, the compensator development process for the LTS-101 is detailed.

4.2 Motivation for Robust Design

Previous compensator designs for the helicopter engines have not successfully reduced the massflow at surge for various reasons. The causes of failure are linked to experimental procedure, equipment, and inadequacy of the compensators themselves. Having fixed many of the experimental problems, as detailed in Chapters 2 and 3, one could return to the compensator design procedures previously used. However, many of these procedures also contain deficiencies. To insure project success, these deficiencies are addressed in parallel to improvements in the experimental apparatus.

Table 4.1 lists the control design attempts that were developed for the MIT-GTL helicopter engines in the past. For each method, deficiencies and comments about

Compensation Method	Designer Implementer	Engine	Date	Explanation
System Identification	Corn	LTS-101	July 1996	Matlab Invfreqs.m 10 poles, 2 zeros, 2 transmission zeros
Proportional	Corn Corn	LTS-101	Aug. 1996	No extension of speedline Excited 68 Hz resonance Best Results: Gain = 1.2
Lead Lag	Didierjean Corn	LTS-101	Aug. 1996	Negligible mass flow decrease Excited 2 Hz and 68 Hz modes Slight decrease in 28 Hz PSD
Classical bode Design	Paduano Corn	LTS-101	Aug. 1996	6 poles, 6 zeros Showed promise, but engine difficulties prevented thorough testing. Depressed 28 Hz mode . Did not decrease mass flow beyond instrument error bars
Preliminary H Infinity	Weigl Corn	LTS-101	Aug. 1996	2 poles, 2 zeros Excited a resonance at 20 Hz.
Sliding Mode Control (Upstream Mass Flow)	Didierjean Never Used	LTS-101	Aug. 1996	Engine is inoperable prior to test
Sliding Mode Control (Plenum Pressure)	Didierjean Never Used	LTS-101	Aug. 1996	Engine is inoperable prior to test
System Identification	Al-Essa	Allison 250-C30P	Jan. 1997	Transfer Functions Obtained
System Identification	Bae	250-C30P	Mar. 1997	10 poles, 8 zeros Created using Invfreqs.m in Matlab
Constant Gain	Bae Bae	250-C30P	Mar. 1997	Gain tuned to 20. No change in PSD in semi-vaneless space or scroll sensors Inlet Tap: Slight excitation of 100 Hz acoustic mode, slight stabilization of 30 Hz surge mode
Pole - Zero Placement	Bae Bae	250-C30P	Apr. 1997	5 dB suppression of 100 Hz PSD (which usually triggers surge). However, no extension. 30 Hz excited by 5 dB, caused a surge.
Linear Quadratic Gaussian	Bae Bae	250-C30P	May 1997	Unclear if extended or not. Suppressed 100 Hz at inlet, but maintained 100 Hz at semi vaneless space and scroll. Excited 30 Hz at inlet.
Cancellation	Bae Bae	250-C30P	May 1997	Unclear extension.. Inlet tap: excited 30 Hz, but suppressed 100 Hz. Semi vaneless space: suppressed both modes of interest Scroll: No change.

Table 4.1 Summarization of MIT Testing Prior to 1998.

experimental results are given. Three main deficiencies are addressed in this research. First, a multivariable method is desired to maximize the amount of sensor information used to determine the appropriate control signal. Second, a systematic procedure for obtaining control laws is needed. This method should not require experienced tuning of pole and zero locations, as required by classical design techniques. Finally, an approach with robustness to model uncertainty is desired. Previous experience suggests that introducing robustness to variations in eigenvalue locations yields controllers that are experimentally viable.

This last point deserves extra attention, because it is a central aspect for the chosen control design procedure. Uncertainty of the plant eigenvalues is recognized as a primary robustness issue by Weigl [20]. In high speed axial compressor stabilization experiments, he notes that eigenvalues change significantly with throttle position, rotor speed, and ambient conditions. In the helicopter engines, these changes are also present. Compressible models for surge, presented in Chapter 6, as well as observed behavior in the Allison engine indicate that the important eigenvalues are sensitive to changes in the compressor mass flow rate. In particular, the open loop surge mode is observed to shift from ~30 Hz to 27.8 Hz as the engine is throttled towards surge in the Allied Signal engine. Corn [15] observes that the 65 Hz acoustic mode shifts with changes in nozzle position, and Bae [19] observes similar shifts in the Allison engine. Humidity also appears to effect the engine's behavior. Days with high humidity can cause instability to occur at higher massflows than normal, even when the massflow is corrected with a humidity correction factor.

The requirement for a systematic, multivariable, robust control law design procedure was previously satisfied by Weigl [20] in the context of rotating stall control in a high speed compressor stage. Weigl's design procedure proved very effective and is adopted as the initial

framework for this research. This chapter presents an overview of the design procedure, discussing several topics that are key to understanding the H-infinity control law design procedure applied here. Refer to Weigl [20] and the tutorial by Kwakernaak [33] for a more detailed discussion.

4.3 H-Infinity Control Law Design Overview

Several topics are important to understanding the H-infinity Control law design process. The robust control framework includes plant dynamics, a compensator, and unknown error dynamics (Figure 4.1). The plant dynamics, P(s), include the Allied Signal LTS-101 helicopter engine, inlet ducting, control computer time delays, digital filter lags, and high speed valve actuator dynamics. Recall from chapter 3.6 that the plant dynamics are assumed linear and time invariant. K(s) is the robust compensator and is detailed later. The control scheme is multiple-input, single-output (MISO) for this case. $\Delta(s)$ represents the unknown perturbation dynamics, which are assumed stable. $\Delta(s)$ accounts for uncertainties, such as plant model variation, unmodeled dynamics, and unknown disturbances. The inputs and outputs of $\Delta(s)$ are weighted so that the physical situation is properly modeled when the infinity norm of $\Delta(s)$ is constrained to be less than one. The infinity norm is defined as follows:

$$\|\Delta(s)\|_\infty = \max_\omega \bar{\sigma}(\Delta(j\omega)) < 1 \qquad (4.1)$$

The infinity norm is equivalent the single input, single output (SISO) maximum value of a Bode magnitude plot.

The plant, compensator, and unknown perturbation dynamics interact in the following

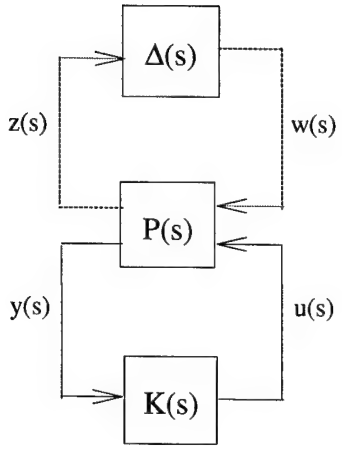

Figure 4.1 Robust Control Problem

feedback manner. u(s) is the control command signal from the MISO control law. y(s) is a vector of measured plant outputs, which are the processed pressure measurements from the Kulites chosen for feedback. z(s) refers to error signals that are deviant from typical plant output. The goal of robust design is to keep these error signals small. w(s) represents various unknown disturbances.

The plant dynamics in Figure 4.1 are easily manipulated into state space form (Doyle et al [34] and Glover [35]):

$$\begin{bmatrix} \dot{x}(t) \\ z(t) \\ y(t) \end{bmatrix} = \left[\begin{array}{c|cc} A & B_1 & B_2 \\ \hline C_1 & D_{11} & D_{12} \\ C_2 & D_{21} & D_{22} \end{array}\right] \cdot \begin{bmatrix} x(t) \\ w(t) \\ u(t) \end{bmatrix} \qquad (4.2)$$

The controller, K(s) is found by solving the controller and observer Riccati equations. Refer to Appendix D for explanation of the H-infinity solution.

The goal of the H-infinity compensator design problem is to establish performance objectives and incorporate these into the definition of z, w, and Δ. In the helicopter engine

application, the objective is to maintain closed loop engine stability at low mass flows (i.e. at massflows that result in surge during open loop engine tests with mean air injection). The weighted mixed sensitivity problem provides one approach that has yielded successful stabilization in other Gas Turbine Lab research applications [20,36,37]. Figure 4.2 displays the weighting transfer functions which determine z(s). Changing these weights shapes the important closed loop transfer functions. The weightings are included in the H-infinity design problem by incorporating them into the plant dynamics (P(s)) prior to solving for the compensator. The three weighting transfer functions in Figure 4.2 are now detailed.

First, $W_1(s)$ shapes the sensitivity transfer function S(s), ensuring that the error between the reference input (r(s)) and the error signal (e(s)) is small. This is important at low frequencies for good low frequency tracking performance. Compressor stabilization is not a tracking problem, so this weighting will be replaced by eigenvalue perturbation circles as described later. S(s) is defined as follows:

$$S(s) = \frac{e(s)}{r(s)} = (I + P(s)K(s))^{-1} \qquad (4.3)$$

Appendix E.1 shows the derivation for S(s) and how to represent it in terms of state space variables. In addition, all general state space manipulations that are used in the derivations are shown in Appendix F. The H-infinity solution assures that the sensitivity transfer function satisfies the following inequality:

$$\left\| W_1(s)S(s) \right\|_\infty < 1 \qquad (4.4)$$

This in turn guarantees that S(s) is constrained as follows:

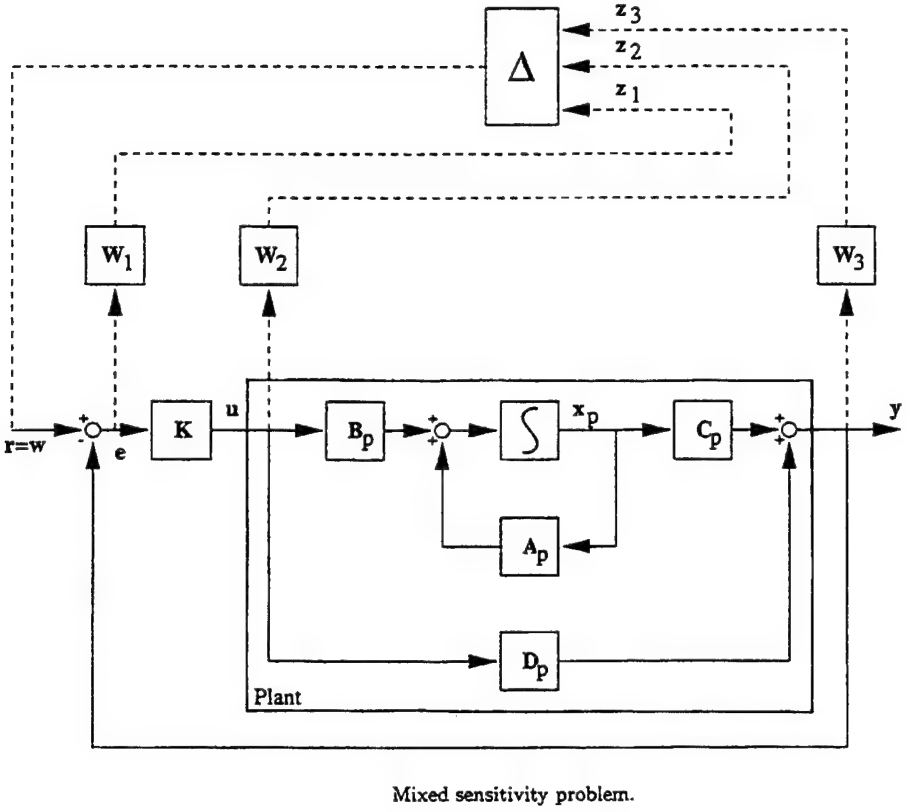

Mixed sensitivity problem.

Figure 4.2 H-Infinity Design: Mixed Sensitivity Approach

$$\bar{\sigma}(S(j\omega)) < \left|W_1^{-1}(s)\right| \qquad (4.5)$$

Second, $W_2(s)$ shapes the controller gain and bandwidth. Controller magnitude should be reduced to avoid actuator saturation. The controller bandwidth is weighted to satisfy limited actuator bandwidth. Appendix E.2 shows the derivation and state space representation for the following actuator transfer function:

$$R(s) = \frac{u(s)}{r(s)} = K(s) \cdot (I + P(s)K(s))^{-1} \qquad (4.6)$$

The H-infinity solution assures that the following inequality is satisfied.

$$\left\| W_2(s)R(s) \right\|_\infty < 1 \qquad (4.7)$$

This inequality guarantees that R(s) is constrained as follows:

$$\bar{\sigma}(R(j\omega)) < \left| W_2^{-1}(s) \right| \qquad (4.8)$$

Finally, $W_3(s)$ shapes the closed loop transfer function from the reference input (r(s)) to the measured output (y(s)). This important transfer function is known as the complimentary sensitivity transfer function (See Appendix E.3) and is defined:

$$C(s) = \frac{y(s)}{r(s)} = P(s) \cdot K(s) \cdot (I + P(s)K(s))^{-1} \qquad (4.9)$$

Again, the following inequality is assumed by the H-infinity solution:

$$\left\| W_3(s)C(s) \right\|_\infty < 1 \qquad (4.10)$$

This ensures that C(s) is constrained as follows:

$$\bar{\sigma}(C(j\omega)) < \left| W_3^{-1}(s) \right| \qquad (4.11)$$

This transfer function reduces the closed loop resonant peaks. $W_3^{-1}(s)$ is rolled off at high frequency to prevent the compensator from exciting higher order acoustic resonances, many of which are neglected in the plant model.

4.4 Eigenvalue Perturbation H-Infinity Design

As section 4.2 states, Weigl [20] implements a variation of the mixed sensitivity H-infinity design problem described above. $W_1(s)$ is replaced by an eigenvalue perturbation weighting scheme [Smith 38]. Refer to Figure 4.3 for a schematic on the mixed sensitivity

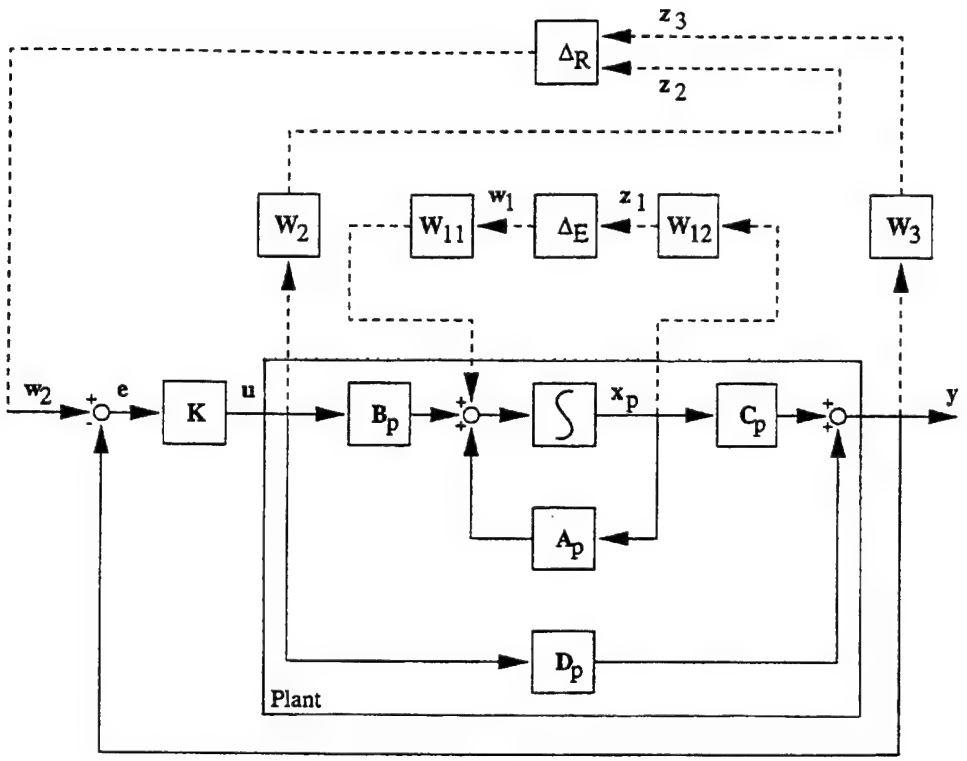

Mixed sensitivity with eigenvalue perturbations.

Figure 4.3 H-Infinity Approach Used to Stabilize the LTS-101

H-infinity design problem with eigenvalue perturbations. This method focuses on the uncertainty in critical eigenmodes prior to surge. Smith develops and proves the technique of including a circular region centered around the desired plant eigenvalues in the H-infinity compensator design process. Using the robust toolbox routines from Matlab, this method designs a compensator that maintains closed loop stability for perturbed eigenvalues anywhere inside the user defined circles. This includes when particular eigenmodes may be open loop unstable as defined by the eigenvalue perturbation circles.

The eigenvalue perturbation circles account for variation in frequency, as determined by the radius of the circle. This problem is well suited for the compressor stabilization

problem. In addition, the scheme's robustness should not destabilize the compressor at high mass flows. For more details about the eigenvalue perturbation design algorithm, refer to [20]. Equation 4.12 displays the resulting augmented plant matrix for the eigenvalue perturbations, as well as the weighting described in the previous section.

$$\begin{bmatrix} \dot{x}_p(t) \\ \dot{x}_2(t) \\ \dot{x}_3(t) \\ z_1(t) \\ z_2(t) \\ z_3(t) \\ e(t) \end{bmatrix} = \left[\begin{array}{ccc|ccc} A_p & 0 & 0 & W_{11} & 0 & B_p \\ 0 & A_2 & 0 & 0 & 0 & B_2 \\ B_3C_p & 0 & A_3 & 0 & 0 & B_3D_p \\ \hline W_{12} & 0 & 0 & 0 & 0 & 0 \\ 0 & C_2 & 0 & 0 & 0 & D_2 \\ D_3C_p & 0 & C_3 & 0 & 0 & D_3D_p \\ -C_p & 0 & 0 & 0 & I & -D_p \end{array}\right] \begin{bmatrix} x_p(t) \\ x_2(t) \\ x_3(t) \\ w_1(t) \\ w_2(t) \\ u(t) \end{bmatrix} \quad (4.12)$$

4.5 Control Compensation Development for the LTS-101

At this point, it is useful to automate the methodology for compensator testing and modification. First, the engine dynamics are loaded. These contain the state space results of the system identification described in Chapter 3.6. This state space system describes the dynamics between the valve command and the chosen set of pressure transducers. Included are the high speed valve dynamics and LTS-101 dynamics, as measured by the Kulite static pressure taps. The plant dynamics are limited to either 10 or 12 internal states. This limitation arises due to compensator implementation considerations. In H-infinity control design, each state in the plant results in a state in the compensator. By limiting the number of states in the model, the implemented compensator size is also reduced. Recall from Chapter 3.6 that the best compensators are designed using the following three outputs: two inlet pressure taps

(designated I01 and I04) and a throat tap (designated T05).

Next, in order to accurately portray the compensation requirements, one must consider other aspects lumped into the plant development. For instance, the control computer contains an associated delay, depending on the size of the implemented discrete compensator matrices. A pure time delay is used to model this delay.

$$D(j\omega) = e^{-s\tau} = e^{-j\omega\tau} \qquad (4.13)$$

The measured magnitude drift in the control is less than -2 dB and is neglected by a pure time delay (Figure 4.4).

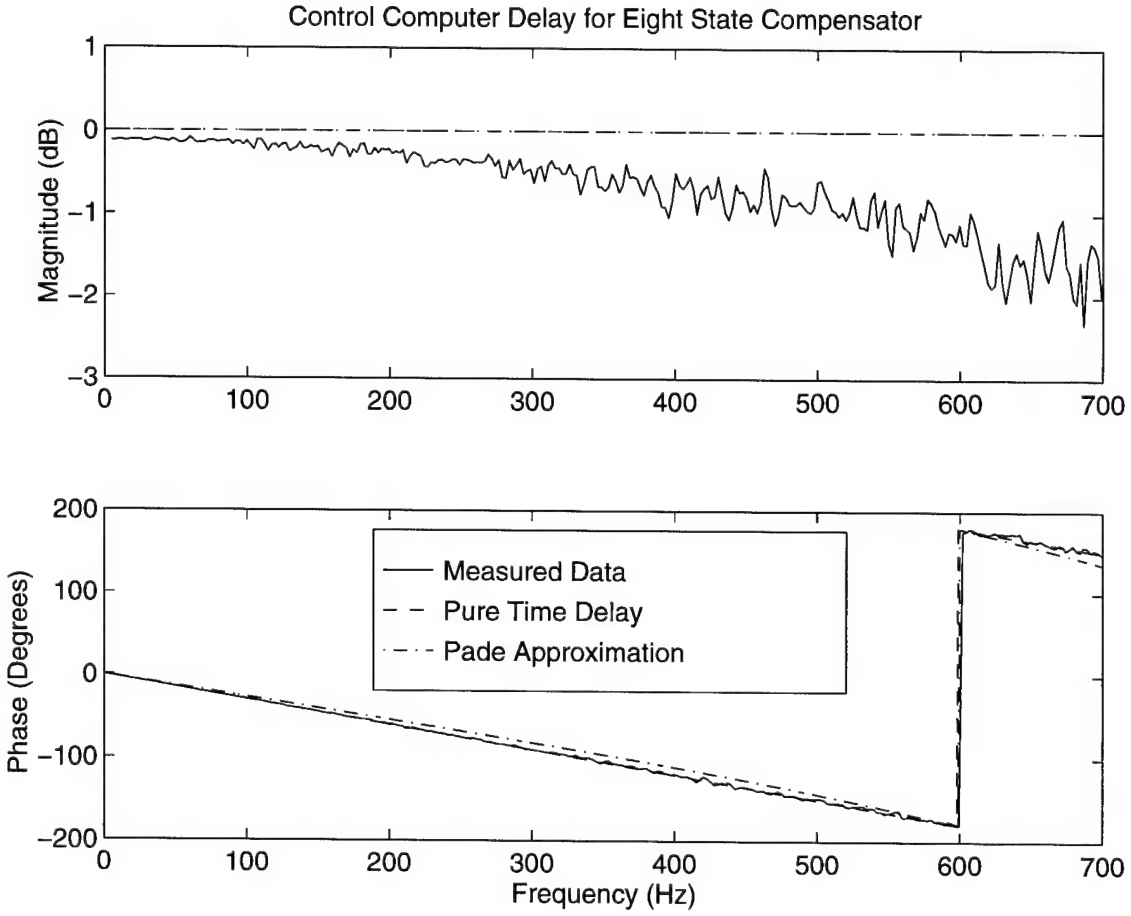

Figure 4.4 Control Computer Delay for Eight State Compensator

The time delay is incorporated into the state space system using a polynomial approximation (Refer to [39] for details). Since the eventual compensator size is limited to fewer than 10 states, a third order Pade approximation is chosen to minimize the number of states needed to represent the pure time delay in the overall system. The Pade approximation is a variant of a power series expansion:

$$e^{-s\tau} \cong \frac{e^{-s\tau/2}}{e^{s\tau/2}} = \frac{1-\frac{\tau}{2}s+\frac{\tau^2}{4\cdot 2!}s^2-\frac{\tau^3}{8\cdot 3!}s^3}{1+\frac{\tau}{2}s+\frac{\tau^2}{4\cdot 2!}s^2+\frac{\tau^3}{8\cdot 3!}s^3} \qquad (4.16)$$

The pure time delay is verified with each implemented compensator design. The following time delay parameter guidelines are used for the initial design iteration (Table 4.2). Because the Pade approximation deviates with frequency, the goal for defining Tau and the correction factor (CF) is to match the phase properties (Figure 4.4).

$$e^{-s\tau} \cong \frac{1-\frac{\tau\cdot CF}{2}s+\frac{(\tau\cdot CF)^2}{4\cdot 2!}s^2-\frac{(\tau\cdot CF)^3}{8\cdot 3!}s^3}{1+\frac{\tau\cdot CF}{2}s+\frac{(\tau\cdot CF)^2}{4\cdot 2!}s^2+\frac{(\tau\cdot CF)^3}{8\cdot 3!}s^3} \qquad (4.15)$$

A high pass filter, shown in Figure 4.5, is also incorporated to remove the DC

	8 State Compensator	9 State Compensator	10 State Compensator
Tau (τ)	.000835	.000845	.001
Correction Factor (CF)	.9	.9	.9

Table 4.2 Time Delay Parameters for Pade Approximation

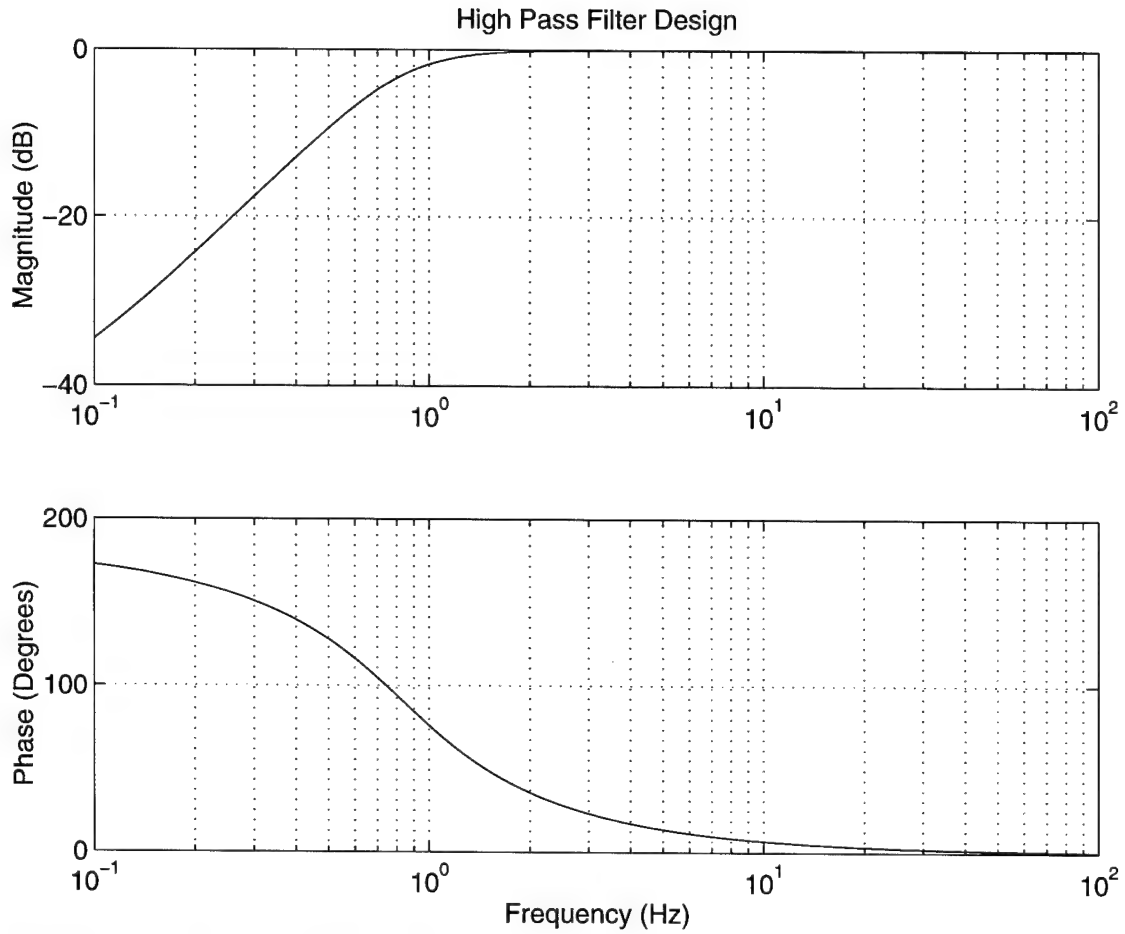

Figure 4.5 Digital High Pass Filter

component of the pressure signals. The design process for these experiments follows predecessor's approaches by neglecting the four state high pass filter during the compensator design. The rationale is to avoid using some of the compensator states to balance the high pass filter poles at very low frequencies. The consequences of this design decision are detailed in Chapter 5.5. The compensator worked; however, the high pass filter may induce a low frequency surge that sometimes occurs while at normally open loop stable operating points. The high pass filter produces a 90° phase shift at 1 to 2 Hz, while depressing the magnitude only ~-4 dB.

At this point, the design code perturbs the plant. Engine runs with mean air injection indicate 28 Hz surge precursors, followed by a surge cycle at this frequency. To represent the neutrally stable plant, the eigenvalues associated with the surge mode are shifted to the neutral axis, as shown in Figure 4.6. After the user defined weights are assigned (including the radii of the eigenvalue perturbation circles), a mixed sensitivity H-infinity design satisfies the constraints and stabilizes the perturbed plant. It is important to note that the continuous time compensator is the same size as the augmented plant, which includes the weighting states. Generally, seventeen to nineteen states define the continuous time compensator for the LTS-

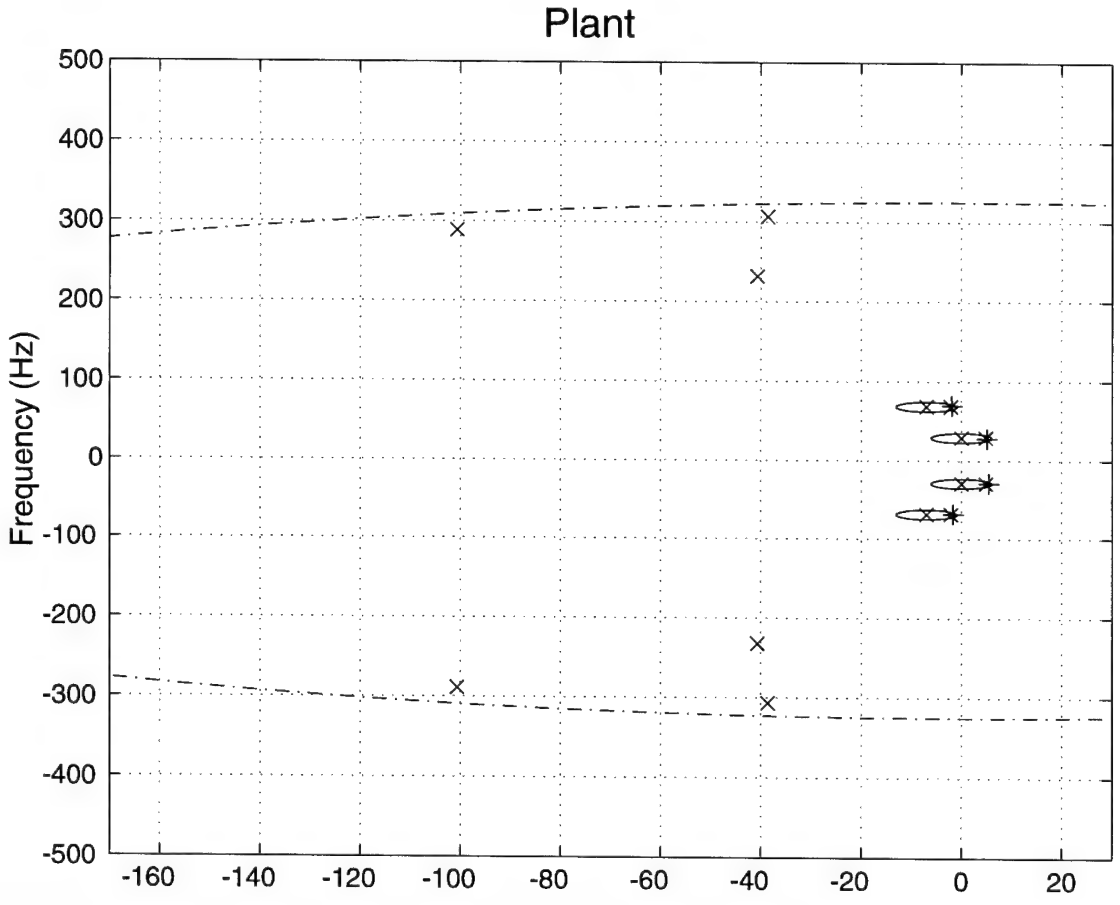

Figure 4.6A Perturbed Plant, Including Eigenvalue Perturbation Circles
Note: * indicates a perturbed mode.

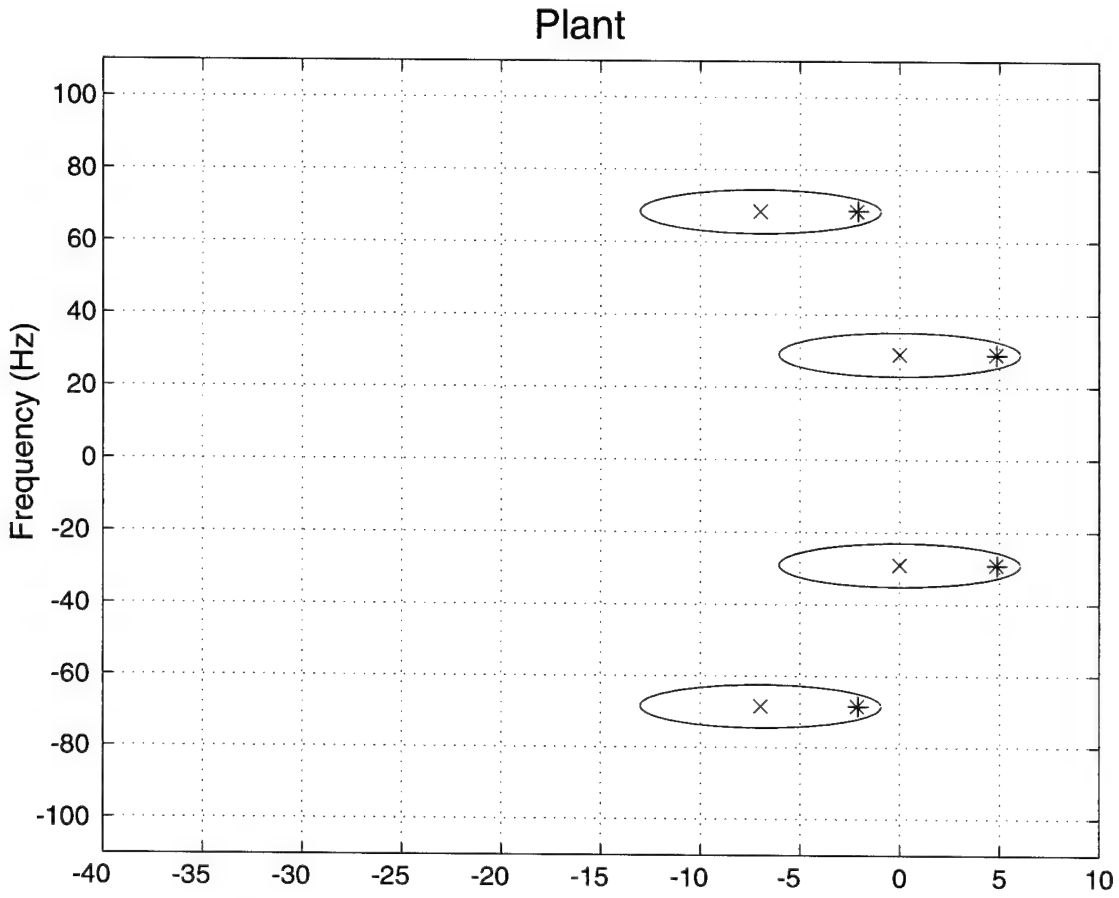

Figure 4.6B Perturbed Plant: Focus on Surge Mode and First Acoustic Mode.
Note: The ∗'s near the edges of the perturbation circles are perturbed eigenvalue locations, used to test the robustness of a designed compensator.

101, depending on the initial size of the plant dynamics matrices (Table 4.3). The final best continuous time compensator design is shown in Figure 4.7. Figure 4.8 shows the continuous time compensator pole-zero map.

The methodology for determining weighting values depends on the particular compensator design emphasis. The author found two goals drove the designs: 1) Maximize the radius of the perturbation circles around the eigenvalues in order to keep these modes closed loop stable over a large range of massflows. 2) Minimize the surge mode closed

loop peak by attempting to make the most stringent W3 weightings for the design. A trade off exists between increasing perturbation circle size (W1) and decreasing W2 and W3. Successful compensators are designed with both approaches; however, the best design focuses on maximizing the W1 perturbation circle around the surge mode and first acoustic resonance

Contribution to Size of Augmented Plant	Number of States
Plant Dynamics (as Identified)	10 or 12
Control Computer Delay (Pade Approximation)	3
High Pass Filter (4 States)	0
W_3 weightings (one first order lead lag per output)	3
W_2 weighting (one first order lead lag per input)	1
Total	17 or 19

Table 4.3 Augmented Plant State Size

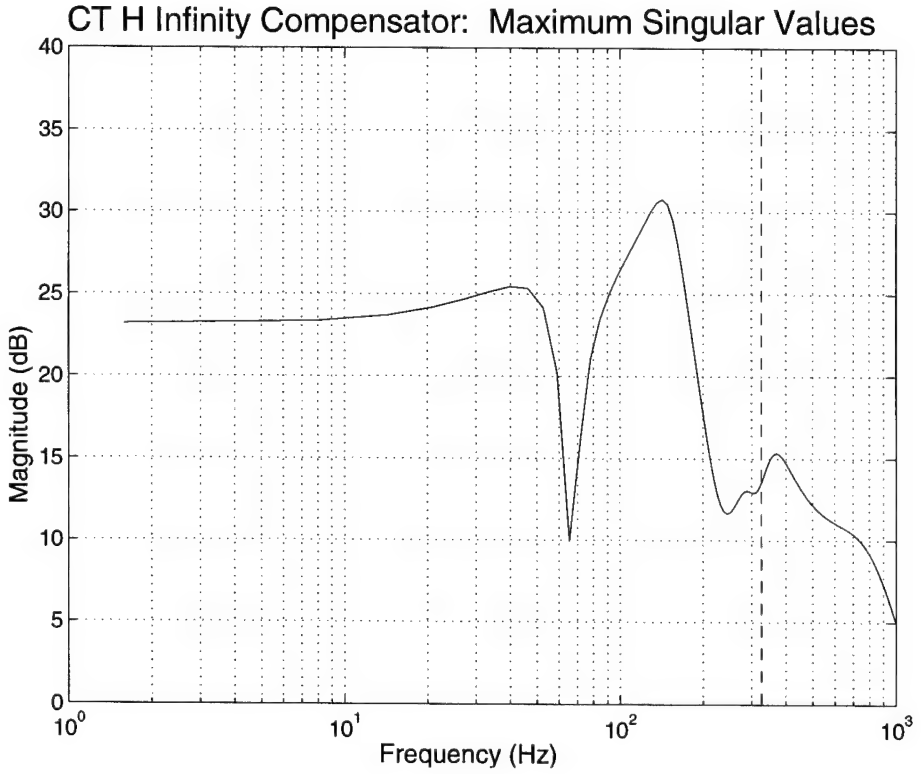

Figure 4.7 Continuous Full State H-Infinity Compensator. Maximum Singular Values of the Transfer Function Matrix.

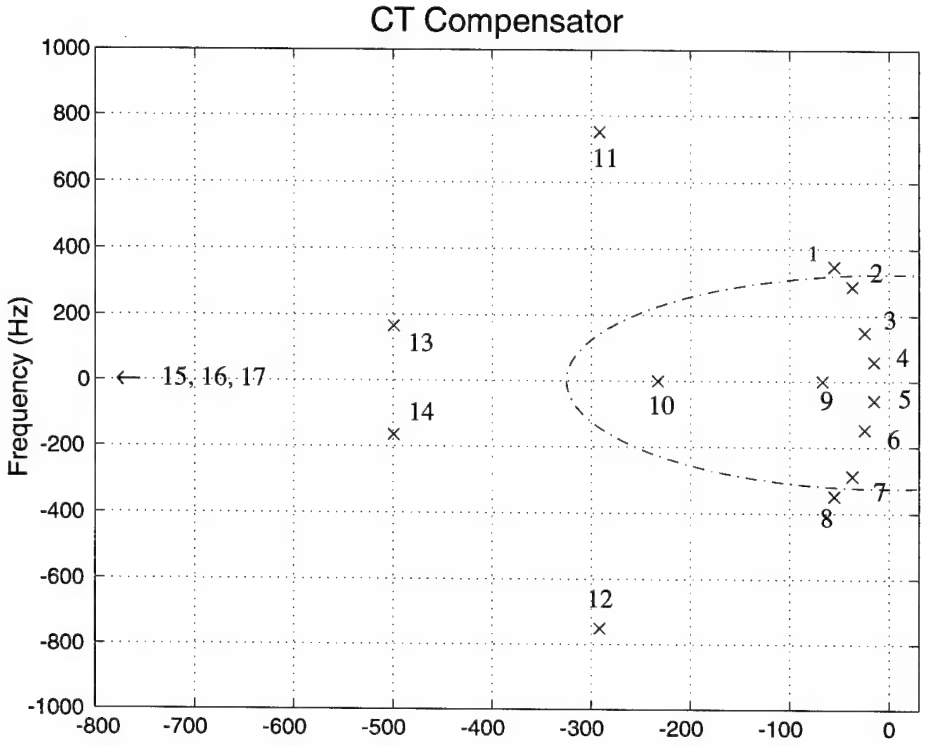

Figure 4.8 Full State Continuous Compensator Pole Zero Map.

(~68 Hz).

The next step in the design process involves plotting three important transfer functions with respect to the weighting parameters, W1, W2, and W3. Recall from Chapter 4.2 that the sensitivity transfer function, S(s), shows the relation between reference input and error signal (Figure 4.9). This transfer function satisfies the W1 constraints via the eigenvalue perturbation circles. R(s) describes the relation between reference input and control command output, and must remain below the W2 constraint (Figure 4.10). The complimentary sensitivity transfer function, C(s), describes the relation between the reference input and measured output (Figure 4.11). W3 bounds this transfer function.

When the design is only barely able to meet the design constraints, the robust control toolbox in Matlab displays an inconsistency. The code indicates that it has found an optimal

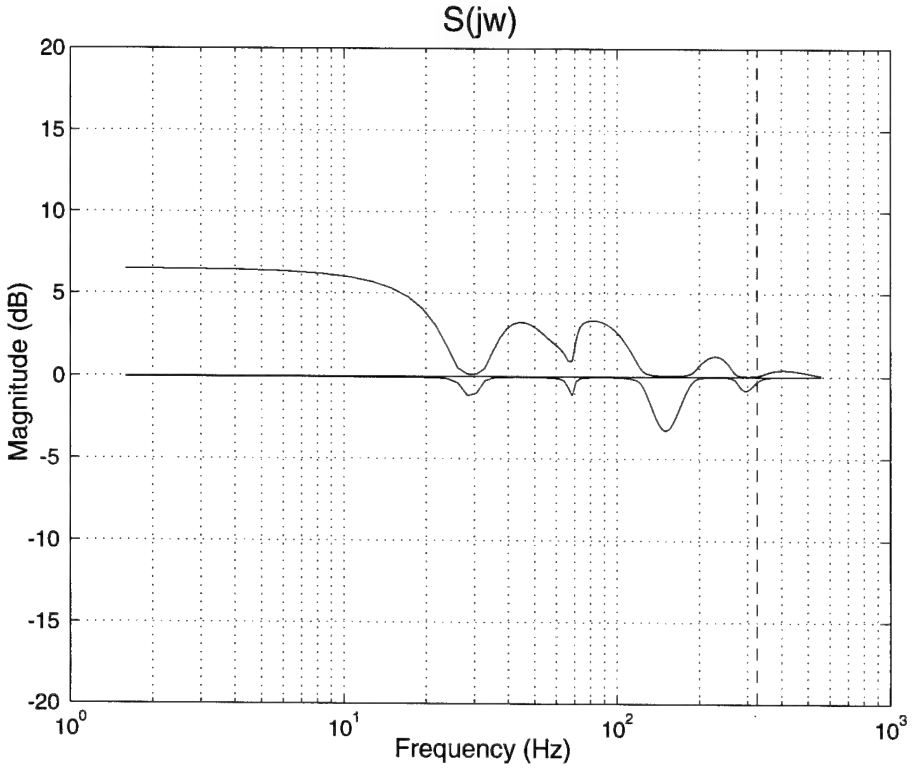

Figure 4.9 Sensitivity Transfer Function.

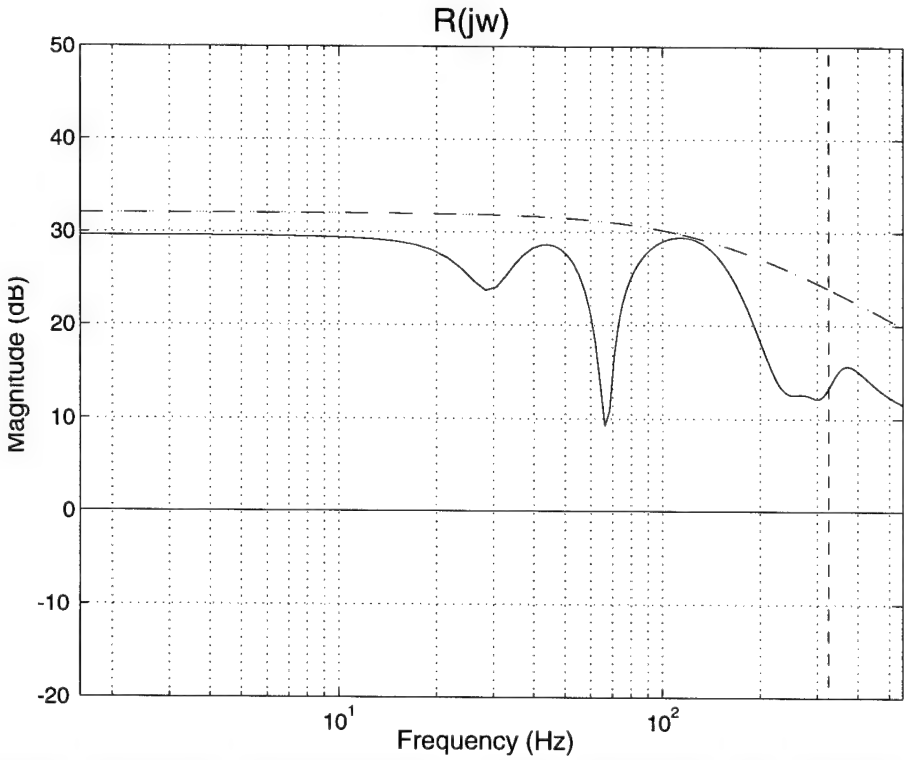

Figure 4.10 Actuation Transfer Function (solid): Shaped by W2 (dashed).

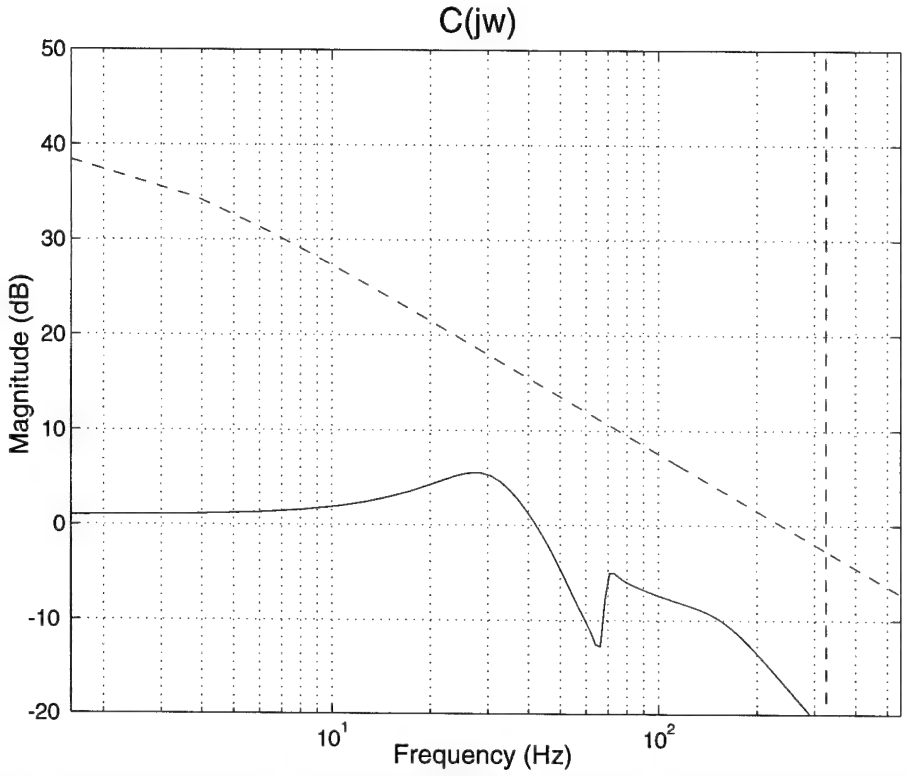

Figure 4.11 Complimentary Transfer Function (solid): Shaped by W3 (dashed).

controller that satisfies the W1, W2, and W3 weighting constraints; yet, when the transfer functions are plotted prior to state reduction, they may fail to satisfy the constraint. In order to adjust for numerical misbehavior within the robust toolbox, constraints are loosened to assure that a valid compensator is found.

The final step in the continuous time domain is to verify that the closed loop eigenvalue real parts are all negative, indicating stability. Figure 4.12 shows the closed loop eigenvalues of the best continuous time compensator with the plant. Notice that all poles are in the left hand plane, indicating stability.

As indicated in earlier segments, the control computer limits the number of states in the implemented compensator. The maximum allowable discrete time compensator state

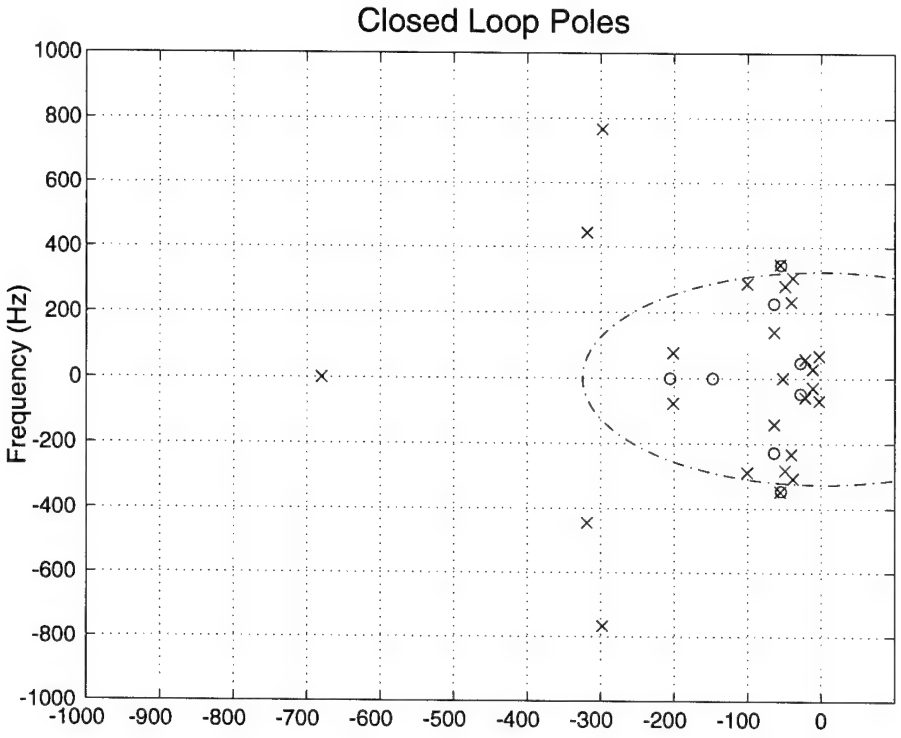

Figure 4.12 Closed Loop Poles and Zeros with Continuous, Full State Compensator Note that all poles are stable "Worst Case" open loop eigenvalues are used for this plot (See Figure 4.6)

matrix size is 10 x 10. However, the best results were obtained from 8 and 9 state compensators, with a decreased control computer delay. The user defines the number of desired discrete compensator states after viewing the Hankel singular values (Figure 4.13). The reduced state, discrete compensator is plotted versus the full state, continuous time compensator to see how well the maximum singular values match (Figure 4.14). The frequencies less than the 330 Hz actuator bandwidth are important.

As a final step, the reduced state, discrete compensator should satisfy the weighting constraints. First, the discrete compensator implementation is modeled in the continuous time domain. Figure 4.15 displays the full state compensator with the reduced state, prewarped continuous compensator. Then, the appropriate state space matrices are manipulated to plot

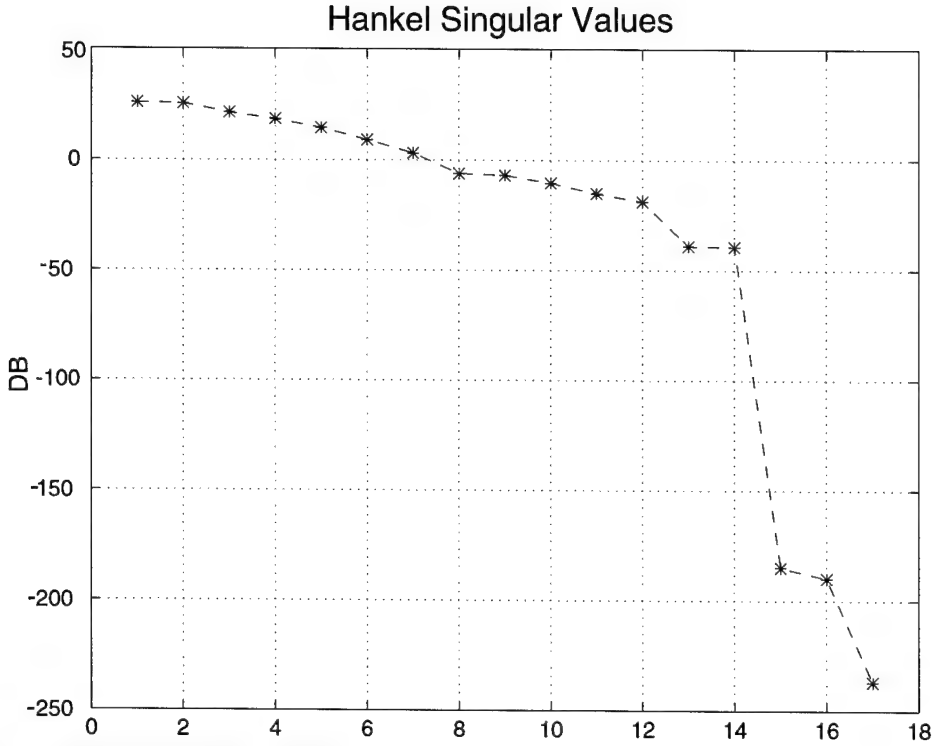

Figure 4.13 Hankel Singular Values

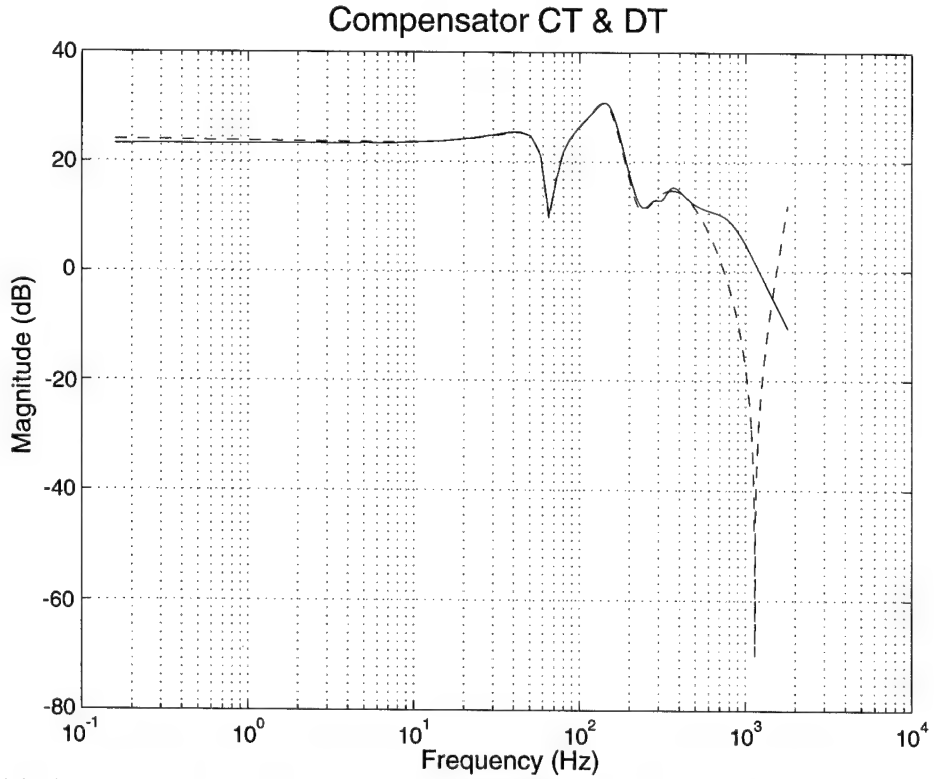

Figure 4.14 Compensators: - Full State Continuous - - Reduced State Discrete

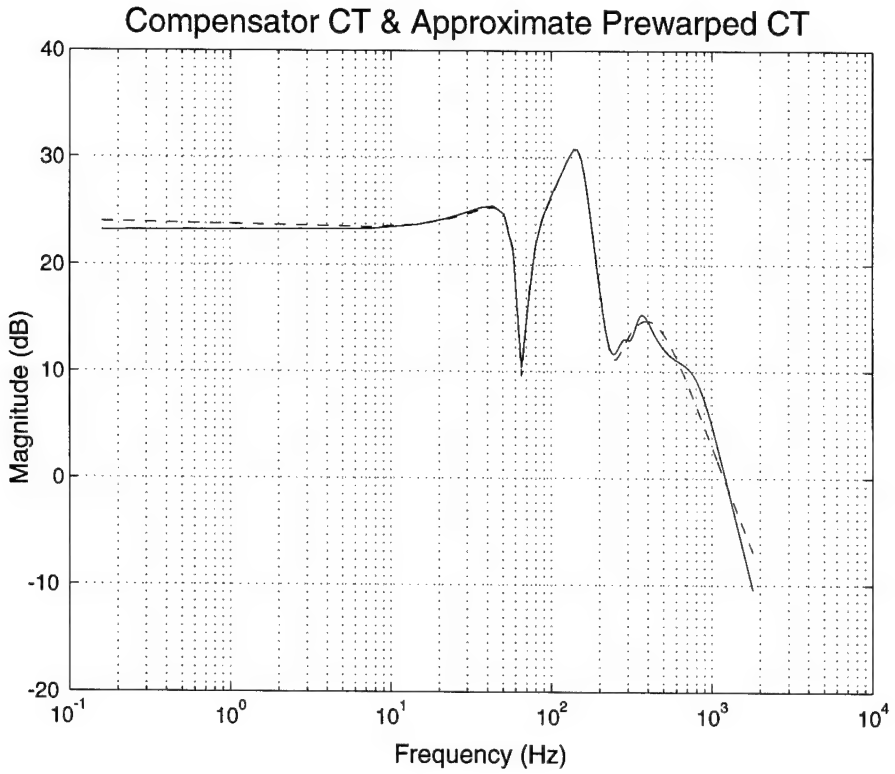

Figure 4.15 Continuous Time Compensators: - Full State - - Prewarped Reduced State

the various transfer functions of interest (Figure 4.16). The final check is to ensure the closed loop eigenvalues are stable. Figure 4.17 contains the pole-zero map of the closed loop system with perturbed plant and the reduced state, digitally implemented compensator. Note that the digitally implemented compensator is reconverted to the continuous time domain for the plot.

At this point, the design is implemented in a FORTRAN control algorithm. To check the implemented compensator design, the HP63365 spectrum analyzer performs a continuous sinusoidal frequency sweep between 5 and 1000 Hz to assure that the control implementation works correctly. Figure 4.18 shows the prescribed pressure transducer to valve command transfer function. The primary implemented design consideration is that the control computer

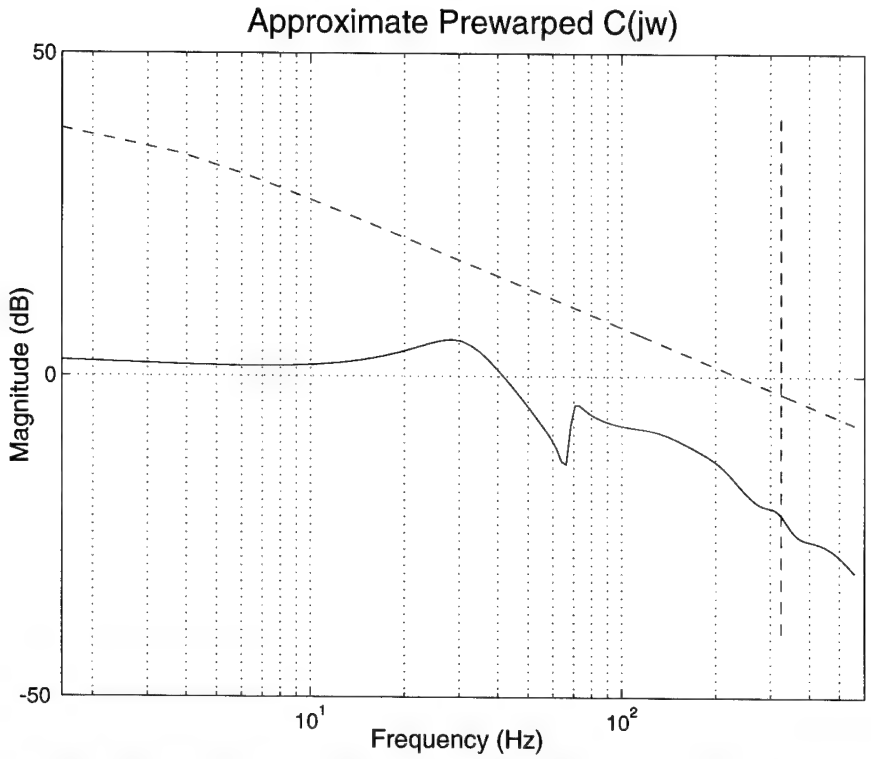

Figure 4.16 Complimentary Sensitivity Transfer Function with Prewarped Continuous Compensator.

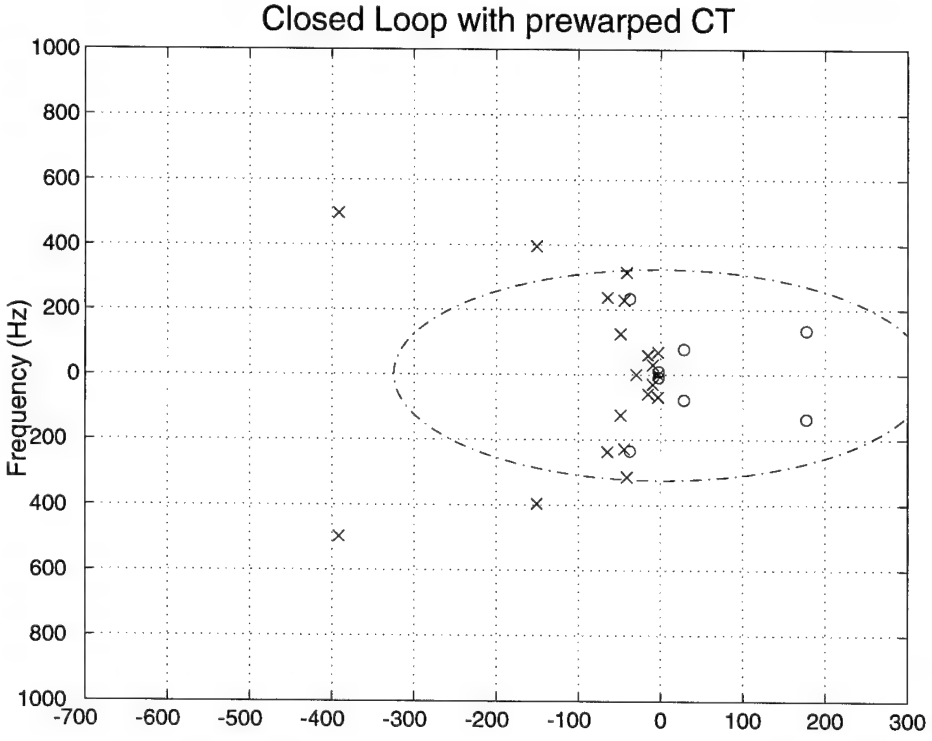

Figure 4.17 Closed Loop System Identification with Prewarped Continuous Compensator

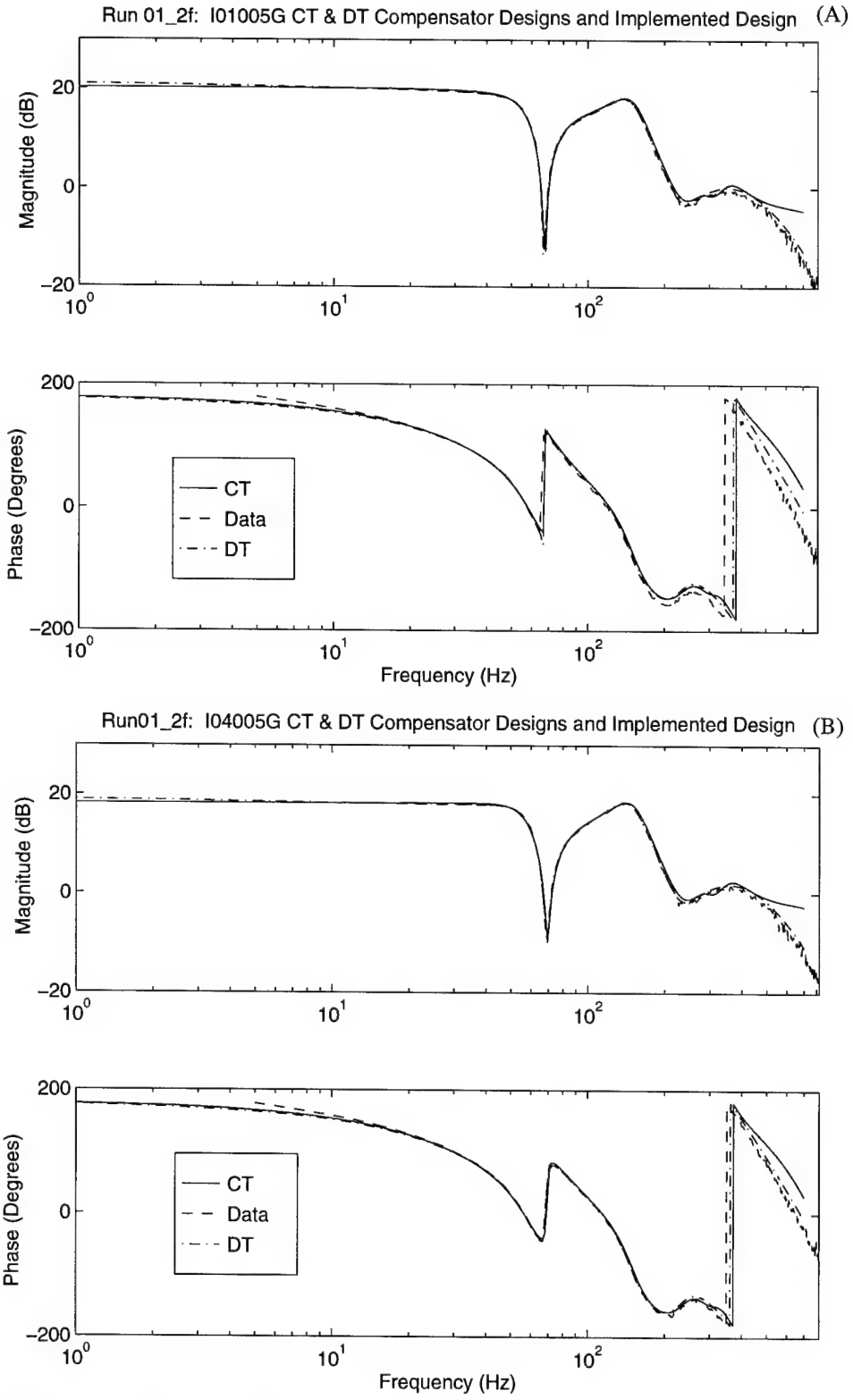

Figure 4.18A, B Continuous, Discrete, and Implemented Compensators: Inlet Taps.

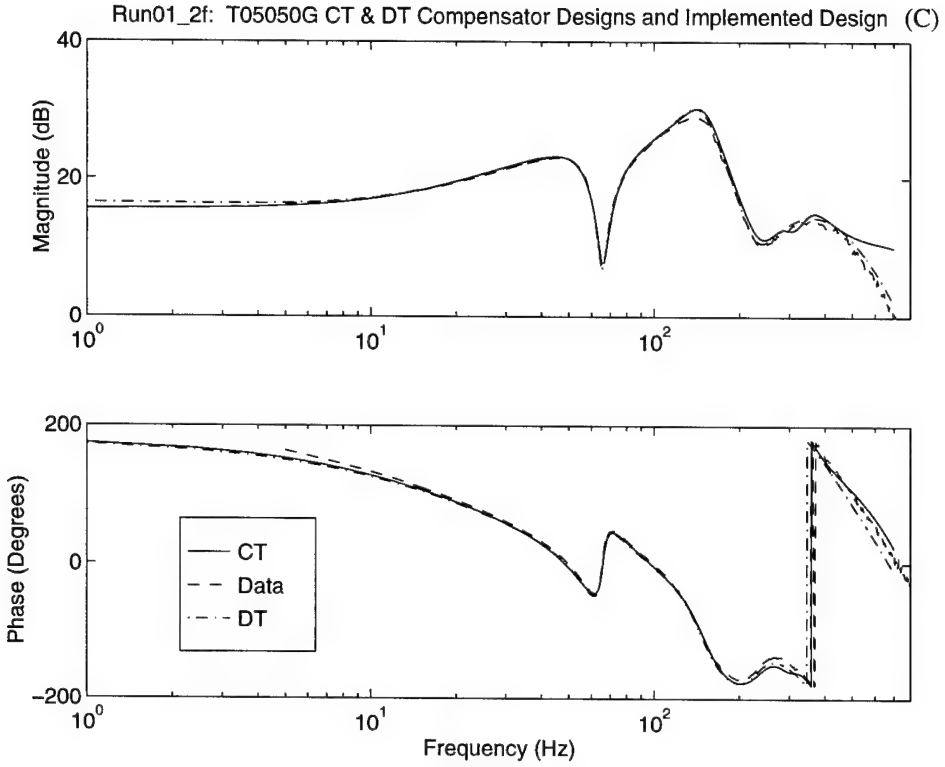

Figure 4.18 C Continuous, Discrete, and Implemented Compensator: Throat Tap

has difficulty matching large compensator peaks. Therefore, peaks are reduced by repeating the design process with loosened weighting constraints.

The H-infinity design process involved several iterations to satisfy all constraints. Table 4.4 summarizes this procedure. In order to thoroughly exhaust design ideas, fifteen H-infinity compensators were created and available for testing. Because of lengthy test time requirements, seven designs were experimentally implemented. Three compensators reduced corrected massflows below the open loop surge point. Chapter 5 summarizes the experimental results.

Steps in the Design Process:
1. Create the desired transfer functions via forced response testing.
2. Perform system identification to fit a state space representation to the experimental data. This is done for up to three user selected outputs.
3. Truncate the state space representation if necessary to obtain the design plant model.
4. Limit the system identification eigenvalues if necessary, based on knowledge of the LTS-101 rig set up.
5. Adjust eigenvalue locations to represent conditions just prior to open loop surge. This usually involves moving the 28 Hz eigenvalues to the $j\omega$ axis.
6. Select a weighting emphasis.
7. Define the size of the eigenvalue circles for all eigenvalues that are considered uncertain.
8. Define the W2 weighting to shape the actuator transfer function.
9. Define the W3 weighting to shape the complementary sensitivity transfer function.
10. After the written script defines a stable compensator, check the important transfer functions to assure they satisfy the weighting constraints.
11. Assure that all eigenvalues of the closed loop system is stable.
12. Discretize and reduce the number of compensator states, based on the Hankel Singular Values.
13. Assure that the reduced order, discrete compensator maximum singular value plot aligns closely with the full state compensator maximum singular values (MSV) plot. Assure that the prewarped reduced compensator MSV plot aligns with the full state

MSV plot.
14. Assure that the weight constraints are satisfied with the reduced order compensator.
15. Assure that the eigenvalues for the closed loop system with discretized compensator is stable.
16. Implement the compensator, and assure that the implemented design matches the desired theoretical design. This sometimes requires reducing large compensator peaks if necessary.
17. Plot the implemented control computer delay, and assure that time delay constant (τ) matches the one used in the design.

Table 4.4 Steps in the H-Infinity Design Process.

Chapter 5

Closed Loop Engine Behavior

5.1 Introduction

The primary goal of active control is to reduce the stalling compressor corrected massflow beyond the open loop surge line. This extension of the operating envelope results in an increase in engine thrust. Two metrics are used to quantify the performance benefits of active control: 1) corrected massflow and 2) thrust. The first metric is the reduction of the compressor massflow beyond the open loop surge point, with other operating conditions held constant. A 1% reduction in the total engine massflow is considered significant. However, the calculated operating point can vary from day to day, depending on weather conditions, by as much as 1%. Therefore, multiple open and closed loop speedline measurements are obtained multiple times during the same test period. To measure the second metric, the test facility is equipped with a 2000 lb load cell that measures the force produced by the exhaust air traveling through the variable area nozzle. An increase in force correlates to an increase in turbine output power.

This chapter presents results from the first successful implementation of active control on a helicopter engine. The first section discusses experiments with this controller. The test results exhibited some important features and were used to motivate subsequent changes to the H-infinity control laws. The main compensator design changes are discussed in section two. In addition, this section presents the data showing the improvement in experimental performance. The third section explains one sided blowing with the best H-infinity

compensator and offers an explanation for the improved results. Finally, design shortcomings which degrade the closed loop performance are discussed.

5.2 First Successful Range Extension

This section details the first success in controlling the engine and reducing the compressor massflow. After several unsuccessful attempts, an H-infinity compensator was able to demonstrate a massflow reduction. Because of the exploratory nature of these baseline tests, the test procedure used differs from other tests. The procedure is as follows: with the engine operating at compressor massflow rates near the open loop surge point, the compensator was turned on. The linear actuator position was extended a small amount, reducing the exit nozzle area. After the engine stabilized at this new operating point, the compensator was turned off and the engine was monitored for surge precursors. This procedure for slowly stepping down the nozzle area was repeated until the engine was successfully "dropped into a surge." At the final closed loop stable operating point, the engine surged ~12.1 seconds after the controller was turned off. The compressor exit map shows the operating range extension for this test (Figure 5.1). The compressor exit massflow is the sum of the massflow measured at the inlet and the mass addition with injection.

The waterfall plots in Figure 5.2 show the time period before and after the compensator was turned off at the run's lowest corrected massflow. The inlet pressure taps (Figure 5.2A) show that the surge mode (27 Hz) is suppressed until the compensator is removed at -900 milliseconds. Note that this closed loop design shows an excited acoustic resonance at ~68 Hz. The vane plenum tap accents this acoustic mode excitation (Figure 5.2C).

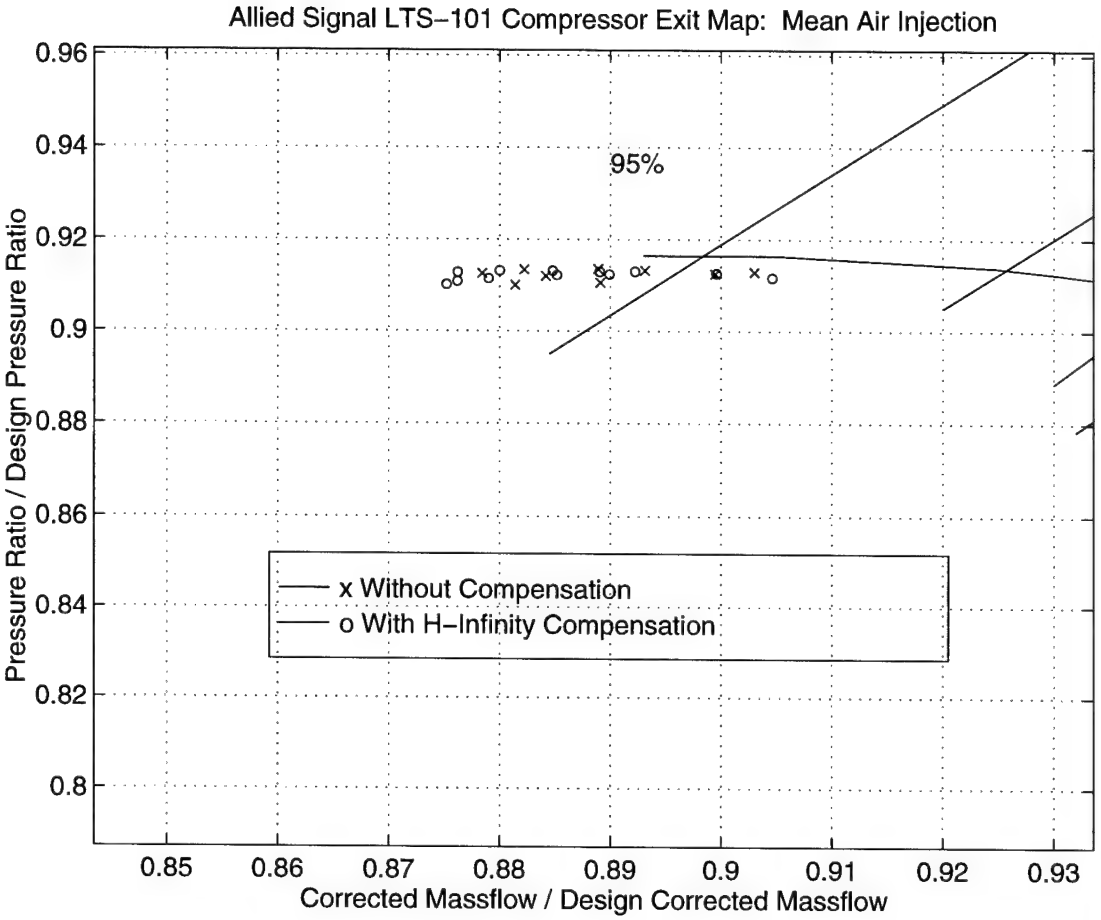

Figure 5.1 LTS-101 Compressor Exit Map: First Massflow Reduction with Compensator

Figures 5.3, 5.4, and 5.5 show the vane plenum pressure power spectral density for the time increments approaching and immediately prior to the open loop surge. All pressure tap PSDs are included in Appendix G for these same loading conditions. Again, these plots show acoustic excitation (68 Hz, 150 Hz, 250 Hz). The vane plenum tap also indicates a low modal excitation, with a frequency well below the surge mode. Due to this additional excitation, the performance of this original compensator is limited and requires redesign.

The valve command and valve position PSDs show that the feedback compensation technique channels energy into the acoustic modal frequencies (Figure 5.6). The largest peak

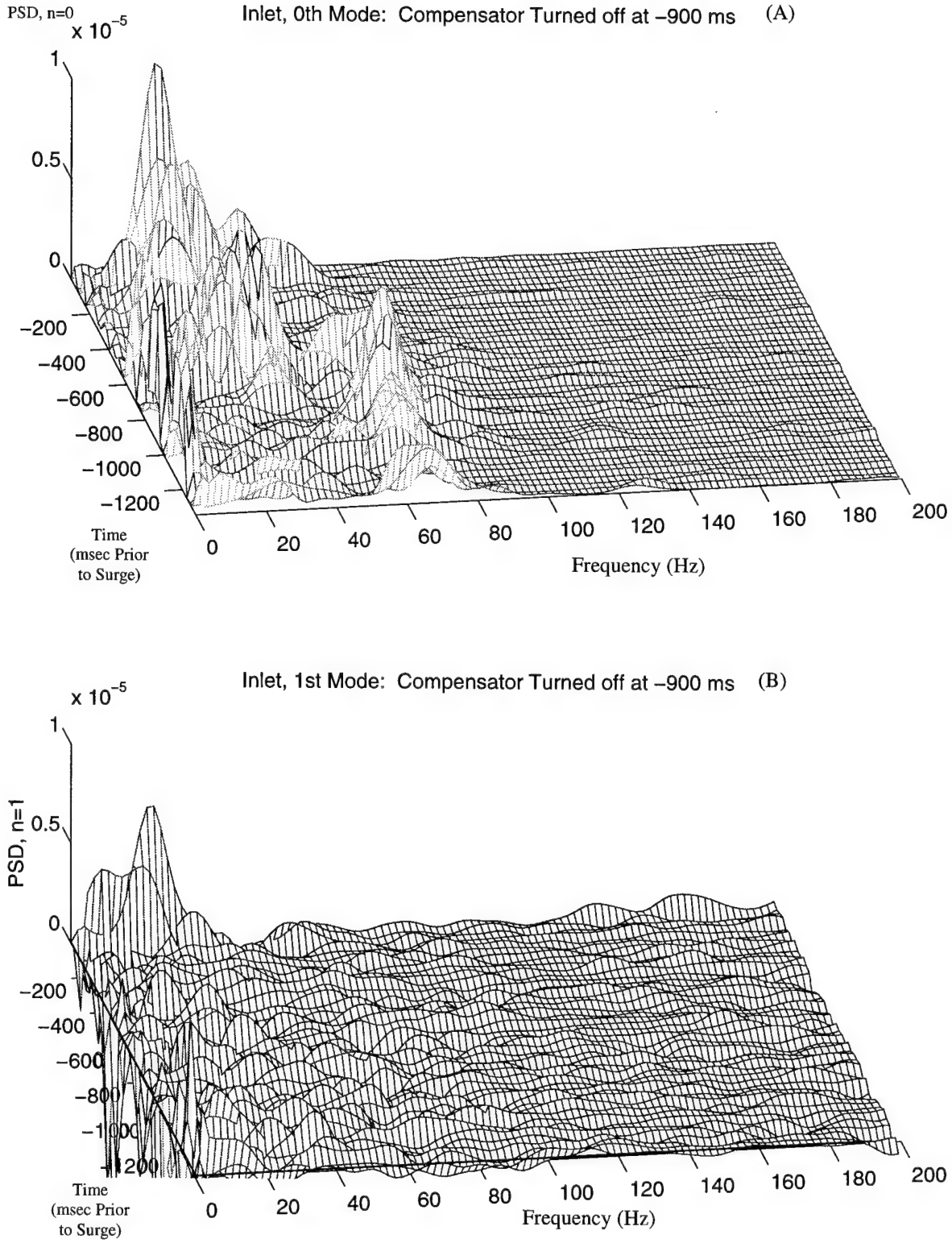

Figure 5.2A, B Waterfall Plots of First Successful Extension. Compensator Removed.

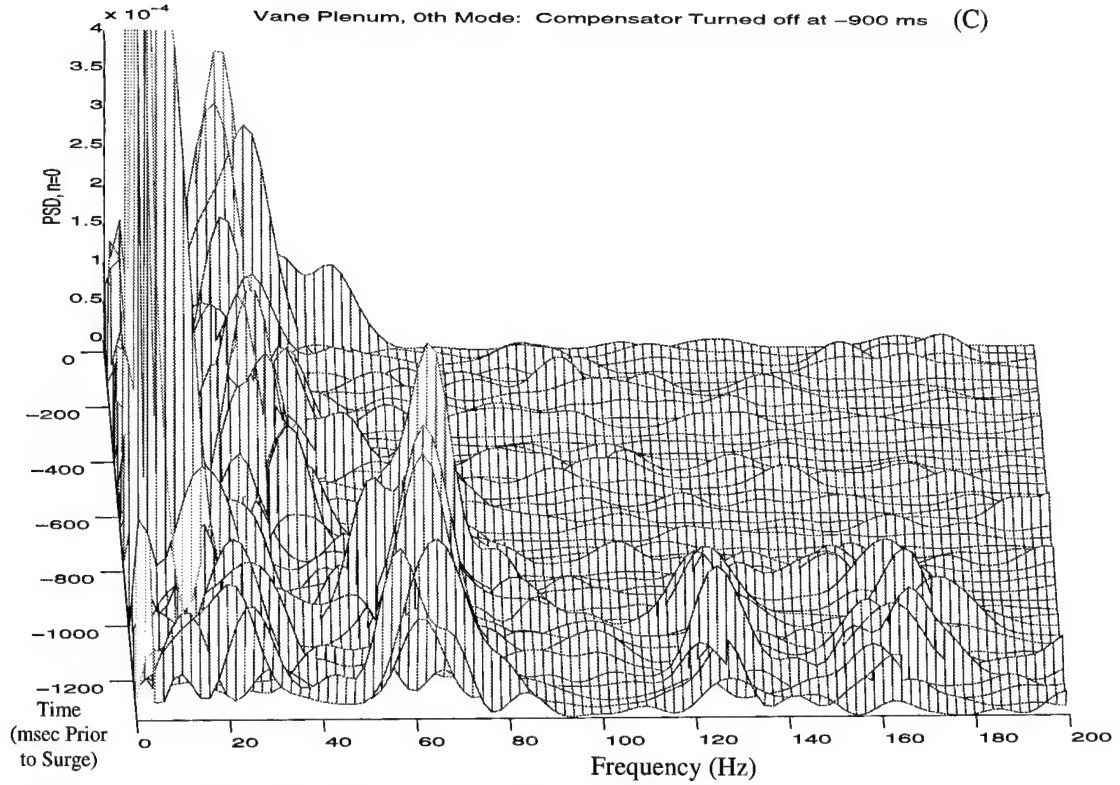

Figure 5.2C Waterfall Plots of First Successful Extension. Compensator Removed

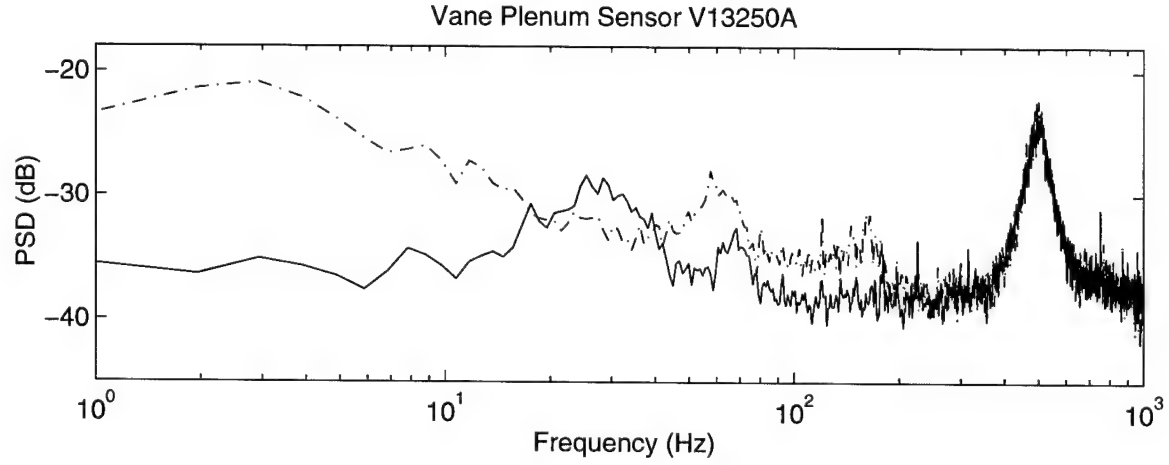

Figure 5.3 Power Spectral Density at a Load of ~ 1180 lb Force.
Note: the solid line indicates open loop PSD, while the dash pot line is for the closed loop case

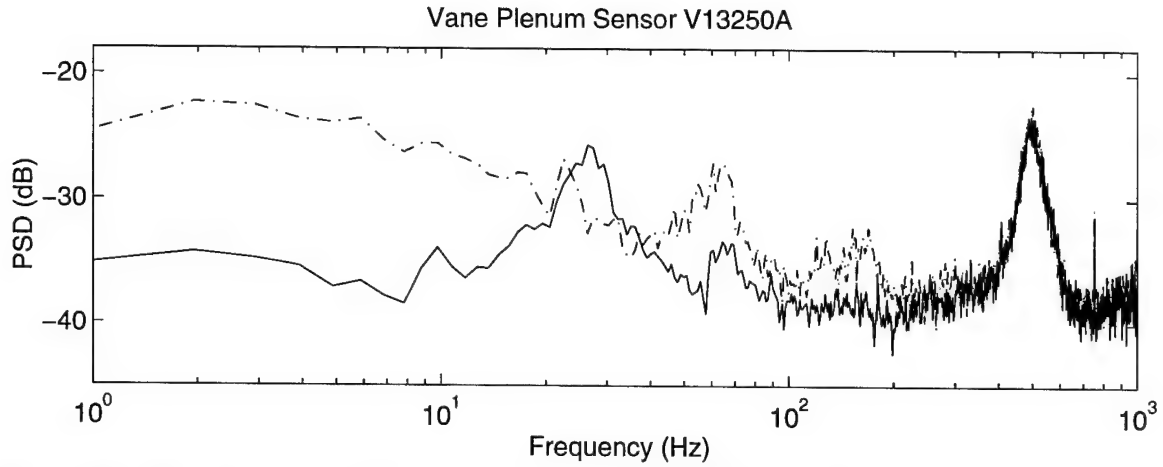

Figure 5.4 Power Spectral Density at a Load of ~ 1190 lb Force.
Note: the solid line indicates open loop PSD, while the dash pot line is for the closed loop case

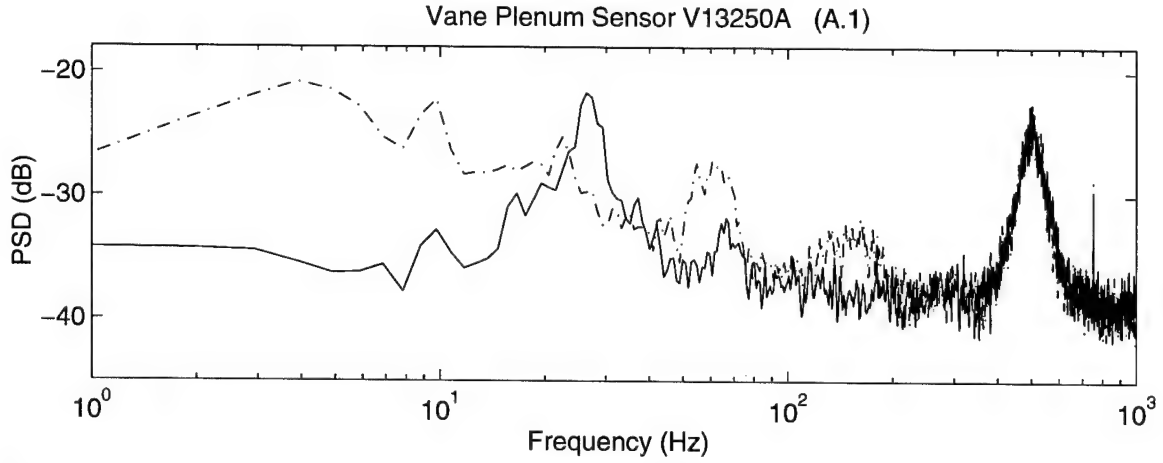

Figure 5.5 Power Spectral Density at a Massflow Immediately Prior to Open Loop Surge.
Note: the solid line indicates open loop PSD, while the dash pot line is for the closed loop case

occurs at 68 Hz, while another distinct peak occurs at ~160 Hz. Bae's [19] results indicate that acoustic resonances can trigger deep surge cycles during feedback stabilization attempts on the Allison 250 helicopter engine. Brian Corn also records a surge triggered by the first acoustic resonance during forced response testing [40]. Therefore, the experimental performance described here indicates that acoustic resonances are significant and can trigger

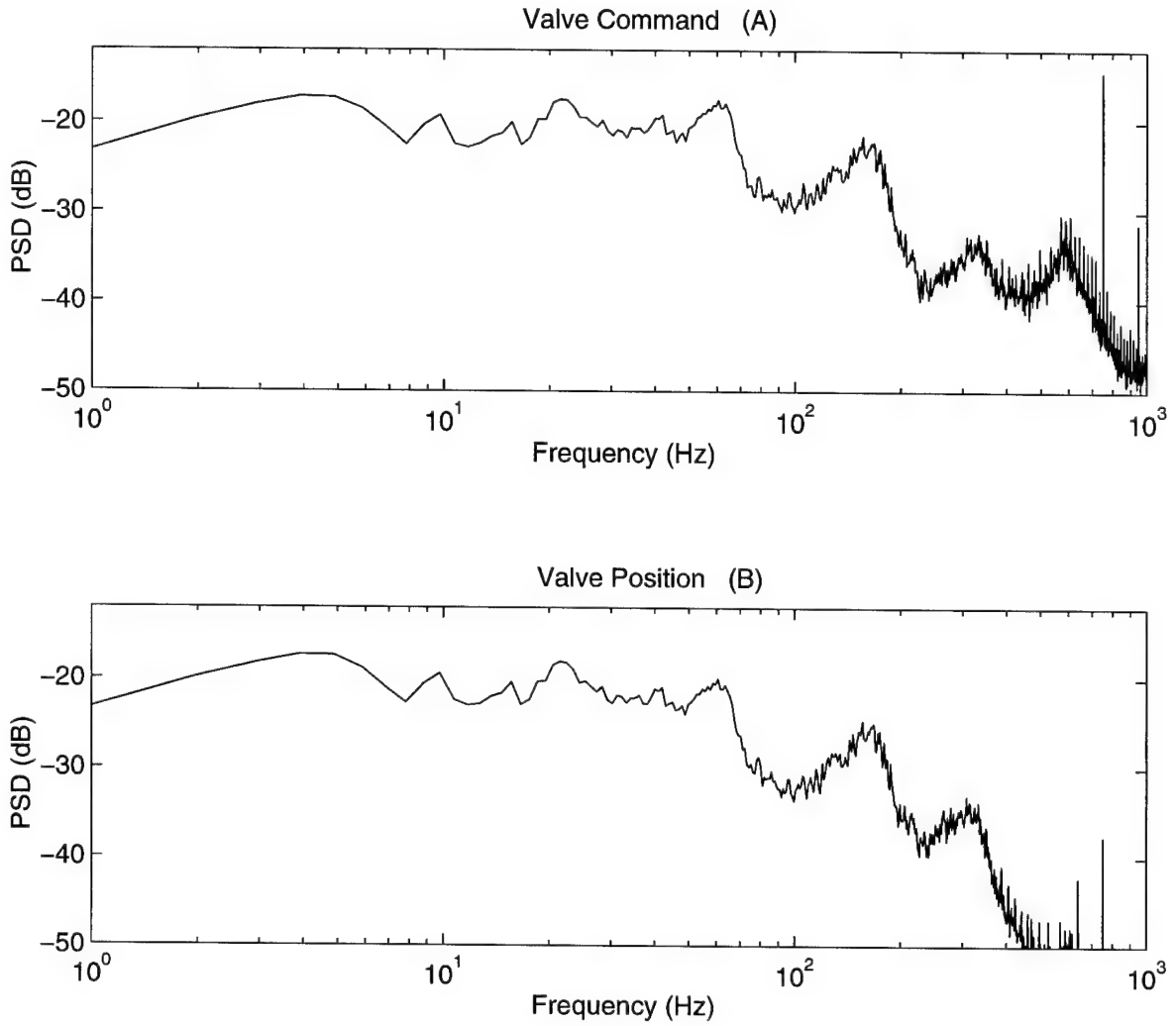

Figure 5.6 Power Spectral Density of Valve Position and Valve Command for Closed Loop Case at Operating Point That is Open Loop Unstable.

surge if excited by injection.

Based on this evaluation and the observed 68 Hz mode for the closed loop PSD (See Figure 5.5), a compensator redesign was required which specifically targets the 68 Hz mode. On the other hand, the 150 Hz mode in Figure 5.6 appears relatively stable in Figures 5.4 and 5.5, even with relatively large sinusoidal excitation. FORSE (which is explained in Chapter

3.6) results agree with this experimental observation, fitting a relatively well damped eigenvalue to the 150 Hz mode. In fact, during plant model order reduction to 10 or 12 states, the FORSE code actually removed the mode from the 150 Hz region because it is so stable. The engine test results support the FORSE cost function analysis regarding the stability of the 150 Hz mode. Recall from Chapter 4.4 results (Specifically, Figure 4.15 and 4.18) that the compensator exhibits its largest peak at 150 Hz; yet, the engine is not driven unstable by this excitation. Therefore, the goal in redesign is to prevent destabilization of this 150 Hz mode, but not to attempt to increase its damping. On the other hand, the 68 Hz mode is treated as a mode where damping can become very light and which can go unstable due to improper feedback.

5.3 Best H-Infinity Design

Several compensator redesign iterations were completed, but only the results from the design with the best performance are discussed here. The development of the best H-infinity compensator is discussed in Chapter 4.4. The PSDs shown in Figure 5.7 demonstrate the surge mode suppression at the operating point with lowest open loop corrected massflow. Note that the compensator does not excite the first acoustic resonance at 68 Hz. Also note that much of the compensation energy channels into a 150 Hz peak in the compensator, as indicated in Figures 4.15 and 4.17. Yet, Figure 5.7 reveals a well dampened eigenvalue at 150 Hz. The vane plenum tap shows excitation in the 2 Hz region; yet, this low frequency excitation does not appear to trigger surge.

The waterfall plots in Figure 5.8A, B and time traces in Figure 5.9A, B reveal valuable surge precursor information for the open loop and closed loop engine runs. The open loop

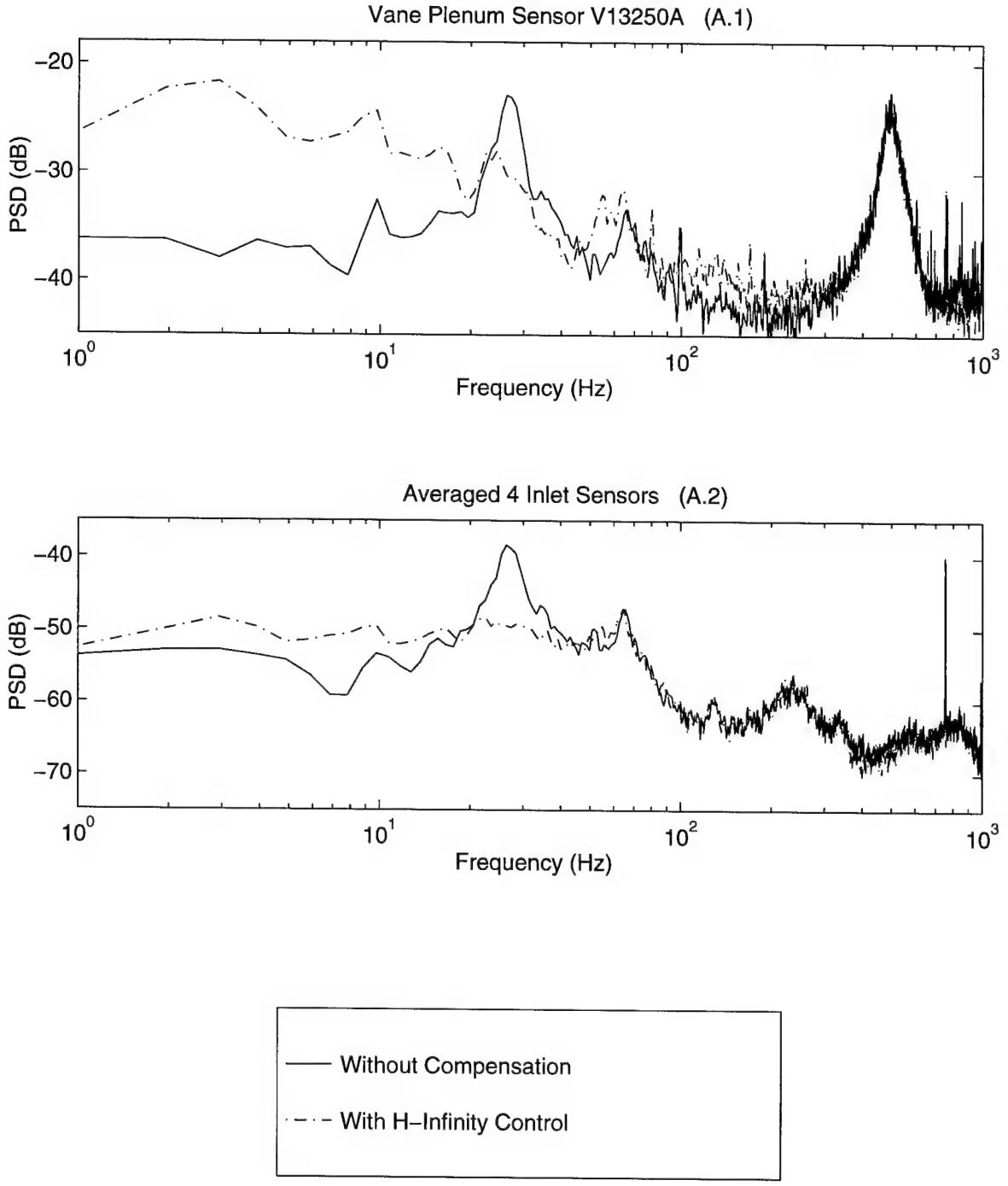

Figure 5.7A Best H-Infinity Compensator for the Closed Loop Power Spectral Density: Immediately Prior to Surge for Open Loop Operating Point

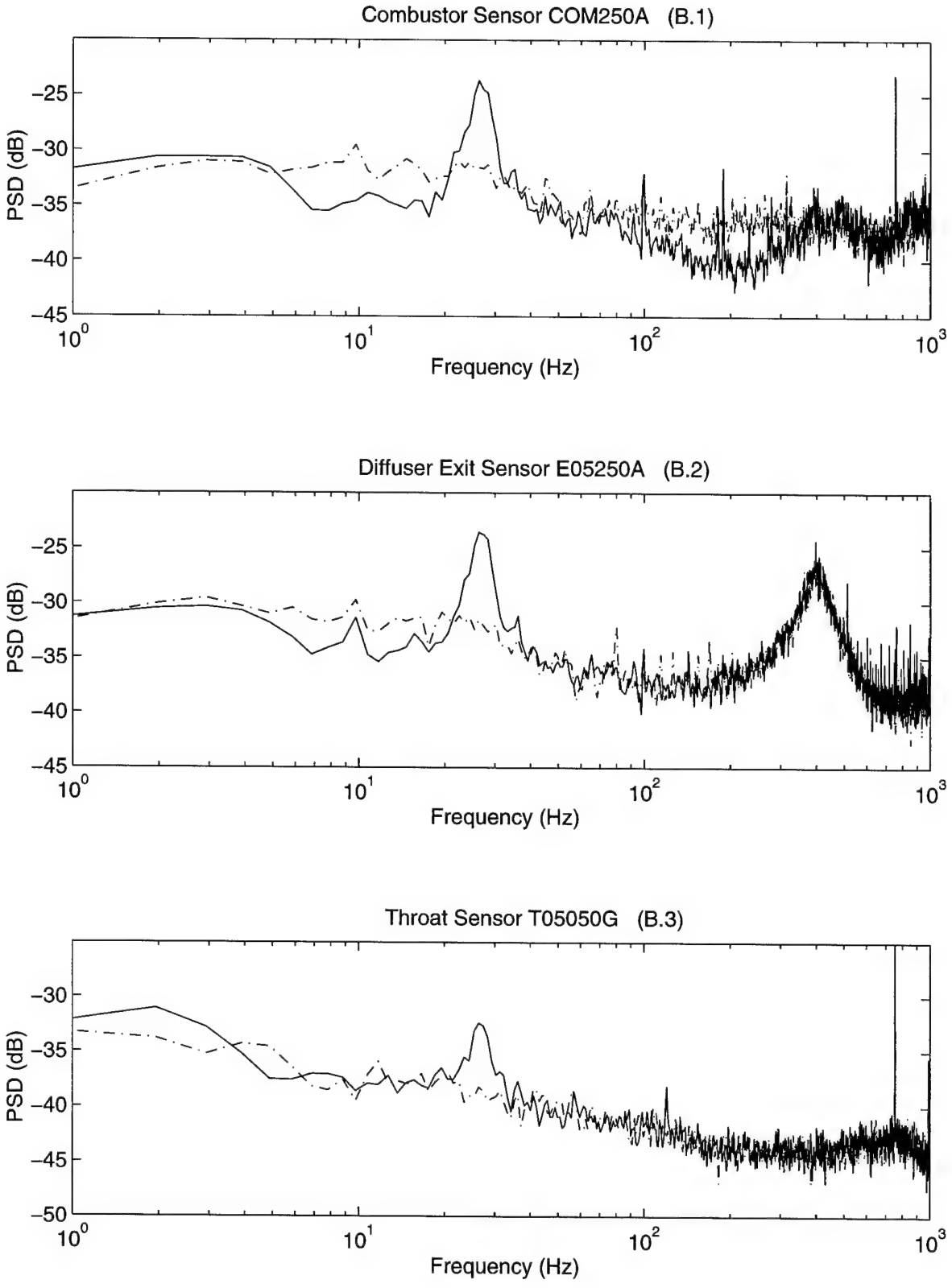

Figure 5.7B Best H-Infinity Compensator for the Closed Loop Power Spectral Density: Immediately Prior to Surge for Open Loop Operating Point

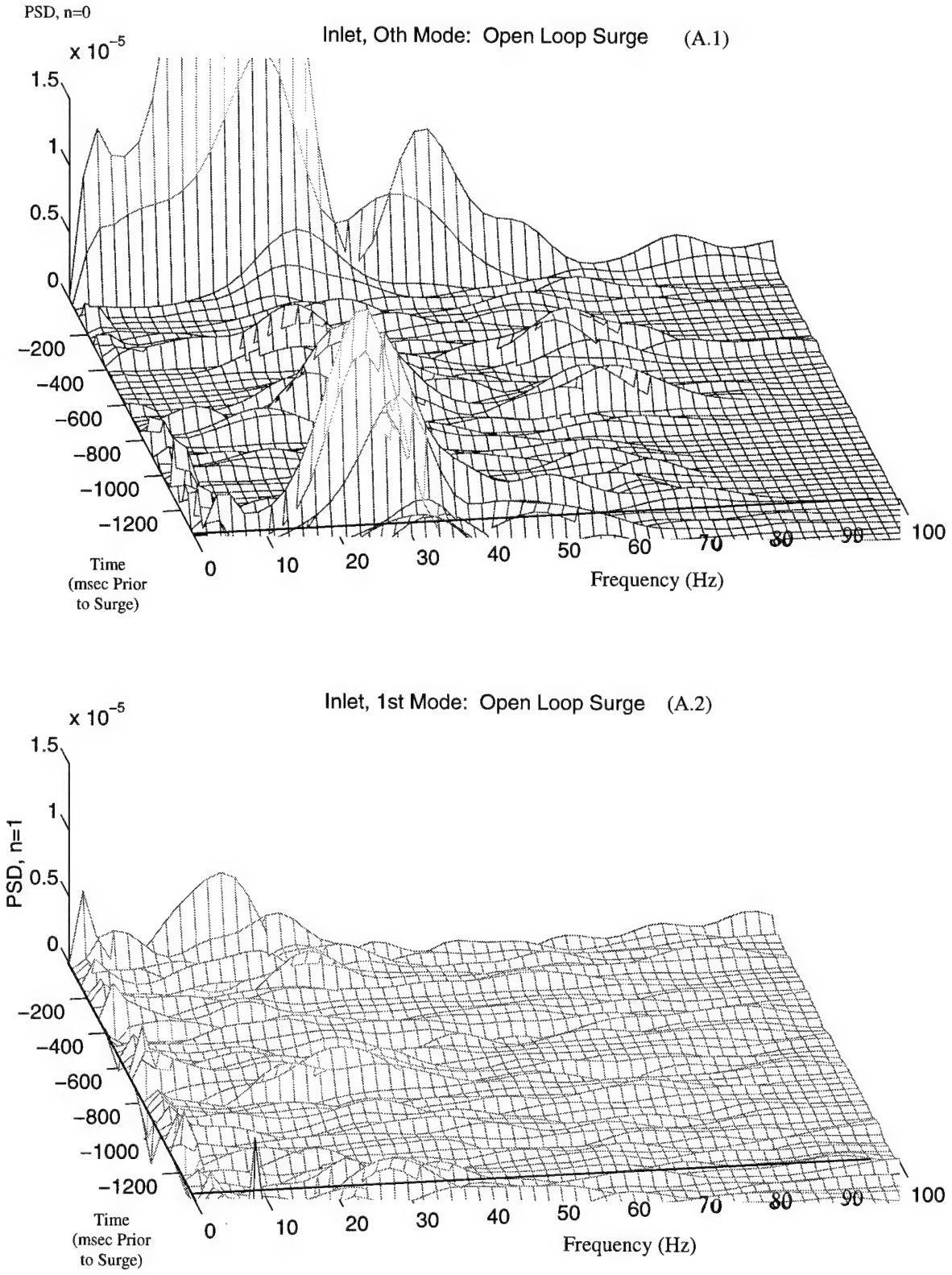

Figure 5.8A Open Loop Surge Waterfall Plot

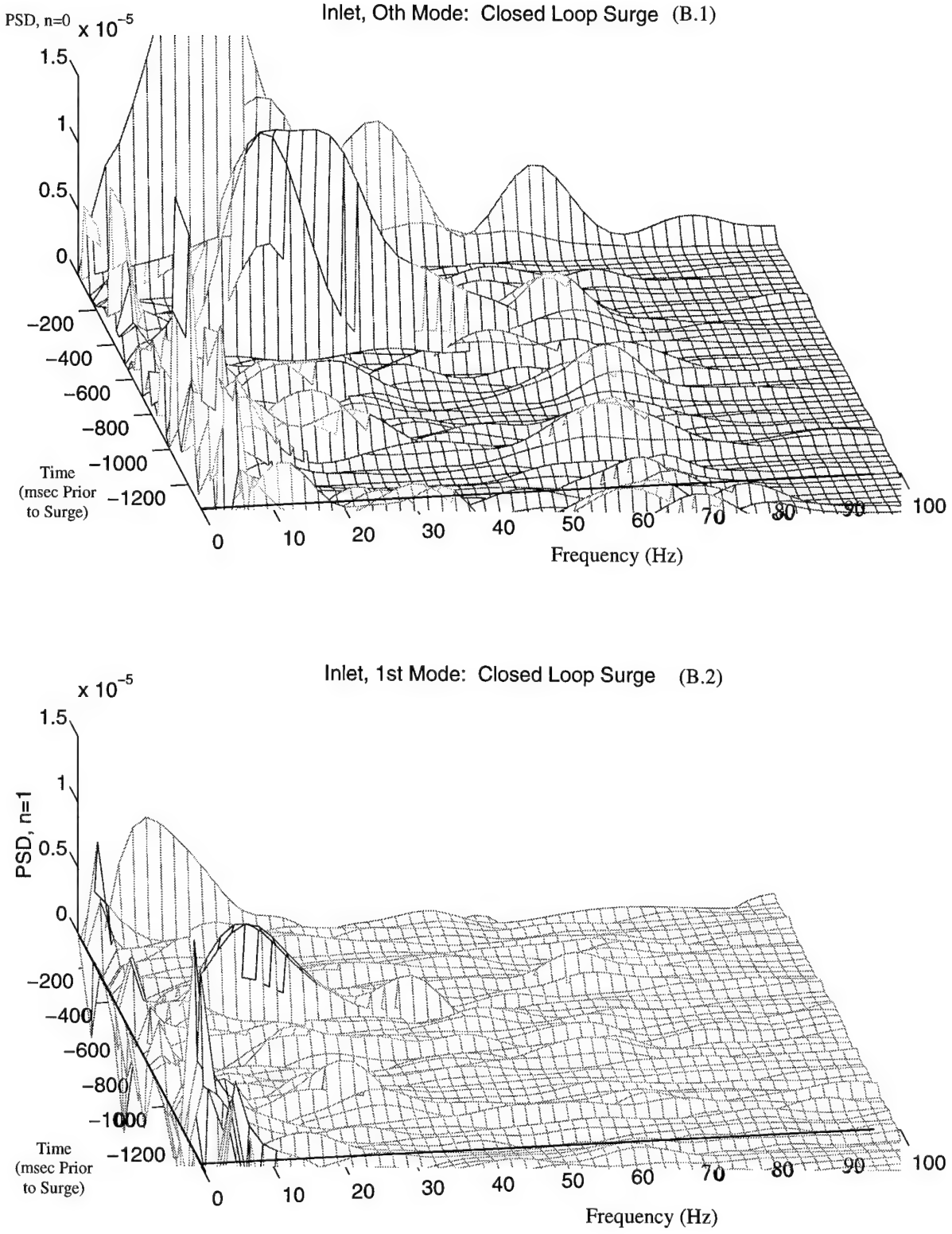

Figure 5.8B Closed Loop Surge Waterfall Plot.

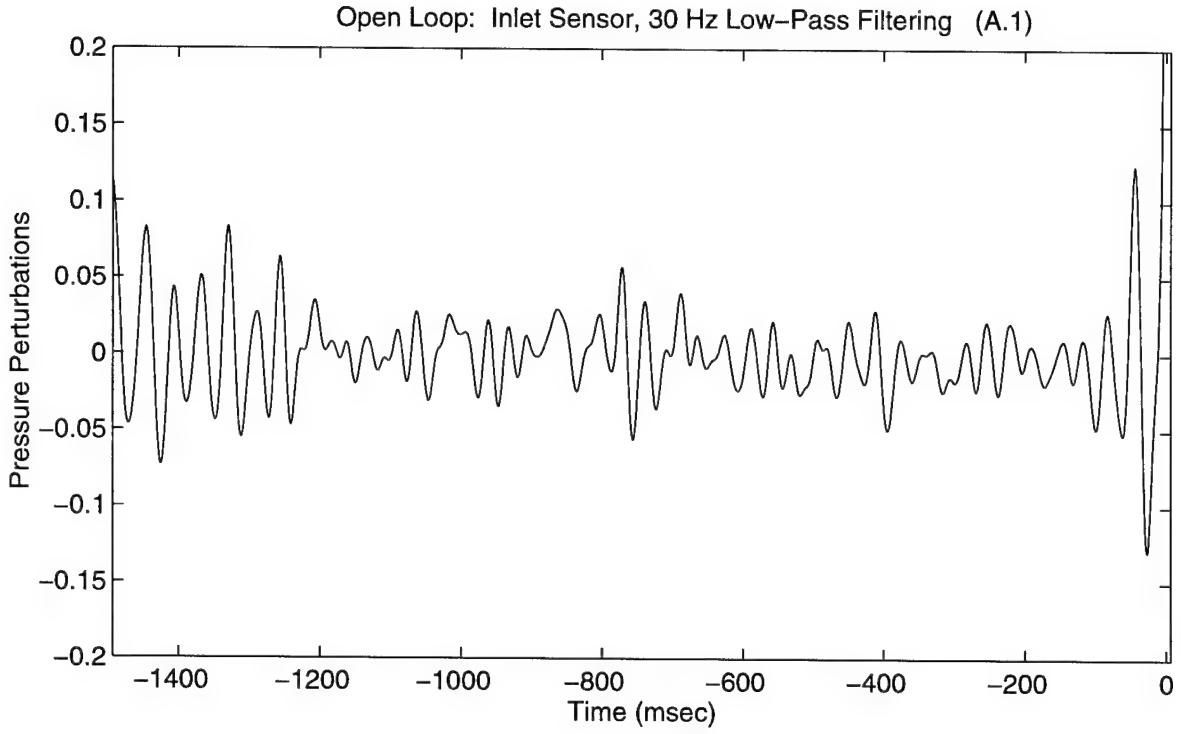

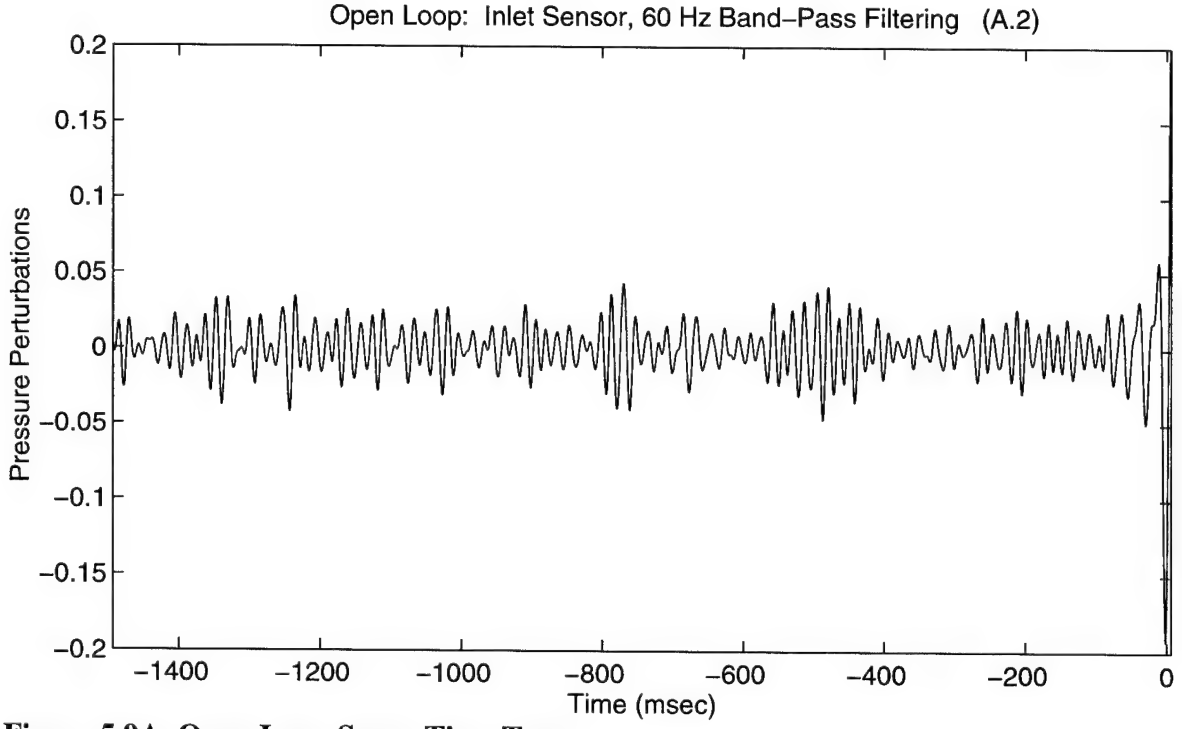

Figure 5.9A Open Loop Surge Time Trace

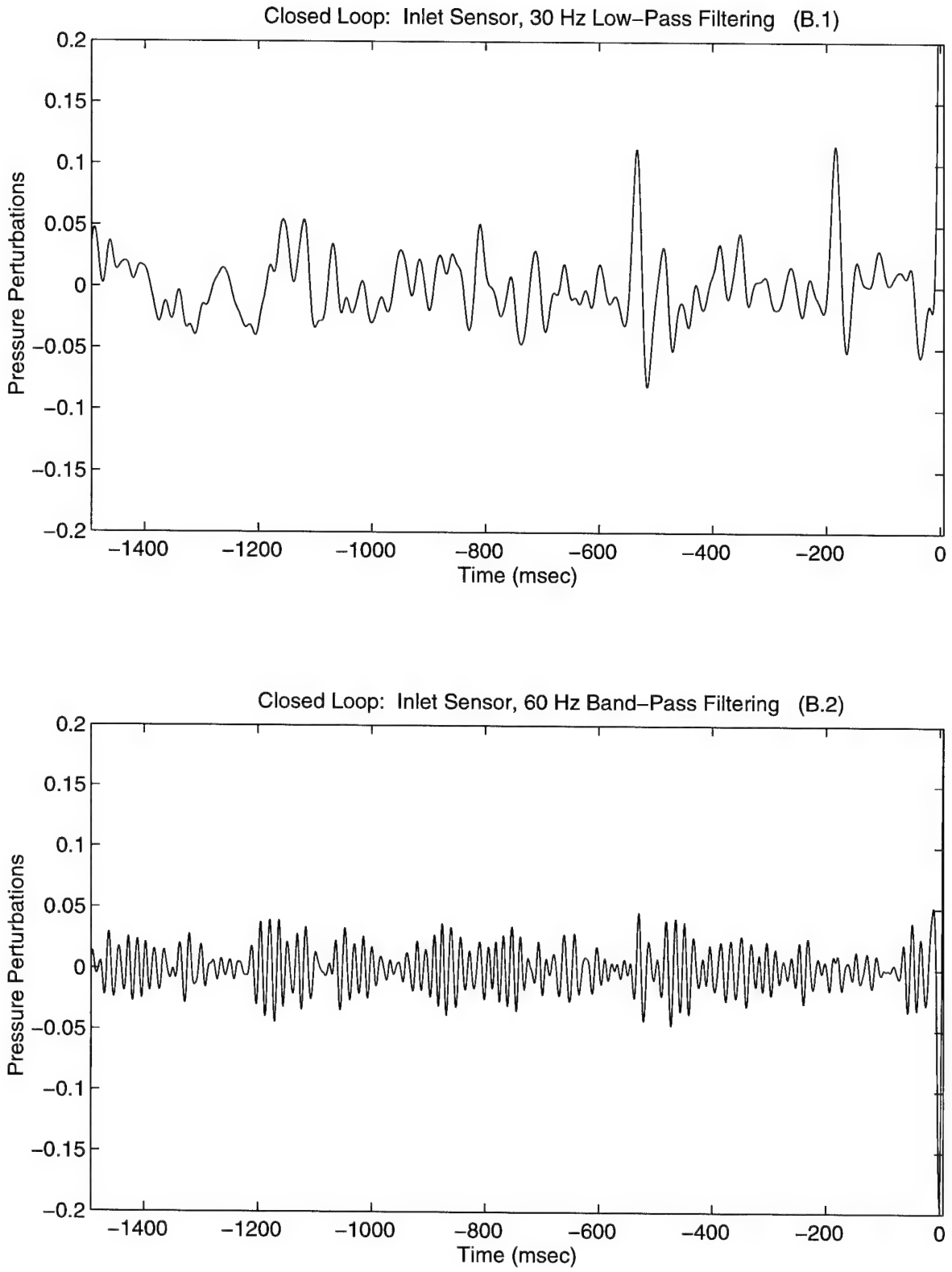

Figure 5.9B Closed Loop Surge Time Trace

surge case (Figure 5.8A) indicates that the surge mode (28 Hz) is perturbed at various time segments prior to the surge event. On the other hand, the closed loop waterfall plot (Figure 5.8B) indicates a single 22 Hz precursor prior to the surge event. This single perturbation then moves to 28 Hz and into surge. A second major difference between the open and closed loop case relates to precursor occurrence. The open loop waterfall plot has numerous random perturbations well before surge. However, the closed loop compensator suppresses all 28 Hz mode perturbations until just prior to surge. This indicates that the compensation scheme is correctly focused to mitigate these modal disturbances. At the last moment prior to surge, a perturbation becomes too large for the compensator to suppress.

In addition to the high speed data, the steady state data reveals important performance metrics for comparison between open and closed loop runs. The compressor exit map (Figure 5.10) indicates the mean operating point extension prior to surge. Recall from Section 5.2 that the compressor exit massflow is the sum of the massflow measured at the inlet and the mass addition with injection. This metric used to quantify engine performance is summarized in Table 5.1. Corrected massflow is presented using two different measures. The "percent of corrected mass flow decrease" is the amount of extension divided by the corrected mass flow at the open loop surge line:

$$\frac{Open\ Loop\ \dot{m}_{corr}@_{Surge} - Closed\ Loop\ \dot{m}_{corr}@_{Surge}}{Open\ Loop\ \dot{m}_{corr}@_{Surge}} \qquad (5.1)$$

Because the engine has a high open loop corrected mass flow, this measure results in small values. Table 5.1 shows a 0.59% massflow decrease for the compressor inlet map and a 0.68% massflow decrease for the compressor exit map. "Speedline extension" is an alternative measure that compares the extension to the typical operating range at 95% $N1_{corr}$.

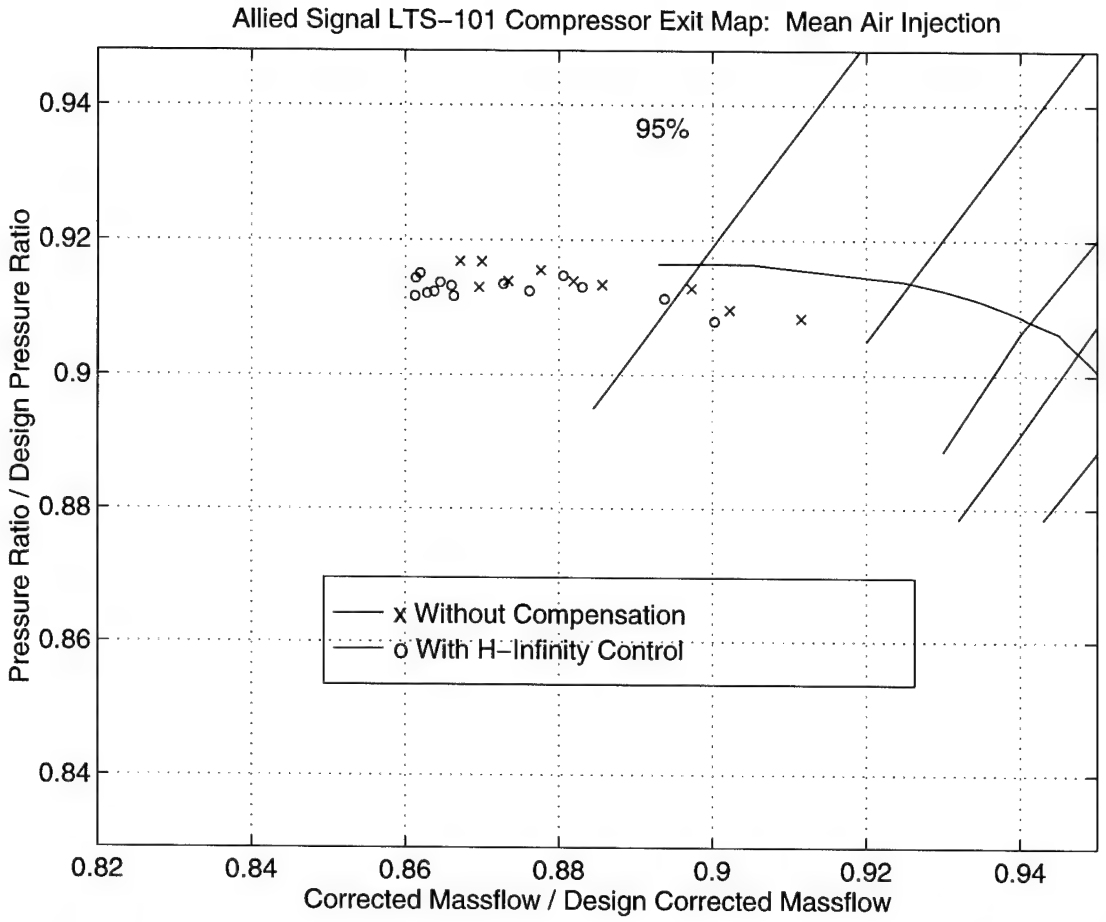

Figure 5.10 Compressor Exit Map: Best H-Infinity Compensator for the Closed Loop Case.

	"Best" H Infinity Design
Compressor Inlet	
% Massflow Decrease	0.59%
% Extension of Speedline	6.1%
Compressor Exit	
% Massflow Decrease	0.68%
% Extension of Speedline	7.1%
Force Increase	20.23 lb
Force Increase (as a % of the open loop engine force prior to surge)	1.716 %

Table 5.1 Best H-Infinity Design Results

Thus, the percent speedline extension is the amount of extension divided by the length of the open loop speed line:

$$\frac{Open\ Loop\ \dot{m}_{corr}@_{Surge} - Closed\ Loop\ \dot{m}_{corr}@_{Surge}}{Open\ Loop\ \dot{m}_{corr}@_{Nozzle\ Choke} - Open\ Loop\ \dot{m}_{corr}@_{Surge}} \qquad (5.2)$$

Using this speedline extension metric, the compressor inlet and exit maps indicate a 6.1% and a 7.1% increase, respectively.

The second performance measure is force, as measured by the load cell. The major drawback of this measurement is the associated voltage drift inherent in the load cell. The engine vibration environment causes drift in the load cell voltage output, especially near surge. The load cell force measurement averaged 20.23 pounds greater for the closed loop case over the open loop force output (See Table 5.1); however, the measurement indicated a 5.478 pound standard deviation in this measurement.

The valve command and valve position, presented in Figure 5.11 show that the compensator does not saturate during closed loop operation. Recall from Chapter 2.3.3 that the valve saturates at ~±7.5 volts. Since this voltage limit is not reached prior to surge initiation, the compensator performance is limited by the theoretical design. Although this particular design yields the best results among those designs tested, additional compensator modification may capitalize on more control authority and provide additional extension of the surge line.

One topic that is of immediate interest is whether the controller is in fact stabilizing an unstable operating point, and if so, determining the severity of the instability. To answer this question, one simply turns off the controller at the lowest attainable corrected massflow under

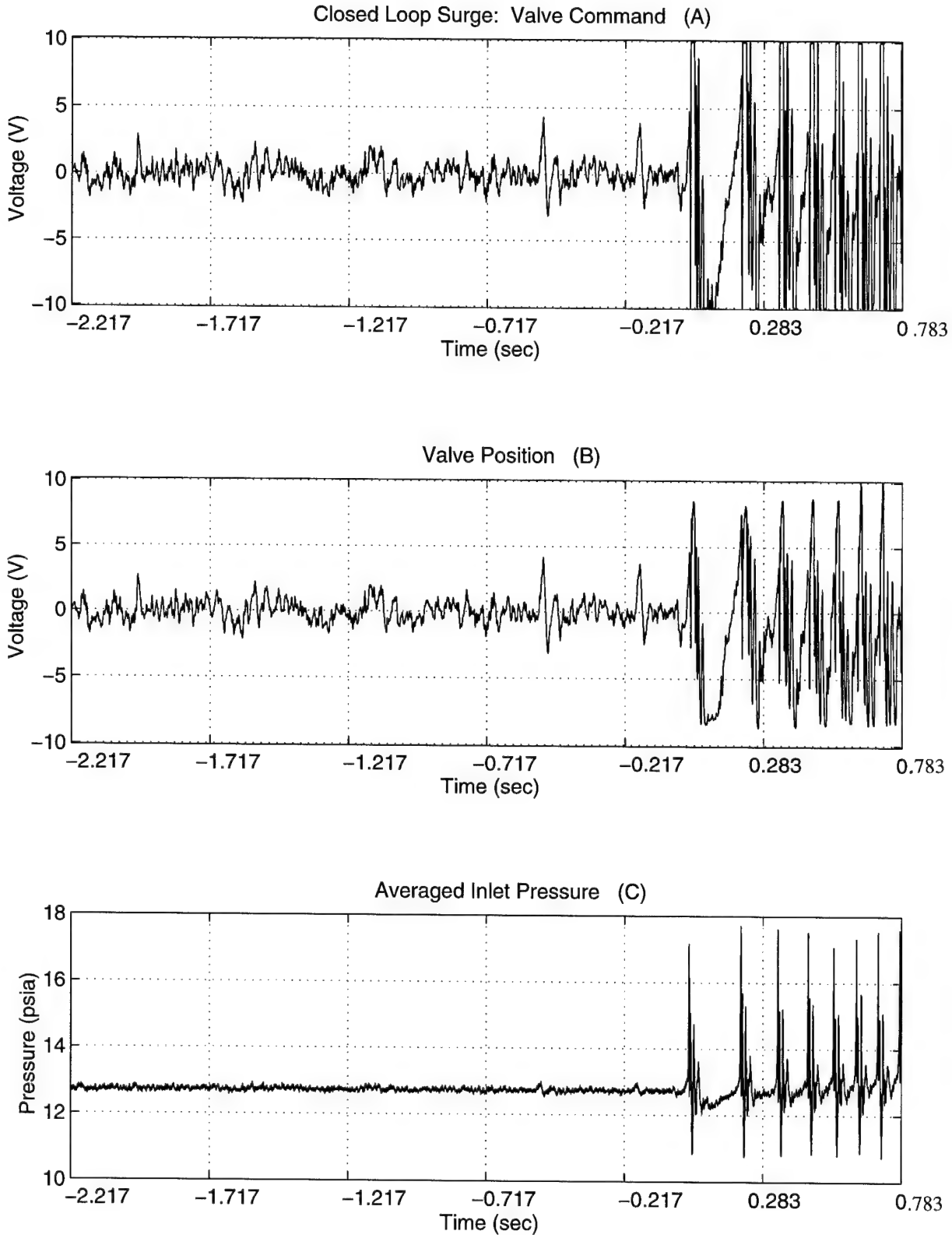

Figure 5.11 Time Trace of Valve Command, Valve Position, and Inlet Pressure Taps Prior to Closed Loop Surge.

closed loop operation. The compensator was turned off while the engine was operating at a corrected massflow of ~0.862 $\dot{m}_{design}$ at 95% $N1_{corr}$ (Figure 5.10). Surge ensued approximately five seconds later (Figure 5.12). The surge mode and first acoustic mode experienced large perturbations after the control was turned off at this low massflow operating point (Figures 5.13 and 5.14). However, since the system took five seconds to enter surge, one can infer that at the lowest achievable massflows with control, the engine is close to neutral stability rather than at a significantly unstable operating point.

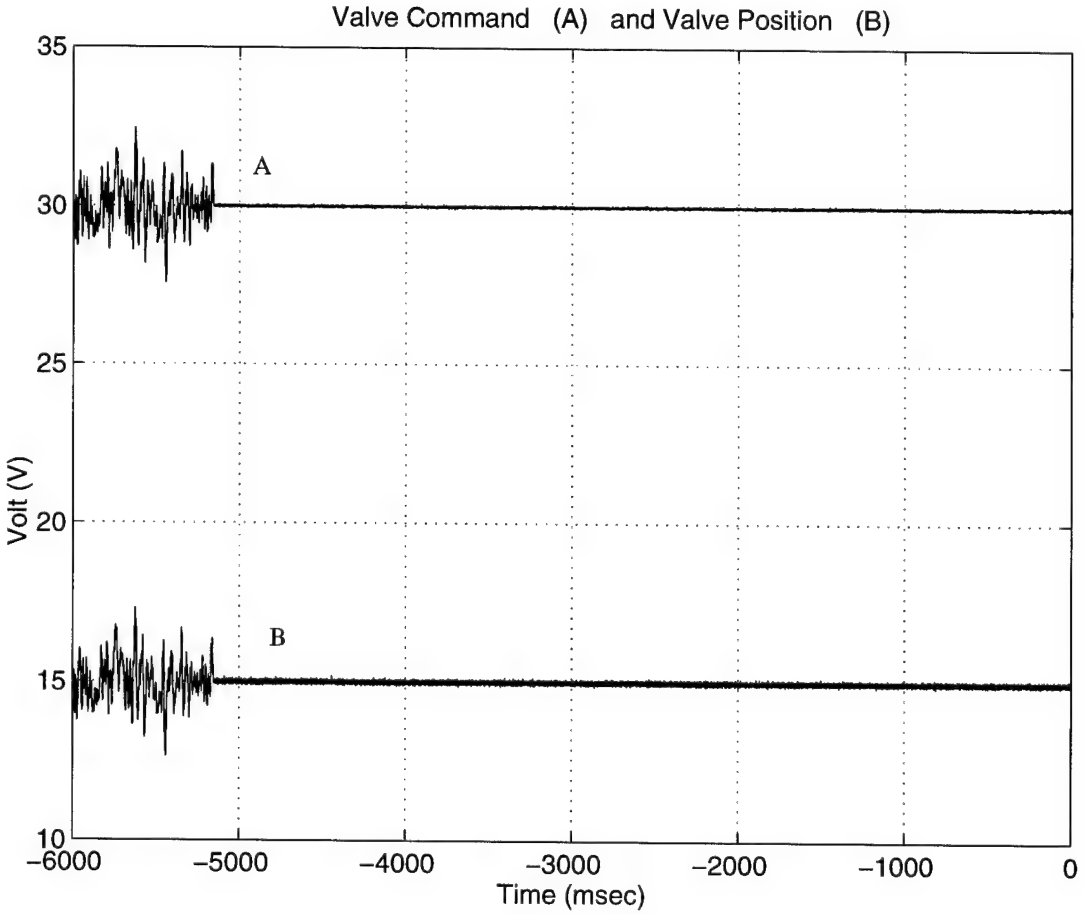

Figure 5.12 Time Trace. Removing Compensator at Normally Unstable Open Loop Massflow

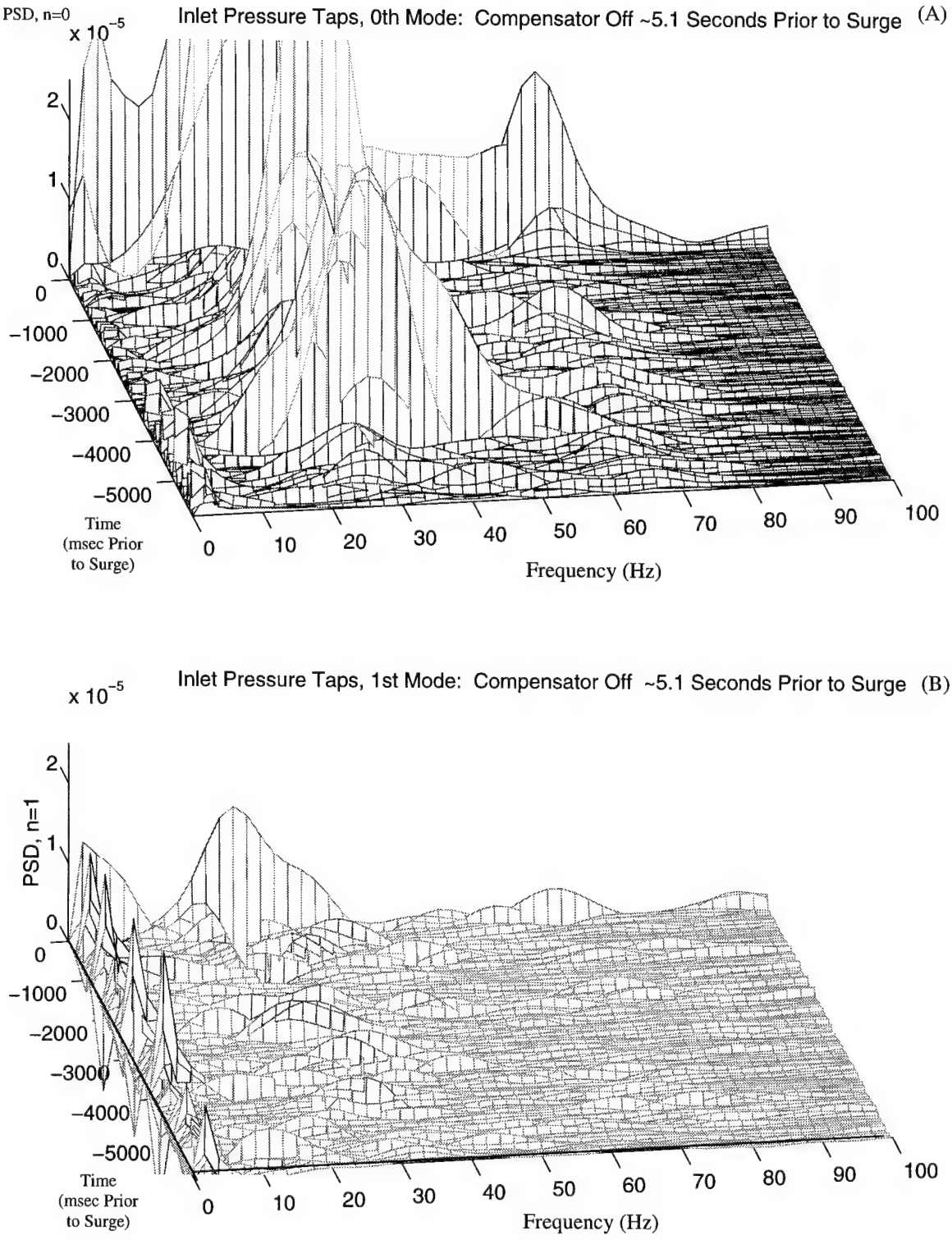

Figure 5.13 Waterfall Plot of Turning Off Controller at Normally Unstable Massflows

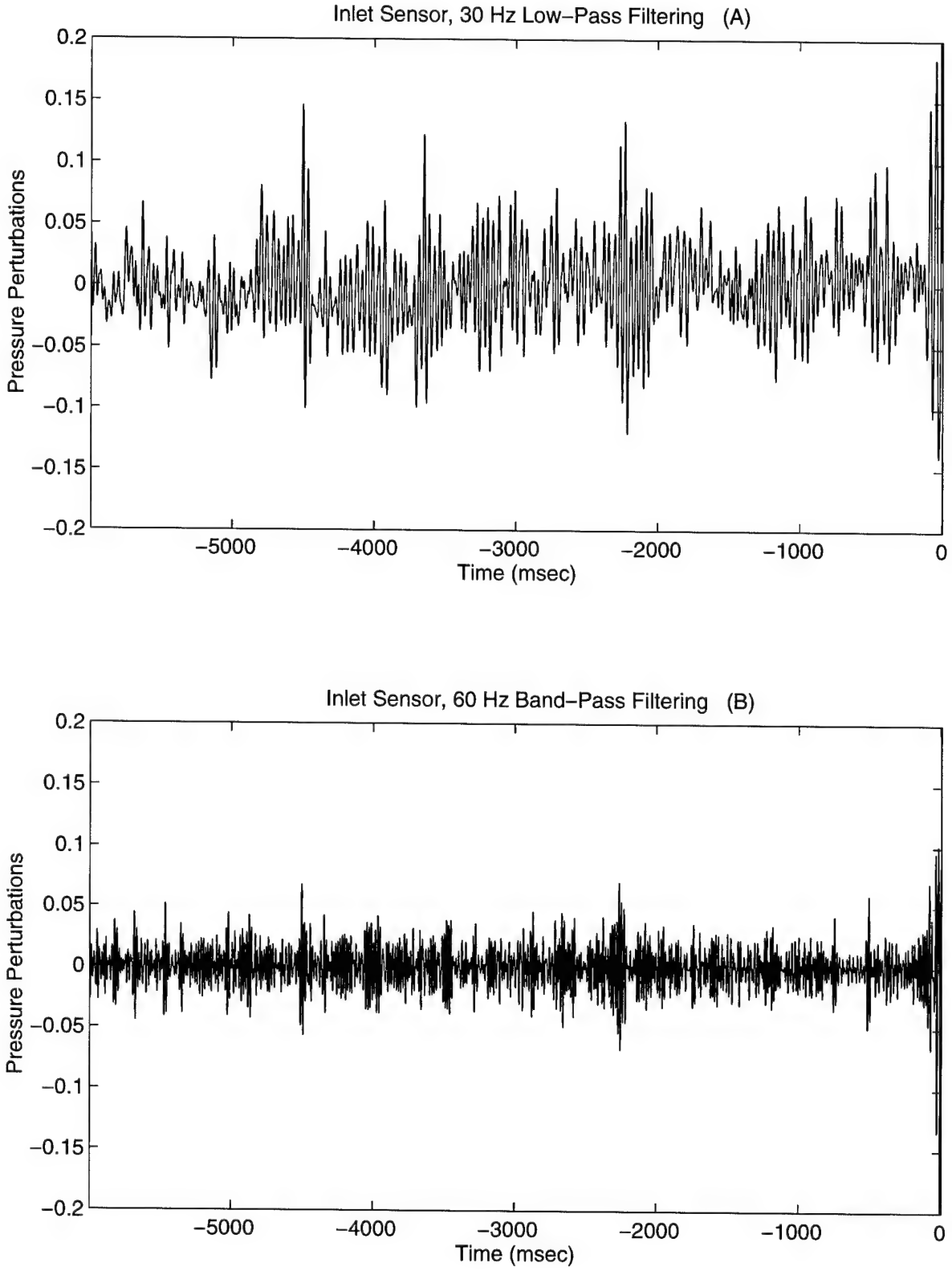

Figure 5.14 Time Trace of Filtered Inlet Pressure Sensor. Compensator Turned Off at ~5.1 Seconds

5.4 One Sided Blowing

The compensator design discussed in Section 5.3 injects air sinusoidally about a mean injection rate (i.e. both more and less than the mean level). On the other hand, "one sided blowing" compensators only add additional air injection to the mean air injection level. Weigl [20] achieves a significant performance increase by implementing such a design in the NASA Lewis single stage compressor. Hence, the experiments described in this section attempt to achieve similar corrected massflow reductions on the LTS-101 with a one sided compensator scheme.

Two effects contribute to compressor stabilization when one sided compensation is used. First, when air is modulated at the correct frequency, the injection has a stabilizing influence on the surge and first acoustic resonances; this is the same effect obtained with the two sided control discussed in Section 5.3. The second effect is that the mean air injection level increases as the feedback action increases actuator valve activity. (See Figure 5.15). Corn [15] demonstrated that any increase in air injection facilitates a decrease in the corrected massflow and pressure ratio. The same effect is present in this case with respect to corrected massflow; however, the change in the mean level of air injection produces a negligible decrease in the pressure ratio. Therefore, the first effect (i.e. unsteady stabilization) is probably dominant.

In order to test the one sided blowing concept, the best H-infinity compensator is adjusted to add air to the mean air injection at the desired compensator frequencies. In other words, the valve command signal is clipped to remove all voltage values less than the mean injection level (Figure 5.15). As the previous explanation predicts, the one sided speed line is

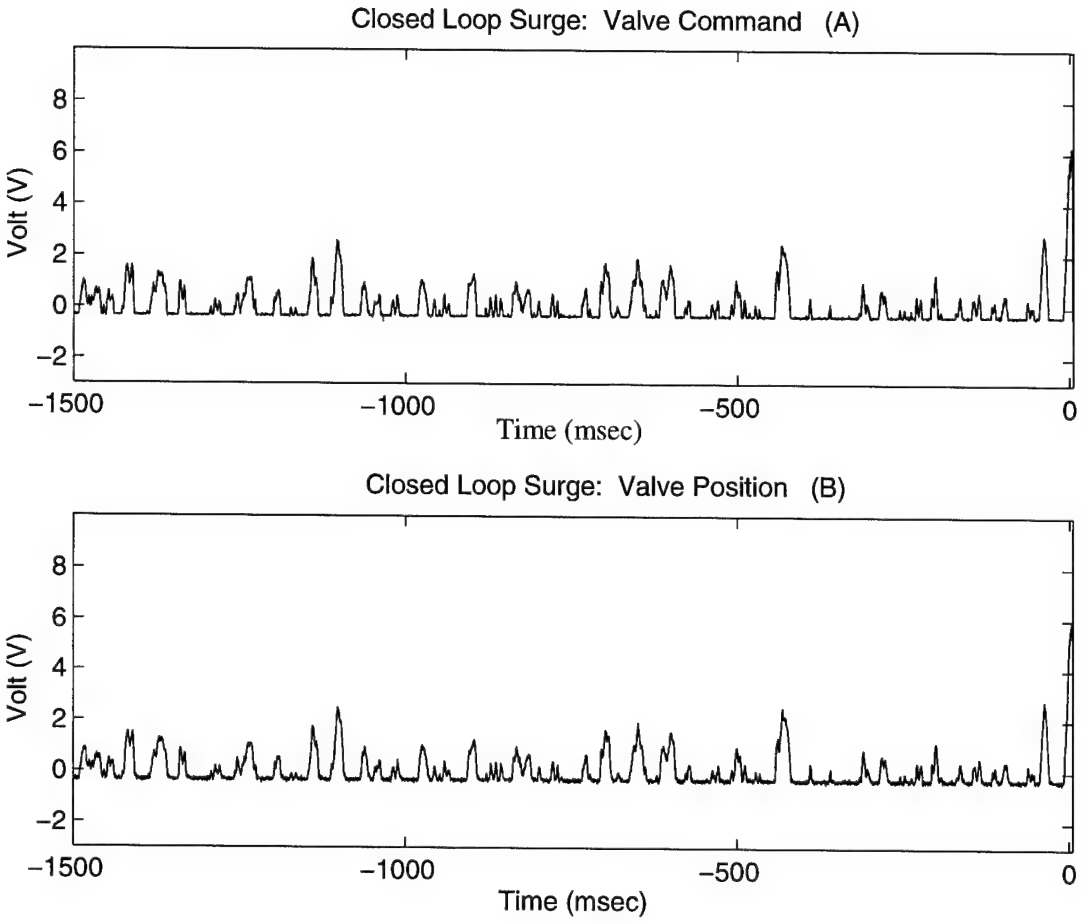

Figure 5.15 Time Trace of One Sided H-Infinity Compensator

extended well beyond the open loop speed line. Figure 5.16 shows the compressor inlet map, with a corresponding massflow decrease of 0.98%. Table 5.2 summarizes the improvement. Note that the average force with the one sided compensation scheme is 42.65 lb greater than the force at the average open loop surge operating point.

The closed loop waterfall plot for the one sided blowing in Figure 5.17 shows similar behavior to the two sided waterfall plots discussed in Section 5.3. The surge mode perturbations are successfully eliminated prior to surge (Figure 5.17). The perturbations are more noticeable for this one sided injection case than in the two sided case. However, the one

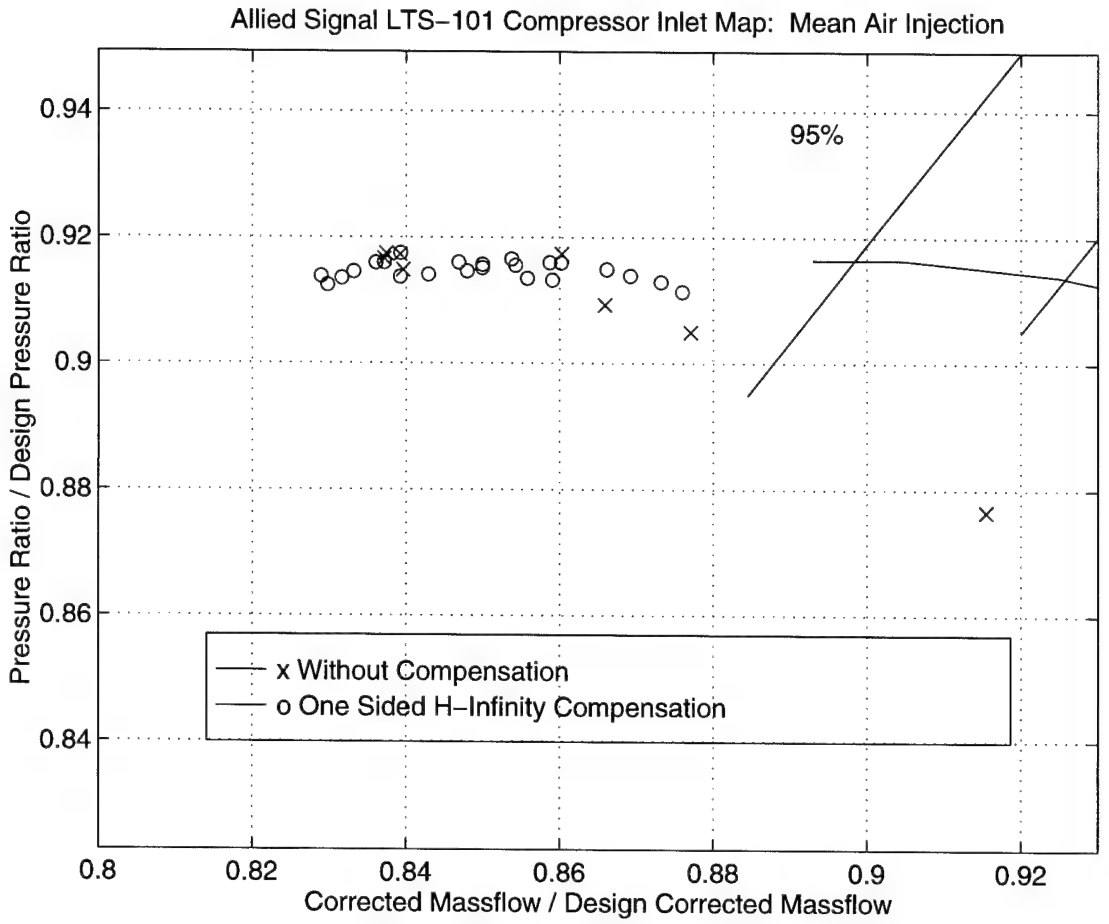

Figure 5.16 Compressor Inlet Map. This Shows the Extension with One Sided Compensation.

Metric	"Best" H-Infinity Design	One Sided H-Infinity Design
Compressor Inlet		
% Massflow Decrease	0.59%	0.98%
% Extension of Speedline	6.1%	10.7%
Compressor Exit		
% Massflow Decrease	0.68%	0.95%
% Extension of Speedline	7.1%	10.4%
Force Increase	20.23 lb	42.65 lb
Force Increase (as a % of the open loop engine force prior to surge)	1.716%	3.660%

Table 5.2 Summarization of Closed Loop Results

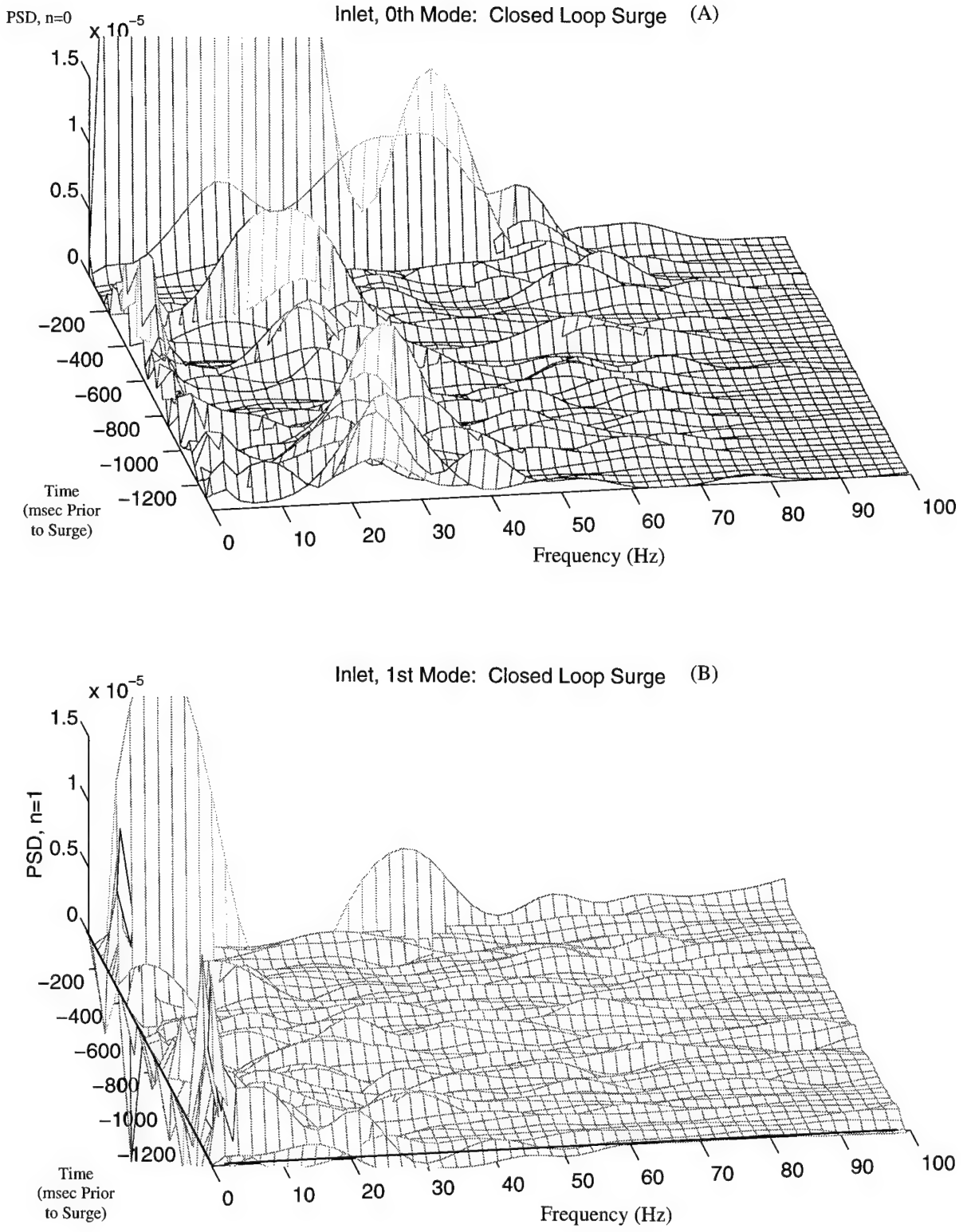

Figure 5.17 Waterfall Plot of the One Sided Compensation

sided case presented in Figure 5.17 is at a lower massflow than the waterfall plot of the two sided case in Figure 5.8B. Note that the acoustic resonances are not excited.

Besides the steady state metrics already discussed, there is considerable interest in determining if any noticeable perturbation shifts consistently appear in the steady state data prior to engine surge. Figure 5.18 shows the massflow ratio immediately prior to surge as a function of time. The massflow variation appears random, with no sudden corrected massflow drop immediately prior to surge inception. This observation is limited by the steady state instrumentation resolution, in which data is collected each one second. Note that at surge inception, the sharp spike on the corrected mass flow time traces results from a slight lag in the P3 measurement compared to the inlet pressure measurement (See arrows on Figure 5.18). Recall from Chapter 2.2 that corrected massflow is determined from the bellmouth

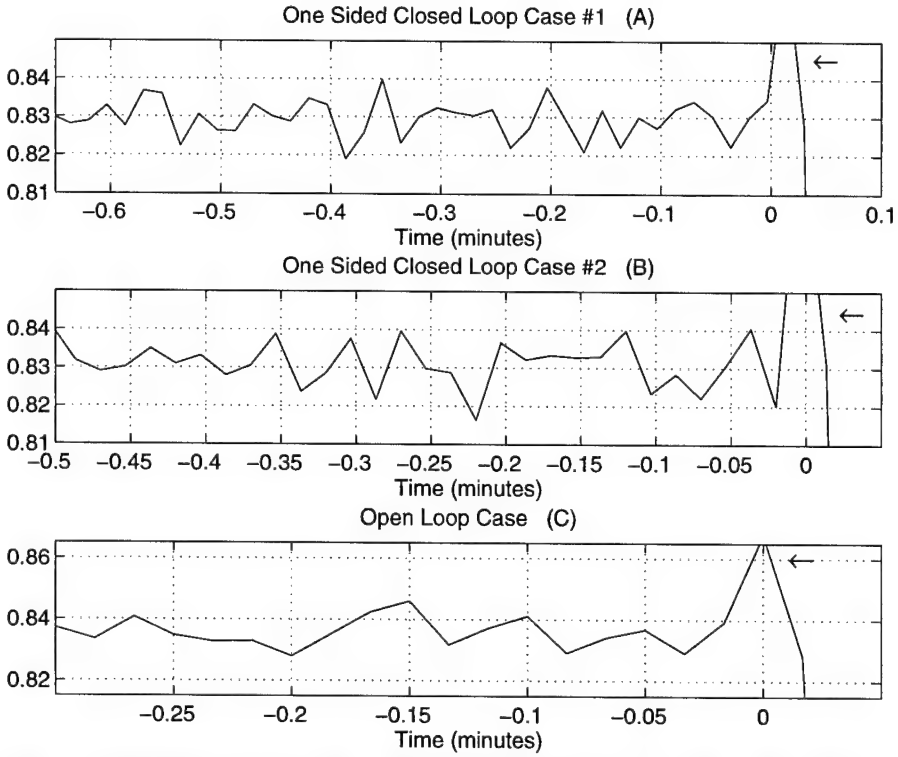

Figure 5.18 Variation in Non Dimensional Corrected Massflow Vs. Time

calibration using P_3, P_1, and $P_{ambient}$.

In further analyzing the time increments prior to surge inception, the open and closed loop corrected massflow and pressure ratio fluctuations appear normally distributed in Figures 5.19 and 5.20. If more data points are obtained at these operating points, the distributions follow a bell curve distribution. This is significant for determining the operating point variation on the compressor inlet map (Figure 5.21). As discussed in Chapter 3.3.3, the

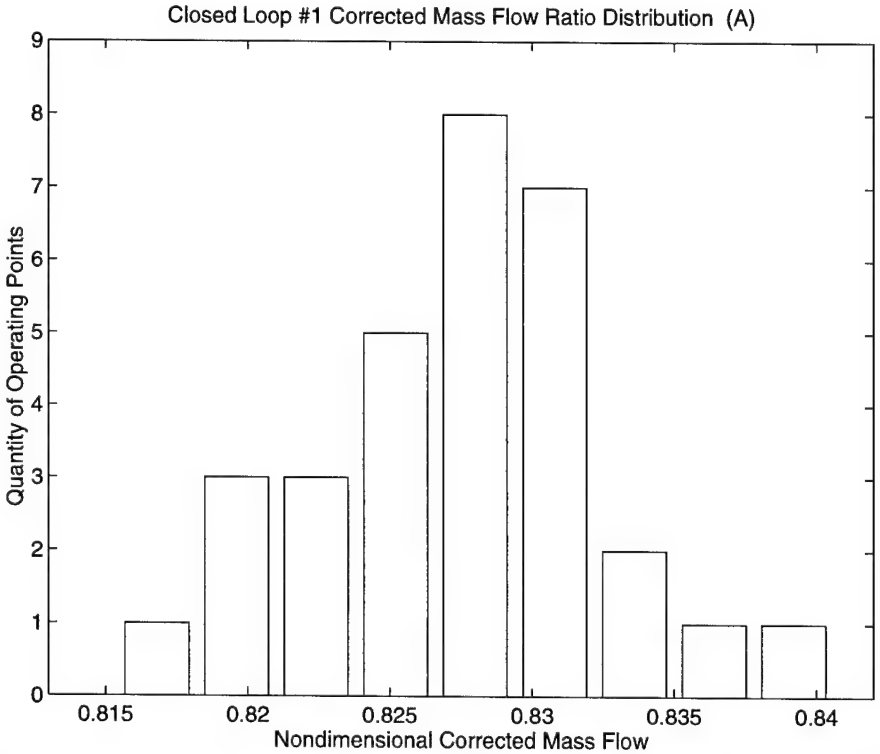

Figure 5.19A Histogram of System Corrected Massflow During One Sided Closed Loop Operation

Note: The convention for Figures 5.19 and 5.20 are:
Closed Loop #1: Is the final stable operating point prior to surge from the first successful one sided closed loop speedline.
Closed Loop #2: Is the final stable operating point prior to surge from the first successful one sided closed loop speedline.
Open Loop: Is the final stable operating point prior to surge from one of the open loop "reference" speedlines.

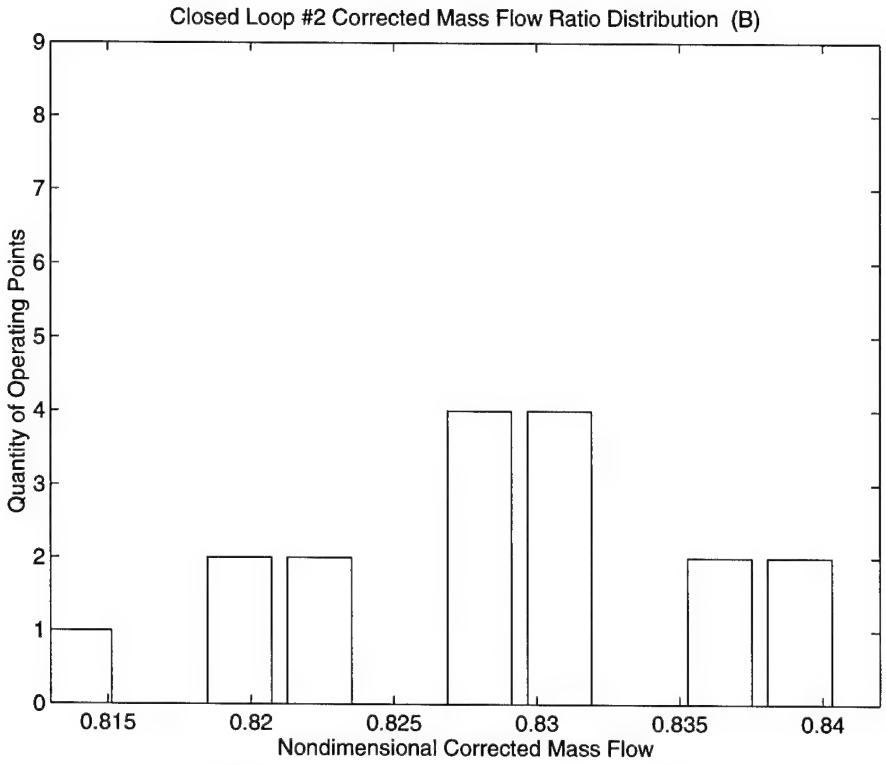

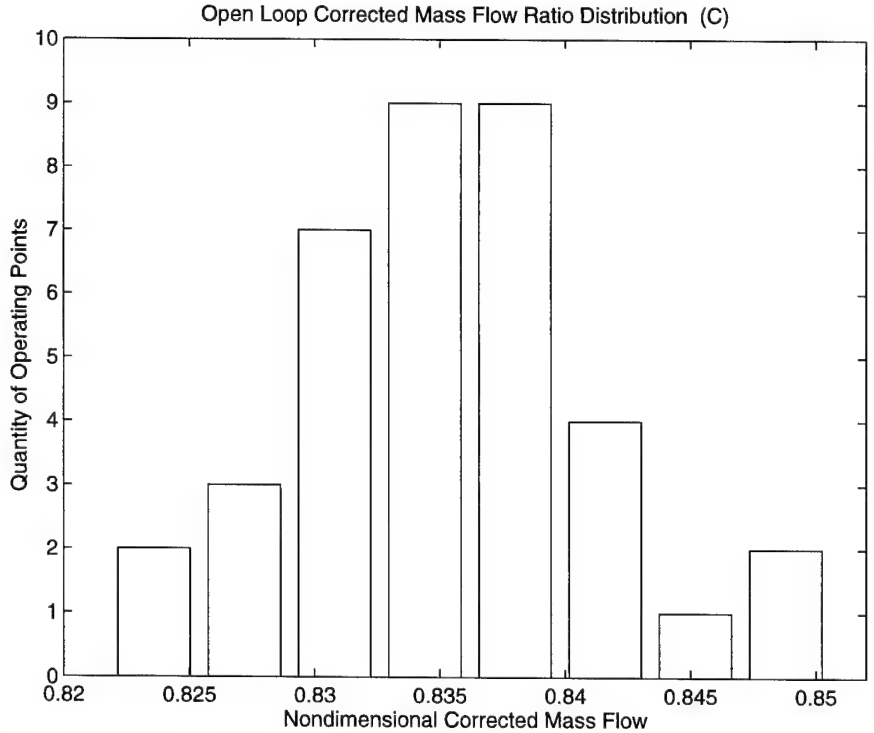

Figure 5.19B, C Histogram of System Corrected Massflow
B) During Second One Sided Closed Loop Operation C) During Open Loop Operation
Note: Refer to Figure 5.19A caption for details.

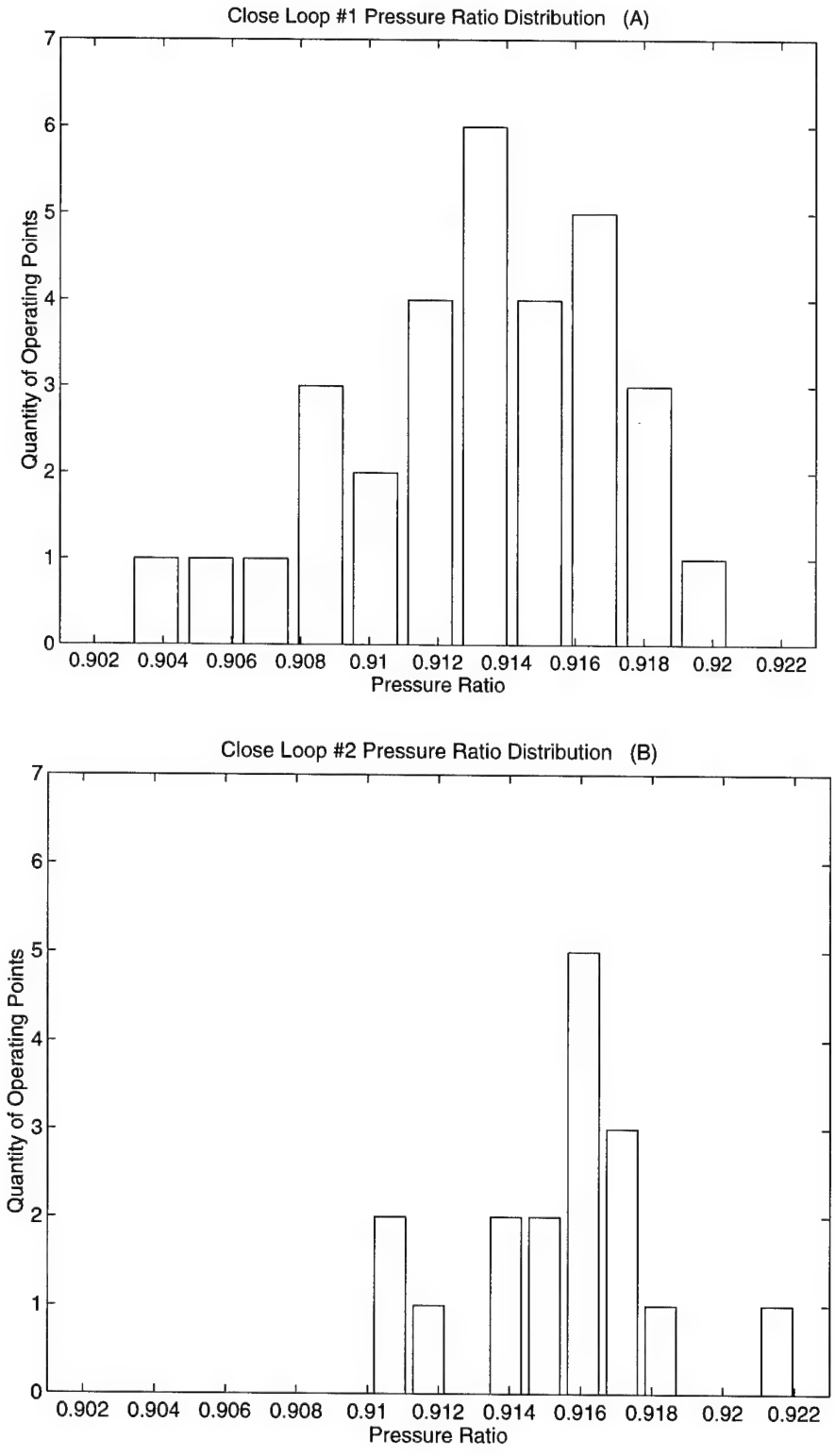

Figure 5.20A, B Histogram of System Pressure Ratio During Both One Sided Closed Loop Operations. Note: Refer to Figure 5.19A caption for details.

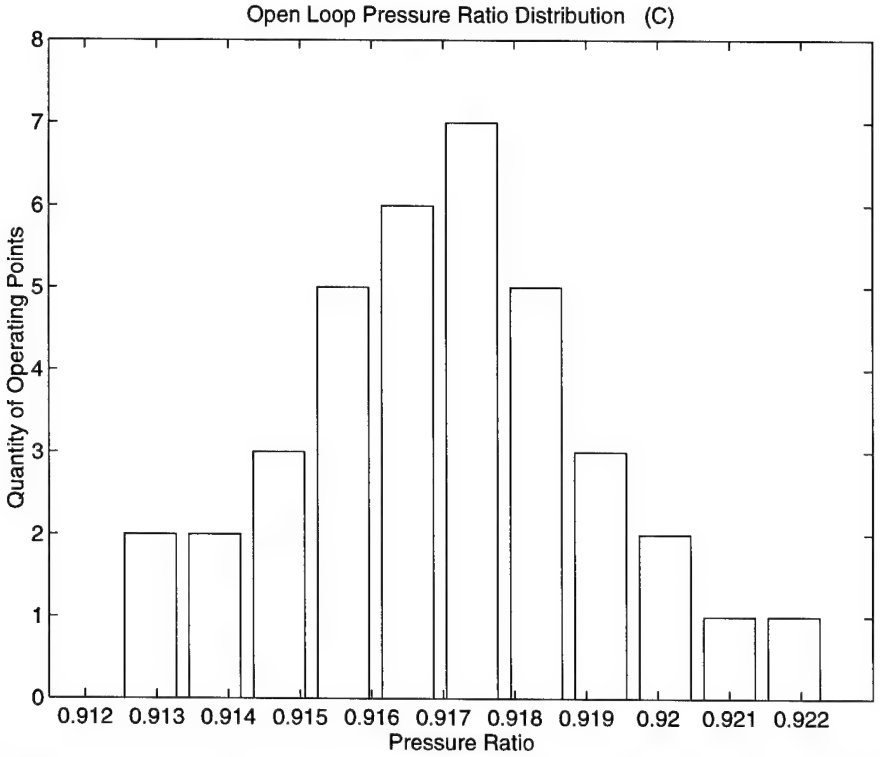

Figure 5.20C Histogram of System Pressure Ratio During Open Loop Operation. Note: Refer to Figure 5.19A caption for details.

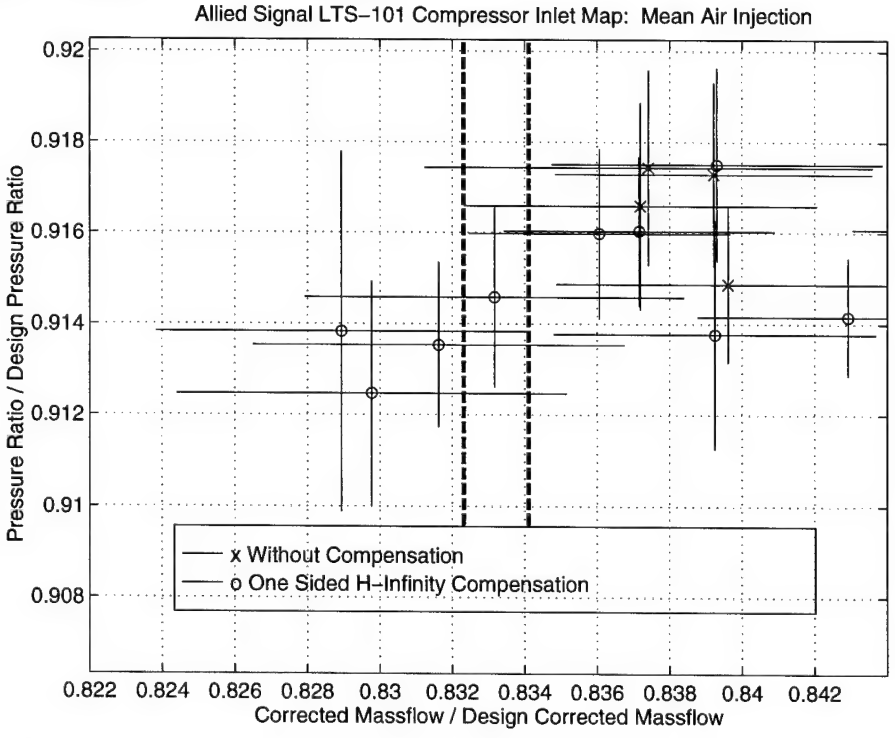

Figure 5.21 Open and Closed Loop Operating Points, With Error Bars Indicating One Standard Deviation of Variation in Measurement. Note: The dark dash lines indicate the amount of overlap between open and closed loop standard deviations.

lines in Figure 5.21 extend to show the standard deviation of the measured quantities at each operating point. One can not conclude with 95% certainty that the normally distributed closed loop operating point prior to surge is always beyond the mean of the open loop surge line. However, one can conclude with 95% certainty that the mean closed loop surge line is extended from the open loop surge line. In addition, based on a similar uncertainty analysis for instrumentation measurement error (as in Chapter 3.3.3), the closed loop surge line is beyond the open loop surge line (with 95% certainty).

5.5 Design Shortcomings

Several details about the compensation design require additional explanation. First, compensator designs used for these experiments did not consider the high pass filter. This filter is used to decrease the magnitude of the signal output at low frequencies. The four state high pass filter causes a 90° phase difference at around 1 Hz (Figure 5.22) between the plant used to design the compensators and the actual system with this filter. The magnitude for the high pass filter does not significantly decrease the actual plant transfer magnitude for frequencies above one Hz.

For many of the experiments, eliminating the high pass filter did not affect the closed loop performance. However, the engine does occasionally surge at a low frequency while operating at corrected mass flows well above the surge line. Figures 5.23 and 5.24 show low frequency oscillations at approximately 2 Hz. The waterfall plot in Figure 5.23 shows a large amplitude disturbance between 1 and 2 Hz that causes surge. In addition, consider the initial surge precursor in Figure 5.24B with a superimposed 2 Hz sinusoid. The frequency of the large pressure oscillation decreases prior to the full surge cycle.

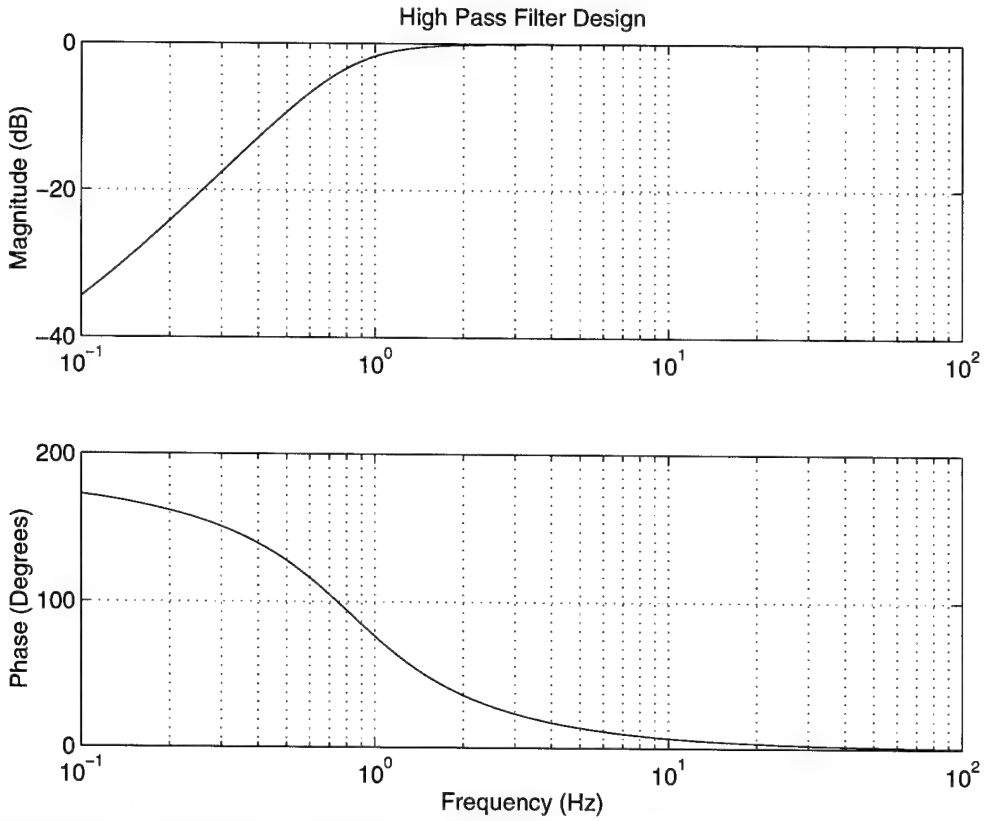

Figure 5.22 High Pass Filter Used on Control Computer

A second contributor to the low frequency surge pertains to the assumed eigenvalue locations at operating points with high corrected massflows. The eigenvalue locations associated with the plant at high corrected massflows differ from those used for compensator design. Thus, the compensator can potentially destabilize the high massflow dynamics.

These two factors contribute to the unusual precursor and surge. Low frequency precursors and surge do not occur while operating the engine near the surge line. Therefore, to avoid this problem, one could use the compensator only at low massflows near the open loop surge line.

The low frequency surge prevented conclusive testing of compensators designed with a competing system model, as discussed in Chapter 3.5. Recall that this competing plant

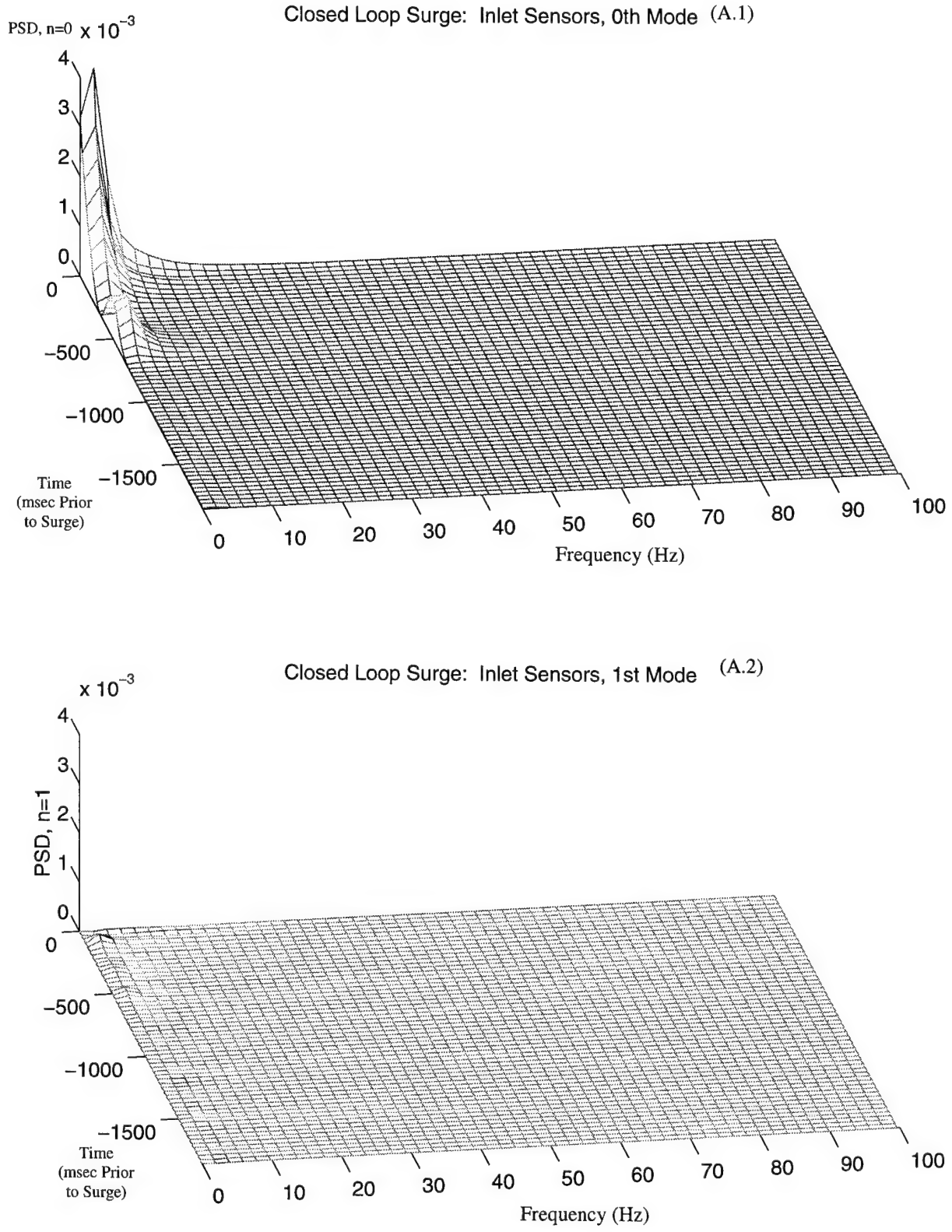

Figure 5.23A Low Frequency Surge at High Massflows.

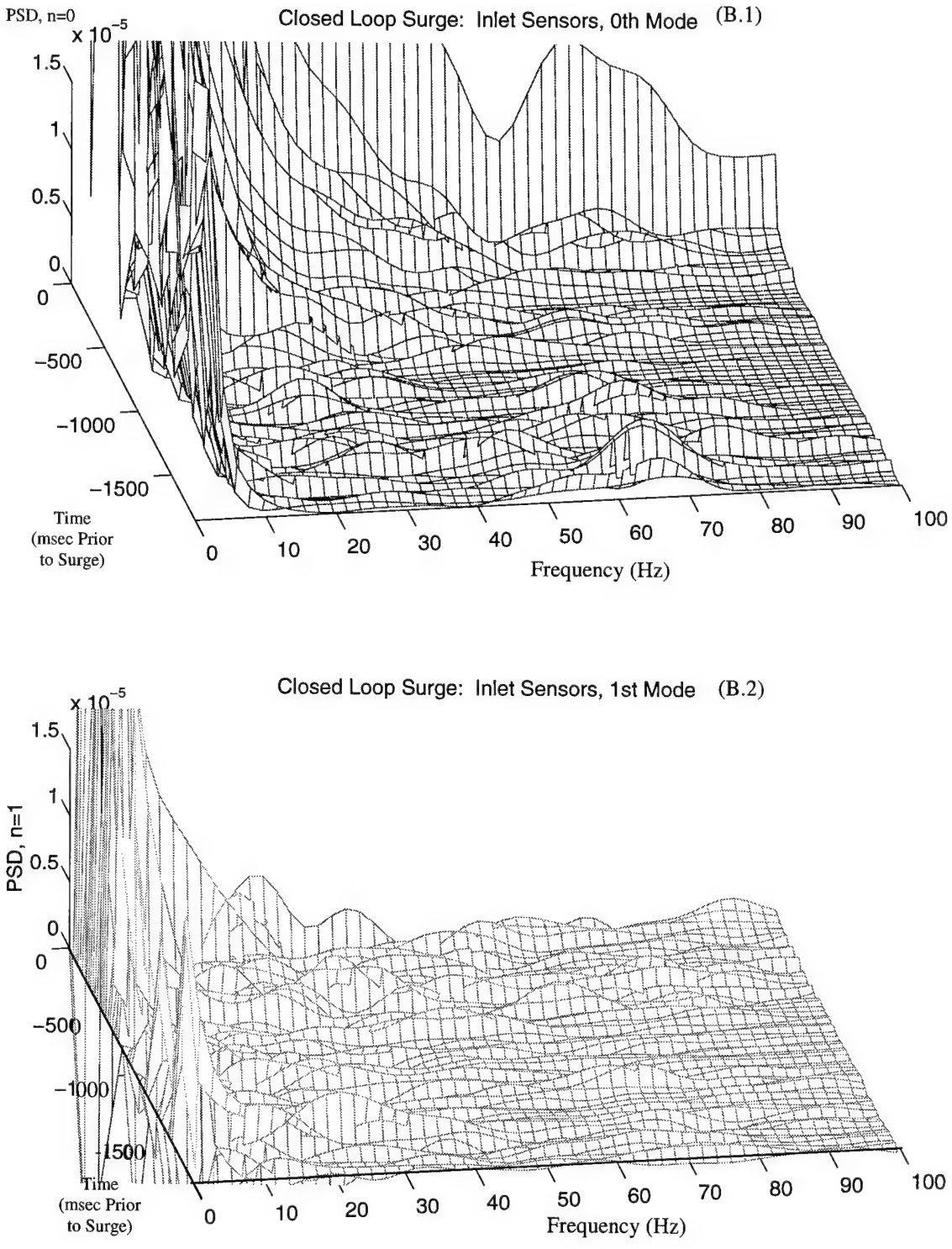

Figure 5.23B Low Frequency Surge at High Massflows.

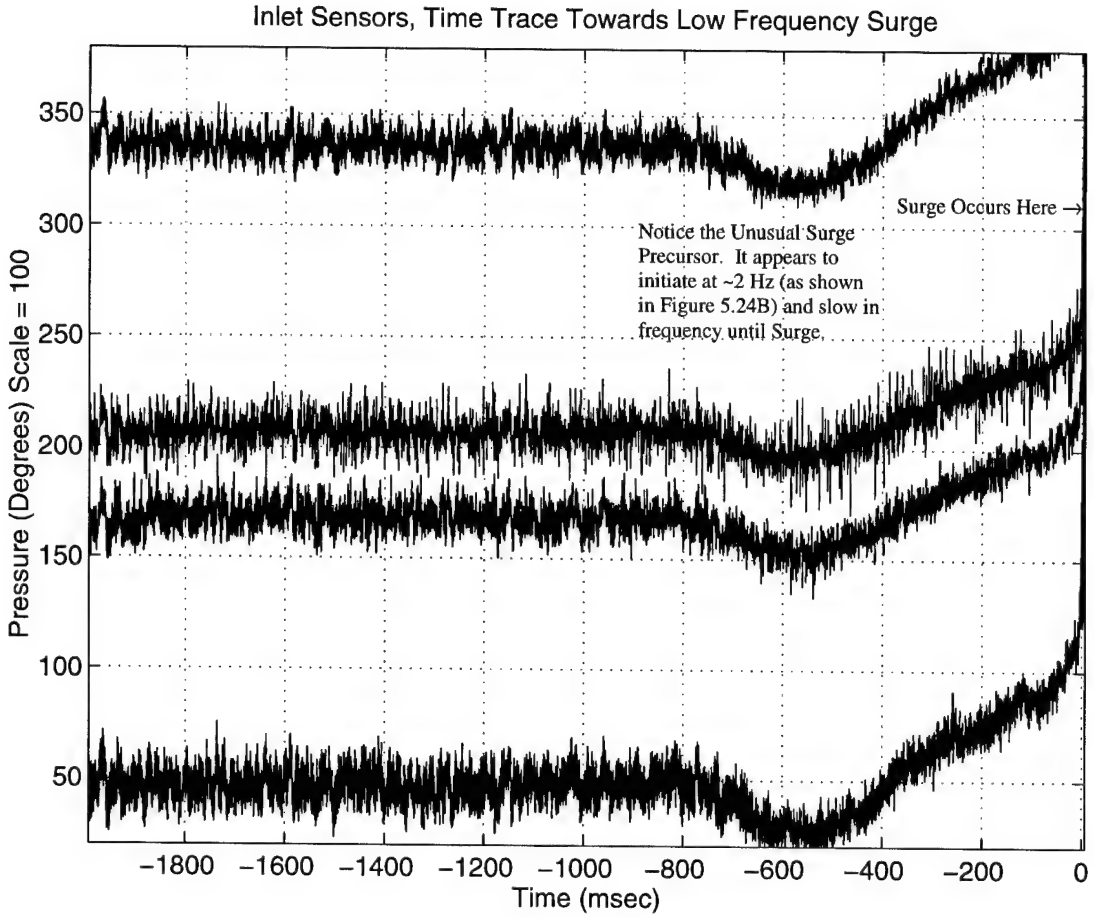

Figure 5.24A Unfiltered Time Trace of a Low Frequency Surge While Operating Closed Loop

model contains a 22 Hz mode in addition to the 28 Hz mode. A larger physical system, including the engine and entire inlet ducting, could induce such a mode. A compensator was designed using the competing plant model. The goal was to test whether eigenvalues tied to the larger system (including engine and inlet ducting) become unstable when the surge mode (at 28 Hz) is stabilized. Another possible explanation for the closed loop surge rationalizes that the surge mode is pushed to a lower frequency by the controller until the surge occurs. Because of the low frequency surges and experimental testing time constraints, these questions are unresolved.

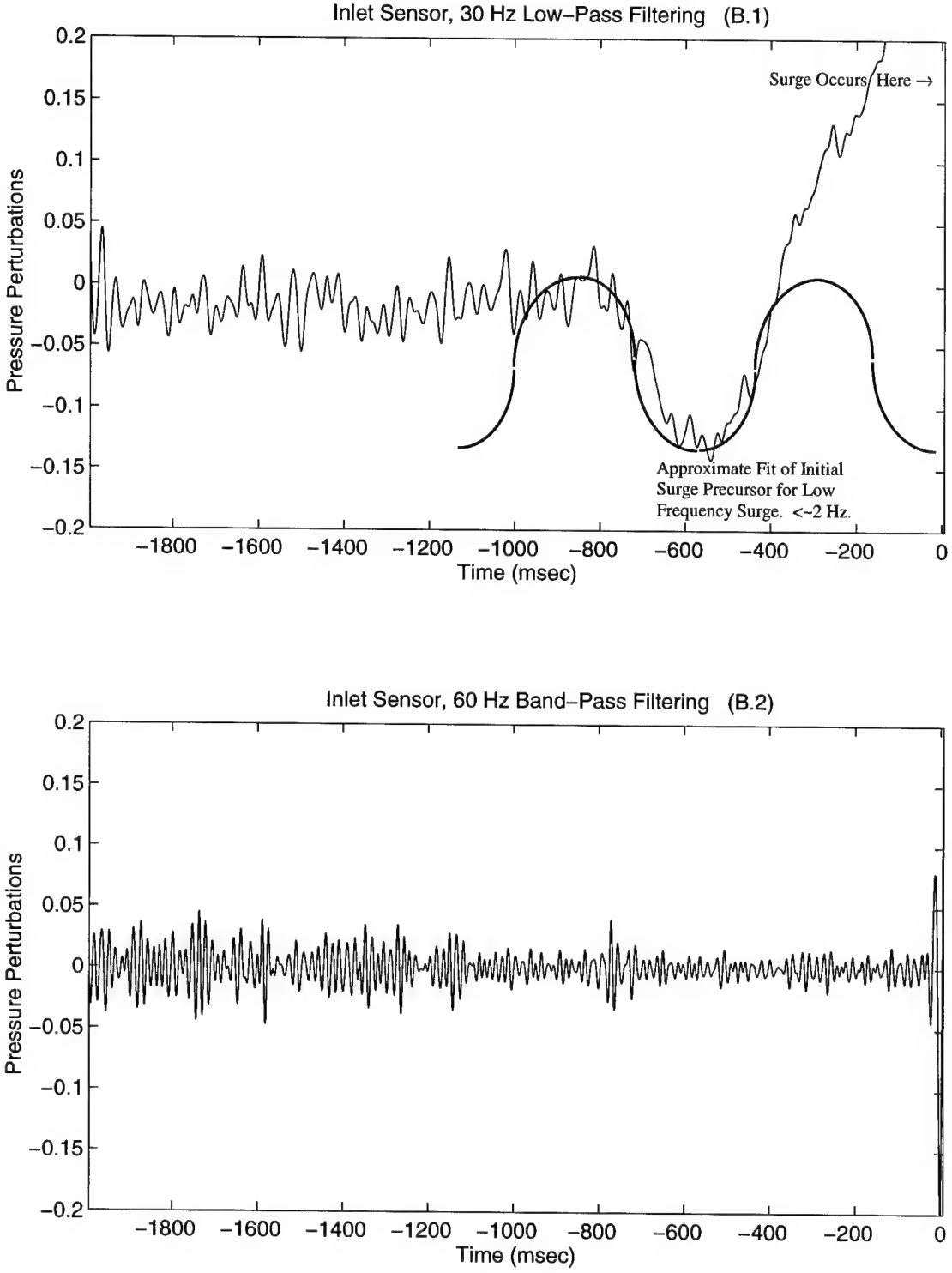

Figure 5.24B Filtered Time Trace of a Low Frequency Surge While Operating Closed Loop

The second significant design shortcoming pertains to engine degradation and associated changes in its behavior. As the engine experienced more surge events, the power spectral density plots began to show large increases in the magnitude of a peak at 10 Hz. Figure 5.25 shows the PSD plots near the beginning and end of the set of runs performed for this thesis. Repetitive surges cause engine degradation, thus changing the engine dynamics. Although identification of a new model could resolve this issue, time constraints prevented this. As a result, low frequency surges occurred more frequently near the end of the research presented here.

The current method of obtaining a transfer function from a single operating point near surge does not predict changes in the plant structure. As a result, the compensator is designed for an outdated plant and may produce unknown effects on the evolving engine dynamics. A similar consideration arises if the engine is repaired or modified. In such cases, a new plant model is required to get good results from an H-infinity compensator. These comments provide motivation to consider modeling techniques that accommodate engine modifications in a timely manner.

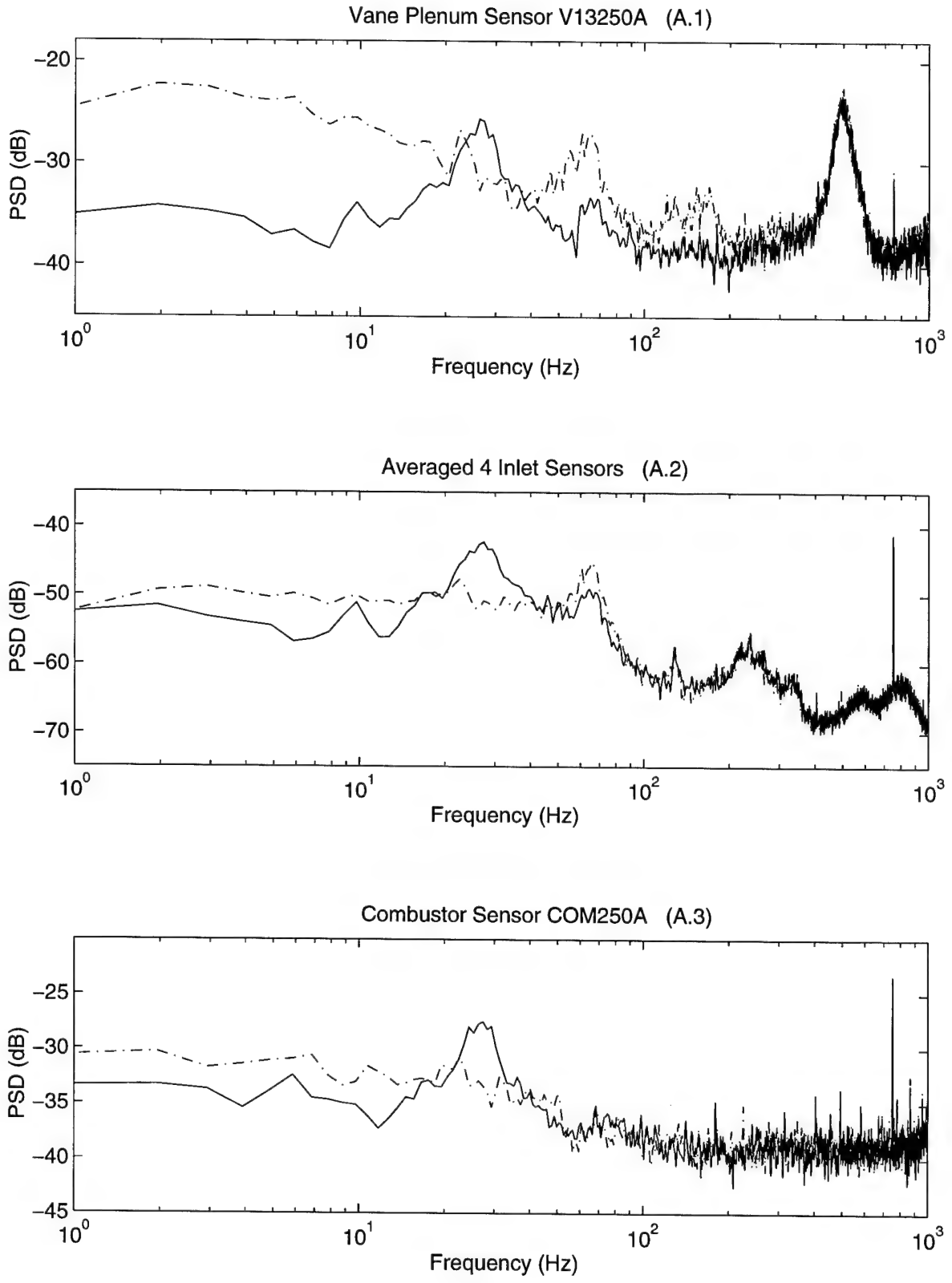

Figure 5.25A Open and Closed Loop Power Spectral Density Plots Prior to Open Loop Surge Point: Early in Experimental Testing. Notice the absence of a 10 Hz peak.

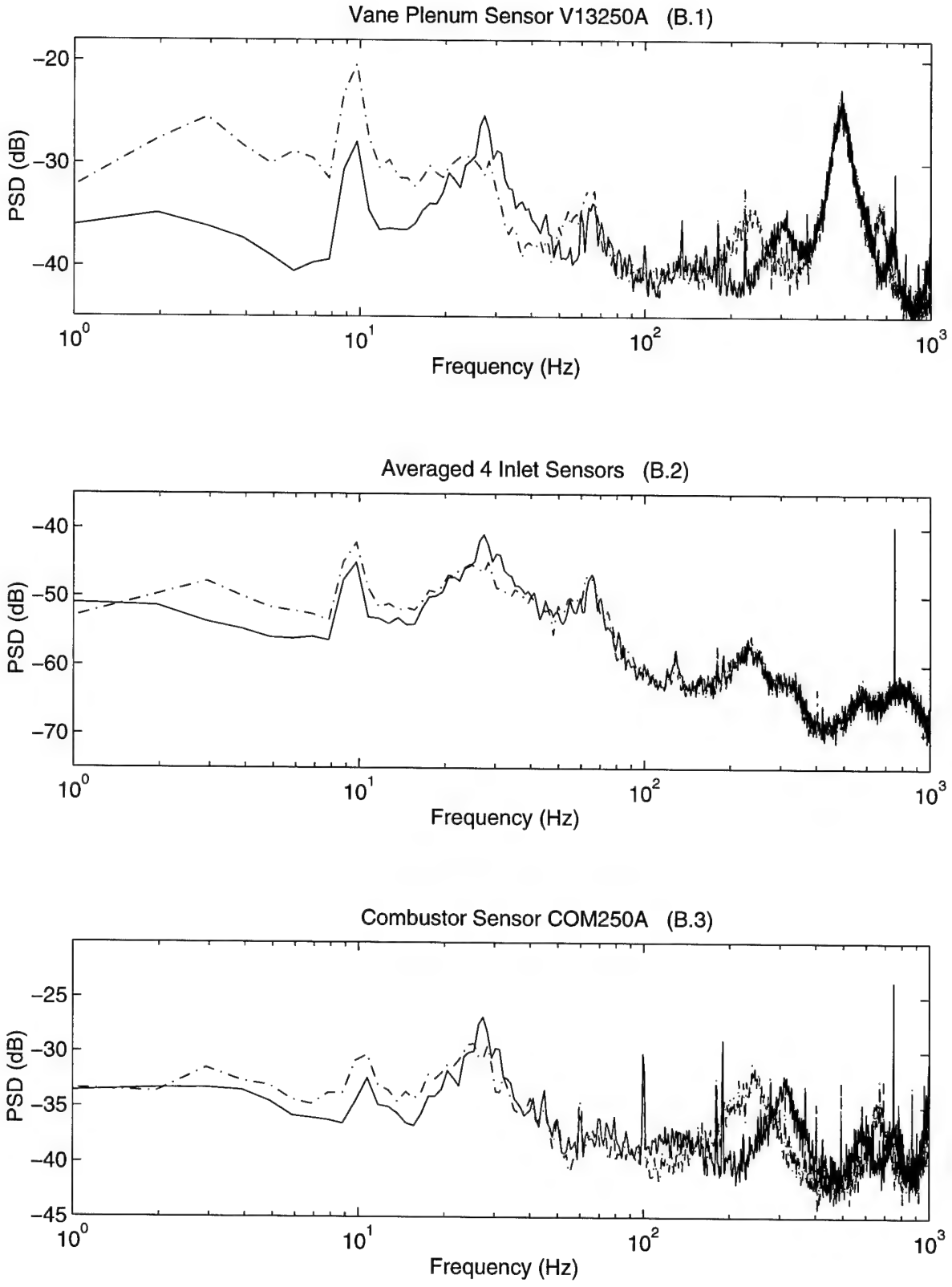

Figure 5.25B Open and Closed Loop Power Spectral Density Plots Prior to Open Loop Surge Point: Late in Experimental Testing. Notice 10 Hz Peak

Chapter 6

LTS-101 Engine Modeling

6.1 Introduction

Modeling the LTS-101 is important in the control design process. Ideally, one can use a "first principles" type model in compensator development. If the engine phenomena are accurately captured, the resulting models could replace those obtained by cumbersome forced response tests described in Chapter 3.5. Models also permit easy prediction of the effect that changes to the system configuration create. For example, if the inlet duct is lengthened on the experimental rig, a model adjustment predicts modal frequency shifts. In addition, a model provides a universal means to represent common features on various engines. Therefore, if a reasonable model representation predicts experimental data for one type of engine, the model may accurately portray a larger turboshaft engine when adjusted for geometric configuration.

At this point, modeling results do not predict the LTS-101 forced response transfer functions well enough to use in the control design process. However, modeling is a valuable instrument to understand the engine. This chapter explains the techniques used to represent experimental data, specifically the forced response relation between the input, which is the valve command signal and the output, which is the inlet pressure signal (Figure 6.1).

6.2 Lumped Parameter Model

In this section, lumped parameter fluid elements are used to examine the surge mode.

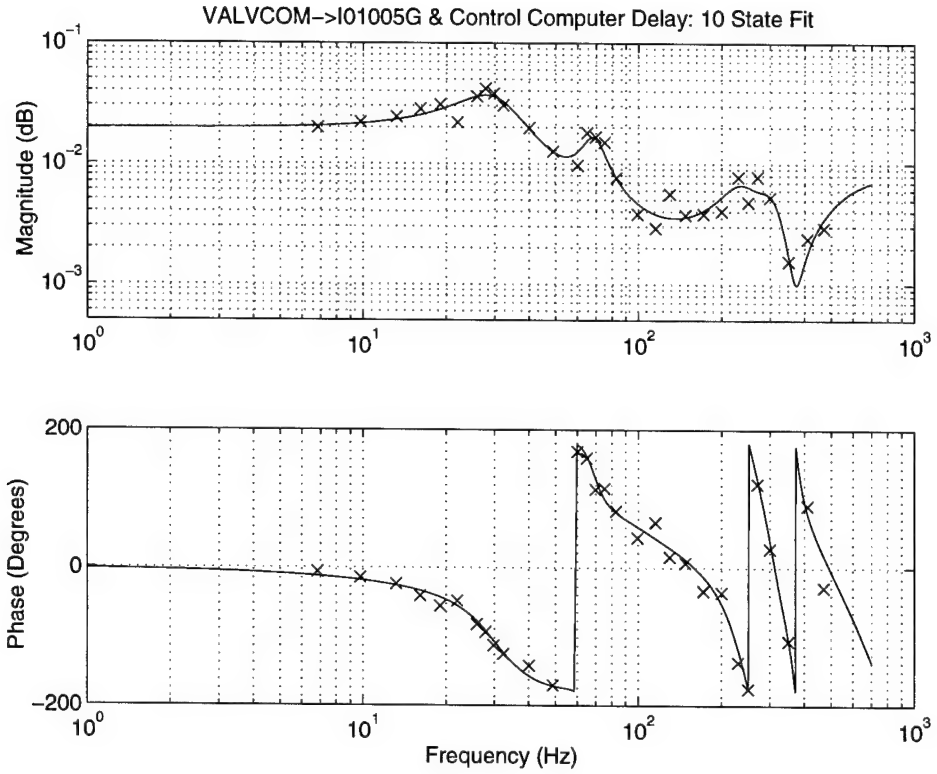

Figure 6.1 SIMO System Identification from Experimentally Determined Transfer Functions. (Same as Figure 3.26A).

First, the engine is divided into numerous components. A simplified first or second order differential equation represents each component and a constant operating point is assumed. This engine research focuses on engine stability following a small perturbation. Likewise, the primary modeling interest entails model stability for a small perturbation. The massflow and pressure perturbations are the two states of interest for this model.

In order to facilitate component linking, variables are nondimensionalized. ϕ is the nondimensional axial flow while ψ is nondimensional pressure.

$$\phi = \frac{\dot{m}}{\rho * U_{ref} * A} \tag{6.1}$$

If the density and area are assumed constant,

$$\phi = \frac{u}{U_{ref}} \tag{6.2}$$

$$\psi = \frac{P}{\rho * U_{ref}^{2}} \tag{6.3}$$

The basic component relationships are written as transmission matrices in Appendix H. Common inputs and outputs link components together. The LTS-101, modeled in Figure 6.2, is composed of a lumped inlet duct, actuator disk, lumped diffuser duct, lumped plenum, and lumped exit duct. Equation 6.4 is an intermediate step that links several transmission matrices using the number designation from Figure 6.2.

$$\begin{bmatrix} \psi_6 \\ \phi_6 \end{bmatrix} = \begin{bmatrix} Lumped \\ Exit \\ Duct \end{bmatrix} \cdot \begin{bmatrix} Lumped \\ Plenum \end{bmatrix} \cdot \begin{bmatrix} Lumped \\ Diffuser \\ Duct \end{bmatrix} \cdot \left(\begin{bmatrix} 1 & 0 \\ 0 & 1 \end{bmatrix} \cdot \begin{bmatrix} Actuator \\ Disk \end{bmatrix} \cdot \begin{bmatrix} Lumped \\ Inlet \\ Duct \end{bmatrix} \begin{bmatrix} \psi_1 \\ \phi_1 \end{bmatrix} + \begin{bmatrix} 0 \\ a_y \end{bmatrix} [\phi_0] \right) \tag{6.4}$$

After multiplying the transmission matrices, boundary conditions are applied. One assumes that there are negligible pressure perturbations in the atmosphere. Therefore ψ_6 and ψ_1 are

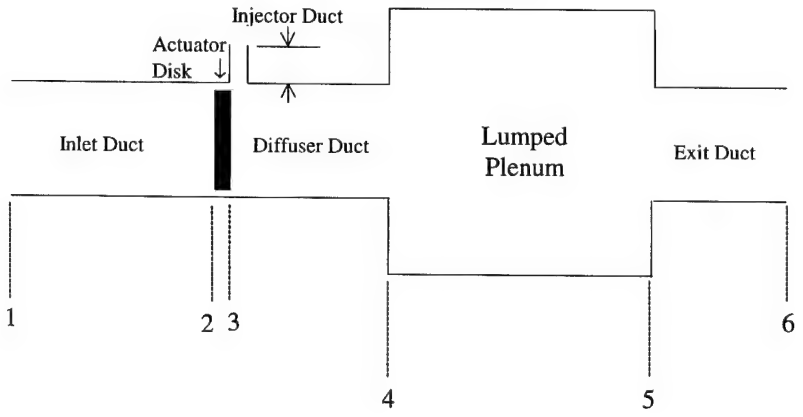

Figure 6.2 Lumped Parameter Model for the LTS-101

assumed to equal zero; thus allowing one to write the following equation:

$$\begin{bmatrix} 0 \\ \phi_6 \end{bmatrix} = \begin{bmatrix} a(s) & b(s) \\ c(s) & d(s) \end{bmatrix} \begin{bmatrix} 0 \\ \phi_1 \end{bmatrix} + \begin{bmatrix} e(s) \\ f(s) \end{bmatrix} [\phi_0] \quad (6.5)$$

where the quantities a(s) through f(s) are the result of expanding equation 6.4. Considering the first relationship in this matrix:

$$0 = b(s) \cdot \phi_1 + e(s) \cdot \phi_0 \quad (6.6)$$

This yields a relation between injector axial flow and inlet axial flow:

$$\frac{\phi_1}{\phi_0} = -\frac{e(s)}{b(s)} \quad (6.7)$$

To find the output based on this transfer function, one can use transmission matrices to relate inlet static pressure at the compressor face and inlet axial flow:

$$\begin{bmatrix} \psi_2 \\ \phi_2 \end{bmatrix} = \begin{bmatrix} Inlet \\ Duct \end{bmatrix} \cdot \begin{bmatrix} \psi_1 \\ \phi_1 \end{bmatrix} \quad (6.8) \qquad \text{where} \begin{bmatrix} Inlet \\ Duct \end{bmatrix} = \begin{bmatrix} a_1(s) & b_1(s) \\ c_1(s) & d_1(s) \end{bmatrix}$$

Note that the inlet duct transmission matrix is written in symbolic notation. This allows quick acoustic duct replacement in later sections that refer to this section. After applying the atmospheric pressure perturbation boundary condition ($\psi_1 = 0$), one can determine that:

$$\psi_{inlet} = b_1(s) \cdot \phi_1 \quad (6.9)$$

where ψ_2 is redefined as ψ_{inlet}.

One also must relate ϕ_0 to the injector massflow. Throughout this thesis, a lump duct is assumed to connect the injector to the diffuser duct. Therefore, to link the injector, one can use an analysis similar to that above.

$$\begin{bmatrix} \psi_0 \\ \phi_0 \end{bmatrix} = \begin{bmatrix} 1 & -s \cdot \frac{L_{inj}}{L_{ref}} \\ 0 & 1 \end{bmatrix} \begin{bmatrix} \psi_{inj} \\ \phi_{inj} \end{bmatrix} \quad (6.10)$$

Which yields the following:

$$\phi_0(s) = \cdot\phi_{inj}(s) \qquad (6.11)$$

Substituting 6.9 and 6.11 into 6.7, one arrives at the final symbolic relation between the injector axial flow and the inlet static pressure.

$$\frac{\psi_{inlet}}{\phi_{injector}} = -\frac{e(s)}{b(s)} \cdot \frac{1}{b_1(s)} \qquad (6.12)$$

The model dimensions are derived from the LTS-101 dimensions. Several major assumptions are used to simplify this analysis. First, converging and diverging duct lengths are replaced with constant area ducts. Effective duct lengths are calculated by a conversion described in Pinsley [41]. The inlet duct accounts for the effective length of the inlet duct and distance through the compressor to the diffuser. The second lumped duct accounts for the diffuser length. Next, the model's injector only includes the components downstream of the high speed valve. The valve represents an air flow choke point in the injector duct. A lumped duct with massflow specified directly by valve area represents the effect of choking. Third, density is assumed constant throughout the model.

The lumped parameter transfer function, based on the LTS-101 data, is shown in Figure 6.3. For illustrative purposes, this transfer function between injector massflow input to inlet static pressure output ($\frac{\psi_{inlet}}{\phi_{injector}}$) is assumed to represent the behavior between the voltage command and the measured inlet static pressure ($\frac{\psi_{inlet}}{V_{comm}}$). The relation between ϕ_{inj} and V_{comm} is added to the final version of the model. The primary shortcoming of the lumped

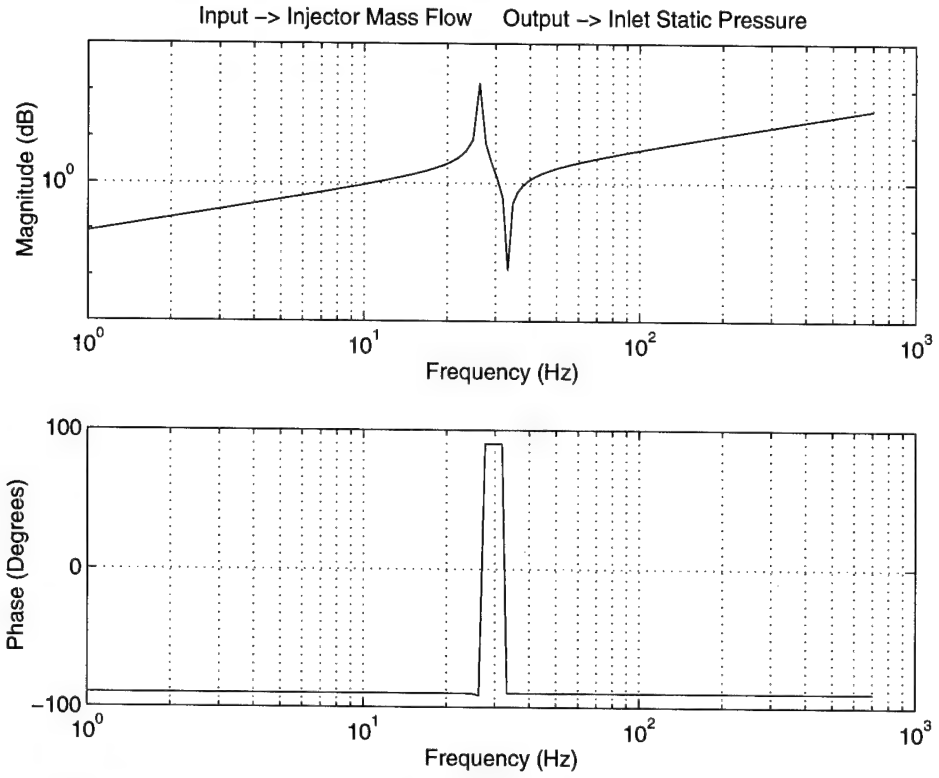

Figure 6.3 $\frac{\psi_{inlet}}{\phi_{injector}}$ **: Lumped Parameter Model Output. 98.4% Plenum Reduction and Reference Length Increased by a Factor of 6.4829.**

parameter model is that it only represents the surge mode. In addition, the model does not accurately represent the phase relationship between injected massflow input and inlet static pressure output. Furthermore, in order to match the surge mode frequency at ~28 Hz, two geometric parameters were adjusted; the resulting values, required to achieve a matching surge frequency, are unrealistic. The plenum volume was reduced by 98.4% of the LTS-101 volume estimate. Second, the reference length for the plenum B parameter, which is the entire effective duct length, is increased by factor of 6.4829. Although this model serves as a baseline in predicting the surge mode frequency, better assumptions are required for

reasonable geometric values.

6.3 Acoustic Duct Model

The lumped parameter model assumes that the air moves as slug flow and can not capture the acoustics. The first major model improvement is replacing the inlet and diffuser ducts with acoustic resonant ducts (Figure 6.4). See equation 6.13 for the transmission matrices.

$$\begin{bmatrix} \psi_6 \\ \phi_6 \end{bmatrix} = \begin{bmatrix} Lumped \\ Exit \\ Duct \end{bmatrix} \cdot \begin{bmatrix} Lumped \\ Plenum \end{bmatrix} \cdot \begin{bmatrix} Acoustic \\ Diffuser \\ Duct \end{bmatrix} \cdot \left(\begin{bmatrix} 1 & 0 \\ 0 & 1 \end{bmatrix} \cdot \begin{bmatrix} Actuator \\ Disk \end{bmatrix} \cdot \begin{bmatrix} Acoustic \\ Inlet \\ Duct \end{bmatrix} \begin{bmatrix} \psi_1 \\ \phi_1 \end{bmatrix} + \begin{bmatrix} 0 \\ a_y \end{bmatrix} [\phi_0] \right) \tag{6.13}$$

where an acoustic duct is defined

$$\begin{bmatrix} Acoustic \\ Duct \end{bmatrix} = \begin{bmatrix} \cos(L*\omega / a) & -i*\sin(L*\omega / a) \\ -i*\sin(L*\omega / a) & \cos(L*\omega / a) \end{bmatrix} \tag{6.14}$$

(See Appendix H for details.) In addition, temperature variation is accounted for within each duct. As the temperature increases for each duct, the corresponding speed of sound increases. The lumped parameter exit duct is maintained, as this system produces the most realistic output. This is realistic for the LTS-101 geometry, since the air moves slowly from the

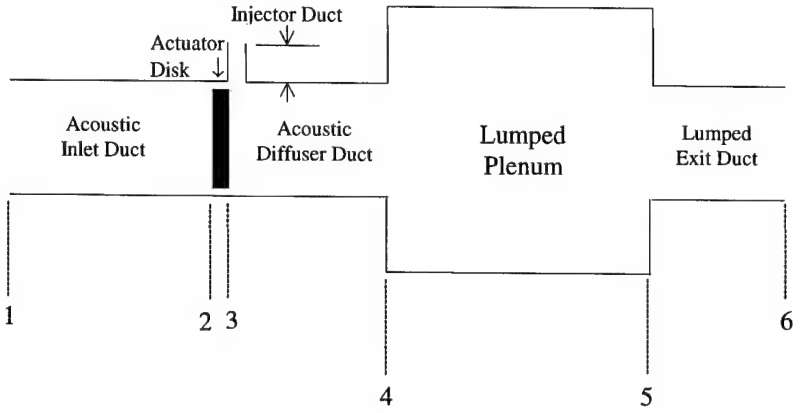

Figure 6.4 Acoustic Duct Model of LTS-101

combustor through a short duct length enroute to the gas producer turbine and exit nozzle.

$\frac{\psi_{inlet}}{\phi_{injector}}$ from this model produces a more accurate representation of the experimental output (Figure 6.5). The model phase plot roles off similarly to the experimental transfer function with phase unwrapping adjustment. As for shortcomings, the plenum volume was reduced by 80% in order to match the surge mode frequency. All other geometric parameters are as estimated. The first acoustic frequency at ~88 Hz is too large. After increasing inlet duct length by 22.64% and decreasing the plenum volume to 13% of its measured value, the acoustic mode can shift to ~79 Hz (Figure 6.6). The geometric values are still considered unreasonable, indicating the need for assumption revision.

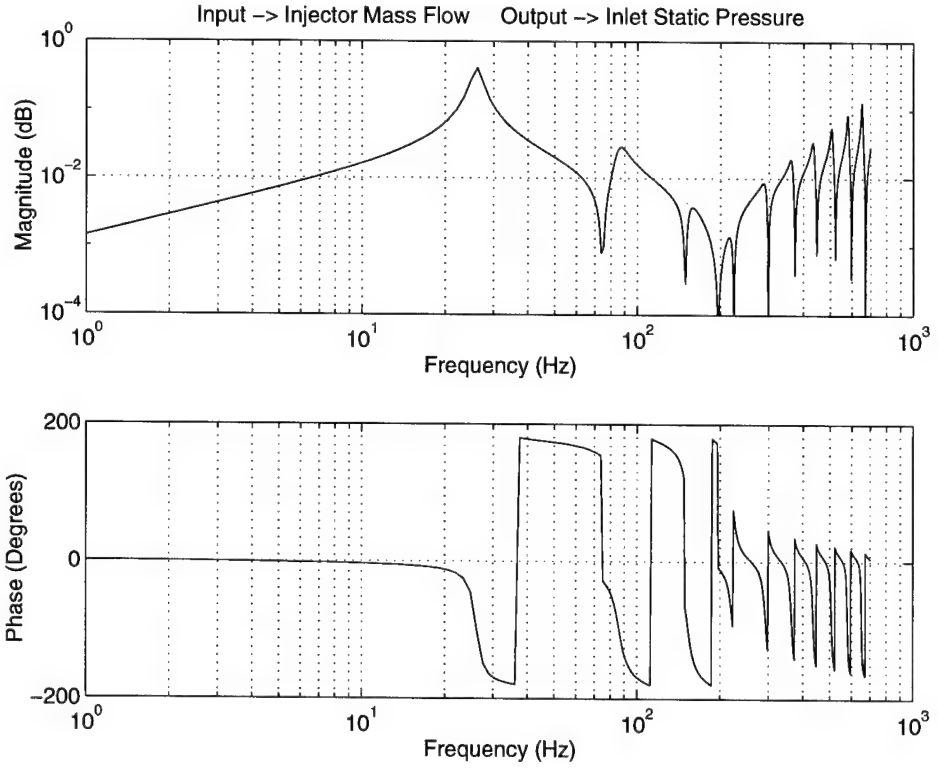

Figure 6.5 $\frac{\psi_{inlet}}{\phi_{injector}}$ **: Acoustic Duct Model Output. 80% Plenum Reduction**

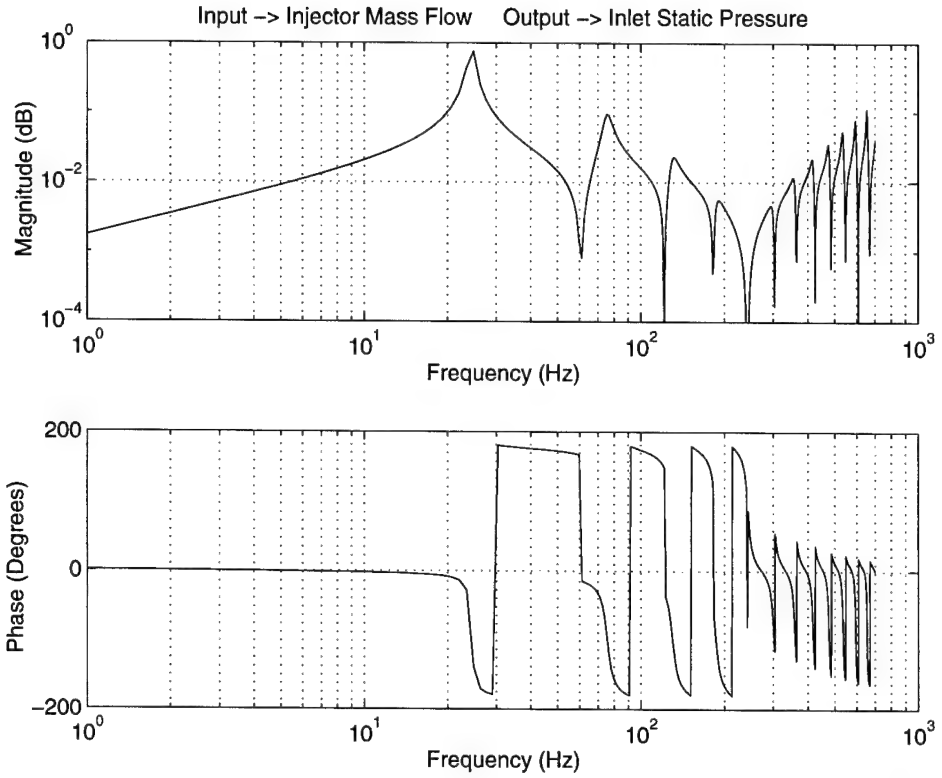

Figure 6.6 $\frac{\psi_{inlet}}{\phi_{injector}}$ **: Acoustic Duct Model Output. 87% Plenum Reduction and 22.64% Inlet Duct Increase.**

6.4 Acoustic Plenum Addition

The fact that the LTS-101 has an annular plenum suggests that acoustic variations may be associated with this component. Air flows from the diffuser and surrounds the combustor liner. Air flows into the liner via holes and is discharged through a converging channel towards the turbine. Several modeling assumptions are made to account for the geometry that governs this flowpath. The plenum volume is broken into three components (Figure 6.7). The airflow experiences a sudden expansion as it enters the plenum chamber. The plenum becomes an acoustic duct with a length equal to the engine liner. The original plenum volume is maintained between the acoustic and lumped plenums. Finally, the air exits the duct via a

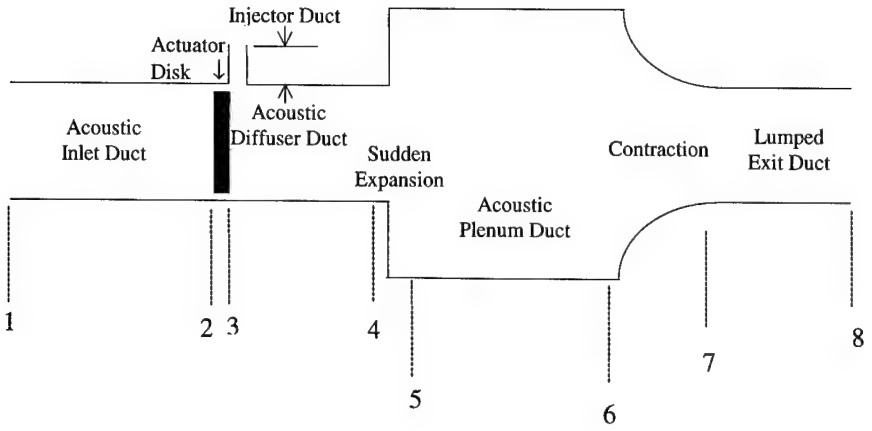

Figure 6.7 Final Acoustic Model of LTS-101 With Acoustic Plenum Addition.

smooth contraction. Equation 6.14 describes the distributed plenum replacement.

$$\begin{bmatrix} \psi_8 \\ \phi_8 \end{bmatrix} = \begin{bmatrix} Lumped \\ Exit \\ Duct \end{bmatrix} \cdot [Contraction] \cdot \begin{bmatrix} Acoustic \\ Plenum \\ Duct \end{bmatrix} \cdot \begin{bmatrix} Sudden \\ Expansion \end{bmatrix} \cdot \begin{bmatrix} Lumped \\ Diffuser \\ Duct \end{bmatrix} \cdot \left(\begin{bmatrix} 1 & 0 \\ 0 & 1 \end{bmatrix} \cdot \begin{bmatrix} Actuator \\ Disk \end{bmatrix} \cdot \begin{bmatrix} Lumped \\ Inlet \\ Duct \end{bmatrix} \begin{bmatrix} \psi_1 \\ \phi_1 \end{bmatrix} + \begin{bmatrix} 0 \\ a_y \end{bmatrix} \phi_0 \right) \tag{6.15}$$

The acoustic plenum is derived using a contraction, acoustic plenum duct, and sudden expansion that are defined as flows (See Appendix H).

$$[Contraction] = \begin{bmatrix} 1 & \Phi_o (1 - a_r^2) \\ 0 & a_r \end{bmatrix} \tag{6.16}$$

$$\begin{bmatrix} Sudden \\ Expansion \end{bmatrix} = \begin{bmatrix} 1 & 2\Phi_o (a_r - a_r^2) \\ 0 & a_r \end{bmatrix} \tag{6.17}$$

$$\begin{bmatrix} Acoustic \\ Plenum \\ Duct \end{bmatrix} = \begin{bmatrix} \cos(L*\omega/a) & -i*\sin(L*\omega/a) \\ -i*\sin(L*\omega/a) & \cos(L*\omega/a) \end{bmatrix} * \begin{bmatrix} \psi_0 \\ \phi_0 \end{bmatrix} \tag{6.18}$$

where a_r is an area ratio pertaining to the component's entrance and exit areas and Φ_0 refers to the mean axial flow.

In order to verify the acoustic plenum model, the original lumped duct model is reconsidered. Figure 6.8 compares the lumped plenum and acoustic plenum models, with all other duct components treated as lumped parameter ducts. Recalling the lumped plenum model in Figure 6.3, the plenum was reduced considerably to model the surge mode at 28 Hz. Therefore, this convergence test for the acoustic plenum will model the surge mode at 10 Hz. This permits more reasonable geometry for the test. The primary difference between the parameters is that the acoustic plenum effectively increases the surge mode frequency for a given plenum volume. In addition, when combined with the acoustic duct model, the additional duct length decreases the acoustic frequencies. Recall that as duct length increases, the corresponding acoustic frequency decreases.

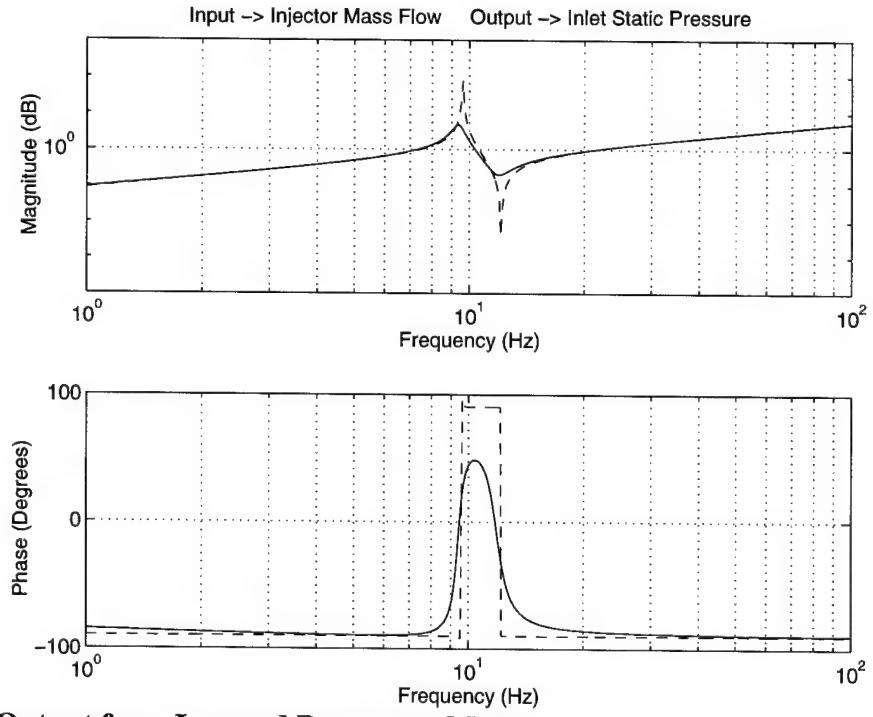

Figure 6.8 Output from Lumped Parameter Models: - Includes an Acoustic Plenum -- Includes a Lumped Plenum

Figure 6.9 shows the magnitude and phase of the final $\frac{\psi_{inlet}}{\phi_{injector}}$ relationship. This is generated from the following relationship.

$$\begin{bmatrix} \psi_8 \\ \phi_8 \end{bmatrix} = \begin{bmatrix} Lumped \\ Exit \\ Duct \end{bmatrix} \cdot [Contraction] \cdot \begin{bmatrix} Acoustic \\ Plenum \\ Duct \end{bmatrix} \cdot \begin{bmatrix} Sudden \\ Expansion \end{bmatrix} \cdot \begin{bmatrix} Acoustic \\ Diffuser \\ Duct \end{bmatrix} \cdot \left(\begin{bmatrix} 1 & 0 \\ 0 & 1 \end{bmatrix} \cdot \begin{bmatrix} Actuator \\ Disk \end{bmatrix} \cdot \begin{bmatrix} Acoustic \\ Inlet \\ Duct \end{bmatrix} \begin{bmatrix} \psi_1 \\ \phi_1 \end{bmatrix} + \begin{bmatrix} 0 \\ a_y \end{bmatrix} [\phi_0] \right) \quad (6.15)$$

The plenum volume is as geometrically estimated, and the inlet duct length is 35% longer than the estimate. Notice that the surge mode is at ~26 Hz, while the first acoustic mode is at ~74 Hz. If the plenum volume is decreased by 10% and the inlet duct length is adjusted to 29.1% of the estimate length, the surge mode returns to 27 Hz and the first acoustic resonance becomes 78 Hz (Figure 6.10). In addition, modeling assumptions make the phase lag larger

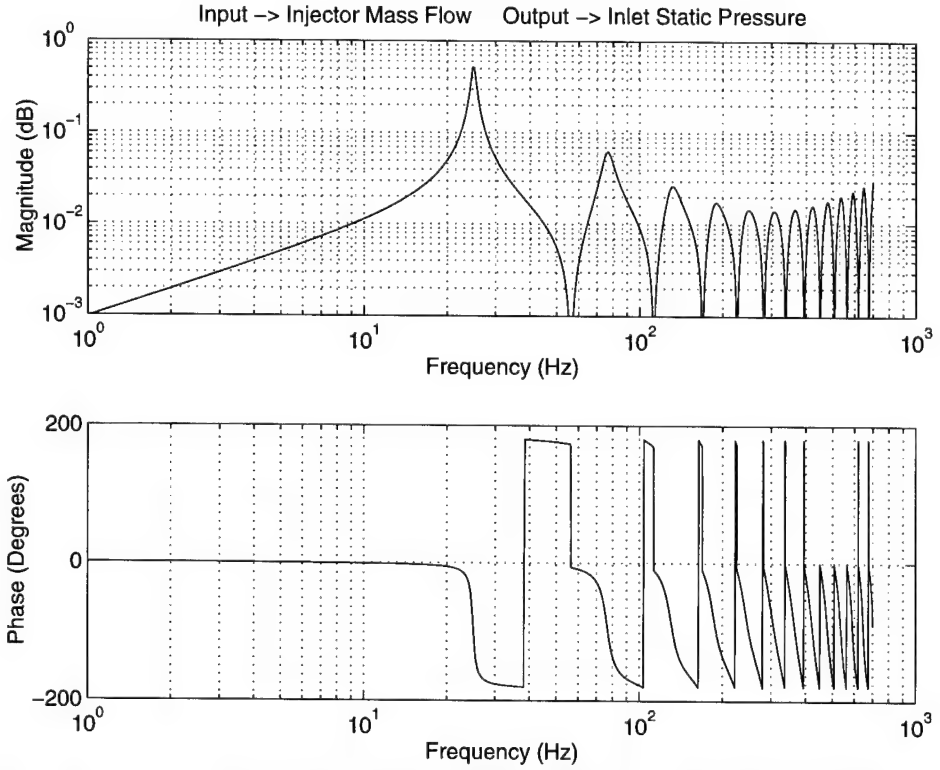

Figure 6.9 $\frac{\psi_{inlet}}{\phi_{injector}}$ Output from Acoustic Model. Full Sized Plenum. 32.3% Increased Inlet Duct

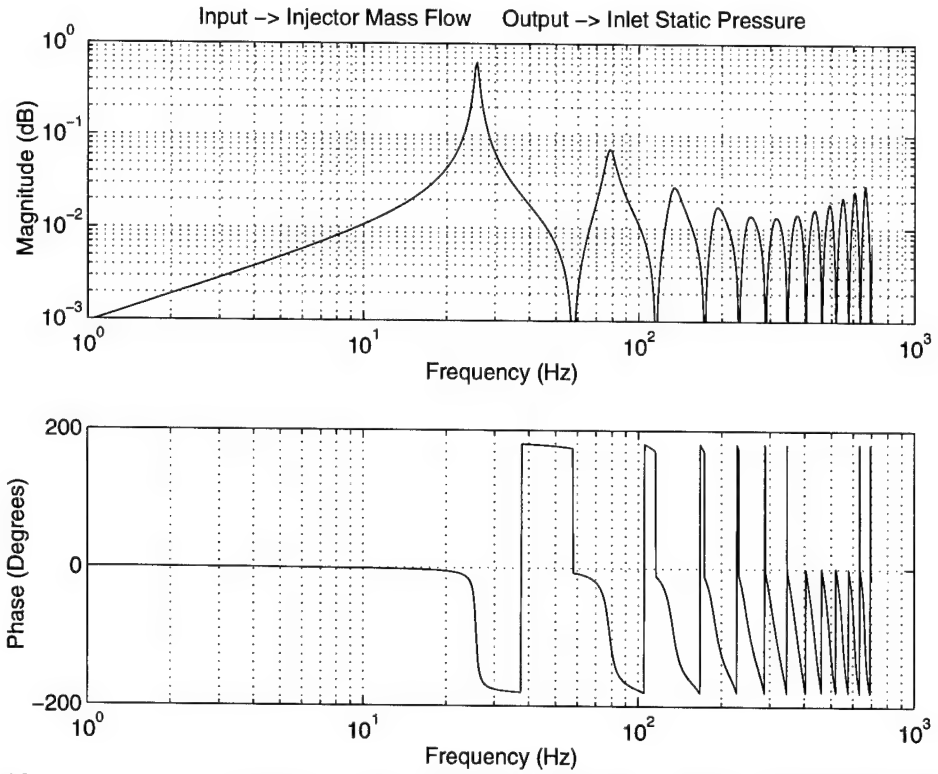

Figure 6.10 $\frac{\psi_{inlet}}{\phi_{injector}}$ **Output from Acoustic Model. Full Sized Plenum. 29.1% Increased Inlet Duct and 10% Decreased Plenum**

than in experimental data. This is reasonable for the gross assumptions that are made in this analysis.

Finally, the model's ($\frac{\psi_{inlet}}{V_{comm}}$) relation is plotted against the experimental data (Figure 6.11). To transition from ϕinj to V_{comm}, the valve dynamics (Figures 6.12 and 6.13) and the $\frac{\phi_{inj}}{V_{pos}}$ for mean air injection are added. Matlab's invfrqs.m is used to place four poles and two zeros to the experimentally measured valve dynamics. Note that the valve dynamics add extra phase to the model. In addition, a compressor lag is added to the model to decrease the magnitude of the high frequency peaks, as is observed in the experimental data.

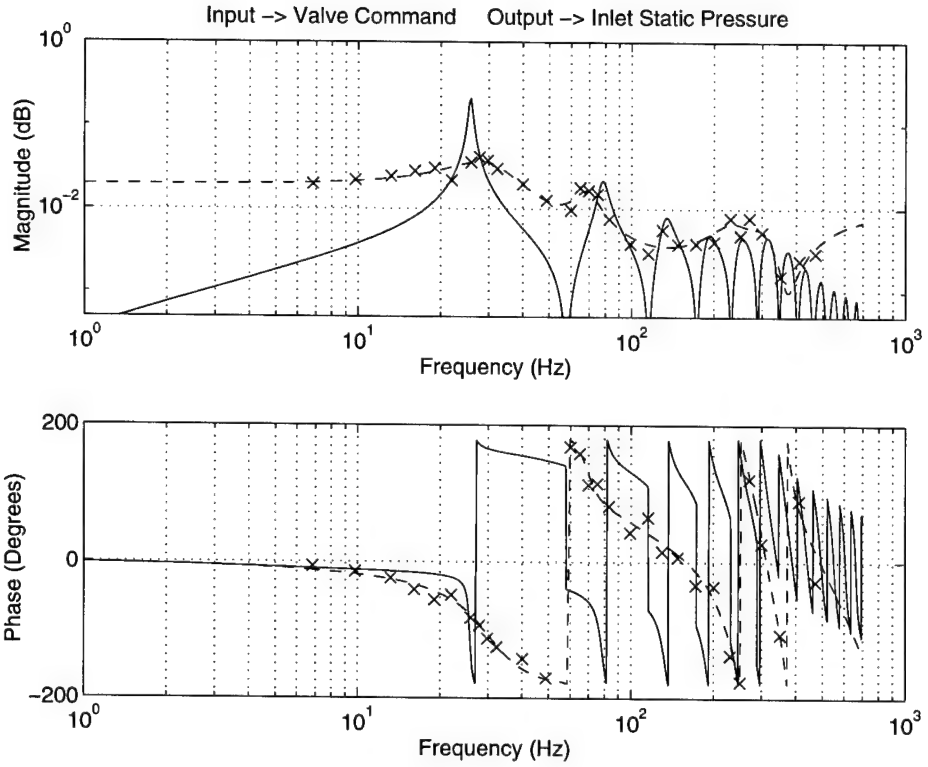

Figure 6.11 $\frac{\psi_{inlet}}{V_{comm}}$ **Output from Final Acoustic Model**

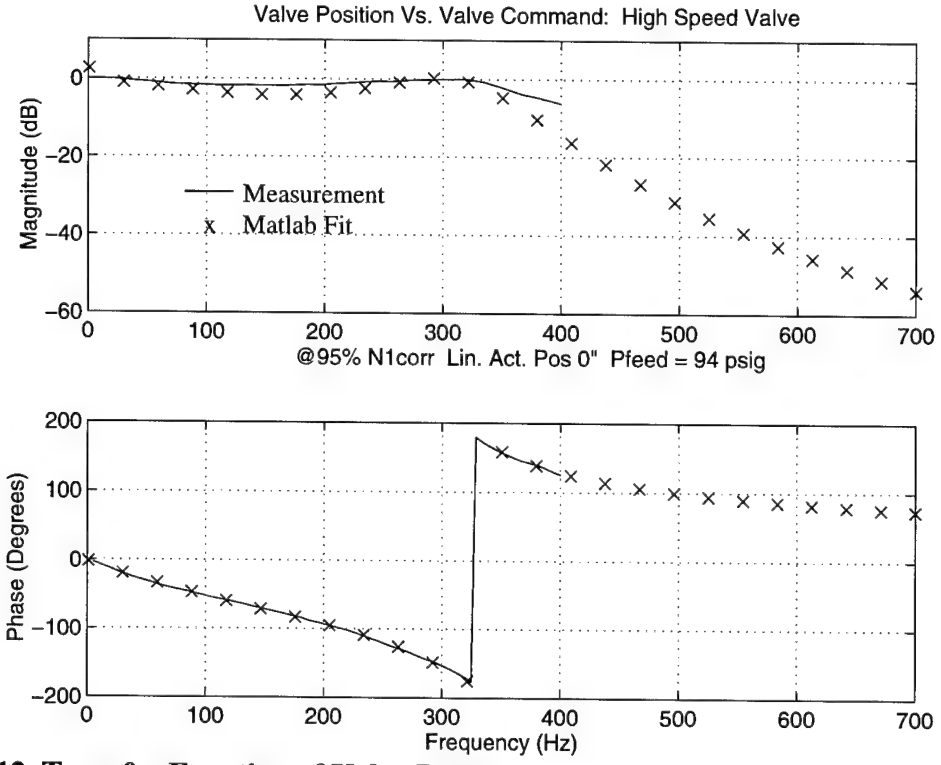

Figure 6.12 Transfer Function of Valve Dynamics

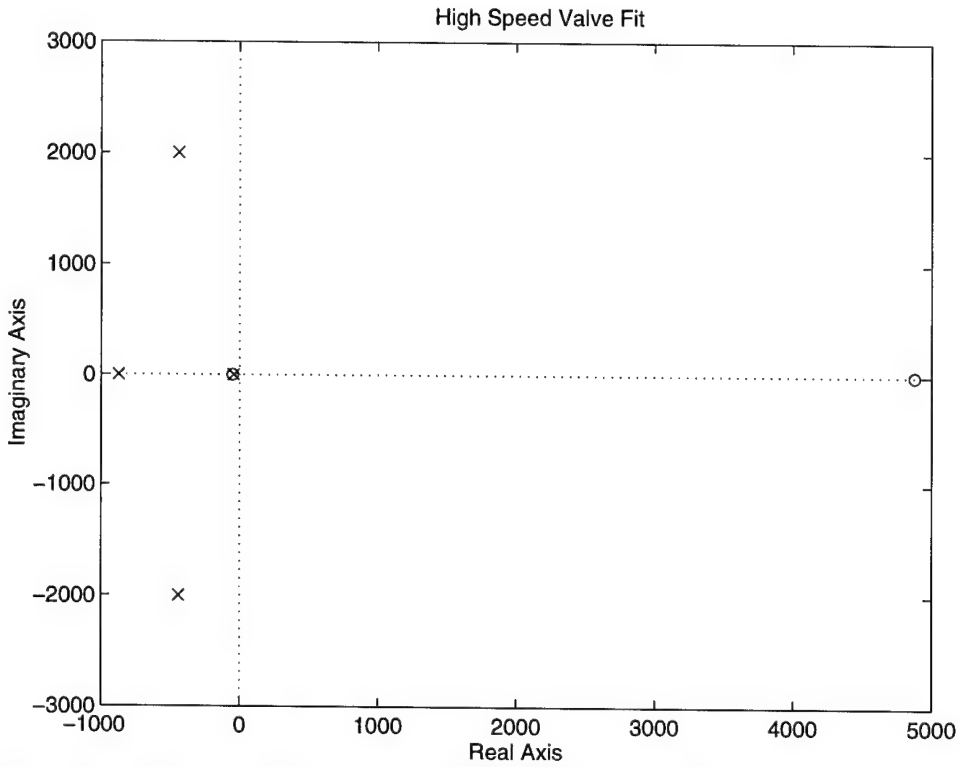

Figure 6.13 Pole - Zero Locations of the Transfer Function Fit.

6.4 Modeling Conclusions

The modeling experience demonstrates the difficulty in representing the engine acoustics. Much detail is neglected in the simplified model. As a result, the author is forced to make an educated guess and "see how it affects the output". The final model suggests that most of the engine components are acoustic in nature. Adjustments for converging and diverging ducts are essential in order to achieve the correct frequencies. Perhaps a more important model accomplishment is the indication that the 68 Hz mode is an acoustic resonance in nature. The acoustic model places the first acoustic mode within ~6 Hz of the experimental data while the surge mode is at 27 Hz. The fact that the model does not accurately portray the data indicates shortcomings in the model. These shortcomings include inaccurate assumptions and components poorly modeled by the selected transmission matrices.

Chapter 7

Conclusions

7.1 Summary of Research Efforts

The overall objective of this thesis is to experimentally demonstrate active stabilization of compressor surge on a small helicopter engine, and to measure the resulting operating range improvement. Using 95 psig diffuser throat injection, a relatively large, surge free region of near zero characteristic slope at the speedline peak is created. With mean air injection, the system has a 27 Hz surge mode, and a series of higher frequency acoustic resonances, the first of which occurs at 68 Hz.

Surge is stabilized in the LTS-101 using active feedback control. At 95% N1 corrected, an H-infinity compensator achieves a 0.98% reduction in stalling massflow. This equates to a 10.7% increase in the overall operating range of the engine. The one sided H-infinity compensator achieves range extension by damping the surge mode, while avoiding excitation of the acoustic resonances. Less complex feedback schemes are unable to achieve compressor massflow reduction. In addition, this research incorporates a rigorous, systematic robust control redesign approach.

Finally, a linear, acoustic model is derived for the transfer function relation between high speed valve command and the static pressure signal at the inlet. The model predicts the 27 Hz surge mode, and attributes the 68 Hz mode to acoustic resonances of the system.

7.2 Main Results and Conclusions

The most significant thesis contribution is to present the first experimental surge line decrease on a small helicopter engine. As a result, this experimental evidence establishes the viability of the "smart engines" active control theory in centrifugal compressors with large pressure ratios per stage.

Additional contributions pertain to the objectives listed in the introductory chapter:

1. Following the engine rebuild, a number of mechanical modifications promote project success for this thesis. Specifically, the new linear motion controller and actuator eliminate loading transients that often triggered surge in experiments prior to this effort. This modification permits engine surges to occur from mechanical or aerodynamic perturbations.

2. Performance has degraded as the engine experienced more surge events. The critical engine modes resonate at approximately the same frequencies (I.E. 28 Hz and 68 Hz); however, power spectral density plots began to show a large increase in peak magnitude at 10 Hz. This 10 Hz mode has unknown implications for future engine runs.

3. Forced response testing yields transfer function information between 7 and 680 Hz. After considering a number of transfer function combinations, one throat and two inlet transfer functions provide the best single-input multiple-output transfer function fit.

4. Closed loop stabilization extends the surge line. However, the first design excites the first acoustic resonance by unacceptable amounts. The best compensator does not excite this 68 Hz mode.

5. The best two sided compensator provided a 0.68% reduction in compressor exit stalling massflow. This equates to a 7.10% increase in the compressor exit operating range. While using the same H-infinity scheme, one sided injection yielded a 0.98% reduction in compressor inlet stalling massflow. Likewise, this is a 10.7% increase in the compressor inlet operating range. The one sided injection increases the engine's force output by 3.66% over the open loop case.

6. The compensation redesign procedure is developed and is available for further closed loop engine testing.

7. Acoustic modeling approximates the valve command input to inlet static pressure tap relation. The model predicts a surge mode at 27 Hz and various acoustic frequencies. Based on the model, the 68 Hz mode is attributed to acoustic system resonances.

8. Low frequency surge, perhaps triggered by the digital high pass filter, occurs at normally open loop stable massflows. This problem occurred more frequently as the engine experienced more surge events. In addition, the power spectral density plots began to show large increases in the magnitude of a peak at 10 Hz. It is suspected that the

two problems are interrelated. These factors prevented compensator testing using a design with additional plant dynamics. When compared to the plant used in the most successful compensators, the plant with additional dynamics gives a superior fit to the data. These additional modes are physically explained.

7.3 Future Recommendations

Several questions are unresolved and require further investigation:

1. The closed loop engine surge remains unexplained. Compensators that use a plant with additional low frequency modes are untested. This plant may improve compensator performance. The closed loop surge precursors initially resonate at 22 Hz prior to resonating at 28 Hz. If further testing indicates improves speedline extension, the extended inlet duct may explain a dominant 22 Hz mode if the surge mode is suppressed with compensation.

2. Compensators were not tested for the case with no mean air injection. One sided injection compensation schemes make this possible. The "best compensator" probably requires modification to provide such extension. Recall from [14] that the surge mode is at 22 Hz for the no air injection case.

3. A compensator that directly incorporates a high pass filter requires development and testing.

4. The magnitude of the 10 Hz peak increased with additional engine surges. A new series of forced response test is necessary to generate transfer functions that account for changing engine dynamics.

References

1. Emmons, H. W., C. E. Pearson, and H. P. Grant. "Compressor Surge and Stall Propagation." Trans. of the ASME. Vol. 79, April 1955, pp. 455-69.

2. Greitzer, E. M. "Surge and Rotating Stall in Axial Flow Compressors, Part I: Theoretical Compression System Model." ASME Journal of Engineering for Power. Vol. 98, April 1976, pp. 190-98.

3. Greitzer, E. M. "Surge and Rotating Stall in Axial Flow Compressors, Part II: Experimental Results and Comparison with Theory." ASME Journal of Engineering for Power. Vol. 98, April 1976, pp. 199-217.

4. Epstein, A. H., J. E. Ffowcs Williams, and E. M. Greitzer. "Active Stabilization of Aerodynamic Instabilities in Turbomachines." AIAA Journal of Propulsion and Power. Vol. 5, No. 2, March-April 1989, pp. 203-11.

5. Bodine, A. G. "Sonic Control of Dynamic Compressor Instability." Symposium on Compressor Stall, Surge, and System Response. 6-9 March 1960, pp. 21-22.

6. Amann, C. A., G. E. Nordenson, and G. D. Skellenger. "Casing Modification for Increasing the Surge Margin of a Centrifugal Compressor in an Automotive Turbine Engine." ASME Journal of Engineering for Power. Vol. 97, July 1975, pp. 329-36.

7. Fink, D. A. "Surge Dynamics and Unsteady Flow Phenomena in Centrifugal Compressors." MIT Gas Turbine Laboratory Report No. 193, 1988.

8. Huang, X. Y. and J. E. Ffowcs Williams. "Active Stabilization of Compressor Surge." Journal of Fluid Mechanics. Vol. 204, pp. 245-62.

9. Pinsley, J. E., G. R. Guenette, E. M. Greitzer, and A. H. Epstein. "Dynamic Control of Centrifugal Compressor Surge Using Tailored Structures." Journal of Turbomachinery. Vol. 113, October 1991, pp. 723-32.

10. Gysling, D. L., J. Dugundji, E. M. Greitzer, and A. H. Epstein. "Dynamic Control of Centrifugal Compressor Surge Using Tailored Structures." Journal of Turbomachinery. Vol. 113, October 1991, pp. 710-22.

11. Simon, J. S. "Feedback Stabilization of Compression Systems." MIT Gas Turbine Laboratory Report No. 216, March 1993.

12. Ffowcs Williams, J. E. and W. R. Graham. "An Engine Demonstration of Active Surge Control." ASME Paper 90-GT-224.

13. Ffowcs Williams, J. E., M. F. L. Harper, and D. J. Allwright. "Active Stabilization of Compressor Instability and Surge in a Working Engine." ASME Journal of Turbomachinery. Vol. 115, January 1993, pp. 68-75.

14. Borror, S. L. "Natural and Forced Response Measurements of Hydrodynamic Stability in an Aircraft Gas Turbine Engine." M. S. Thesis, Department of Aeronautics and Astronautics, Massachusetts Institute of Technology, May 1994.

15. Corn, B. A. "Surge Dynamics of a Helicopter Engine Gas Generator." M. S. Thesis, Department of Aeronautics and Astronautics, Massachusetts Institute of Technology, February 1998.

16. Didierjean, L. and J.D. Paduano. "A Surge Model for High Pressure Ratio Centrifugal Compressor Engines." PRET working paper, Department of Aeronautics and Astronautics, Massachusetts Institute of Technology, 25 March 1996.

17. Didierjean, L. and J. D. Paduano. "Active Surge Control of HP Centrifugal Compressors." PRET working paper, Department of Aeronautics and Astronautics, Massachusetts Institute of Technology, 25 July 1996.

18. Al-Essa, F. K. S. "An Experimental Study of Compressor Stability in a 450 kW Helicopter Gas Turbine Engine." M. S. Thesis, Department of Mechanical Engineering, Massachusetts Institute of Technology, September 1997.

19. Bae, J. W. "An Experimental Study of Surge Control in a Helicopter Gas Turbine Engine." M. S. Thesis, Department of Aeronautics and Astronautics, Massachusetts Institute of Technology, February 1998.

20. Weigl, H. J. "Active Stabilization of Rotating Stall and Surge in a Transonic Single Stage Axial Compressor." MIT Gas Turbine Laboratory Report No. 226, July 1997.

21. Bell, J. T. "Measurements of Forced and Unforced Aerodynamic Disturbances in a Turbojet Engine." M. S. Thesis, Department of Aeronautics and Astronautics, Massachusetts Institute of Technology, May 1993.

22. Setra Technical Data. "Pressure Transducer Handbook." 1997.

23. McNulty, G. S. "A Study of Dynamic Compressor Surge Control Strategies for a Gas Turbine Engine." M.S. Thesis, Department of Aeronautics and Astronautics, Massachusetts Institute of Technology, September 1993.

24. Berndt, R. G. "Actuation for Rotating Stall Control of High Speed Axial Compressors." M. S. Thesis, Department of Aeronautics and Astronautics, Massachusetts Institute of Technology, February 1995.

25. Simon, J. S., C. M. Van Schalkwyk, and L. Didierjean. FORTRAN code for control law programs.

26. Corn, B. A. LTS-101 Gas Generator Data Archieve. Run 78. 1 August 1996. Created by Eric B. Nelson. 1998.

27. Corn, B. A. LTS-101 Gas Generator Data Archieve. Run 80. 6 August 1996. Created by Eric B. Nelson. 1998.

28. Corn, B. A. LTS-101 Gas Generator Data Archieve. Runs 78-90. July-August 1996.

29. Dean, R. C., Jr. "The Time Domain of Centrifugal Compressor and Pump Stability and Surge." ASME Journal of Fluid Engineering. Vol. 99, March 1977, pp. 53-63.

30. The MathWorks, Inc. "Matlab, Signal Processing Toolbox." User's Guide, December 1996.

31. Jacques, R. "Forse Transfer Function ID." Space Engineering Research Center, Massachusetts Institute of Technology, 1994.

32. Ljung, L. "System Identification: Theory for the User." Prentice Hall, New Jersey, 1987.

33. Kwakernaak, H. "Robust Control and H-Infinity Optimization: Tutorial Paper". Automatica, Vol. 29, No. 2, 1993, pp. 255-73.

34. Doyle, J. C., K. Glover, P. Khargonekar, and B. Francis. "State Space Solution to Standard H_2 and H_∞ Control Problems." IEEE Transactions on Automatic Control. Vol. 34, No. 8, 1989, pp. 831-47.

35. Glover, K. and J. C. Doyle. "State Space Formulae for All Stabilizing Controllers that Satisfy an H_∞ - Norm Bound and Relations to Risk Sensitivity." Systems and Control Letters. Vol. 11, 1988, pp. 167-72.

36. Spakovszky, Z. S. H. J. Weigl, J. D. Paduano, C. M. Van Schalkwyk, K. L. Suder, and M. M. Bright. "Rotating Stall Control in a High-Speed Stage with Inlet Distortion, Part I - Radial Distortion." ASME Gas Turbine and Aeroengine Congress and Exposition. Stockholm, Sweden. Paper 98-GT-265.

37. Spakovszky, Z. S. C. M. Van Schalkwyk, H. J. Weigl, J. D. Paduano, K. L. Suder, and M. M. Bright. "Rotating Stall Control in a High-Speed Stage with Inlet Distortion, Part II- Circumferential Distortion." ASME Gas Turbine and Aeroengine Congress and Exposition. Stockholm, Sweden. Paper 98-GT-264.

38. Smith, R. S. "Technical Notes and Correspondence: Eigenvalue Perturbation Models for Robust Control." IEEE Transactions on Automatic Control. Vol. 40, No. 6, June 1995, pp. 1063-66.

39. Paduano, J. D. "Using Matlab to Study Time-Delay Approximations." Lecture Handout for course 16.357. Massachusetts Institute of Technology. 5 September 1996.

40. Corn, B. A. LTS-101 Gas Generator Log Book. Run 75. 29 July 1996.

41. Pinsley, J. E. "Active Control of Centrifugal Compressor Surge." M. S. Thesis, Department of Aeronautics and Astronautics, Massachusetts Institute of Technology. October 1988.

42. Appleby, B. D. "Robust Estimator Design Using the H_∞ Norm and μ Synthesis." Ph. D. Thesis, C.S. Draper Laboratory, Department of Aeronautics and Astronautics, Massachusetts Institute of Technology. February 1990.

43. Paduano, J. D. "Transmission Matrices for Selected Compact Acoustic Elements." Lecture Handout for course 16.357. Massachusetts Institute of Technology. 19 September 1996.

Appendix A

Checklists

The purpose of this Appendix is to document the checklist procedures for LTS-101 operation

A.1 LTS-101 Engine Pre-Start Checklist (For Test Engineer)

Items with two boxes should be initialed by test engineer and technician. Record any special notes at end of checklist and store with engine run data.

Run #: _____ Date: _____

General Preparation

{ } Turn on steady state pressure transducers, & Kulite amplifiers. These should warm up for at least an hour

{ } Set filter board cutoff frequency. Should be set before each run as a precaution (to make sure it is working).
-- Middle Panel/Bottom. Lever.
-- On Computer, go to a:\Filter Type > setfilt Type Frequency > 1020.0 Hz Type > F10 key

{ } Turn on power to junction box (on stand, if not already on).
-- by Blowdown Compressor's back wall

{ } Start charging the engine's Batteries.

{ } Balance Kulites early during the warm-up period.

{ } Turn on pressure transducer cooling fan 30 minutes before expected calibration time.
-- in machine shop (plug in to outlet. The outlet is low on the wall behind milling machine.)

{ } Open oil vent valve downstairs.
-- little yellow lever on blue container. This step is not necessary every engine run.

{ } Turn on 1) air dryer, 2) cooling water for compressor, and 3) air compressor. Let them warm up for 30 minutes.
-- Sign off the log, press the start button, and then put the yellow lever at the far wall in line (for on).

{ } O.K. air usage with other students who may be using oil-free air (especially if actuator will be used.)

{ } Open air line to roof for about five minutes to blow out any water which might be in line. Close when finished.
-- Lever in line for on. At the ladder to the downstairs.

{ } Warn shop personnel and others in immediate area.

{ } Check that fuel amount is sufficient for run.

{ } If concerned about water leakage, spread absorbent "kitty litter".

{ } Engine inspected by second technician if changes made to stand.

{ }{ } Visual inspection of engine to verify that all wires are attached and fittings are secure. a) flow fence b) fittings under shroud c) fuel controller fittings.

{ } Check that roof inlets are open and heater on roof is off.

{ } Place plastic disk into Allison's inlet duct to seal it off.

{ } Open blast gate.

{ } Check that no instrumentation is hooked to Allison.

{ } Turn on cameras, lights, and monitors.

{ } Clean area around engine such that it is free of loose papers, tools, etc.

{ } Open oil vent valve on test stand. Verify Allison vent valve is closed.

{ } Fuel solenoid switch on junction box is set to LTS-101.

{ } Push the throttle position off of the home position (for start-up purposes).

{ } Start up Genesis.

{ } Check settings for vibrometer. -- Filter out -- Disp Mils p_p -- Range 0-1.5 -- Power on

{ } Balance bridge amplifiers a final time. --*We don't ever change this.*

{ } Detach and unplug battery charger. Close knife switch on battery.

{ } Turn on control panel in hall. Set EGT setpoint 3 to 899°C.
-- Little black box on blue stand marked EGT > Press setpts > Press 899 > Press setpts twice until you see "run".

{ } Supply ear and eye protection for individuals who might enter test cell (2 sets minimum).

{ } Set up log book entry.

{ } Make sure that P3 line is either capped or attached to the pressure gauge outside the cell.

Instrumentation

{ } Check output to valve and make sure valve monitoring line is attached.
-- switch three way valve in back of barometric Setra to calibration (large tube).

{ } Make sure barometric and 100 psi Setra digital pressure gauges are set to read in. H_2O.
-- There are two of them. Press conv button for both. ***Set Setra selector switch to 1.***

{ } Within c:\, type: gconfig ; then restart computer (<cntrl><alt><del>) go to c:\genesis2 Calibrate P1, P3, and P5 using automatic Genesis routine (currently 'calibmod run'). Verify that 100 psia con be supplied for the high pressure reference. Adjust regulator so that this amount is supplied.
-- Turn on three panels on rack.
-- Turn on vacuum pump.
-- Open valve of high pressure (yellow lever in line, by dial) < Press Return > on computer when completed.

{ } Verify that Vacuum in P calibration line and the high pressure in the P3 and P5 calibration line are relieved. Manually relieve if necessary.
-- These are two little black levers in the back of the blue Setra holder.

{ } Use 'calibp1 MoDaHoMi', 'calibp3 MoDaHoMi', and 'calibp5 MoDaHoMi' to determine scales and offsets. Manually record in log book.
-- Ex. Ap081301

{ } Switch Setra **back to psia** and selector switch to 1.

{ } Switch valve behind barometric Setra such that it will read cell pressure. -- *(to small tube).*

{ } Make sure Zip Drive is not attached to the high speed data acquisition computer.

{ } Calibrate Kulites using adtdvm.exe. Note atmospheric pressure in logbook.
-- Use the High Speed Data Acquisition Checklist.

{ } If not using a Kulite port, assure that caps are securely fastened.

{ } Initialize data logging, making sure trigger line is attached.
-- See High Speed Data Acquisition Checklist.

{ } Prepare the high speed data acquisition system.
-- f:\run96\15sec
-- cd h01 type > run
-- chose the following two options when you want the data set: 1) Acquire and 2) Begin Acquire (to begin the first data set).

{ } Take sample scan of data to verify disk space and data logging is functional.
-- High Speed Data Acquisition Computer.

{ } Verify that a usable monitor and computer is attached outside.

{ } Turn high pressure reference line off. *-- Yellow lever out of line. It's located by dial.*

{ } Recommended that you cut air supply to shock tube and Sloan guys.
-- Turn the red knob clockwise to close. In the stock room.

Immediately Prior to Start

{ } Turn on cooling water to shroud. *-- Yellow, lever in line is for on (under shroud, in back).*

{ } Turn on cooling water to Kulites. *-- Yellow Lever, in line for on.*

{ } Turn on oil cooling fan. *-- Switch front: above circuit box.*

{ } Reset Genesis computer (or Genesis will lock the computer up!).

{ } Make sure that *.prn files are deleted from c:\genesis directory before beginning. (Note: *.prn files are the steady state data files generated during the run before they are converted to run??.dt1 and run??.dt2 Matlab formats by savelyc.exe. If you have non-converted files, convert them before deleting. You should execute savelyc ??, where ?? is the run #, immediately after a test is run.)

{ } Turn on power strip connected to linear motor, throttle stepper motor controller, and the V command box for the high speed Moog valve.
-- Turn on three panels here. Important for linear motion controller.
-- Actuator may return to home position (Steps to assure C code initialization is working).
-- Jog the actuator in extension via keyboard.
-- Run positioning program (Currently #5) via keyboard.

{ } Turn on V command box unit. Check to see that the voltages balance at ~40 volts.

{ } Start Genesis engine program (currently 'runtime lycomv4 start').
-- DO NOT START GENESIS BEFORE LINEAR MOTION CONTROLLER STEPS.

{ } Manually enter calibration scales and offsets.
-- Press <a> when complete.

{ } Turn off data logging (alt-l).

{ } Test throttle and linear actuator. Return throttle to 0° and linear actuator to home. Set linear actuator back to inactive (alt-a).

{ } Double check that Setra pressures gauges read in psia and the selector switch is on 1.

{ } Make sure any other equipment needed for run (stop watch, function generator, spectrum analyzer, etc.) is available.

{ } Call Bob Flemming. Inform him that we are using the air and are running the engine.

{ } Shut the large shop doors on lower level.

{ } Clear cell and give nearby a last warning.

{ } Test fire ignite. Listen for proper operation.

Ready, set, go.

A.2 LTS-101 Engine Shut Down Checklist (For Test Engineer)

{ } Turn off data logging (alt-l).

{ } Turn off fuel pump, etc.

{ } Visual inspection of engine.
-- Verify all wires are attached and fittings secure. a) flow fence b) fittings under shroud c) fuel controller fittings.

{ } Turn off air dryer and air compressor. Sign off the usage sheet.

{ } Reopen the air supply for the shock tube experiment.
-- red knob turned counter clockwise for open.
{ } Turn off pressure transducer cooling fan.
-- in Machine shop (Recall the outlet is low on the shop wall.)
{ } Turn off oil cooling fan. *-- switch front: above circuit box.*

{ } Turn off V command box.

{ } Turn off power strip connected to linear motor, throttle stepper motor controller, and V command box.

{ } Open knife switch on battery. Plug in and attach battery charger, if desired.

{ } Turn off cameras, lights, and monitors for cameras.

{ } Save steady state data on Genesis computer.
-- Hook up the zip drive to the Genesis computer. Remove the printer port, and genesis adapter to do so.
-- Within c:\genesis\, orient *.prn files. The system uses whatever is in enga000.prn & engb000.prn. So, copy enga00?.prn enga000.prn and engb00?.prn engb000.prn.
-- Then type savelyc ?? (yes, there is a space in the command. ?? stand for the run number. This program converts enga000 to Run??_x.dt1 & engb000 to Run??_x.dt2, which are binary codes that Matlab can use.
-- type > cd rundata
-- type > dir You will see Run??.dt1 & Run??.dt2. Return to c:\.
-- Go to d:\ type > mkdir run?? Then ? cd run?? Then > mkdir steady
-- Finally, convert the files: Go into c:\genesis\rundata Type copy run??.dt1 d:\run??\steady\run??.dt1 & copy run??.dt2 d:\run??\steady\run??.dt2

{ } Save the high speed data via zip disk.
-- Hook up the zip drive and reboot <cntrl><alt><del>
-- Create a directory within g:\run?? called 15sec > mkdir 15sec Enter the new 15sec directory. Then create the appropriate number of pointer directories called h01 h02 h??
-- Get within the appropriate h?? directory (so within g:\run??\15sec\h??) and type copy f:\run??\15sec\h01 etc. and copy f:\run??\45sec\L01 etc.
-- Get the calibration data as well in f:\lycomcal\cal005\ (and cal050 and cal250 if appropriate).

{ } Turn off all other computers and monitors, analyzers, etc. at the control station.

{ } Turn off steady state pressure transducers, computer with filter board and its monitor, and genesis computer. Assure that the vacuum was in fact turned off.

{ } Turn off power to junction box. -- *located at Blowdown Compressor back wall.*

{ } Turn off cooling water to shroud. -- *Yellow, on is in line (under shroud, in back).*

{ } Turn off cooling water to Kulites. -- *Yellow, on is in line.*

{ } Make sure any other equipment needed for run (stop watch, function generator, spectrum analyzer, etc.) is put away.

{ } If the engine surged, re pop the inlet into place if it came off. This step is usually performed after the engine cools. However, don't forget ....

{ } Write down necessary comments in log book entry.

A.3 High Speed Data Acquisition Checklist (For Test Engineer)

Run #: _____ Date: _____

{ } Amplifiers should have warmed up for 30 minutes.

{ } Start up the computer based filter and set the cutoff frequency (700 Hz)
-- Go to a:\filter
-- Type > setfilt Retype > 1020 Hz press F10 key See a:\filter on the screen.

{ } Balance 5 psig Kulite amps (R10, R12, R13, R14) for calibration.

{ } Calibrate 5 psig Kulites.
-- Hook up Setra and bike pump. Setting should be psi.
-- Exit to DOS. go to f:\lycomcal\cal005
-- Assure the following two files are within cal005: log1.cfg and log1.hdr
-- Type > adtdvm
-- answer the following questions: type > log1.hdr > T > 1 sec > F > <return>
> 390
-- To start the process: type > Q
-- Note: <control Z> can be used to break the calibration at any time.

The following are time increments where data is recorded:
-- 0:00 - 0:30 min. { ~ Patm
-- 1:30 - 2:00 min. { ~ 15.5 psia
-- 3:00 - 3:30 min. { ~ 16.5 psia

-- 4:30 - 5:00 min. { ~ 17.5 psia
-- 6:00 - 6:30 min. { ~ ≤ 18.5 psia (be careful of the 5 psig limit!!!!)

{ } Open 5 psig Kulites to atmosphere (turn the black lever back towards engine.

A. 4 LTS-101 Engine Operating Procedure (For Engine Operator)

Start / Run

1. Open manual fuel valve and turn on fuel pump.
2. Turn on data logging (alt-l).
3. Turn on fuel solenoid (alt-f).
4. Turn on starter and ignitor (alt-s and alt-l, respectively).
5. At 10% N1, set throttle at 25°
6. At 30% N1, run off starter and ignitor. Note highest EGT in logbook.
7. Go to idle (50% N1, throttle setting ~45°) for 3 minutes. Oil pressure should be at least 20 psig.
8. Enter cell to turn hotwires to "flow" setting.
9. Proceed with test plan. Oil pressure should be at least 80 psig at 95% N1.
10. Set hotwires to standby when test is complete.

Shut Down

1. Set engine to idle (50% N1, 45° throttle setting) for a 3 minute cool down.
2. Command throttle to 0°.
3. Turn off fuel solenoid (alt-f), fuel pump, and close valve.
4. Turn off data logging.
5. Exit Genesis, and save data.
6. Turn off all rack panels except the one containing the steady state pressure transducers.

7. Turn off oil cooling fan.

8. Perform a calibration of the steady state pressure transducers.

9. After engine has cooled sufficiently, turn off cooling water.

10. Execute savelyc ??, where ?? is the last two digits of the run number, and use engebn.m in Matlab to process and print steady state data.

Note: For emergency shutdown, shut off fuel solenoid immediately. It may be necessary to run the engine on the starter for ~3 minutes for cooling after N1 falls below 30%.

Refer to Tables A.1 and A.2 for a summarization of the commands and a range of expected data parameters.

Starting		
	<Alt> s	Toggle Starter
	<Alt> i	Toggle Ignitor
	<Alt> f	Toggle Fuel Solenoid
Nozzle		
	<Alt> a	(De)Activate Nozzle Commands
Throttle		
	<Alt> e	Move +1°
	<Alt> w	Move -1°
	<Alt> r	Move +5°
	<Alt> q	Move -5°
	<Alt> y	Move +0.1°
	<Alt> t	Move +0.1°
Instrumentation		
	<Alt> l	Toggle Data Logging
	<Alt> n	Trigger Inlet Pressure Tap Scanning
	<Alt> b	Trigger High Speed Data Acquisition
	<Alt> m	Mark Data
Emergency		
	~	Panic (Return to Idle)
	<esc>	Real Panic (sets throttle to 0° and exits run mode.)
Cooling Water		
	H	Add water (open valve)
	C	Decrease water (close valve)

Table A.1 Genesis Command Summary

	Idle Low	Idle High	95 % $N1_{corr}$ Low	95% $N1_{corr}$ High
Oil Pressure (psig)	59	63	80	100
T_{T3} (°C)	80	110	260	290
T_{T4} (°R)	800	900	1200	1250
EGT(°C)	290	320	340	385
Π_C	2.1	2.2	7	7.2
Inlet Pressure (psig)	-0.04	-0.05	-0.34	-0.37
$\dot{m}_{corr}$ (lb/s)	1.7	1.8	4.7	4.8
Actuator Load (lb)	280	300	160	210

Table A.2 Real Time Data Ranges.

A.5 Switch Over Checklist

{ } Turn the three way valve connected to the P1 transducers to the Allison/LTS-101 Label.
-- on lower rack (pressure transducers) top

{ } Flip the switch on the front of the pressure transducer rack to the Allison/LTS-101 label. This switch selects the P1 transducer that gets connected to the A/D card.
-- Double click (pressure transducers) front face

{ } Switch the DB25 connector on the back of the 16-bit A/D board.
-- Back of panels, take out connector labeled ACPC 16 for LTS-101. Labeled LTS-101 for Allison.

{ } Switch the thermocouples at the back of the rack.

	Allison Thermocouples	On Back of Panel	Reference Number	LTS-101 Thermocouples
{ }	#8 EGT (red label)	#7 -- first group	ref #8	EGT (green label # 17)
{ }	#5 Inlet Temperature (red label)	#4 -- first group	ref #5	Inlet Temp. (green label #13)
{ }	#1 Oil Temperature (red label)	#0 -- first group	ref #1	Oil Bearing Temperature
{ }	#2 Water Brake Temperature	#1 -- first group	ref #2	Shroud Temperature
{ }	#8 T/C cable (for H/S valve temp -- green label)	#0 -- second group	ref #9	Inlet Temp. (green label #12)

{ } LTS-101: TC cable #10 Shared with Allison. Disconnect the thermocouple line, and connect to red TC #5 at the exhaust duct, just after the nozzle. (Note: the roof temperature on Genesis is actually this measurement at the down stream duct temperature.)
Allison: TC cable #10 is shared with LTS-101. Disconnect the thermocouple line, and connect to TC #4. (Note, TC #4 is buried under the insulation coating.)

{ } Switch Com Port 3 out of the computer to the Allison / LTS-101.
Allison: Goes to the 6 dB Analog Devices Card.
LTS-101: Goes to the linear motion controller.
-- on the floor, by the linear motion controller. You need the male to male adapter to connect the linear motion controller.

{ } Unplug the stepper motor for the Allison and plug in the linear motion controller for the LTS-101 (and vice versa). *-- Power strip under the work bench.*

{ } Switch the two connections to the Compumotor.
1) Encoder for LTS-101 and Allison.
2) Power for stepper motor: LTS-101 and Allison.

{ } Switch the fuel line so that it is connected to the Allison/LTS-101. There are two valves to change: -- Fuel actuator for LTS-101, turbine governor throttle lever for Allison.
a) the 3 way valve. *-- Turn black handle up, tough turn for LTS-101. From front of LTS-101, left side. Up for LTS-101, down for Allison.*
b) Apollo yellow handled valve *-- Out of line for LTS-101*

{ } Move the switch on the LTS-101 junction box to the Allison/LTS-101 position. This switch selects which fuel solenoid is actuated by Genesis. *-- Gray box, right side of LTS-101.*

{ } Open the oil vent on the engine you plan to run and shut it on the other engine.
-- copper tube, yellow handle, in line for LTS-101, out of line to shut off Allison (and vice versa). Make sure the oil tank is full.

{ } Connect the battery of the engine you plan to run and disconnect the batter of the other engine.

{ } Open the exhaust for the engine you plan to run and shut it off for the other engine.

{ } Seal Allison inlet air duct with fiberglass piece. Connect the LTS-101 inlet air duct insert (or vice versa).

{ } Change the T45 / EGT Newport to the engine you plan to run (back of the Newport panel).
-- yellow: Allison T45 is between gas and power turbine. LTS-101 EGT is downstream of gas generator turbine.

{ } Switch the N1 Newport to the engine you plan to run.
-- Back of Newport panel on the right hand side. Gray wires.

Appendix B Open Loop Power Spectral Density Plots

The purpose of this appendix is to show the PSD plots for all sensors at different operating points.

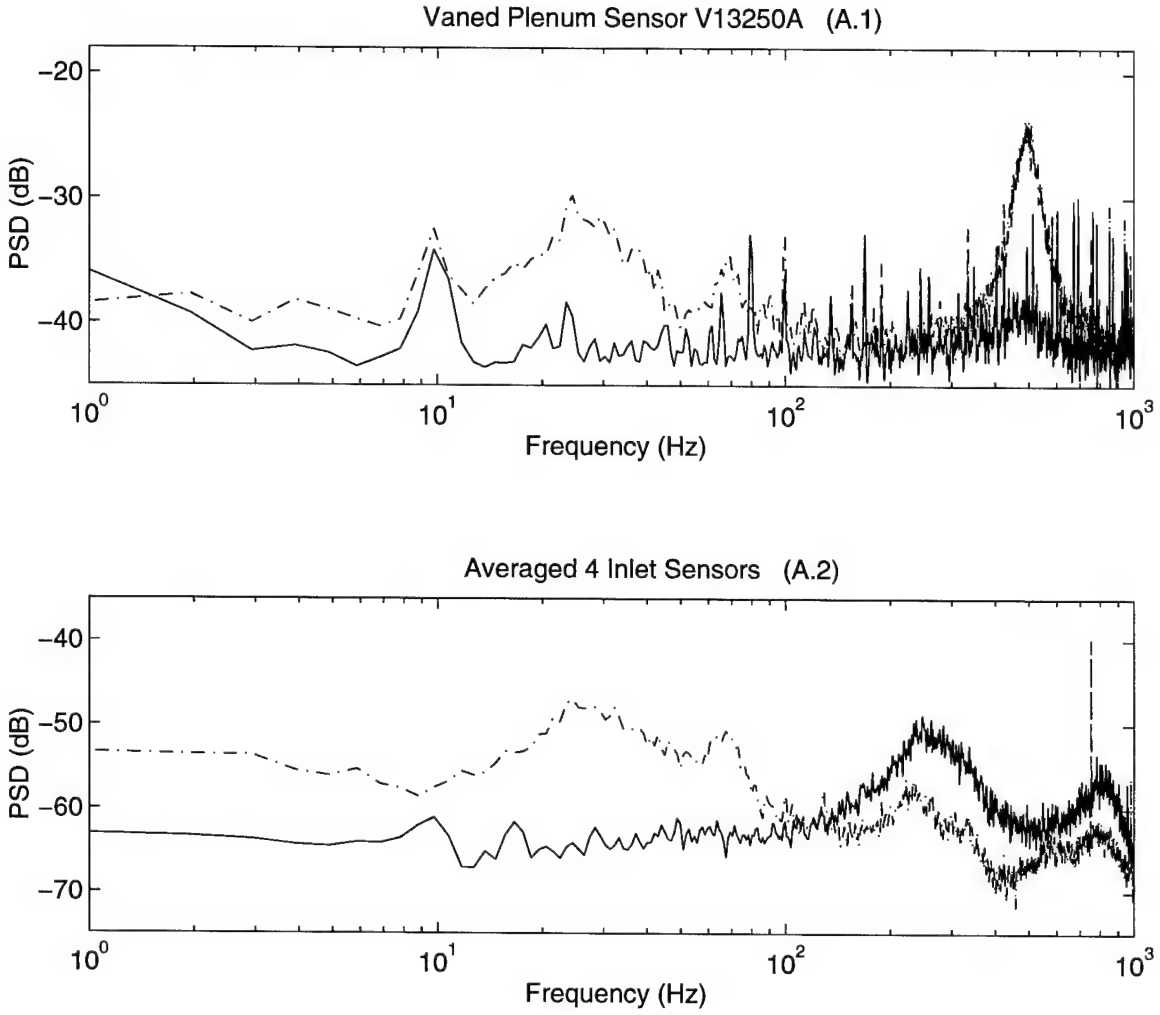

Figure B.1A Power Spectral Density: Dark Line -- Prior to Choked Exit Nozzle Dash Pot Line -- Intermediate Loading Condition

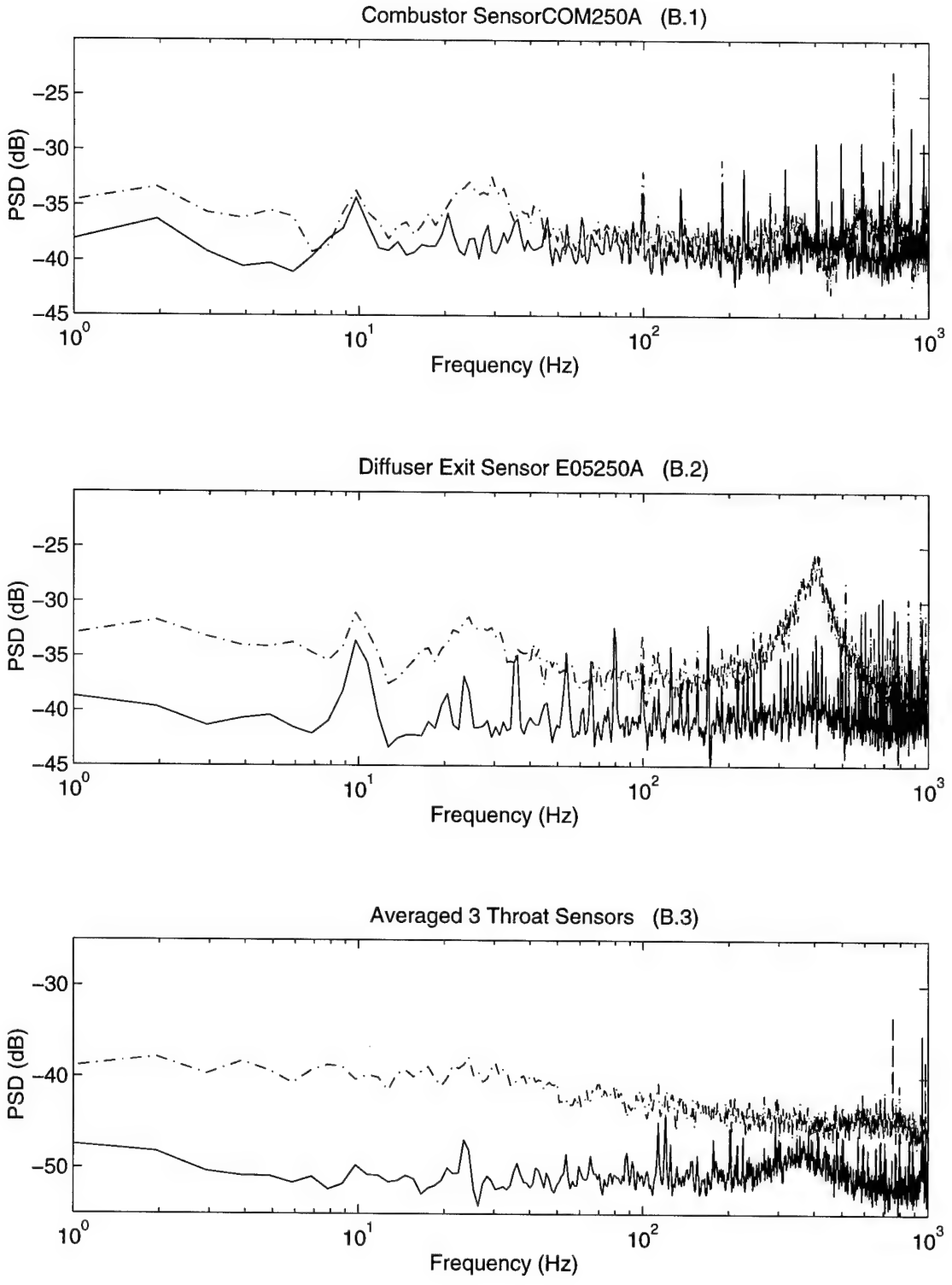

Figure B.1B Power Spectral Density: Dark Line -- Linear Actuator Position at 1.15" Dash Pot Line -- Linear Actuator Position at 1.275".

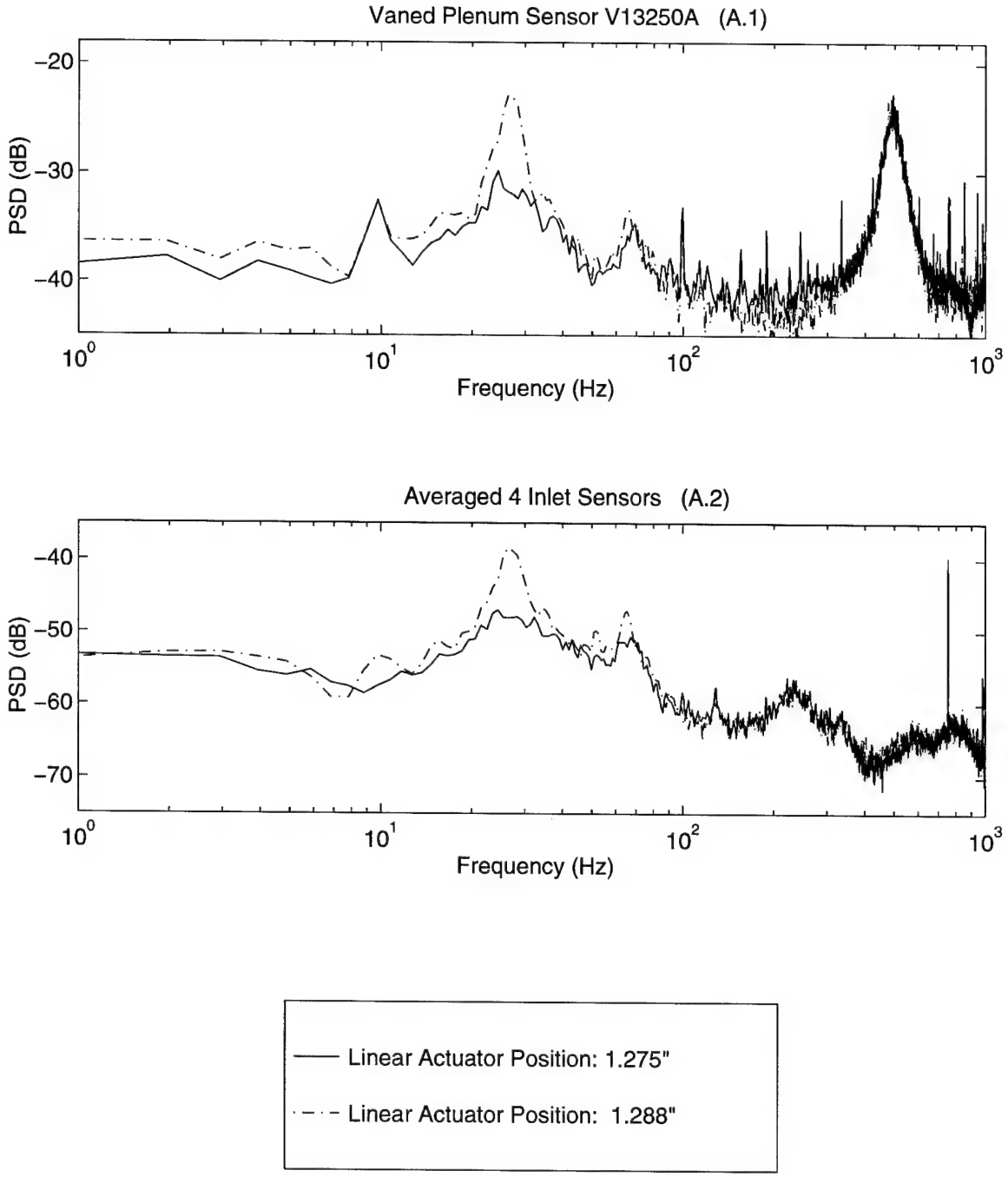

Figure B.2A Power Spectral Density: Dark Line -- Intermediate Loading Condition Dash Pot Line -- Operating Prior to Surge

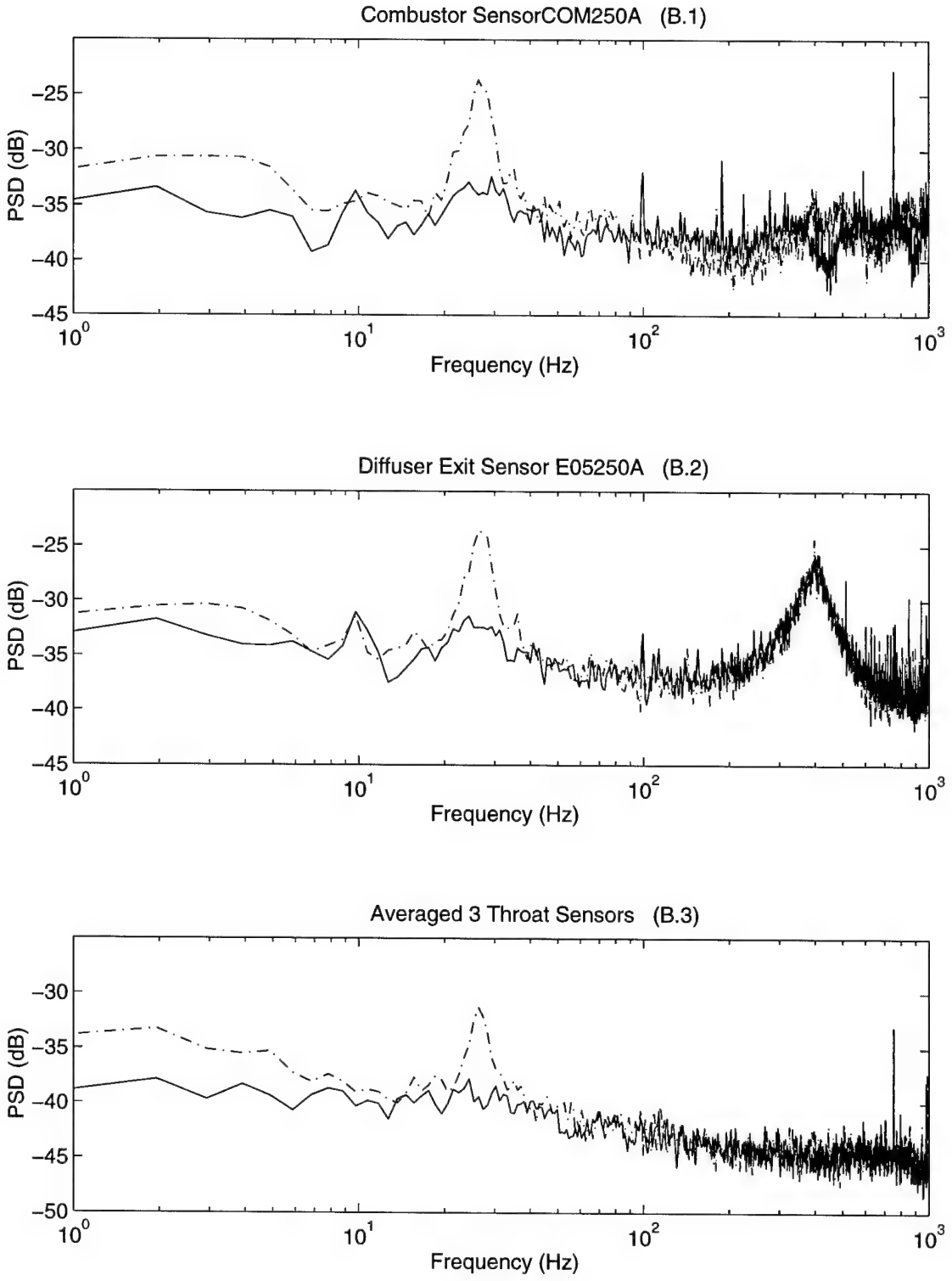

Figure B.2B Power Spectral Density: Dark Line -- Linear Actuator Position at 1.275" Dash Pot Line -- Linear Actuator Position at 1.288"

Appendix C

Discrete Forcing Frequencies

The purpose of this appendix is to show the frequency values that are selected to obtain transfer functions for these experiments. The nominal forcing frequencies are the desired values for this experiment. The actual forcing frequencies are those frequencies that are discretely implemented at a rate of 2000 Hz.

Defining equations: $$x = round\left(\frac{Nom.Freq.}{2000/4096}\right) \quad \text{(C.1)}$$

$$Force\ Freq. = x*(2000/4096) \quad \text{(C.2)}$$

Nominal Frequency (Hz)	Actual Frequency (Hz)
7	6.8359
10	9.7656
13	13.1836
16	16.1133
19	19.0430
22	21.9727
26	25.8789
28	27.8320
30	29.7852
32	32.2266
40	40.0391
49	48.8281
60	60.0586
65	64.9414
70	69.8242
75	75.1953
83	83.0078
99	99.1211
115	115.2344
130	129.8828
148	147.9492
172	171.8750
200	200.1953
230	229.9805

250	250.0000
270	270.0195
300	299.8047
350	350.0977
410	410.1563
470	470.2148
550	549.8047
680	680.1758

Table C.1 Forcing Frequency Conversion Chart for Transfer Functions.

Appendix D

H-Infinity Design Problem

The purpose of this appendix is to demonstrate a simplified example of the standard H-infinity problem. The compensator solution for this problem is obtained with Matlab. This appendix is a summarization from [20]. Recall the state space representation of the plant dynamics.

$$\begin{bmatrix} \dot{x}(t) \\ z(t) \\ y(t) \end{bmatrix} = \left[\begin{array}{c|cc} A & B_1 & B_2 \\ \hline C_1 & D_{11} & D_{12} \\ C_2 & D_{21} & D_{22} \end{array}\right] * \begin{bmatrix} x(t) \\ w(t) \\ u(t) \end{bmatrix} \tag{D.1}$$

Assumptions for simplified problem:

$$D_{11} = 0 \tag{D.2}$$

$$D_{22} = 0 \tag{D.3}$$

$$D_{12}^T \begin{bmatrix} C_1 & D_{12} \end{bmatrix} = \begin{bmatrix} 0 & I \end{bmatrix} \tag{D.4}$$

$$\begin{bmatrix} B_1 \\ D_{21} \end{bmatrix} D_{21}^T = \begin{bmatrix} 0 \\ I \end{bmatrix} \tag{D.5}$$

(A, B_1) and (A, B_2) are stabilizable.

(A, C_1) and (A, C_2) are detectable.

The controller is found by solving the following controller and observer Riccati equations for the constant matrices X_∞ and Y_∞:

$$X_\infty A + A^T X_\infty + C_1^T C_1 + X_\infty B_1 B_1^T X_\infty - X_\infty B_2 B_2^T X_\infty = 0 \qquad \text{(D.6)}$$

$$Y_\infty A + A Y_\infty + B_1 B_1^T + Y_\infty C_1^T C_1 Y_\infty - Y_\infty C_2^T C_2 Y_\infty = 0 \qquad \text{(D.7)}$$

The H-infinity problem is solvable if the following conditions are satisfied:

$$X_\infty \geq 0 \qquad \text{(D.8)}$$

$$Y_\infty \geq 0 \qquad \text{(D.9)}$$

$$\lambda_{max}(X_\infty Y_\infty) < 1 \qquad \text{(D.10)}$$

A possible dynamic controller that solves the H-infinity problem is:

$$\dot{\hat{x}}(t) = A_\infty \hat{x}(t) - L_\infty y(t) \qquad \text{(D.11)}$$

$$u(t) = F_\infty \hat{x}(t) \qquad \text{(D.12)}$$

where:

$$A_\infty = A + B_1 B_1^T X_\infty + B_2 F_\infty + L_\infty C_2 \qquad \text{(D.13)}$$

$$L_\infty = -(Y_\infty^{-1} - X_\infty)^{-1} C_2^T \qquad \text{(D.14)}$$

$$F_\infty = -B_2^T X_\infty \qquad \text{(D.15)}$$

Appendix E

Transfer Function Derivation for H-Infinity Design

The purpose of this appendix is to show the state space transfer function derivation that must satisfy the weighting constraints. First, recall the robust control problem.

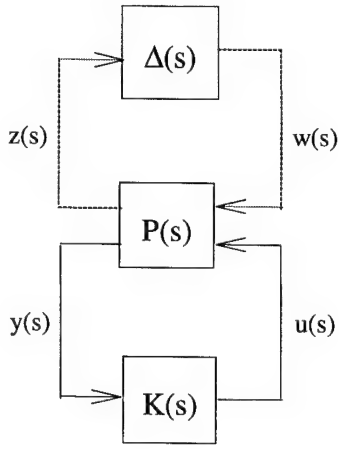

Figure E.1 Robust Control Problem

where:

$$P(s)=\begin{bmatrix} A_p & B_p \\ C_p & D_p \end{bmatrix} \tag{E.1}$$

$$K(s)=\begin{bmatrix} A_c & B_c \\ C_c & D_c \end{bmatrix} \tag{E.2}$$

Symbol	Definition
P(s)	Plant Dynamics
K(s)	Compensator which minimizes the impact of the disturbance on the error signal
Δ(s)	Uncertainty in plant dynamics model
y(s)	Measured plant output
u(s)	Control input
w(s)	Unknown plant disturbance
z(s)	plant output error signals, which are minimized.

Table E.1 Terminology Definition

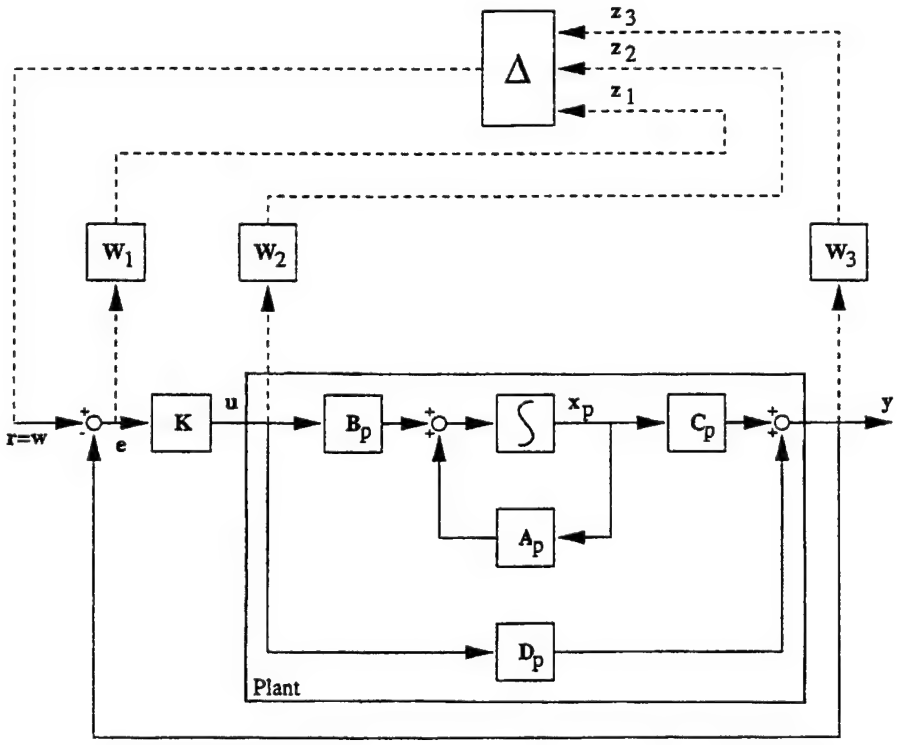

Mixed sensitivity problem.

Figure E.2 Mixed Sensitivity H-Infinity Problem.

E.1 Sensitivity Transfer Function Derivation

W_1 shapes the sensitivity transfer function (S).

$$S = \frac{e(s)}{r(s)} = (I + P(s)K(s))^{-1} \tag{E.3}$$

According to Appleby (Appendix F):

$$P_1(s)P_2(s) = \begin{bmatrix} A_1 & B_1 \\ C_1 & D_1 \end{bmatrix} * \begin{bmatrix} A_2 & B_2 \\ C_2 & D_2 \end{bmatrix} = \left[\begin{array}{cc|c} A_1 & B_1C_2 & B_1D_2 \\ 0 & A_2 & B_2 \\ \hline C_1 & D_1C_2 & D_1D_2 \end{array}\right] \tag{E.4}$$

Therefore:

$$P(s)K(s) = \left[\begin{array}{cc|c} A_p & B_pC_c & B_pD_c \\ 0 & A_c & B_c \\ \hline C_p & D_pC_c & D_pD_c \end{array}\right] \tag{E.5}$$

To define the identity matrix in state space terms:

$$\text{I} = \begin{aligned} \dot{x} &= [0]\underline{x} + [0]\underline{u} \\ y &= [0]\underline{x} + [I]\underline{u} \end{aligned} \tag{E.6}$$

where: D_I is the size of the number of inputs. Therefore:

$$I = \begin{bmatrix} 0 & 0 \\ 0 & I \end{bmatrix} \tag{E.7}$$

According to Appleby in Appendix E,

$$P_1(s)+P_2(s)=\left[\begin{array}{cc|c} A_1 & 0 & B_1 \\ 0 & A_2 & B_2 \\ \hline C_1 & C_2 & D_1+D_2 \end{array}\right] \tag{E.8}$$

Therefore

$$I+P(s)K(s)=\left[\begin{array}{ccc|c} 0 & 0 & 0 & 0 \\ 0 & A_p & B_pC_c & B_pD_c \\ 0 & 0 & A_c & B_c \\ \hline 0 & C_p & D_pC_c & I+D_pC_c \end{array}\right] \tag{E.9}$$

Finally, in general:

$$P_1(s)^{-1}=\left[\begin{array}{c|c} A-BD^{-1}C & -BD^{-1} \\ \hline D^{-1}C & D^{-1} \end{array}\right] \tag{E.10}$$

Therefore,

$$S=(I+P(s)K(s))^{-1}$$

$$=\left[\begin{array}{c|c} \left[\begin{array}{cc} A_p & B_pC_c \\ 0 & A_c \end{array}\right]-\left[\begin{array}{c} B_pD_c \\ C_c \end{array}\right]*\left[I+D_pD_c\right]^{-1}*\left[\begin{array}{cc} C_p & D_pC_c \end{array}\right] & -\left[\begin{array}{c} B_pD_c \\ B_c \end{array}\right]*\left[I+D_pD_c\right]^{-1} \\ \hline \left[I+D_pD_c\right]^{-1}*\left[\begin{array}{cc} C_p & D_pC_c \end{array}\right] & \left[I+D_pD_c\right]^{-1} \end{array}\right]$$

(E.11)

Consider each segment of the Sensitivity transfer function in state space form.

$$A_S = \begin{bmatrix} A_p & B_pC_c \\ 0 & A_c \end{bmatrix} - \begin{bmatrix} B_pD_cJC_p & B_pD_cJD_pC_c \\ B_cJC_p & B_cJD_pC_c \end{bmatrix}$$

$$= \begin{bmatrix} A_p - B_pD_cJC_p & B_pC_c - B_pD_cJD_pC_c \\ -B_cJC_p & A_c - B_cJD_pC_c \end{bmatrix} \quad \text{(E.12.1)}$$

$$B_S = \begin{bmatrix} -B_pD_cJ \\ -B_cJ \end{bmatrix} \quad \text{(E.12.2)}$$

$$C_S = \begin{bmatrix} JC_p & JD_pC_c \end{bmatrix} \quad \text{(E.12.3)}$$

$$D_S = \begin{bmatrix} J \end{bmatrix} \quad \text{(E.12.4)}$$

E.2 Actuator Transfer Function Derivation

This transfer function is shaped by W_2.

$$R(s) = \frac{u(s)}{r(s)} = K(s)*(I + P(s)K(s))^{-1} = K(s)*S(s) \quad \text{(E.13)}$$

Again, using the general form described in section D.1 for $P_1(s)*P_2(s)$:

$$A_R = \left[\begin{array}{c|cc} A_c & B_c*\begin{bmatrix} -JC_p & -JD_pC_c \end{bmatrix} \\ \hline 0 & A_p - B_pD_cJC_p & B_pC_c - B_pD_cJD_pC_c \\ & -B_pJC_p & A_c - B_cJD_pC_c \end{array}\right]$$

$$= \begin{bmatrix} A_c & -B_c JC_p & -B_p JD_p C_c \\ 0 & A_p - B_p D_c JC_p & B_p C_c - B_p D_c JD_p C_c \\ 0 & -B_p JC_c & A_c - B_c JD_p C_c \end{bmatrix} \quad \text{(E.14.1)}$$

$$B_R = \begin{bmatrix} B_c \\ \hline B_p D_c J \\ B_c J \end{bmatrix} \quad \text{(E.14.2)}$$

$$C_R = \left[C_c \mid D_c \left[-JC_p \quad -JD_p C_c \right] \right] = \left[C_c \mid -D_c JC_p \quad -D_c JD_p C_c \right] \quad \text{(E.14.3)}$$

$$D_R = \left[D_c J \right] \quad \text{(E.14.4)}$$

E.3 Complimentary Sensitivity Transfer Function Derivation

This transfer function is confined by W_3.

$$C(s) = \frac{y(s)}{r(s)} = P(s) * K(s) * (I + P(s)K(s)))^{-1} = P(s) * R(s) \quad \text{(E.15)}$$

Again, using the general form described in section D.1 for $P_1(s) * P_2(s)$:

$$A_c = \left[\begin{array}{c|cc} A_p & B_p * \left[C_c \quad -D_c JC_p \quad -D_c JD_p C_c \right] \\ \hline & A_c & -B_c JC_p & -B_p JD_p C_c \\ 0 & 0 & A_p - B_p D_c JC_p & B_p C_c - B_p D_c JD_p C_c \\ & 0 & -B_p JC_c & A_c - B_c JD_p C_c \end{array}\right]$$

$$= \begin{bmatrix} A_p & B_p C_c & -B_p D_c J C_p & -B_p D_c J D_p C_c \\ 0 & A_c & -B_c J C_p & -B_c J D_p C_c \\ 0 & 0 & A_p - B_p D_c J C_p & B_p C_c - B_p D_c J D_p C_c \\ 0 & 0 & -B_c J C_p & A_c - B_c J D_p C_c \end{bmatrix} \quad \text{(E.16.1)}$$

$$B_c = \begin{bmatrix} \dfrac{B_p D_c J}{B_c J} \\ B_p D_c J \\ B_c J \end{bmatrix} \quad \text{(E.16.2)}$$

$$C_c = \left[C_p \;\middle|\; D_p \left[C_c \quad -D_c J C_p \quad -D_c J D_p C_c \right] \right]$$

$$= \left[C_p \quad D_p C_c \quad -D_p D_c J C_p \quad -D_p D_c J D_p C_c \right] \quad \text{(E.16.3)}$$

$$D_c = \left[D_p D_c J \right] \quad \text{(E.16.4)}$$

Appendix F

Transfer Function Manipulations for State Space Systems

The following information is provided in [42].

Given a transfer function

$$P(s) = C(sI - A)^{-1}B + D \tag{F.1}$$

This thesis uses standard form to represent the state space system:

$$P(s) \doteq \left[\begin{array}{c|c} A & B \\ \hline C & D \end{array}\right] \tag{F.2}$$

The transfer function manipulations are:

$$P^T(s) \doteq \left[\begin{array}{c|c} A^T & B^T \\ \hline C^T & D^T \end{array}\right] \tag{F.3}$$

$$P(-s) \doteq \left[\begin{array}{c|c} -A & -B \\ \hline C & D \end{array}\right] \tag{F.4}$$

$$P^{-1}(s) \doteq \left[\begin{array}{c|c} A - BD^{-1}C & -BD^{-1} \\ \hline D^{-1}C & D^{-1} \end{array}\right] \tag{F.5}$$

$$P_1(s) + P_2(s) = \left[\begin{array}{cc|c} A_1 & 0 & B_1 \\ 0 & A_2 & B_2 \\ \hline C_1 & C_2 & D_1 + D_2 \end{array}\right] \tag{F.6}$$

$$P_1(s)P_2(s) = \left[\begin{array}{c|c} A_1 & B_1 \\ \hline C & D_1 \end{array}\right] * \left[\begin{array}{c|c} A_2 & B_2 \\ \hline C_2 & D_2 \end{array}\right]$$

$$= \left[\begin{array}{cc|c} A_1 & B_1C_2 & B_1D_2 \\ 0 & A_2 & B_2 \\ \hline C_1 & D_1C_2 & D_1D_2 \end{array}\right] = \left[\begin{array}{cc|c} A_2 & 0 & B_2 \\ B_1C_2 & A_1 & B_1D_2 \\ \hline D_1C_2 & C_1 & D_1D_2 \end{array}\right] \qquad \text{(F.7)}$$

Appendix G Open and Closed Loop Power Spectral Density Plots

The purpose of this appendix is to show the PSD plots for all sensors at different operating points. The closed loop plots are from the "best two sided compensator".

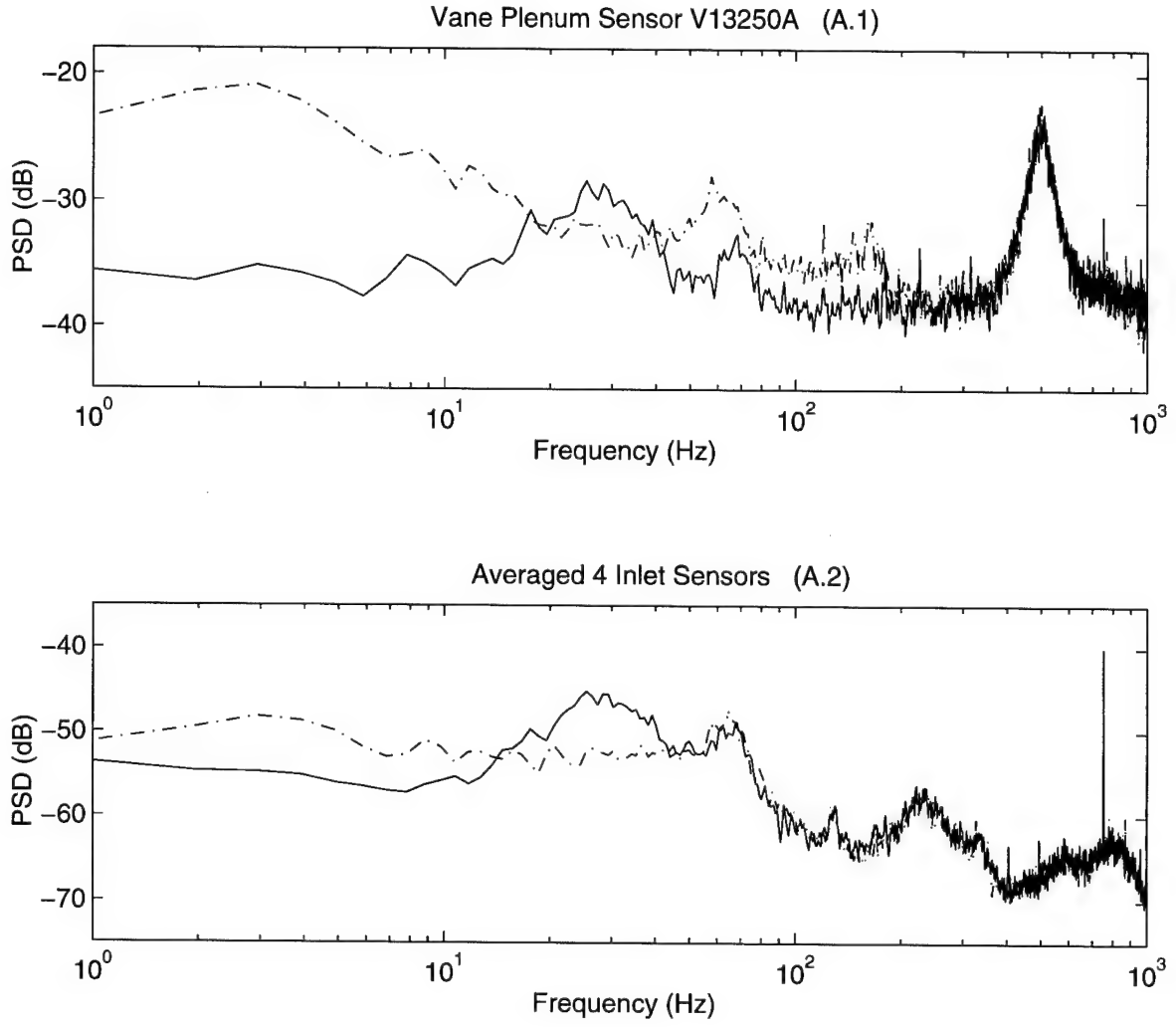

Figure G.1A Power Spectral Density at a Load of ~ 1180 lb Force.

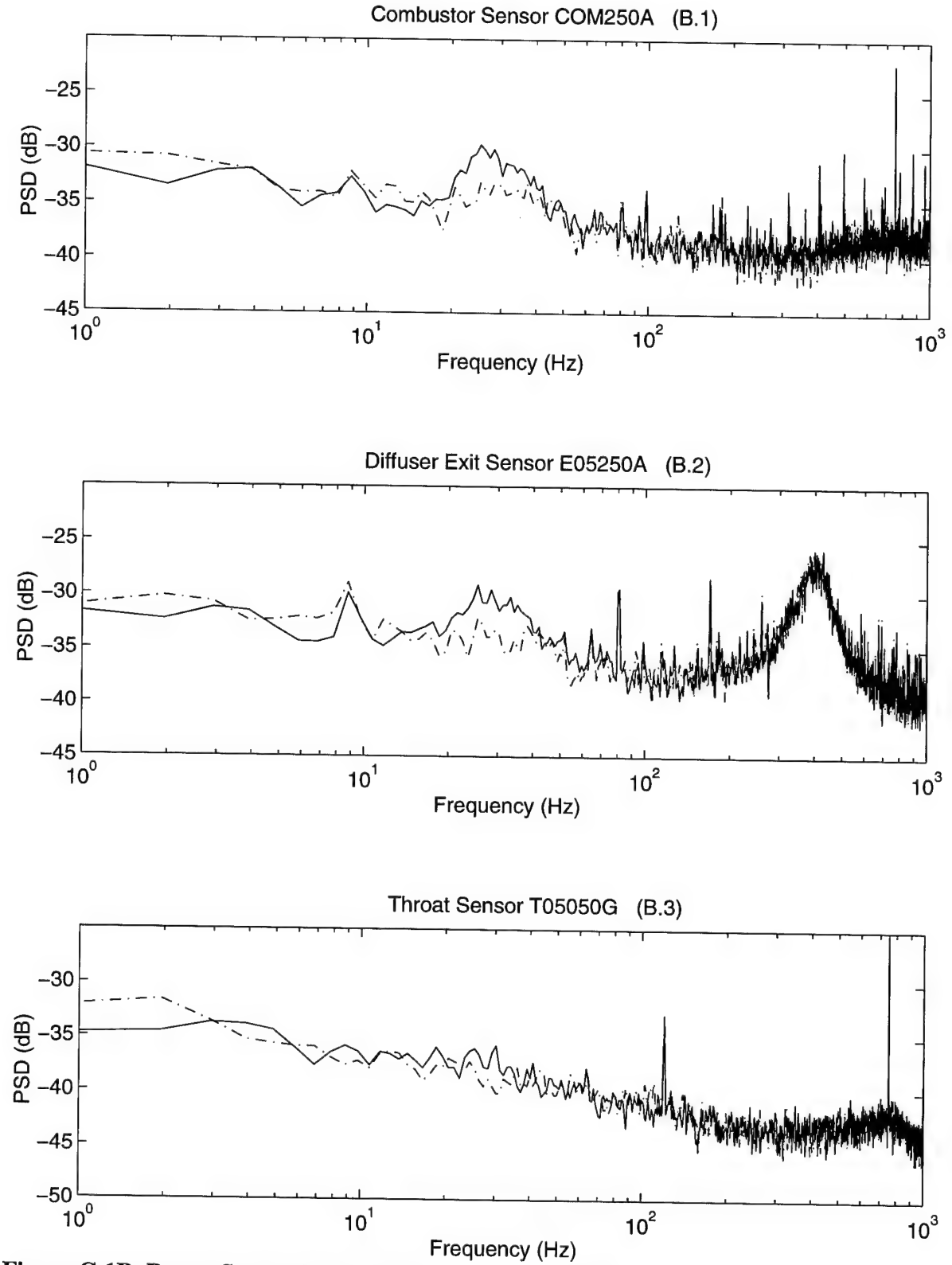

Figure G.1B Power Spectral Density at a Load of ~ 1180 lb Force.

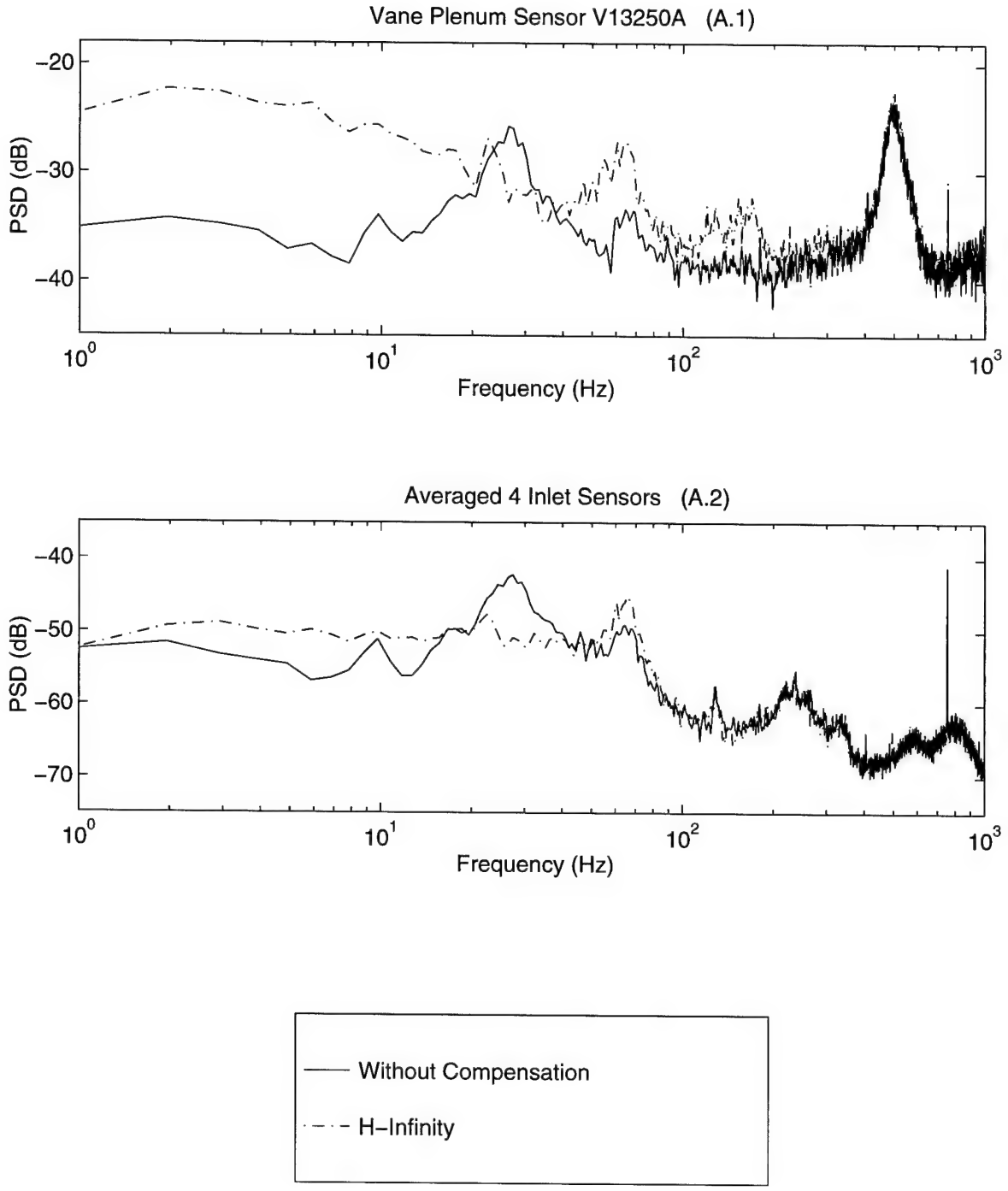

Figure G.2A Power Spectral Density at a Load of ~ 1190 lb Force.

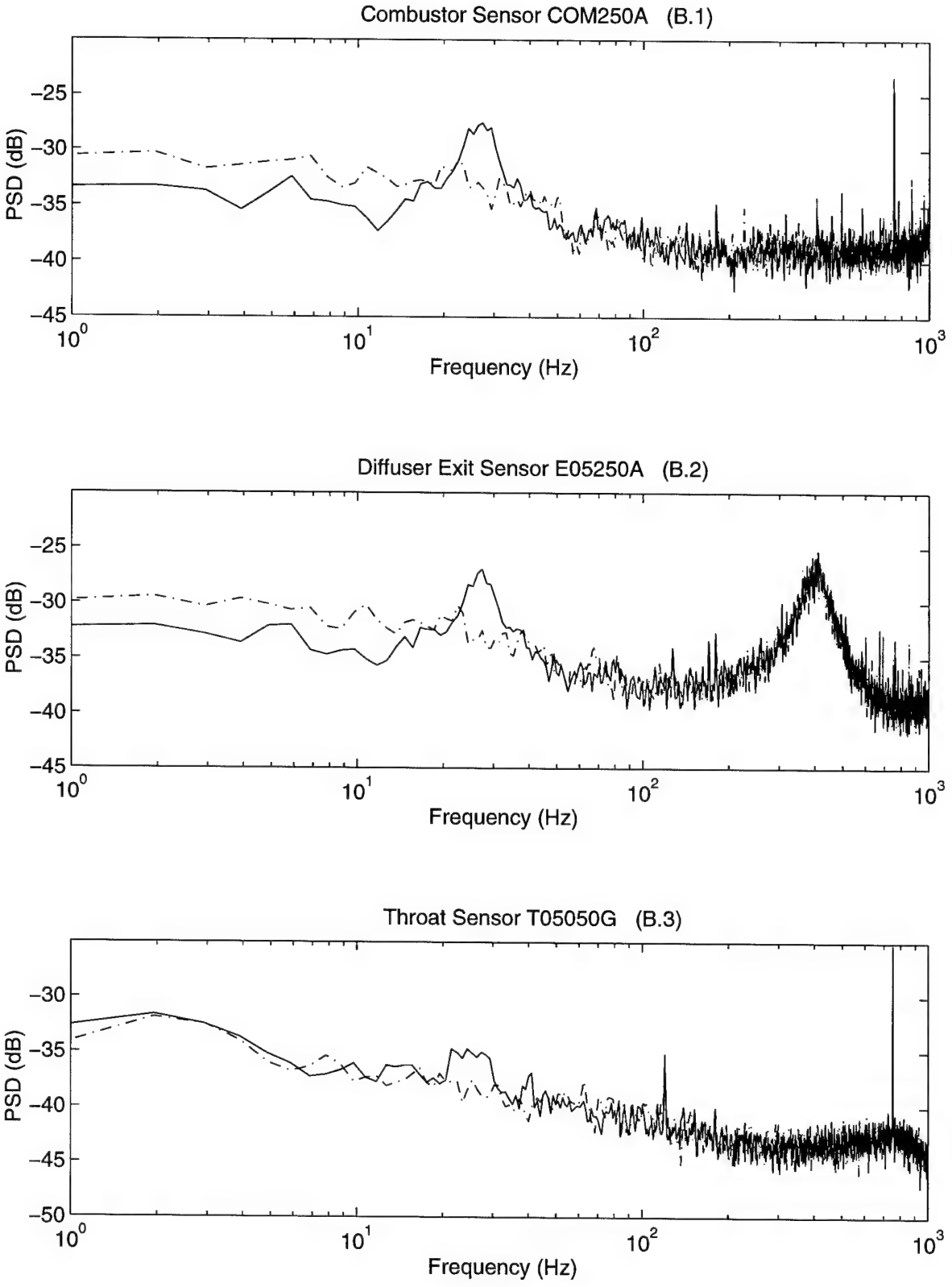

Figure G.2B Power Spectral Density at a Load of ~ 1190 lb Force.

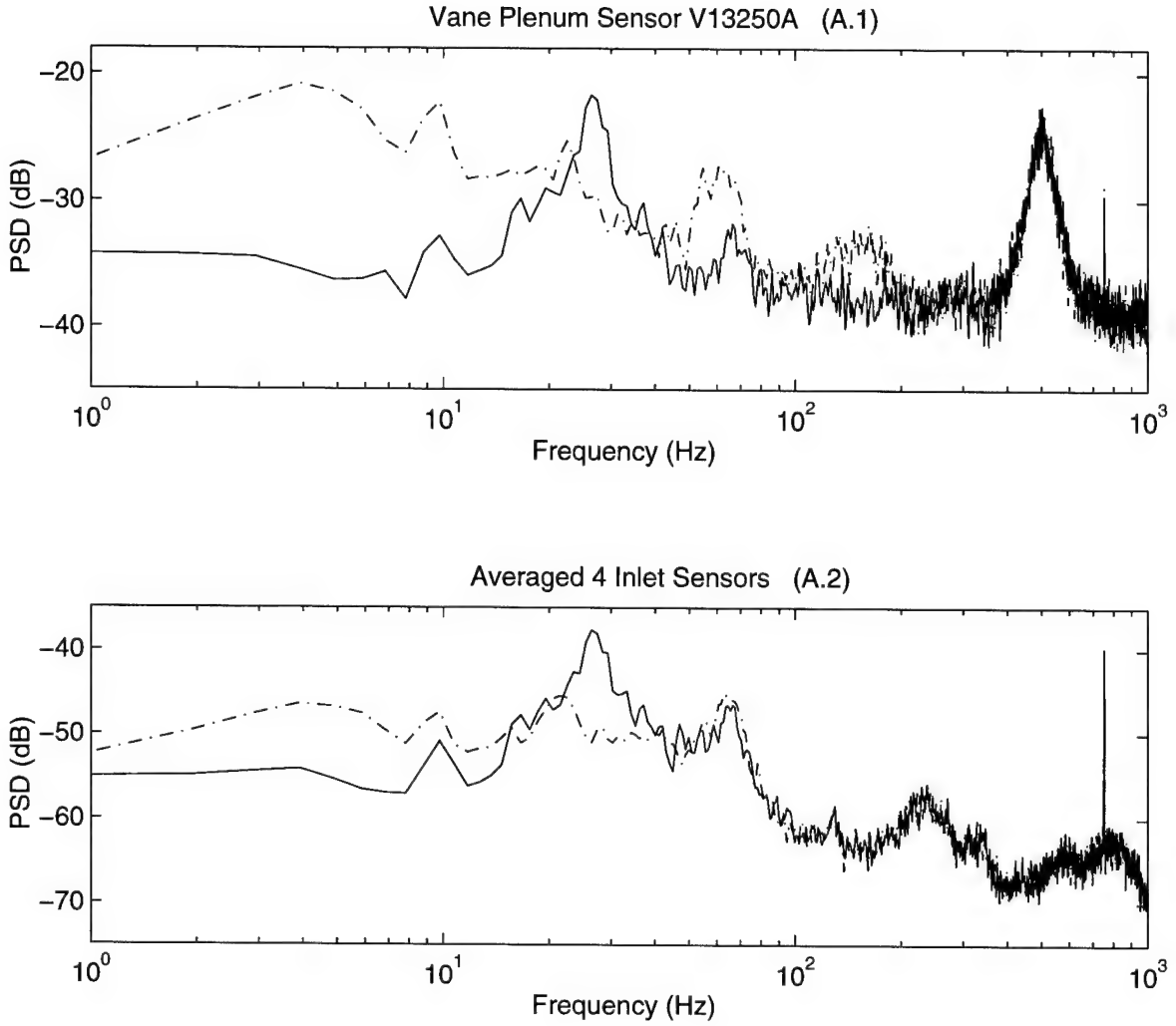

Figure G.3A Power Spectral Density at a Massflow Immediately Prior to Open Loop Surge.

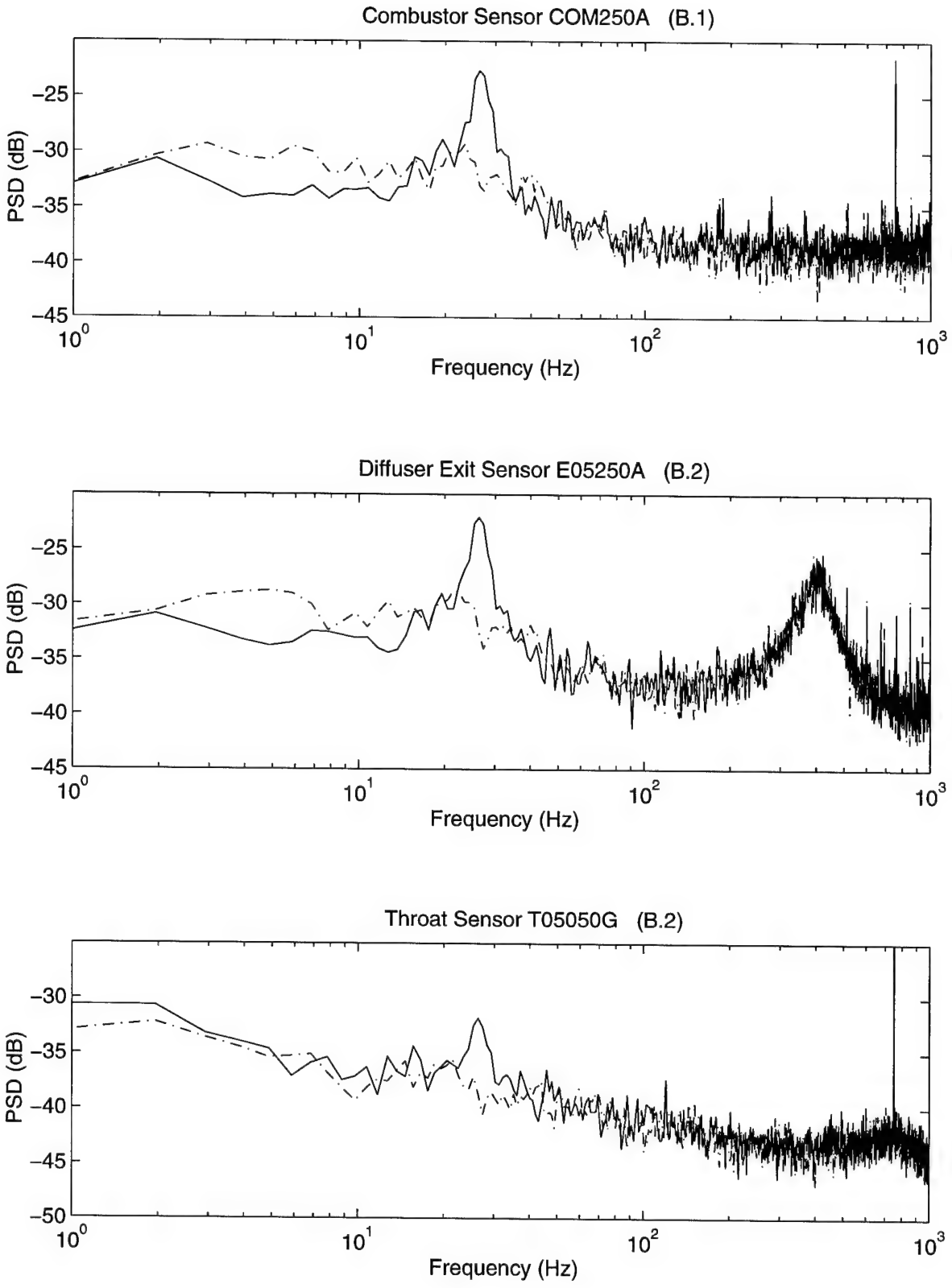

Figure G.3B Power Spectral Density at a Massflow Immediately Prior to Open Loop Surge.

Appendix H

Transmission Matrices of Compact Acoustic Elements

The purpose of this appendix is to define the relationships used in the modeling chapter. These relationships are defined in [43]

H.1 Nondimensionalization

$$\psi = \frac{P}{\rho a^2} \tag{H.1}$$

$$\phi = \frac{u}{a} \tag{H.2}$$

$$s = i\omega = i\frac{1/t}{a/L} \tag{H.3}$$

All velocities are defined from left to right.

H.2 Components

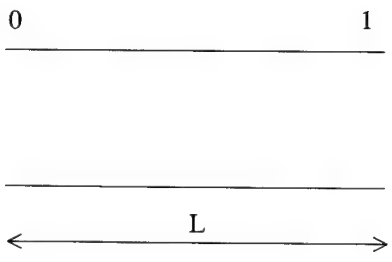

Figure H.1 Short Duct

$$\begin{bmatrix} \psi_1 \\ \phi_1 \end{bmatrix} = \begin{bmatrix} 1 & -s \\ 0 & 1 \end{bmatrix} * \begin{bmatrix} \psi_0 \\ \phi_0 \end{bmatrix} \qquad \text{Short Duct} \qquad \text{(H.4)}$$

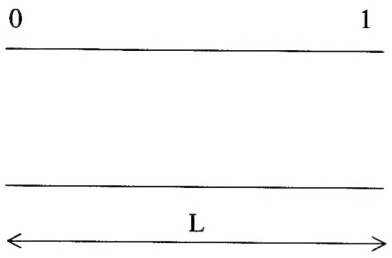

Figure H.2 Acoustic Duct

$$\begin{bmatrix} \psi_1 \\ \phi_1 \end{bmatrix} = \begin{bmatrix} \cos(L*\omega/a) & -i*\sin(L*\omega/a) \\ -i*\sin(L*\omega/a) & \cos(L*\omega/a) \end{bmatrix} * \begin{bmatrix} \psi_0 \\ \phi_0 \end{bmatrix} \quad \text{Acoustic Duct} \quad \text{(H.5)}$$

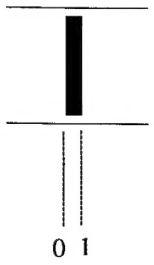

Figure H.3 Actuator Disk: Represents the Compressor

$$\begin{bmatrix} \psi_1 \\ \phi_1 \end{bmatrix} = \begin{bmatrix} 1 & m_c \\ 0 & 1 \end{bmatrix} * \begin{bmatrix} \psi_0 \\ \phi_0 \end{bmatrix} \qquad \text{Actuator Disk} \qquad \text{(H.6)}$$

Where $m_c = \dfrac{d\Psi_T}{d\Phi} * \left(\dfrac{U_{ref}}{a} \right)^2$, U_{ref} = The reference velocity in definition of ψ_c.

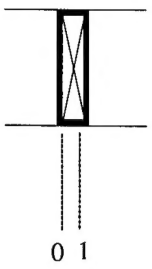

Figure H.4 Throttle

$$\begin{bmatrix} \psi_1 \\ \phi_1 \end{bmatrix} = \begin{bmatrix} 1 & -m_T \\ 0 & 1 \end{bmatrix} * \begin{bmatrix} \psi_0 \\ \phi_0 \end{bmatrix} \qquad \text{Throttle} \qquad \text{(H.7)}$$

Where $m_T = \frac{d\Psi_T}{d\Phi} * \left(\frac{U_{ref}}{a} \right)^2$, U_{ref} = The reference velocity in definition of ψ_T.

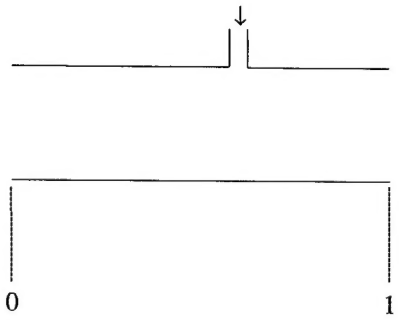

Figure H.5 Continuity: Injector Air Addition

$$\begin{bmatrix} \psi_1 \\ \phi_1 \end{bmatrix} = \begin{bmatrix} 1 & 0 \\ 0 & 1 \end{bmatrix} * \begin{bmatrix} \psi_0 \\ \phi_0 \end{bmatrix} + \begin{bmatrix} 0 \\ a_s \end{bmatrix} \phi_{inj} \qquad \text{Air Injection} \qquad \text{(H.8)}$$

Where $\phi_s = \frac{V_{injector}}{a}$; $a_s = \frac{A_{speaker}}{A_{duct}}$,

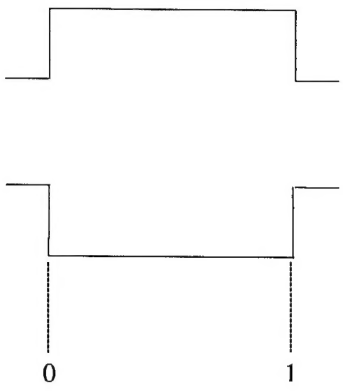

Figure H.6 Lumped Combustor

$$\begin{bmatrix} \psi_1 \\ \phi_1 \end{bmatrix} = \begin{bmatrix} 1 & 0 \\ -s/a_1 & a_0/a_1 \end{bmatrix} * \begin{bmatrix} \psi_0 \\ \phi_0 \end{bmatrix} \qquad \text{Lumped Combustor} \qquad \text{(H.9)}$$

Where $a_o = \frac{A_o}{A_{ref}}$; $a_1 = \frac{A_1}{A_{ref}}$; *and* $L = \frac{V}{A_{ref}}$

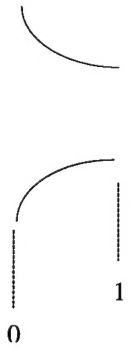

Figure H.7 Contraction With Mean Flow

$$\begin{bmatrix} \psi_1 \\ \phi_1 \end{bmatrix} = \begin{bmatrix} 1 & \Phi_o(1-a_r^2) \\ 0 & a_r \end{bmatrix} * \begin{bmatrix} \psi_0 \\ \phi_0 \end{bmatrix} \qquad \text{Contraction} \qquad \text{(H.10)}$$

Where $a_r = \frac{A_o}{A_1}$ and Φ_0 is the mean flow (valid if M < 1)

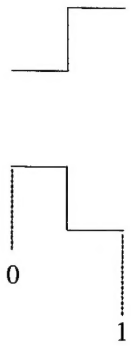

Figure H.8 Sudden Expansion With Mean Flow

$$\begin{bmatrix} \psi_1 \\ \phi_1 \end{bmatrix} = \begin{bmatrix} 1 & 2\Phi_o(a_r - a_r^2) \\ 0 & a_r \end{bmatrix} * \begin{bmatrix} \psi_0 \\ \phi_0 \end{bmatrix} \qquad \text{Sudden Expansion} \qquad \text{(H.11)}$$

Where $a_r = \dfrac{A_o}{A_1}$ and Φ_0 is the mean flow (valid if M < 1)